The Design of Optical Waveguide Devices

Roderick William Charles Vance

A thesis submitted for the degree of

Doctor of Philosophy at the

Australian National University

29^{th} of July, 1994

Foreword

This thesis is an account of research undertaken in the Optical Sciences Centre within the Institute of Advanced Studies at the Australian National University between March 1992 and July 1994 whilst I was enrolled for the degree of Doctor of Philosophy.

The work presented herein is my own but my supervisors and co-workers contributed to my research as follows:

- In Chapter-3, Dr. John Love was responsible for identifying the need to investigate the source of coupler back-reflexions as well as suggesting the solution of the simplified coupled mode equations as the basic method to for effecting this study. The details of this research, following straightforwardly from this important guidance, are otherwise my own work;

- In Chapter-4, the simulation of commercial couplers and the calculation of optimally short designs using delineation curves were suggested by Dr. John Love;

- In Chapter-5, Dr. Adrian Ankiewicz initiated the investigation of the effects of tapering on the noise performance of erbium doped fibre amplifiers. The detailed formulation, using a state-space approach, the derivation of the integral equations describing noise-optimal tapers and the details of their solution are wholly my own work;

- The planar coupler design project of Chapters-6, 7, 8 and 9 is totally my own work although I benefitted from discussions with several mathematicians, as detailed in the "Acknowledgements", in formulating a Lie group theoretic approach to the problem;

- In Chapter-10, Dr. John Love was responsible for the basic ideas of *(i)* the use of mode-multiplexed communications, *(ii)* the generalisation of the formerly studied two-channel splitters to higher numbers of channels and *(iii)*

the identification of crosstalk and loss arising from misalignment in the splicing of mode-multplexing splitters to external waveguides as important system design issues.

None of this work has been submitted for any other degrees at this or any other institution of learning.

Roderick W. C. Vance

"It's a funny old world, idn't, eh?"
—Alexei Sayle, "Stuff"

Publications

Accepted Works

Vance, R. W. C. & Love, J. D., Asymmetric adiabatic multiprong for mode-multiplexed systems, *Electronics Letters*, **29**, 1994, pp. 2134-2136

Vance, R. W. C. & Love, J. D., Design procedures for planar passive coupled waveguide devices, *IEE Procedings-J: Optoelectronics*, **141**, 1994, pp. 231-241

Vance, R. W. C. & Ankiewicz, A., State-space description of optimal erbium amplifier tapers, *Applied Optics*, **33**, 1994, pp. 6992-7001

Vance, R. W. C., Planar ring-resonator realisation of symmetric 3×3 fibre coupler, *Electronics Letters*, **29**, 1994, pp. 1222-1224

Vance, R. W. C. & Barrow, R., General linear differential interferometers, *Journal of the Optical Society of America, A*, **12**, 1995, pp.346-353

Vance, R. W. C., Matrix Lie-group theoretic design of coupled linear optical waveguide devices, *SIAM Journal of Applied Mathematics, in press*

Love, J. D., Vance, R. W. C. & Joblin, A., Asymmetric, adiabatic multipronged planar splitters, *Optical and Quantum Electronics, in press*

Submitted for Publication

Vance, R. W. C., Planar linear coupler design procedure using Mach-Zehnder interferometer cascades, *submitted to IEEE Journal of Lightwave Technology*

Vance, R. W. C. & Love, J. D., Back-reflexion from fused biconic couplers, *submitted to IEEE Journal of Lightwave Technology*

Sumer is icumen in

— *Traditional "Cuckoo Song" c.1250 welcoming Midsummer*

Acknowledgments

On the Third of February, 1986, as a raw graduate in electronics engineering, I began a two-year association and friendship with two truly remarkable engineers, Chuck Ziegler and John Payne. For my growth and development as a professional engineer, I owe to these two men far more than to any other person or aspect of either my working life or education. My heartfelt thanks goes out to them as well as to the other members of the "engine-room" in the small Melbourne firm where I spent those important two years — especially the two Daves Sutcliffe & Wilson, David Miles, Ray Durrell and our project leader Kevin Jones, who saw to it, with both humour and supreme knack and deftness, that a whit of sanity somehow prevailed.

I then joined a much more grandiose firm and in the four years thereafter my engineering career stumbled along somewhat more labouredly, yet this time in my professional life was important insofar as I was, at least, introduced to optical fibre devices and sensing. Ross Barrow lit the way for me here, sharing with me a prodigious, hands-on experience in the field that he had gained in the foregoing years. Also deserving special thanks are co-workers Peter Stone and Chris Baharis as well as those who encouraged me to undertake my PhD. studies — Drs. Anis Inayat-Hussain, David Fox and Ian Bassett.

Here at the Australian National University, I should most sincerely like to thank my supervisors Drs. John Love and Adrian Ankiewicz. Although heavily-overladen with the outside commitments and offices befitting to a distinguished academic, John always somehow found the time to discuss our work and explain his ideas, as well as to give encouragement when many of mine were stillborn and most of the rest, although having taken root, shrivelled and withered away without bearing

fruit. However, just the weeest few throve, but without John's support, they would never have been brought together in this thesis. John also put considerable effort into proofreading and helping me redraught my thesis and showed admirable forbearance in this task. Quite clearly annoyed by the shredded, hacked and bludgeoned style of my first draught, yet ever the English gentleman, the worst he could euphemistically say was to describe its reading as a "penance", to my hearty amusement — I'd have used some stronger downunder adjectives to describe it on rereading what I had written. Adrian supervised my work on erbium amplifier tapers and I was utterly astounded and enlightened by the breadth of his knowledge for not only guided wave optics, but also the broader affairs of the world. A meeting with Adrian and his sardonic, off-beat sense of humour would never fail to lift my spirits and help me laugh at the riling, the petty, the outlandish and the absurd, which there are many examples of in any large organisation.

Dr. Simon Hewlett happily gave many hours of his time to discuss and explore new ideas. My work has gained much from his comments and I have made specific reference to his help wherever I could in the thesis. However, this is not always possible as, being office-mates, we exchanged our ideas freely and his knowhow wasn't so much as taught to me as it "rubbed-off" on me. I therefore cannot remember and explicitly acknowledge every instance of his generous help, although it has unquestionably been a significant contribution.

I also received considerable outsider help. Many thanks are owing to Danny Wong, David Psaila, David Thorncraft and Paul Robinson of the Optical Fibre Technology Centre at the University of Sydney for their training in the art of fused biconic coupler fabrication and technical support in the experiments outlined in Chapter-3. Dr. Mark Sceats, also of the Optical Fibre Technology Centre, gave many helpful discussions on the nature of surface roughness on glass-air interfaces and its possible role in the production of back reflexions from fused biconic couplers. For the work in Chapter-7, I had to become acquainted with the theory of Lie groups and in this self-teaching effort I thank the many mathematicians I corresponded with through the Internet newsgroup sci.math, especially Marcel Roelofs of the Research Institute for Applications of Computer Algebra at Computer Algebra Netherland for providing me a copy of his own Lie algebra manipulation software

packages, even going so far as to upgrade them for floating-point Lie computations. Dr. Michael Hall of the Department of Theoretical Physics at the Australian National University reviewed and checked my work of Chapter-7 and put considerable effort into proofreading my papers on the topics therein. Above all, I thank the late Dr. Roger Richardson, of the Centre for Mathematics and its Applications at the Australian National University for generously giving many hours of his time to help with my self-teaching effort. For the work in Chapter-9 I also thank the Broken Hill Proprietary Company Ltd. for permission to include their interferometric magnetometer examples and Drs. Anis Inayat-Hussain and Glenn Bryant for their review of and comments about the mathematical analysis.

Through the last two and a half years, I have learnt enormously about Xwindows under networked Unix, an environment which I was formerly utterly unfamiliar with. For the generous help I have received here, I thank Javid Atai, Adrian Sheppard, Shiu Tin, Julie Dalco, Simon Hewlett and Andrew Tridgell. For welcome down-to-earth help through the tangled welter of University administrative red tape I often had to hack through I warmly thank the departmental administrators Andrea Robins and Rebecca Palavaccini.

Lastly, but not leastly, I gratefully acknowledge my three financial sponsors that made posiible the research to be described: the Australian People, through an Australian Postgraduate Research Award allocated by the Australian National University, the Australian Telecommunications and Electronics Research Board and ANUTech, Pty. Ltd. Let us all hope that in this era of rabid privatisation and commercialisation of State functions, such awards will continue, thanks to some foresightful political leader in this country, to be awarded to future postgraduate students.

Abstract

This thesis investigates novel passive and active devices, with emphasis on their practicality arising from the enhanced control of device dimensions available in planar integrated optics technology, as well as from tapering techniques applicable to fused-biconic couplers and tapered erbium-doped fibre amplifiers (EDFAs). It begins with a brief outline of the main numerical techniques used. Theoretical models are then proposed to explain the origin of back-reflexions from fused-biconic couplers and some models are also experimentally tested. To date, optical fibre connectors and splices have been the main source of reflexions but their design and fabrication have now reached such sophistication that the fused-biconic coupler has become the main source. Although small, reflexions can destabilise network source lasers, thus the theories proposed in this thesis may well be applicable to the improvement of network noise performance through low-reflexion couplers. The study of fused-biconic couplers also includes an investigation of tapering control with the aim of shortening existing devices.

The advantages of the dimension control afforded by tapering to erbium doped fibre amplifiers are explored by formulating an analytical description of these devices and deriving integral equations for taper designs optimising saturation power, EDFA length and output signal-to-noise ratio for a given gain. These equations are solved numerically and the resulting EDFA taper designs are appraised and compared with conventional devices.

An extensive study of planar linear coupler design then forms a major part of the thesis. The main problem addressed is that, whereas many useful optical devices make use of *nonplanar* arrangements of optical fibres, wholly *planar* emulations of these devices must be devised if they are to be incorporated into integrated optics systems. The main result is the derivation of a fully general, systematic design procedure for a *planar* design to realise an $N \times N$ linear coupler with *any* given transfer matrix. The procedure is used to derive full designs of planar mimics for the symmetric 3×3 and 5×5 fibre couplers. The proof of the universality of the design procedure is also illustrated in the 2×2 coupler case, where the design steps can be visualised as rigid rotations of the Poincaré Sphere.

This work is very general, with a wide range of potential applications. The spe-

cific 3×3 and 5×5 coupler examples have application in optical signal processing, integrated optic interferometric sensors and coherent communications. The devices produced by the general procedure are concatenations of basic building-block couplers interspaced by controlling optical delay-lines and it may be possible to control their transfer matrices *dynamically* if the delays are electro-optically adjusted, thus achieving such devices as *(i)* an adjustable $N \times N$ cross-point switch able to distribute any group of incoming signals to any group of outputs or *(ii)* adjustable couplers for adaptive signal processing.

The planar device designs also illustrate the importance, to resilience against temperature and source-frequency drifts, of *differential* behaviour, *i.e.* where the transfer functions depend only on the *difference between* two optical pathlengths rather than the absolute length of each path. The thesis presents a full characterisation of the most general possible linear optical system with this dependence and shows it to be a generalised Mach-Zehnder or Michelson interferometer. The use of optical feedback, such as in a resonating ring, is therefore shown to be inappropriate if differential behaviour is a system requirement.

The thesis concludes with a study of the *adiabatic forked splitter*, a device which enables a multimoded waveguide's eigenfields to be channelled into separate single-moded guides with minimal interference between them. Hence, the splitter contrasts to the other planar devices studied in this thesis as the latter depend on interference between modes for their behaviour. The splitter concept is generalised up to four modal channels, with systematic design procedures studied in detail and the important design issues underlined. Numerical simulations show the device's basic working to be very tolerant to fabrication errors in device dimensions thereby facilitating practical implementation.

An immediate application is to Mode-Multiplexed Communication Systems, where different signals, even at the same wavelength, are allocated to the different modes of a few-moded fibre trunk. Hop-lengths of several kilometres may be possible and the scheme may well be appropriate for local area networks (LANs) and other short-haul links where extreme bandwidth is required. Another potential application is in Scanning Confocal Microscopy, where the use of different modes of a few-moded receiving fibre can be used to enhance the resolution of the image.

Contents

Chapter 1

Introduction

1.1 Rationale

With optical fibre computer networking becoming commonplace and optical fibre telecommunications foreseen as a leading workhorse for the already beclichéed "Information Superhighway" of the future, the importance of optical waveguide device technology to modern society is now incontestable. Yet, it is also undeniable that the lowly optical fibre is the only optical waveguide device to have influenced mainstream technology significantly, and the optical components within a fibre network remain on the whole primitive and profoundly simple. The development of devices more sophisticated than the fibre, connector, two-waveguide coupler or driving laser has only barely begun. The reason for the dearth of more sophisticated optical building blocks is straightforward: fabrication technology has hitherto been almost bereft of any means of accurately controlling internal device dimensions since Fused Biconic Technology has been the dominant waveguide device fabrication method.

However, Planar Integrated Optics Technology now offers low-loss waveguides with tight, accurate device dimension control and its basic fabrication techniques are now well understood and commercially workable. Already one thesis[Ladouceur, 1992] written within the Australian National University's Optical Sciences Centre has been devoted to this understanding. However, the exploration of new devices made possible by heightened dimension control has only just begun in earnest and so a modest contribution to its headway is a major goal of the present thesis.

A further goal is to explore the possible, although scant, enhancement of opti-

cal devices by the older technique of tapering. The basic, but poorly understood and hitherto almost unheeded, problem of back-reflexion arising from all optical waveguide devices is also explained and quantified.

1.2 General Aims

We emphasise from the outset that the aim of this thesis is to moot and appraise *design* techniques applicable to *general* classes of devices. We shall *not* aim to study new fundamental physics, nor to explore the exact analytical solution of specific problems. For each class of problem studied in this thesis, we seek to either *(i)* give the reader a sound intuition for the system at hand, so that, as a *designer*, he or she may appreciate the general qualitative influence of the available design parameters on the system's behaviour without becoming too befuddled by analytical detail; or *(ii)* reduce the design of a general class of devices to a systematic procedure, thus leaving the designer free to consider other, more important problems such as the use of the device in question as a component in a larger optical system.

Therefore, for example, in Chapter-4 we seek to underline the design trade-off between the size and wavelength performance of commercial fused biconic couplers; in Chapter-5, we seek to give an intuitive visualisation of an erbium doped fibre amplifier's behaviour through consideration of its state-space trajectory. Likewise, the formidable mathematical detail of the theory of matrix Lie groups in Chapters-6, 7 and 8 is directed to one end; namely, the reduction of the design of a planar linear coupler to implement *any* unitary transfer matrix to a wholly mechanical procedure and to prove that this procedure will work in all cases. Thereafter, the complicated theory need be considered no further.

An important aspect of a design procedure is that it should be *robust*, *i.e.* that it can accommodate reasonable manufacturing errors and nonrepeatability. For example, the planar coupler design procedure of §8.3 removes the design effort from the tightly coupled regions of the system, where readily applicable theory will be invalid. Instead, the design effort is shifted onto the choice of readily analysed, readily tuned uncoupled optical delay lines, which can be tuned *after* device manufacture to compensate for inaccuracies and/or nonrepeatability in the coupler's fabrication.

The success of this procedure does *not* depend on the accurate manufacture of the coupler's parts, only on their satisfaction of a broad, readily fulfilled criterion that is unaffected by reasonable device variations.

1.3 Thesis Outline

The thesis begins with an extremely brief outline in Chapter-2 of the main numerical techniques used in the work to be described.

In Chapter-3, we address an important problem in practical couplers - that of reflected power, which can adversely affect the source laser's operation. With optical network size increasing, reflexion countermeasures formerly applicable to smaller networks are no longer appropriate and therefore the source of these reflexions will be studied with the view to formulating means of quelling them. Theoretical models for reflexions will be proposed and, in some cases, experimentally tested.

We close our study of fused-biconic couplers in Chapter-4 by exploring the internal device dimension control needed for device shortening without undue excess loss increase and underline an interesting design trade-off: that device shortening is bought at the price of an increased sensitivity to wavelength. Excess loss in the optimally short device will be shown to increase rapidly to intolerable levels as the wavelength deviates even slightly from its intended value whereas many commercial couplers are quite usable over a much broader bandwidth.

Before progressing to the study of planar integrated devices, we appraise the benefits of tapering to the Erbium Doped Fibre Amplifier (EDFA) for the optimisation of signal-to-noise ratio, gain, saturation power and length in Chapter-5.

In Chapter-6, we begin our study of planar linear coupler design and examine the specific example of a planar version for the Symmetric 3×3 Fibre Coupler, a device useful in interferometric sensors and as a demodulator in coherent communication schemes. The fibre device is inherently nonplanar, so we overcome the planar constraint by designing two separate wholly planar mimics, which are numerically analysed to asses their likely performance.

In Chapter-7, we further examine the implications of the planar constraint, given that many useful fibre devices are inherently nonplanar. The main mathematical

technique used is the Theory of Matrix Lie Groups and I have striven to make its presentation most applicable to coupled waveguide design. It is then shown that any planar linear coupler can realise the transfer matrix of any nonlinear coupler so that dimension control can, in principle, be used to completely overcome the planar constraint. There are some practical limitations to this result, however, as illustrated by examples. We then make headway towards a practical general planar coupler design procedure based on the concatenation of generalised Mach-Zehnder interferometers by presenting a visualisation of the design of a general 2×2 coupler in terms of Poincaré sphere rotations. The procedure is then generalised to $N \times N$ couplers and its universal applicability proven.

In Chapter-8, we use the Mach-Zehnder design procedure to derive a wholly planar implementation of the symmetric 5×5 fibre coupler and yet another planar realisation of the symmetric 3×3 coupler. The 5×5 coupler design is appraised by the Beam Propagation Method and its sensitivity to manufacturing errors is examined. The second half of Chapter-8 examines more intuitively appealing planar designs, which derive their behaviour directly from geometric symmetry, for the symmetric 3×3 and 5×5 fibre couplers.

These symmetric designs are less likely to be practical than the Mach-Zehnder devices because their behaviour depends on *absolute* optical delays, whereas that of the Mach-Zehnder devices depends only on the *difference between* optical delays. This *differential* behaviour affords an optical system superior resilience to environmental temperature variations and to source laser frequency jitter, as shown by direct example in Chapters-8 and 9. Chapter-9 then derives a description of the most general possible linear differential interferometer and shows that if planar devices are to behave differentially, their dependence must be a very *restricted* function of optical length differences.

All the planar devices documented in Chapters-6, 7 and 8 derive their behaviour from interferometric effects, *i.e.* the beating between optical modes. Chapter-10 is instead devoted to the design of a very different device, the *adiabatic forked splitter*, which seeks to separate a waveguide's eigenfields physically so that they *cannot* interfere, thus bestowing an extreme wavelength *independence* on the device. We generalise this concept to several modal channels, study systematic design proce-

dures in detail, underline the important design issues as well as indicating some possible future applications of the device in telecommunications, sensing and scanning confocal microscopy.

With the exception of our investigation of coupler back reflexions, the investigation has been wholly theoretical. I believe that the designs have been developed as far as would be wise to do so in the absence of experimental measurements from working optical prototypes, *i.e.* to the stage where construction of a prototype for concept proof ought to be possible. Further design development before experimental appraisal would be folly, since it would be wasted were the prototype to fail such appraisal. I have sought in this thesis to foresee practical prototyping problems as far as possible. Planar dimension control techniques are now developed enough to test at least the simpler designs of this thesis experimentally, and I expect that this undertaking will be part of the next stage of the planar waveguide development effort at the Australian National University's Plasma Research Laboratory.

1.4 Future of Optical Waveguide Devices

We briefly examine possible future developments in optical technology. Much has been made of the possibility of all-optical computers using nonlinear optical switches to replace electronic ones in an exact, gate-for-gate planar integrated optics analogy of the electronic digital computer. This is unlikely to come to be, since the present state-of-the-art digital optical devices require forbiddingly high switching energy and power consumption[Saleh and Teich, 1991, §21.5]. Such limitations are merely technological, but optical devices are also several orders of magnitude larger than their electronic counterparts, and this is a fundamental limit. For example, the radius of curvature of bent waveguides connecting devices must be at least hundreds of wavelengths to achieve reasonably low loss[Ladouceur, 1992] and this fact constrains an all-optical computer, built as a gate-for-gate analogy of an electronic digital computer, to be an unacceptable size. This fact is illustrated by the design of the planar couplers discussed in remainder of this thesis.

It is more likely that optical technology will undertake tasks making use of the wave nature of light, such as the phased array electro-optic switches discussed in

[Heaton *et al.*, 1992] and the interferometric systems to be studied in Chapters-6, 7 and 8. There are more plausible digital optical computing alternatives than the gate-for-gate analogy and these are being actively researched. They use holographic interconnexions (*i.e.* make direct use of the light's wave nature and its diffraction properties) between massively parallel nonlinear switching arrays, thus offsetting some of the size and power consumption drawbacks of all-optical switches. Such systems are likely to be used for near-real-time digital image processing and artificial intelligence applications such as optical neural networks [Saleh and Teich, 1991, §21.5].

It is possible that optics will never compete with electronics for telecommunications network switching. Some researchers have even concluded[Smith, 1993; Cochrane and Heatly, 1992] that, "The intensive and economic processing of signals at the finer granularity of today's services is and *probably always will be* the domain of electronics". Instead, the prodigious bandwidth of optical systems may be used to return to more circuit-switched rather than packet-switched networks, thus simplifying the networking management. There may well be a need to exploit such a bandwidth-for-switching-complexity swap in the near future, since, with the convergence of telecommunications and computing, the growth of the system complexity seriously threatens telecommunication network reliability owing to the fundamental inability to produce error-free software.

The future of optical technology therefore seems to me impossible to foretell; what does seem certain, though, is that however it may unfold, its future will be an exciting one, which, hopefully, the work of this thesis will make some lowly contribution to.

Chapter 2

Review of Numerical Techniques

High speed and ease of reconfiguration are the foremost requirements of numerical techniques for design problems, where a system may have to be analysed many times with different design parameter choices. We shall most certainly shun time-consuming methods wherever possible, even if this means some loss of accuracy.

Our two numerical draughthorses will be the *Beam Propagation Method* (BPM) and the *Fourier Decomposition Method* (FDM). The former is used in this thesis to calculate the propagation of an electromagnetic field through a waveguide system, the latter, an accurate and reasonably fast way of calculating the eigenfields of a waveguide. The FDM can also be used as an extremely accurate method for analysing propagation, but is far too wasteful of time for design. We shall now give an outline of the methods to find out what they can and, perhaps more importantly, *cannot* do.

2.1 Beam Propagation Method (BPM)

The BPM is only applicable to weakly guiding media. It is extremely important to note that it makes a paraxial approximation and, as such, *cannot* be used to analyse waveguides directed at a steep angle to the longitudinal (z) direction or whose fields contain significant plane wave components, as found by the discrete Fourier transform below, directed at steep angles relative to the waveguide. The author has found that maximum workable values for such angles are typically about 0.02 radian for reasonable simulation accuracy.

The BPM rests wholly on the proof[Feit and Fleck, 1978][Marcuse, 1991, §§8.2 - 8.4] that, for a small axial stepsize δz, such a medium can be thought of as slivers of homogeneous media with refractive index n_{cl} and thickness δz interspaced by lenses (Fig-2.1).

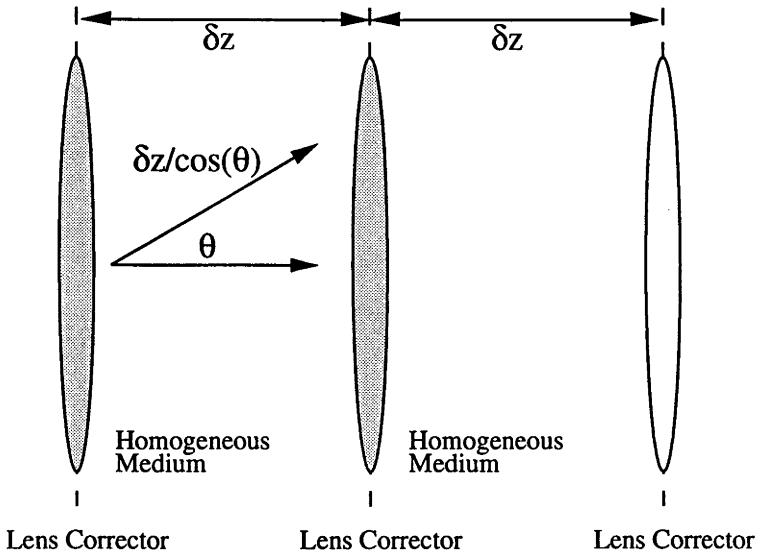

Figure 2.1: Equivalent physical model for the BPM

The light output at position (x, y) on a lens corrector depends *only* on the light input at (x, y, z), hence, the lens's action is *local* and there are no diffraction effects within the lens. If $\psi(x, y)$ is the field input to the lens, the output is:

$$\psi(x,y) \exp\left(i\ k\ \delta z \left(1 - \frac{n(x,y)}{n_{cl}}\right)\right) \tag{2.1}$$

where k is the wavenumber $2\pi n_{cl}/\lambda$ and $n(x, y)$ the refractive index as a function of cross-sectional position (x, y). The lenses model the effect that, owing to the medium's inhomogeneity, the wavefront's phase leads or lags that of an axially travelling plane wave in the homogeneous medium according to whether to local refractive index is greater or less than n_{cl}.

The homogeneous medium propagation accounts for diffraction and many methods can be used to model it. This thesis uses a Fourier transform method, which begins with the observation that a mode in the homogeneous medium is a plane wave of wavenumber k travelling in any direction. A Fourier transform is used to write the input wavefront $\psi(x, y, z)$ as a superposition of such waves, that is, fields with an x, y, z dependence of:

$$\psi_0 \exp\left(i\ \left(k_x x + k_y y + \sqrt{k^2 - k_x^2 - k_y^2}z\right)\right) \tag{2.2}$$

Each plane wave is propagated a distance δz according to (2.2) and the superposition is then inverse Fourier transformed to reassemble the diffracted field $\psi(x, y, z + \delta z)$. Diffraction can now be readily and intuitively thought of as arising from the different delays of the constituent plane waves owing to their slightly different propagation directions and therefore different required propagation times to advance the step δz. Any wave with $k_x^2 + k_y^2 > k^2$ undergoes an attenuation with z owing to a negative real part in the z-exponent. Such waves are evanescent and do not transport power; rather, they represent motionless stores of energy that gather around sudden changes in the waveguide's cross section. Evanescent wave energy is in many ways like the reactive energy oscillating within an inductor or capacitor.

In a computer analysis, the medium and field must necessarily be discretised and the continuous Fourier transform must be approximated by the discrete Fourier transform. Since the latter is a spatially-periodic function, we are actually modelling an infinite two dimensional array of parallel waveguides and the rectangular region analysed is a period cell. If the periodic array is to model the single waveguide accurately, the field $\psi(x, y, z)$ must be vanishingly small at the analysis region's boundaries, so that the cells do not interact. To fulfill this requirement, most Fourier transform BPMs use a loss region near the edge of the simulation region to quell any power radiated from the waveguide before it reaches the neighbouring cells.

The periodic array problems are not intrinsic to the BPM, but rather to the discrete Fourier transform implementation thereof. There are other, finite difference implementations; however, the Fast Fourier transform (FFT) implementation can be used for increased speed and is probably the fastest method given the computer hardware used for the studies of this thesis[1].

The BPM must be used with extreme care when the waveguides in question have dimensions only slightly larger than the light wavelength or where the medium's transverse spatial variation is rapid relative to the wavelength. It is easy to see

[1]Thinking Machines Corporation CM2 and 32-node CM5 supercomputers. These massively parallel machines can be configured to execute the FFT algorithm[Oppenheim and Schafer, 1975] extremely efficiently.

that a reckless or insouciant application of the BPM to such cases can lead to results differing markedly from those found by direct solution of the scalar wave equation. Since the latter's fundamental eigenfield is of comparable width to the waveguide, the Fourier transform of the wavefront has significant components with k_x values greater than $2\pi n_{cl}/\lambda$, *i.e.* there is significant evanescent power in the BPM simulation. The BPM attenuates these components, leaving only waves with low k_x values, *i.e.* corresponding to a field with significant transverse variation over a length scale equal to the wavelength or greater and which differs markedly from the scalar wave equation's predictions. The failure of the BPM to accommodate waveguides making a steep angle with the z-direction arises from the same reason, *i.e.* the presence of planar wave components with high k_x values. Since high-Δ waveguides can also lead to waves significantly skewed, nonparaxial waves[Snyder and Love, 1983, Ch-32], the BPM is untrustworthy in such cases also. By checking the evanescent energy present, the BPM can monitor its own validity[Thylen, 1983]

In closing, it must be noted that, as for any numerical procedure, the "loss" predicted by the BPM for bent waveguides increases dramatically with increasing axial stepsize, because the medium model is a series of translationally invariant layers with abrupt transitions between them. Each time the field encounters such a transition, it finds itself suddenly offset from the waveguide by an amount proportional to the stepsize, thus exciting radiation modes. The *physical* radiation loss from a bend can be thought of in the same way for an infinitesimal stepsize, but the numerical procedure overestimates this loss progressively more seriously with increasing stepsize, as can be understood by considering the extreme case where the stepsize is so long as to model the whole bend by an abrupt transition between the input and output waveguides.

2.2 Fourier Decomposition Method (FDM)

The Fourier Decomposition Method[Henry and Shani, 1991][Marcuse, 1991, §8.5] is probably the most efficient method for calculating scalar wave equation eigenfields. It can also be used for extremely accurate propagation analysis, but is too slow in this application for design. Rectangular modelling domains of dimensions $L_x \times L_y$

are used and all electromagnetic fields are expressed as a linear superposition of the orthonormal basis set members:

$$\left\{\psi_{\mu\nu} = \frac{2}{\sqrt{L_x L_y}} sin\left(\frac{\mu\pi x}{L_x}\right) sin\left(\frac{\nu\pi y}{L_y}\right)\right\}_{\mu=0,\nu=0}^{\infty} \tag{2.3}$$

where μ and ν are integers. The $\psi_{\mu\nu}$ are periodic in x and y so that, like the BPM's FFT implementation, the technique assumes a doubly periodic infinite waveguide array, whose unit cells can only model the behaviour of an isolated waveguide accurately if the field is known to be vanishingly small at the unit cell boundaries. Given the condition that the field should vanish at these boundaries, the orthonormal functions in (2.3) are a *complete* set.

Next, the scalar wave equation for an eigenfield ψ with propagation constant β is considered:

$$\left(\nabla^2 + k^2 n^2(x,y)\right)\psi = \beta^2\psi \tag{2.4}$$

and the action of the operator $(\nabla^2 + k^2 n^2(x,y))$ on the left hand side is expressed as a matrix $\mathbf{H}$ with respect to the basis (2.3). Of course, for practical numerical problems, (2.3) is reduced to a finite number of terms ($\mu = 1...N_x$, $\nu = 1...N_y$). A field is then represented by a two dimensional array[2] $[\phi_{\mu\nu}]$ of superposition weights; for convenience this can be reversibly mapped onto a one-dimensional vector $[\bar{\phi}_\omega]$ of weights by the index mapping $\nu = \omega \bmod N_y + 1$, $\mu = \omega \operatorname{div} N_y + 1$. Then, the matrix expressing the action of the operator in (2.4) is found by calculating the vector of weights describing the image of $\bar{\psi}_\omega = \psi_{\mu,\nu}$ under the action of the operator; this vector, *i.e.* the ω^{th} matrix column, is given by the inner products:

$$\mathbf{H}_{\omega,\sigma} = \left\langle \bar{\psi}_\omega, \left(\nabla^2 + k^2 n^2(x,y)\right)\bar{\psi}_\sigma \right\rangle = \int_{x=0}^{L_x}\int_{y=0}^{L_y} \bar{\psi}_\omega \left(\nabla^2 + k^2 n^2(x,y)\right)\bar{\psi}_\sigma dx dy \tag{2.5}$$

This process is essentially very simple and *precisely* analogous to finding the matrix for, say, a rotation with respect to an orthonormal basis of unit vectors. Here, the matrix element at position (j,k) is the dot product between the j^{th} unit vector and the image of the rotated k^{th} unit vector. Thus, (2.4) becomes $H[\bar{\phi}] = \beta^2[\bar{\phi}]$ and

[2] it i.e. the field is written $\sum_{\mu=1}^{N_x}\sum_{\nu=1}^{N_y}\phi_{\mu,\nu}\psi_{\mu,\nu}$.

the finding of its eigenfields is reduced to the finding of the eigenvectors of **H**. Two conditions facilitate this procedure:

- The matrix **H** is symmetric (or Hermitian, for lossy waveguide materials), thus Householder reduction to tridiagonal form is applicable[Press *et al.*, 1990, §11.2] and the resulting tridiagonal matrix is then readily diagonalised;
- If the waveguide's cross-section comprises rectangular or elliptical[Hewlett, 1994] homogeneous regions, there are simple *analytic* expressions for the components of **H**. Hence, irregularly shaped waveguide regions are approximated by a collection of rectangles[Ladouceur, 1992, §§3.3,5.2].

For accurate propagation analysis, the above procedure must calculate all waveguide's eigenfields at *every* axial step, express the field as a superposition of these eigenfields and then analyse its propagation through the current axial step by applying the correct phase delays to the eigenfields. This procedure is far too slow for design however. To calculate the eigenfields with $N_x = N_y = 32$ takes about two hours on a DECStation 5000/260 with 64 Mbyte RAM and this calculation time varies as the *cube* of N_x and N_y.

[Hewlett and Ladouceur, 1994] has recently greatly broadened the FDM's applicability to include infinite simulation domains and thus conceived elegant, fast and systematic procedures for deriving exact cutoff wavelengths for arbitrary waveguides.

2.3 Conclusions

In this short Chapter we have stated the requirements of our numerical techniques, namely qualitative correctness of their results with an emphasis on speed rather than extreme accuracy, so that the techniques may be convenient for optical system design. The two main numerical techniques, namely the Beam Propagation and Fourier Decomposition Methods, were summarised and their limitations were appraised. Other minor techniques to be used throughout this thesis will be introduced in the relevant Chapters.

Chapter 3

Back-Reflexion from Fused Biconic Couplers

Before progressing to the study of planar integrated devices, we study an important problem in practical fused biconic couplers - that of reflected power, which can adversely affect the source laser's operation. In the past, this problem went mainly unheeded since reflexions from connectors were typically much greater than those from couplers (-50dB to -70dB), whereas now connectors are so highly developed that couplers are becoming the main source of reflexions from networks. Moreover, fibre networks have been small and stand-alone, so that it was workable to use Faraday-effect optical isolators to shield the source lasers from reflexions. However, this isolator is expensive, difficult to align and very much a laboratory instrument. Its initial cost, difficulty of installation and subsequent maintenance make it unwieldy for use in larger networks with many source lasers.

The basic reflexion mechanism is the coupling between the coupler's forward- and backward-propagating bound modes that arises from any longitudinal variation of the cross sectional refractive index profile. Amongst the effects causing such variation are those considered in this Chapter, namely, tapering, surface roughness on the cladding-air interface, fibre bends and twists and, finally, stress arising from bending and packaging. Our basic investigative tool will be the *coupled local mode equations*[Snyder and Love, 1983, §§31-13, 31-14, 31-15] solved to find the coupling between the forward- and backward-propagating fundamental modes arising in response to these effects. Note that even Fresnel reflexions from abrupt waveguide

changes can be analysed with this approach, if they are thought of as reflexions arising from continuous, but extremely rapid, axial waveguide evolution. The order of magnitude of the reflected power arising from each effect will be estimated and compared. Experimental results are also presented that would seem to eliminate at least some of these effects as the likely source of reflexions and the theoretical analysis shows the stress optic effect to be overwhelmingly the strongest, and most likely, reflexion source.

3.1 Coupled Local Mode Equations

In a 2×2 coupler, there are two bound modes and we must take account of coupling from a forward-propagating bound mode to both *(i)* the same and *(ii)* the other backward-propagating mode. We meet both these tasks by approximating a (well-drawn) coupler by a circular multimode fibre; the even and odd bound modes then correspond to the $HE_{1,1}$ and $HE_{2,1}$ modes of the circular waveguide and the coupling co-efficients[1] $C_{-0,+0}$, $C_{-1,+0}$ and $C_{-0,+1}$ between the modes of the appropriate propagation direction are calculated.

Reflexions are always extremely small; the worst-case situation is a Fresnel reflexion from the normal incidence of a fibre's field onto a fibre-air interface and even in this case, the Fresnel equation[Born and Wolf, 1980, §1.5.2] show that only about 4% of the incident power is reflected. We shall see that, in most cases, reflexions are far smaller than this and we shall hereafter assume that almost all of the system's power stays in the incident single bound mode.

With the fundamental $HE_{1,1}$ mode incident and given these assumptions, the coupled local mode equations become[Snyder and Love, 1983, §28-2]:

$$\begin{aligned}
&\frac{db_{+0}(z)}{dz} - i\beta_0(z)b_{+0}(z) \approx 0 \\
&\frac{db_{-j}(z)}{dz} + i\beta_j(z)b_{-j}(z) \approx -C_{-j,+0}(z)b_{+0}(z) \\
&\frac{db_j(z)}{dz} - i\beta_j(z)b_j(z) \approx C_{j,+0}(z)b_{+0}(z); \quad j \neq 0
\end{aligned} \tag{3.1}$$

[1] Here the index 0 in $C_{\pm j,\pm k}$ denotes the $HE_{1,1}$ mode and 1 the $HE_{2,1}$ mode. + indicates the forward (incident) direction and − the backward (reflected).

where $b_j(z)$ is the complex amplitude of the j^{th} forward-propagating mode of the axial distance z along the waveguide, b_{-j} is that of the j^{th} backward propagating mode, the $C_{\pm j,+0}(z)$ are the local modal coupling co-efficients[Snyder and Love, 1983, §31-14] and $\beta_j(z)$ the local modal propagation constants.

Let the taper begin at $z = 0$ and be of length L, *i.e.*, for $z \geq L$ the fibre is translationally invariant and so $b_{-j}(L) = 0$. For these boundary values, (3.1) is readily solved to yield:

$$\begin{aligned} b_{+0}(z) &= \exp\left(i\int_0^z \beta_0(u)du\right) \\ b_{-j}(0) &= \int_0^L C_{-j,+0}(z)\exp\left(i\int_0^z(\beta_j(u)+\beta_0(u))du\right)dz \end{aligned} \tag{3.2}$$

assuming $b_{+0}(0) = 1$. If the odd $HE_{2,1}$ supermode of a coupler is the incident field, $+0$ is replaced by $+1$ in (3.1) and (3.2). For a single mode fibre with unit power input, $|b_{-0}(0)|^2$ gives the total back-reflected power observable at the source laser, since power reflected into higher-order backward-propagating modes is quickly lost through absorption into the jacket surrounding the cladding. For a coupler, the reflected power reaching the source is $|b_{-0}(0) + b_{-1}(0)|^2$ and depends on the relative phase between the bound modes.

In a lossless medium, the coupling co-efficients must obey the basic symmetries:

$$C_{+k,+j} = -C^*_{+j,+k}, \quad C_{-k,-j} = -C^*_{-j,-k}, \quad C_{-j,+k} = C^*_{+k,-j} \tag{3.3}$$

which are equivalent to the Energy Conservation Law[2].

[2]The coupled mode equations can be written in matrix form:

$$\frac{d}{dz}\begin{pmatrix}\mathbf{b}^+\\ \mathbf{b}^-\end{pmatrix} = \left(\begin{array}{c|c} C_{+,+}+iB & C_{+,-} \\ \hline C_{-,+} & C_{-,-}-iB\end{array}\right)\begin{pmatrix}\mathbf{b}^+\\ \mathbf{b}^-\end{pmatrix}$$

where B is the diagonal matrix of propagation constants, $C_{+,+}$, $C_{-,+}$, $C_{+,-}$ and $C_{-,-}$ are the matrices of coupling co-efficients. The power borne by the forward-travelling waves is $\mathbf{b}^{+\dagger}\mathbf{b}^+$ and that by the backward-travelling wave $\mathbf{b}^{-\dagger}\mathbf{b}^-$, hence, the net time-rate of energy transfer in the $+z$ direction across a cross-section is $P = \mathbf{b}^{+\dagger}\mathbf{b}^+ - \mathbf{b}^{-\dagger}\mathbf{b}^-$. For a conservative system $dP/dz = 0$, whence, through the above matrix equation, the symmetries (3.3) follow, analogously to the discussion in Chapter-6. The symmetries can also be derived directly from the expressions of [Snyder and Love, 1983, §§31-14, 31-15] and from the expressions to be derived in the following sections without appeal to energy conservation.

Note that the coupling co-efficients from pure tapers, as derived in [Snyder and Love, 1983, §31-14] are all real, whereas those arising from bends and twists are in general complex, as shown in §3.2.4.

3.2 Coupling Co-efficient Dependence on Perturbations

3.2.1 Tapering of the Core

If the reasoning of [Snyder and Love, 1983, §§31-14, 31-15] is applied to the coupling between backward- and forward-propagating modes, the expressions for the coupling co-efficients can be shown to be correct if the relationships in [Snyder and Love, 1983, Eq-(11-7)] between the components of the two contrapropagating fields are applied. The result is:

$$C_{-j,+k}(z) = -\frac{1}{4}\int_{A_\infty} \hat{\mathbf{z}}.\left(\hat{\mathbf{h}}_j(z) \times \frac{\partial \hat{\mathbf{e}}_k(z)}{\partial z} + \hat{\mathbf{e}}_j \times \frac{\partial \hat{\mathbf{h}}_k}{\partial z}\right) dA \tag{3.4}$$

where the surface integral is to be applied over the infinite cross-section A_∞ for the value of z in question. (3.4) can be simplified to:

$$C_{-j,+k}(z) = -\frac{k}{4}\frac{\mathcal{Y}_0}{\beta_j + \beta_k}\int_{A_\infty} \frac{\partial n^2}{\partial z}\hat{\mathbf{e}}_j(z) \times \hat{\mathbf{e}}_k dA \tag{3.5}$$

where n_{co} is the core refractive index. It is useful to define:

$$\mathcal{Y}_0 = \sqrt{\frac{\epsilon_0}{\mu_0}}; \quad \mathcal{Z}_0 = \sqrt{\frac{\mu_0}{\epsilon_0}} \tag{3.6}$$

where $\mathcal{Y}_0$ and $\mathcal{Z}_0$ are the freespace wave admittance and impedance respectively.

In the weakly-guided case where $\hat{\mathbf{e}}$ and $\hat{\mathbf{h}}$ are almost transverse, $|\hat{\mathbf{e}}|^2 \approx (2/n_{co})\mathcal{Z}_0\hat{\psi}^2$ and (3.5) becomes:

$$C_{-j,+k}(z) \approx -\frac{1}{4n_{co}^2}\int_{A_\infty} \frac{\partial n^2}{\partial z}\hat{\psi}_j\hat{\psi}_k dA \tag{3.7}$$

using $\beta_j \approx \beta_k \approx kn_{co} \approx kn_{cl}$.

Assuming a step-index profile for convenience, $\partial n^2/\partial z = 0$ everywhere on the fibre cross-section but for the core-cladding boundary, where it is infinite. In this

case, (3.7) can be evaluated as in [Snyder and Love, 1983, §28-4] to give:

$$C_{-0,+0} \approx \pi \Delta \hat{\psi}^2(\rho(z))\Omega(z)\rho(z) \tag{3.8}$$

where:

$$\hat{\psi}^2(\rho(z)) = \frac{J_0^2(U)K_0^2(W)}{\pi\rho^2\left(J_1^2(U)K_0^2(W) + J_0^2(U)K_1^2(W)\right)} \tag{3.9}$$

is the normalised intensity evaluated at core-cladding boundary, $\rho(z)$ the core radius and $\Omega(z) \approx d\rho/dz$ the core taper angle. U, V and W are the usual waveguide and modal parameters[Snyder and Love, 1983]. For[3] $\Omega = 10^{-3}$, $\Delta = 0.5\%$, $V = 2.0$, $\rho = 5\mu$m, $C_{-0,+0}$ is of the order of 0.3m^{-1}. If plotted over the length of a typical coupler taper, $C_{-0,+0}$ varies between 0 and 0.3m^{-1} and the spatial frequency of its variation is, for all practical purposes, bandlimited below 10^3m^{-1}, or more typically 10^2m^{-1}.

3.2.2 Tapering of the Cladding-Air Interface

When a fibre is prepared for tapering or fusion into a coupler, its jacket is stripped away before the heating/drawing process to avoid glass contamination. This process leaves an extremely strongly guiding air-cladding interface.

(3.8) can be used directly to calculate the contribution to $C_{-0,+0}$ arising from the cladding-air interface. However, two alternative approaches give simplified expressions for the coupling co-efficients. Reflexion from the interface is only important when the fibre has been tapered enough that the core-cladding interface loses its guiding strength ($V < 1$) and the fundamental mode therefore spreads out enough to interact with the air interface, which then provides all of the fibre's guiding power. The fibre now behaves as a multimoded step-index fibre with a pure silica core and a cladding of air.

The cladding V-parameter (hereafter denoted V_{cl}) of such a fibre is extremely large (≈ 70 for a cladding radius of 15μm when $\lambda = 1.5\mu$m), so a simplification to (3.8) can be derived by taking the limit as $V \to \infty$. In this case, for the $\text{LP}_{0,j}$

[3] *i.e.* Approximate core taper angle in a 125μm diameter fibre tapered down to 25μm over a longitudinal distance of 5mm.

mode, $W \rightarrow V$ and $U \rightarrow U_j$, the j^{th} zero of $J_0(U)$. For a pure taper with the fibre everywhere circularly symmetric, LP_0 modes can only couple into other LP_0 modes. Hence:

$$C_{-j,k} \approx \frac{\Omega U_j U_k}{2\rho^3 k^2 n_{co}^2}; \qquad C_{-0,0} \approx 0.033 \frac{\Omega \lambda^2}{\rho^3} \tag{3.10}$$

For[4] $\Omega = 10^{-2}$, $\rho = 15\mu$m and $\lambda = 1.5\mu$m, $C_{-0,+0} = 0.22\text{m}^{-1}$.

An alternative derivation of (3.10) is as follows. The air-cladding interface is so strongly guiding ($V \approx 70$) that the lower order modes do not penetrate significantly into the air and thus the electric field component tangential to the interface can be considered to vanish, *i.e.* the interface behaves as though it were a perfectly conducting metal. Now, the calculation of the coupling co-efficients in [Snyder and Love, 1983, §31-14] depends crucially on the orthogonality relationships between the local modal fields, which in turn rest wholly on the Reciprocity Law. In a metal-clad system, the Lorentz vectors[Snyder and Love, 1983, §§31-1, 31-2] $\mathbf{F}^c_{j,k} = \mathbf{e}_j \times \mathbf{h}^*_k + \mathbf{e}^*_k \times \mathbf{h}_j$ and $\mathbf{F}_{j,k} = \mathbf{e}_j \times \mathbf{h}_k - \mathbf{e}_k \times \mathbf{h}_j$ are tangential to the metal boundary, since $\mathbf{e}_j$ and $\mathbf{e}_k$ are normal to it. Hence, the line integrals Equation 31-4 of [Snyder and Love, 1983] vanish:

$$\oint_{\partial A_o} \mathbf{F}_{j,k}.\hat{\mathbf{n}} dl = \oint_{\partial A_o} \mathbf{F}^c_{j,k}.\hat{\mathbf{n}} dl = 0 \tag{3.11}$$

where ∂A_o is the metal boundary in the waveguide's cross-section and thus both the conjugated and unconjugated Reciprocity Laws become:

$$\frac{\partial}{\partial z}\oint_{A_o} \mathbf{F}_{j,k}.\hat{\mathbf{n}} dl = \oint_{A_o} \nabla \cdot \mathbf{F}_{j,k} dA; \quad \frac{\partial}{\partial z}\oint_{A_o} \mathbf{F}^c_{j,k}.\hat{\mathbf{n}} dl = \oint_{A_o} \nabla \cdot \mathbf{F}^c_{j,k} dA \tag{3.12}$$

where A_o is the *open* interior of the metal boundary in the waveguide's cross-section, *i.e.* the integrals *exclude* the boundary. Thus, the orthogonality relationships and therefore the coupling co-efficient expressions in §3.2.4 and [Snyder and Love, 1983, §31-14] all hold when the relevant surface integrals all carried out over the open interior of the metal boundary.

The exact vector expressions for the fields of a homogeneous circular dielectric waveguide of radius ρ bounded by a perfect conductor are applied. The local modal

[4]The approximate cladding angle for the taper of §3.2.1.

fields are either TE or TM and there is no coupling *(i)* between TE and TM fields nor *(ii)* between fields of different azimuthal index. The boundary conditions and expressions for TM fields are simpler and so will be used in the following. The electric field's z-component at radius r from the fibre's centre is of the form:

$$e_{z,j} = e_0 J_0\left(U_j \frac{r}{\rho}\right) \tag{3.13}$$

where U_j is the j^{th} zero of $J_0(z)$. The other field components are found by [Snyder and Love, 1983, Eq-(30-9)]; upon substitution into (3.4), with A_∞ replaced by the open interior A_o of the metal boundary, the coupling co-efficients between the forward- and backward-propagating, circularly symmetric TM eigenfields are[5] found to be:

$$\begin{aligned} C_{-j,k} &= \frac{U_k \Omega}{\rho}\left(\sqrt{\frac{\beta_k}{\beta_j}} - \sqrt{\frac{\beta_j}{\beta_k}}\right)\frac{\int_0^1 u^2 J_0(U_k u) J_1(U_j u) du}{J_1(U_j) J_1(U_k)} \\ C_{-j,j} &= \frac{U_j^2 \Omega}{2\rho^3 \beta_j^2} = \frac{U_j^2 \Omega}{2\rho\left(k^2 n_{cl}^2 \rho^2 - U_j^2\right)} \end{aligned} \tag{3.14}$$

For $k^2 n_{cl}^2 \rho^2 >> U_j^2$, as is the case for the lowest order modes, $\beta_j \approx k n_{cl}$ so that (3.14) gives exactly the same results as (3.10).

3.2.3 Reflexion from Surface Roughness

The effect of surface roughness on the cladding-air interface can be readily calculated from (3.10) by considering the roughness, as a function of angular position ϕ, to be

[5] For $k n_{cl} \rho = U_j$, *i.e.* $\beta_j = 0$, the $C_{-j,k}$ become ***infinite*** and this has an interesting physical interpretation. A true metal clad waveguide can cut off all its modes, including the fundamental. Imagine that a metal clad waveguide supporting several bound modes is input into a taper bringing it down to a radius ρ_0 where $k n_{cl} \rho_0 < U_0$ and thereafter the waveguide radius is constant at ρ_0, *i.e.* in the output waveguide, all the modes are evanescent and no real power can be transported. If the metal walls are perfectly conducting, there is no mechanism for loss and therefore all power incident from the input waveguide must be reflected back into the input waveguide. As the taper radius approaches the point where the j^{th} mode is cutoff, the co-efficients $C_{-j,k}$ become infinite in such a way that if the coupled mode equations are integrated, *all* the power in the j^{th} mode is reflected into backward-propagating non-evanescent modes, this reflexion process becoming complete precisely at the point in the taper where $k n_{cl} \rho = U_j$.

represented as a Fourier series:

$$\rho(\phi) = \rho_0 + \sum_{k=1}^{\infty} \left(\rho_{+k} e^{ik\phi} + \rho_{-k} e^{-ik\phi} \right) \tag{3.15}$$

For small roughness, $C_{-0,0}$ is a linear function of perturbations to ρ, and the $\rho_{\pm k}$ terms in (3.16) couple the HE_{11} mode to the $HE_{-(k\pm1),j}$ modes. Thus, the average ρ, *i.e.* ρ_0, contributes to $C_{-0,0}$ and $\rho_{\pm1}$ contributes to $C_{-1,0}$ and $C_{-0,1}$. All the other terms couple the fibre's power to unbound modes and so do not contribute to reflexions. We calculate only the ρ_0 reflexion term, since an order-of-magnitude calculation for the $\rho_{\pm1}$ terms will be comparable.

If ρ_0 varies sinusoidally with z with spatial frequency f and amplitude a, then (3.10) gives a peak coupling co-efficient of:

$$C_{-0,0} \approx \frac{0.2 f a \lambda^2}{\rho^3} \tag{3.16}$$

These values are usually small: for $f = 10^6 \mathrm{m}^{-1}$, $a = 10\mathrm{nm}$ and $\rho = 30\mu\mathrm{m}$, the peak $C_{-0,0}$ is $0.17\mathrm{m}^{-1}$. However, we shall see that the back reflexion is strongly dependent on the spectrum and extremely large reflexions are possible if there is significant spectral content at around twice the fundamental mode's propagation number, *i.e.* corresponding to a Bragg resonance between the forward- and backward-propagating fundamental modes.

The surface roughness's spectral characteristics are difficult to model theoretically and best done experimentally. However, (3.16) and (3.10) yield a good indicator of the presence of either surface roughness- or taper-induced reflexions that allows a strong experimental test: since the reflected power is proportional to $|C_{-0,0}|^2$, the back reflexion is proportional to the inverse *sixth* power of the waveguide radius. Hence, back reflexions will arise almost wholly from the narrowest parts of the taper waist and will be *extremely* sensitive to the degree of tapering *if* the back reflexions arise from the taper. We shall show experimentally in §3.5 that the back reflexions do not seem to be correlated to the degree of tapering, hence, almost certainly, the taper is *not* the main source of back reflexions from fused biconic couplers.

3.2.4 Coupled Mode Equations for Bends and Twists

The waveguides within fused biconic couplers suffer microbending and stress through three main mechanisms: *(i)* To hold the two fibres in close contact throughout the fusing process, they are often entwined and clamped at either end (Figs-3.4, 3.5 §3.5). The number of twists is conserved and the fusion-induced stress relief renders the coupling region unable to support any twist, which is therefore gathered up as two tight knots at either end of the waist (Fig-3.1), with a typical helical pitch of 0.5mm to 1mm. *(ii)* The coupler must be packaged in a steel or plastic sheath and is anchored at both ends within this housing by epoxy glue, which may bend and stress the waveguides as it cures. *(iii)* The core and cladding regions have different co-efficients of thermal expansion, thus high residual stress is set up as the fibres solidify after fusion.

The purpose of §§3.2.4 and 3.2.5 is to estimate the reflexion power arising from microbends and stress.

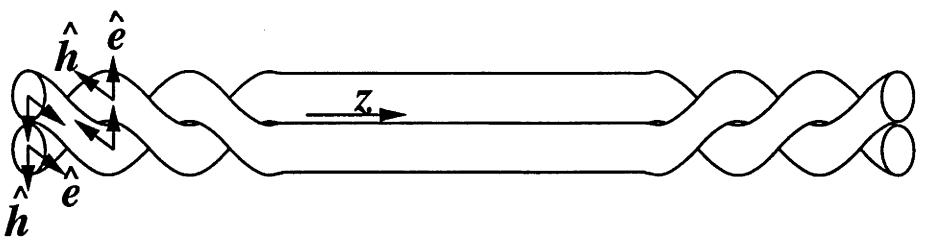

Figure 3.1: Migration of twists towards coupler ends and forced rotation of the electromagnetic field

The derivation of the coupled mode equations for bends and twists is an involved procedure and will be outlined in Appendix-3.7. However, in principle it is straightforward, being essentially a reproduction of the methods of [Snyder and Love, 1983, §31-14] in the orthogonal pipe co-ordinate system[Landau and Lifschitz, 1970; Kath and Kriegsmann, 1988]. As well as the tapering term in (3.4), the following terms, which arise from waveguide twisting and bending, contribute to the coupling co-efficients:

$$4C_{-j,+k} = i\beta_k \mathbf{K} \cdot \int_{A_\infty} \mathbf{r}\,\hat{\mathbf{z}} \cdot \left(\hat{\mathbf{e}}_{k\perp} \times \hat{\mathbf{h}}_{j\perp} - \hat{\mathbf{e}}_{j\perp} \times \hat{\mathbf{h}}_{k\perp}\right) dA - \mathbf{K} \cdot \int_{A_\infty} \hat{\mathbf{z}} \times \left(\hat{e}_{kz}\hat{\mathbf{h}}_{j\perp} + \hat{h}_{kz}\hat{\mathbf{e}}_{j\perp}\right) dA \tag{3.17}$$

where $\mathbf{K}$ is the bend's curvature vector, as defined in Appendix-3.7, with magnitude equal to $1/R$, where R is the radius of curvature. A twist in the waveguide is accounted for by the term in (3.4) provided that the fields are referred to axes attached to the vectors $\hat{\mathbf{u}}$ and $\hat{\mathbf{v}}$ defining the pipe co-ordinates.

Within the weak-guidance approximation, the first term in (3.17) vanishes, since $\hat{\mathbf{h}} = \mathcal{Y}_0 \hat{\mathbf{z}} \times \hat{\mathbf{e}}$. This expression can also be used to simplify the second term:

$$C_{-j,k} = \frac{n_{cl}}{4}\mathbf{K} \cdot \int_{A_\infty} \left(\mathcal{Y}_0 \hat{e}_{zk}\hat{\mathbf{e}}_{\perp j} + \mathcal{Z}_0 \hat{h}_{zk}\hat{\mathbf{h}}_{\perp j}\right) dA \tag{3.18}$$

Now, $C_{-0,+0}$ can readily be shown to vanish for a fibre, by substituting the expressions for the HE_{11} field into (3.18). We assume, as in §3.1, a circular coupler cross-section, so that the HE_{11} fibre mode corresponds to the coupler's even mode, the HE_{21} mode to the odd mode.

By using [Snyder and Love, 1983, Table-14-1] and considering the coupler to be drawn down enough that the core-cladding interface yields negligible guidance (*c.f.* §3.2.2) it can be shown that there is a reflexion *from* the even mode *to* the odd mode and the coupling co-efficient is:

$$C_{-1,+0} = \frac{i\sqrt{2\Delta}}{V} \frac{U_{1,1}}{U_{1,1}^2 - U_{0,1}^2} \sqrt{\frac{J_2(U_{1,1})}{J_0(U_{1,1})}}\mathbf{K} \cdot \hat{\mathbf{x}} \tag{3.19}$$

where $U_{j,k}$ is the k^{th} largest root of $J_j(U) = 0$, *i.e.* $U_{0,1} \approx 2.405$, $U_{0,2} \approx 3.832$. Here $\hat{\mathbf{x}}$ is the HE_{11} (even) mode's transverse electric field direction and $\Delta \approx 0.28$ is the relative index difference of the cladding-air interface as does the waveguide parameter[6] $V \approx 70$, *i.e.* the bending component of the reflexion is defined by:

$$C_{-1,+0} \approx \frac{0.32\kappa i}{V} \approx 4.6 \times 10^{-3}\kappa i \tag{3.20}$$

In the weak guidance approximation, there is no reflexion from the forward-propagating odd mode into the backward-propagating even mode. For typical bends

[6] Representative of the values in the waist region of commercial couplers.

within the coupler with a submillimetre length scale, $\kappa \approx 10^4 \mathrm{m}^{-1}$. This yields $|C_{-1,+0}| \approx 46\mathrm{m}^{-1}$, or two orders of magnitude greater than the values arising from pure tapering.

We now calculate the twisting terms for the coupler. Owing to the strong form birefringence of the cladding-air interface, the local modal fields of the composite coupler cross-section must rotate with the twist. If the spatial angular speed of rotation is Ω, then, in (3.4), $\partial \hat{\mathbf{e}}_k/\partial z = \Omega \hat{\mathbf{z}} \times \hat{\mathbf{e}}_k$, $\partial \hat{\mathbf{h}}_k/\partial z = \Omega \hat{\mathbf{z}} \times \hat{\mathbf{h}}_k$ and the twisting terms, for the weak guidance approximation, are zero.

3.2.5 Coupling from the Stress Optic Effect

The analysis of §3.2.4 assumed that any fibre bending did not affect the refractive index profile of the fibres, whereas the tension and compression of the fibre's cross-section owing to bending gives rise to a well-known, stress-induced refractive index profile change. The strain (ϵ) and stress (σ) profiles arising from bending are[Timoshenko, 1957; Timoshenko and Goodier, 1970; Timoshenko, 1973]:

$$\epsilon = \kappa y; \quad \sigma = E\kappa y = \frac{Ey}{R} \tag{3.21}$$

where E is the fibre's Young's modulus. The distance y is measured in the direction of the radius of curvature (*i.e.* in the direction of $\mathbf{K}$) outwards from the centre of curvature (for tensile stess deemed positive and compressive negative) and $y = 0$ defines the *neutral* axis orthogonal to the radius of curvature (or $\mathbf{K}$) and through the fibre's centre. The stress induces a refractive index change of $\delta n = \mathcal{C}\sigma$, where[Nagano *et al.*, 1978] $\mathcal{C} \approx 4 \times 10^{-5}\mathrm{mm}^2\mathrm{kgwt}^{-1} \approx 4 \times 10^{-3}\mathrm{mm}^2\mathrm{kN}^{-1}$ and, for fused silica, E is between 50 and $80\mathrm{kNmm}^{-2}$, so that $\delta n \approx 0.26y/R$.

The stress-induced refractive index profile clearly has odd symmetry about the neutral axis, hence $C_{-0,0} = 0$. However, as in §3.2.4, there will be coupling between the HE_{11} and HE_{21} modes, *i.e.* between the even and odd bound modes of the coupler. As in §3.2.4, we assume that the coupler's waist cross section in roughly circular, whence the substitution of (3.21) into (3.7) and [Snyder and Love, 1983, Table-14-1] yield:

$$C_{-0,1} = C_{-1,0} \approx \frac{0.27\rho}{\sqrt{2}n_{cl}R^2}\frac{dR}{dz}\frac{\int_0^1 u^2 J_0(U_{0,1}u)J_1(U_{1,1}u)du}{J_1^2(U_{0,1})J_0(U_{1,1})J_2(U_{1,1})} \approx 0.06\frac{\rho}{R^2}\frac{dR}{dz} \quad (3.22)$$

If we assume a sinusoidal fibre bend of period L and amplitude a, then the peak coupling co-efficient is:

$$C_{-0,1} = C_{-1,0} \approx 0.06\frac{8\pi^3\rho a}{L^3} \approx \frac{150\rho a}{L^3} \quad (3.23)$$

For $L = 0.5$mm, $a = 100\mu$m and $\rho = 30\mu$m, the peak coupling co-efficient is 3600m^{-1}, or two orders of magnitude above the coupling arising from pure bending.

3.3 Coupled Mode Equations Solution

If the coupling co-efficients $C_{-0,+0}$, $C_{-0,1}$ or $C_{-1,0}$ vary at a predominant spatial frequency of f and with a peak value of C_{max}, then (3.2) yields a back-reflected power of:

$$P(L) \approx \frac{C_{max}^2 \sin^2(2(kn_{cl} - \pi f)L)}{16(kn_{cl} - \pi f)^2}; \quad P_{ref} = \max(P(L)) \approx \frac{C_{max}^2}{16(kn_{cl} - \pi f)^2} \quad (3.24)$$

where the waveguide length is L and the propagation constants of all bound modes are taken to be approximately kn_{cl}. The powers as calculated by (3.24) for the various mechanisms above are calculated for $kn_{cl} = 6 \times 10^6\text{m}^{-1}$ in Table-3.1.

The surface roughness examples illustrate the dramatic increase in reflected power as the spatial frequency of the roughness approaches that corresponding to the Bragg condition, *i.e.* $f = 2n_{cl}/\lambda$. All the examples illustrate how vanishingly small most reflexions are: the reflexion can be thought of as comprising elements of light scattered from random positions on the waveguide (Fig-3.2); usually the relative phase between these components is random and they suffer destructive interference. However, if the components arise from points interspaced by half the light's wavelength, $\lambda/(2n_{cl})$, in the waveguide, then the scattered components are in-phase and reinforce one another. Such a situation is the Bragg condition and, by the above examples, all reflexions are vanishingly small unless:

- The coupling co-efficient is large, as is the case for the stress-optic effect; or

Effect	C_{max} m^{-1}	Spatial Frequency, f m^{-1}	P_{ref} dB
tapering	0.3	0	-158
bending	40	10^4	-116
surface roughness	0.02	10^5	-181
surface roughness	0.2	10^6	-155
surface roughness	0.38	1.9×10^6	-110
surface roughness	0.3820	1.90986×10^6	-27
stress optic effect	4000	10^4	-75
stress optic effect	10000	10^4	-68

Table 3.1: Back Reflected Powers for Various Mechanisms

- Reflexions arise from an abrupt change in refractive index at an interface (Fresnel reflexions) or from an area less than a few wavelengths long; or

- The Bragg condition is fulfilled, as it will be for reflexions from surface roughness when the roughness spatial spectrum contains significant energy around $f = 2n_{cl}/\lambda$.

The stochastic nature of roughness or microbends can be accounted for as follows. The power reflected from a fibre section of length L is:

$$P = \int_{-\frac{L}{2}}^{\frac{L}{2}} C_{-,+}(u)e^{2ikn_{cl}u}du \int_{-\frac{L}{2}}^{\frac{L}{2}} C^*_{-,+}(v)e^{-2ikn_{cl}v}dv = \int_{-\frac{L}{2}}^{\frac{L}{2}} \int_{-\frac{L}{2}}^{\frac{L}{2}} e^{2\pi ikn_{cl}(u-v)}C_{-,+}(u)C^*_{-,+}(v)dudv \tag{3.25}$$

By taking the expectation $\mathcal{E}()$ of (3.25) and if $C_{-,+}(z)$ is governed by a stationary random process, then $\mathcal{E}(C_{-,+}(u)C^*_{-,+}(v)) = \mathcal{R}(u-v)$, where $\mathcal{R}$ is the autocorrelation function for the process governing $C_{-,+}$. If the correlation length, L_c, is much less than L, *i.e.* $\mathcal{R}(z) << \mathcal{R}(0)$ for $|z| > L_c$ and $L_c << L$, then (3.25) yields:

$$P \approx L \int_{-\infty}^{\infty} e^{2ikn_{cl}w}\mathcal{R}(w)dw = L\mathcal{F}\left(\frac{2n_{cl}}{\lambda}\right) \tag{3.26}$$

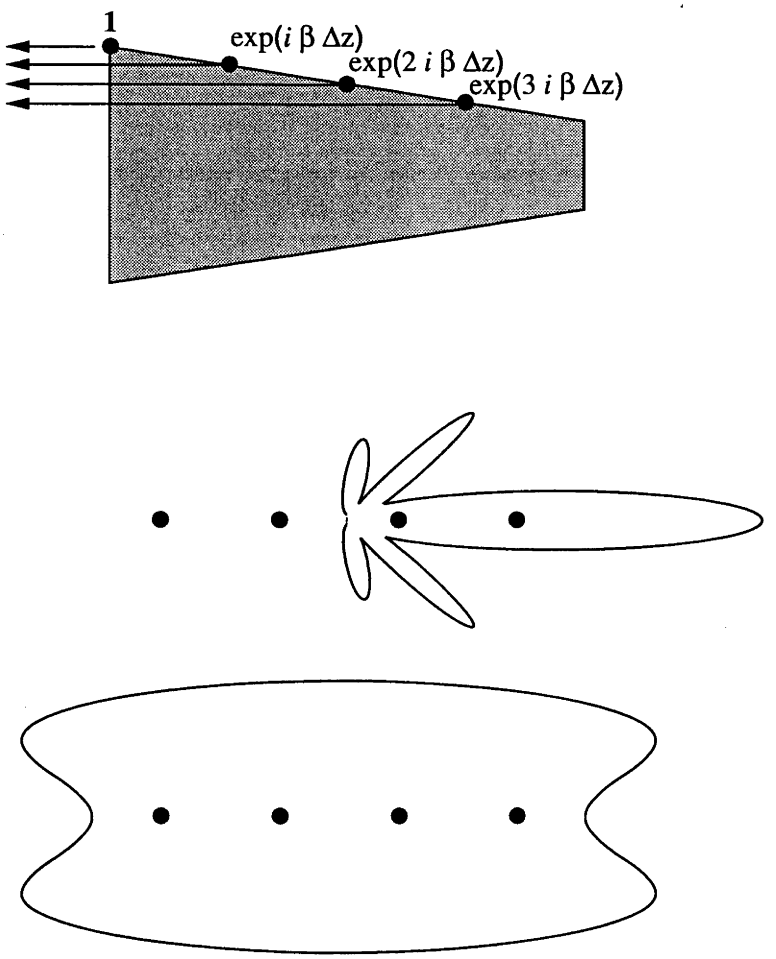

Figure 3.2: Distributed back reflexions: *top* illustrating reflexion from scatterer array; *middle* beam-forming from equivalent phased antenna array; *bottom* radiation pattern from mutually incoherent radiators

where $\mathcal{F}(f)$ denotes the spatial Fourier transform of $\mathcal{R}(z)$ evaluated at spatial frequency f. If the autocorrelation function has the form[7]:

$$\mathcal{R}(z) = C_{max}^2 \exp\left(-\frac{|z|}{L_c}\right) \tag{3.27}$$

then the reflected power is:

$$P \approx \frac{2LL_cC_{max}^2}{1+(2kn_{cl}L_c)^2} \tag{3.28}$$

For $L_c = 100\mu$m, $L = 500\mu$m and $C_{max} = 10^4\text{m}^{-1}$, $P \approx -52dB$. This value of L_c

[7]Corresponding to $\mathcal{F}(f)$ having the Lorentzian shape $2L_cC_{max}^2/(1+4\pi^2f^2L_c^2)$.

would seem plausible and the resulting P is commensurate with the magnitude of the reflexions observed from commercial fused-biconic couplers. Hence:

The calculations of this Chapter show that the most likely cause of the reflexions observed from fused biconic couplers is reflexions from stress optic effect induced refractive index profile changes arising from fibre microbending.

3.4 Source Coherence Considerations

Given that destructive interference generally quells most back reflexions from couplers, it would seem natural to ask whether a partially coherent source gives rise to larger reflexions. If the source has a long coherence length (Fig-3.2), the scatterers act as a phased antenna array which forms a beam directed in the forward-propagation direction. If, however, the scatterers are mutually incoherent, the array will have no beam-forming properties and the scattered field will be more isotropic.

The effect of finite source coherence length can be calculated in one of two, equivalent ways. The first simply notes that any of the expressions calculated above for back-reflexions depends on source frequency and pertains to perfectly coherent sources; if the back-reflected power (as in (3.26)) at light frequency ν is $B(\nu)$, the total backward-reflected power is:

$$P_{ref} = \int_{-\infty}^{\infty} G(\nu)B(\nu)d\nu \tag{3.29}$$

where $G(\nu)$ is the source's power spectral density. Clearly, the effect is to average the reflexion $B(\nu)$ over the source's bandwidth, thus it can be seen that, even with a reasonably wide source bandwidth, the back reflected power will not change dramatically from its perfectly coherent value.

The second method for calculating the back reflexion makes direct use of the ideas in Fig-3.2 by summing up all the back reflected components, whence the total back reflexion is:

$$P = \int_{-\frac{L}{2}}^{\frac{L}{2}} \int_{-\frac{L}{2}}^{\frac{L}{2}} b_{+0}(2u)b_{+0}(2v)C_{-,+}(u)C_{-,+}(v)dudv \tag{3.30}$$

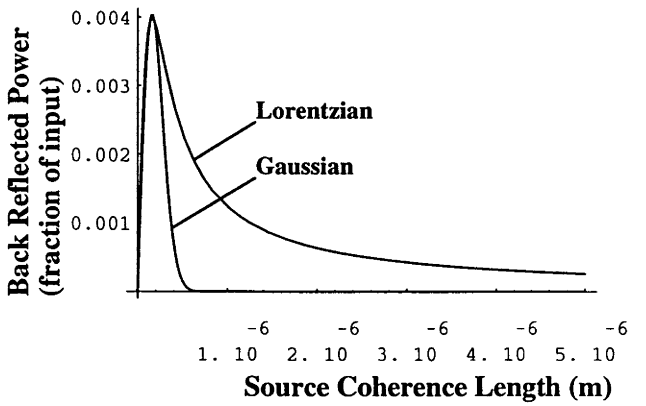

(a)

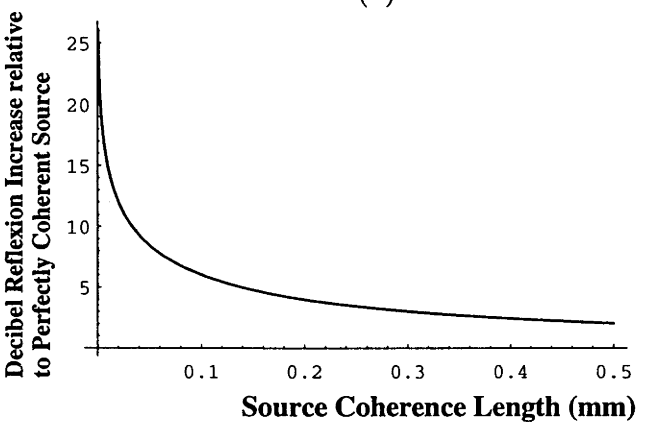

(b)

Figure 3.3: *(a)* Reflected power for Lorentzian and Gaussian source lineshapes and *(b)* dB reflexion increase relative to reflexion for perfectly coherent source as function of coherence length for Lorentzian lineshape

The expectation over the ensemble of all possible source light signals and therefore possible values of $b_{+0}(u)$ followed by a separate expectation over the ensemble of all possible $C_{-,+}$, shows that, for a fibre of length L:

$$P_{ref} = L \int_{-\infty}^{\infty} \Gamma\left(\frac{2n_{cl}u}{c}\right) \mathcal{R}(u) du \tag{3.31}$$

where $\Gamma(\tau)$ is the source laser's time autocorrelation function and $\mathcal{R}(u)$ is as in (3.27). The powers as calculated by (3.31) and (3.29) can be shown to be the same using (3.26) together with the signal-theoretic Wiener-Khinchin theorem[8].

[8]This theorem[Oppenheim and Schafer, 1975] asserts that $G(\nu)$ and $\Gamma(\tau)$ are Fourier transform pairs for light sources whose first and second order statistics are the same whether calculated by

If we assume a unit power source with Lorentzian lineshape, a coherence length l_c and correlation time τ_c ($\tau_c c/n_{cl} = l_c$) and if $\mathcal{R}$ is as in (3.27), then:

$$\Gamma(\frac{n_{cl}z}{c}) = e^{ikn_{cl}z}\exp\left(-\frac{|z|}{l_c}\right);\quad \Gamma(\tau) = e^{ikc\tau}\exp\left(-\frac{c|\tau|}{n_{cl}l_c}\right);$$

$$G(\nu) = \frac{2l_c n_{cl} c}{c^2 + l_c^2 n_{cl}^2(2\pi\nu - kc)^2}; \tag{3.32}$$

$$B(\nu) \approx \frac{2LL_cC_{max}^2}{1+\left(\frac{4\pi n_{cl}\nu L_c}{c}\right)^2};\quad P_{ref} = \frac{2C_{max}^2 l_c L_c L(l_c+2L_c)}{(l_c+2L_c)^2 + 4k^2 n_{cl}^2 L_c^2 l_c^2}$$

The last expression in (3.32) reduces to that in (3.28) for $l_c \to \infty$, as expected and is plotted as a function of source coherence length, L_c, in Fig-3.3*(a)* for $L_c = 100\mu$m, $L = 500\mu$m, $C_{max} = 10^4\text{m}^{-1}$ at $\lambda = 1.5\mu$m and $c = 2.998\times10^8$ is the freespace light speed. As in §3.3, the reflexion for a perfectly coherent source is -52dB, whereas the maximum reflexion, for subwavelength coherence lengths, is about 0.004 or -24dB. Thus, the use of an incoherent source may increase the back reflexions by between 20dB and 30dB. Fig-3.3*(b)* plots the decibel increase in reflected power brought about by the finite source coherence length.

The above results are extremely sensitive to the statistics governing the coupling co-efficient variation. If, instead of the functions used in (3.32) we put $\Gamma = \exp(ikn_{cl}z - z^2/(2l_c)^2)$ and $B = \sqrt{2\pi}C_{max}^2 L_c L\exp(-8(L_c n_{cl}\pi\nu/c)^2)$, then the Gaussian plot in Fig-3.3*(a)* results, *i.e.* the source's linewidth must approach its wavelength before any appreciable increase in back reflexion is observed. The coupling co-efficient variation statistics determine how quickly the low-pass filter function $B(\nu)$ rolls off with increasing ν and, in the Lorentzian case, it rolls off slowly enough that $\int_{-\infty}^{\infty} B(\nu)G(\nu)d\nu$ is influenced by a broadening of the source spectrum.

3.5 Experimental Investigation

Two experiments were undertaken to support the analyses of the foregoing sections. They all involved in-house fabrication of couplers of different characteristics to determine the effects of these characteristics on the back reflexions:

---

time- or ensemble-averaging.

- The back reflexions from couplers of different degrees of tapering were measured to test whether high degrees of tapering can be correlated with strong back reflexions. (3.10) and (3.16) predict a strong increase in reflexion power with greater tapering degrees;

- The back reflexions were measured for light sources of different coherence lengths, to investigate whether a low-coherence source behaves in accordance with the findings of §3.4.

3.5.1 Basic Experimental Apparatus

The basic experimental apparatus is shown schematically in Figs-3.4 and 3.5.

The fibres to be fused are stripped, entwined and clamped firmly to the sliding blocks C. The ring-shaped burner B supplies a high temperature, oxy-propane flame, which fills the whole region within the split in the ring. Under the command of controlling software, motor M3 drives the burner forward with worm-drive W2 until the entwined fibres F are completely immersed in the flame. After a predetermined time to soften the fibres, counterdriving motors M1 and M2 drag the blocks C away from one another with worm-drives W1, thus drawing the coupler. M1 and M2 are servo controlled so that *(i)* the total distance moved by each is precisely the same, so that the coupler being fused is held in the centre of the flame throughout the process; and *(ii)* the acceleration up-to-speed and final drawing speed are precisely controllable and repeatable between different couplers.

DC motors are used to deliver smooth torque, since stepper motors might inadvertently ripple the coupling region, thus producing undesirable spurious coupling to the radiation field through the ripple grating. In the present drawing rig, the pitch of worm drives W1 is 1mm and most stepper motors require 100 to 400 steps per revolution. This translates to an advance of blocks C of a few microns per step, *i.e.* the spatial period of any spurious grating is precisely in the spatial frequency range required for strong coupling to radiation modes, even for very weak gratings. Of course, the motors could be geared down to put any spatial grating frequency well outside this range, however, most stepper motors can achieve a maximum speed of a few hundred revolutions per minute and, if geared down, would not provide the

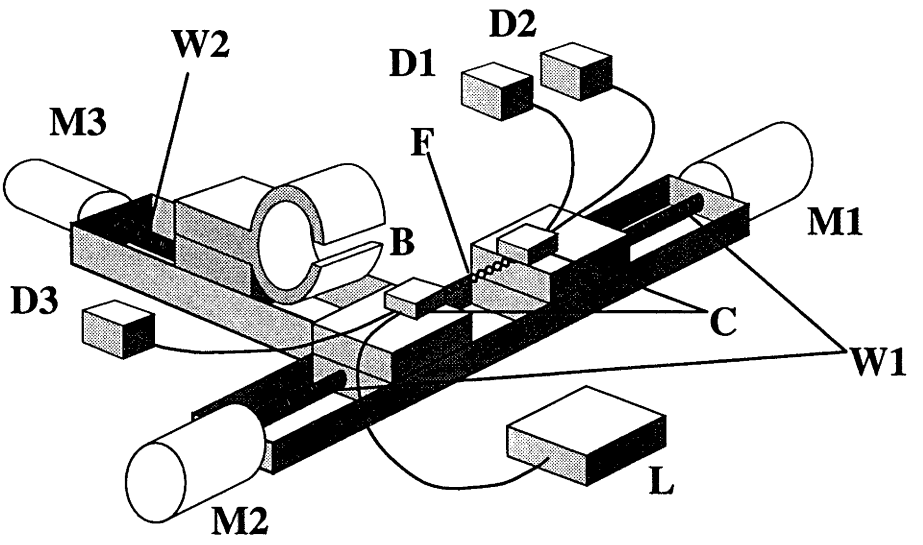

Figure 3.4: Basic Coupler Drawing Hardware

speed range required for both coupler drawing and quick clamp repositioning.

Light is input into the primary fibre with the source L, which was a 2mW, 1.54μm distributed feedback (DFB) laser, whose coherence length is infinite for the purposes of the current experiment[9]. The laser was used to ensure a high power input into the fibre, thus facilitating measurement of the weak reflexion signal. An experiment was also undertaken with a 2mW broadband (40nm linewidth) superbright LED of 1.54μm centre wavelength as a low-coherence source. Silica ($n = 1.447$), monomode fibre was used throughout.

The light output from the two fibres is monitored with detectors D1 and D2 and any light reflected into the secondary fibre from the coupler is monitored by D3. To quell Fresnel reflexions, the ends of the output fibres at D1 and D2 are crushed and steeped in index matching fluid (York Technology, $n = 1.458$). D1, D2 and D3 are InGaAs PIN photodiodes, sensitive to the communication band wavelengths. Under the command of the controlling software, the drawing stops when the coupling ratio, as measured by D1 and D2, reaches the desired value. Then, M3 withdraws B and the finished coupler is released from the drawing rig.

In all cases, Stanford Research SR510 lock-in amplifiers are used to achieve high sensitivity. Both optical input and electrical output attenuators are used with detec-

[9]Fig-3.3 shows reflected power to be almost the same for coherence lengths of several millimetres and for $l_c \rightarrow \infty$.

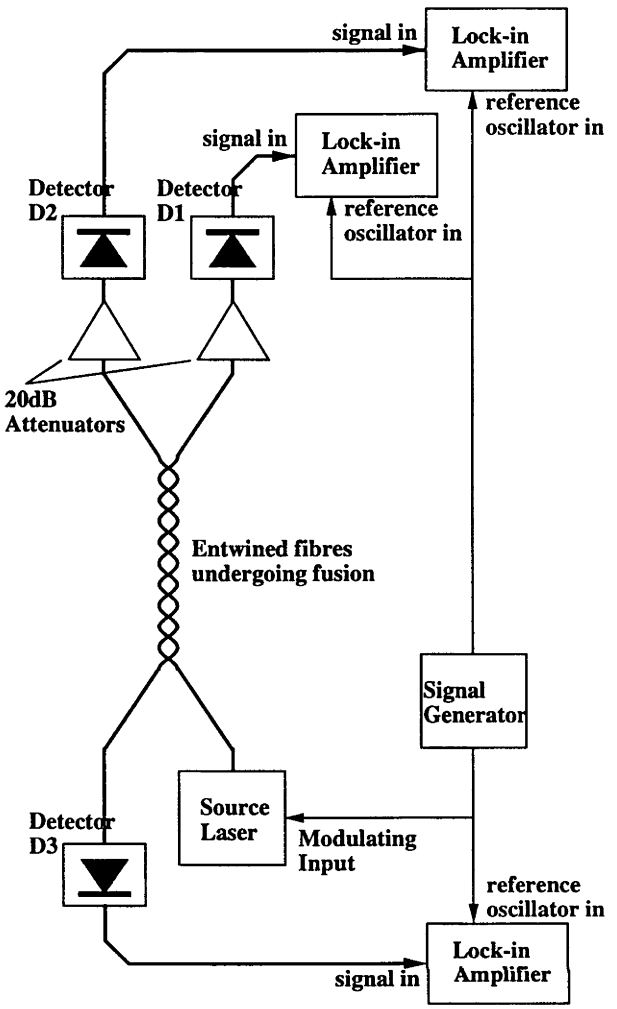

Figure 3.5: Experimental System Block Diagram

tors D1 and D2, so that high light levels can be used without saturating either the detector diode preamplifiers or the lock-in amplifiers. Each diode and corresponding amplifier was calibrated before each drawing by measuring its response to a constant source, thus recording the channel sensitivity.

A signal generator modulates the source intensity, in both the DFB laser and LED cases, with a 50% duty-cycle square-wave, thus providing a carrier frequency for the lock-in amplifiers to track. The chopping frequency is 407Hz, *i.e.* slightly offset from a high-order, even harmonic of the 50Hz (Australian) power mains so as to incur minimal mains contamination. The lock-in amplifiers and the motor-driving board for M1, M2 and M3 are all interfaced to the controlling software through an IEEE-488 GPIB bus. It was found that the experimental dynamic range (*i.e.* maximum measurable power divided by minimum power observable over the

noise floor) is about 70dB with the above experimental setup.

Even though the signal from D3 is monitored throughout the drawing process (Fig-3.6), it is probably not fully meaningful until the coupler is released from its clamps, because the reflexion often changes dramatically upon this release, *i.e.* much of the reflexion arises from the clamps themselves. Already, this observation is strong evidence of the high importance of stress in the production of back reflexions. The clamps bear down on the fibres with about 5N force and it is quite conceivable that a coupler's packaging could stress it to a comparable degree.

After release of the clamps, different parts of the coupler were steeped in index-matching fluid to try to ascertain the origin of reflexions in the coupling region. There was no consistent pattern observed from this test, even though the findings of §3.2.2 predict that reflexions will predominantly arise from the narrowest part of the coupler waist region.

3.5.2 Results and Discussion

Several couplers were made as described above with varying degrees of tapering, to test the dependence of back reflexions on the waist width. Before each experiment, the primary fibre was connected to D1, D2 and D3 in turn and the measured levels recorded so that readings from these detectors throughout the experiment could be calibrated relative to the system input power. The DFB laser was used throughout this experiment, the signals from D1, D2 and D3 were monitored throughout the drawing and typical measurements (those for coupler 8 in Table-3.2) for signal levels against distance advanced by the blocks C are shown in Fig-3.6. Next, the clamps were removed and the back reflected power measured.

Then, the whole coupler, *i.e.* about 20mm on either side of the waist was steeped in index matching fluid, thus allowing almost all the input power to leak away before reaching the coupling region. In this state, it is assumed that any signal at D3 arises from crosstalk in the measurement electronics. Since all the detected signals are phase-locked, this measurement can be simply subtracted from all others to fully account for crosstalk. Lastly, the coupler's waist was examined under a microscope to ascertain the waist width and degree of tapering. The results for several couplers are summarised in Table-3.2.

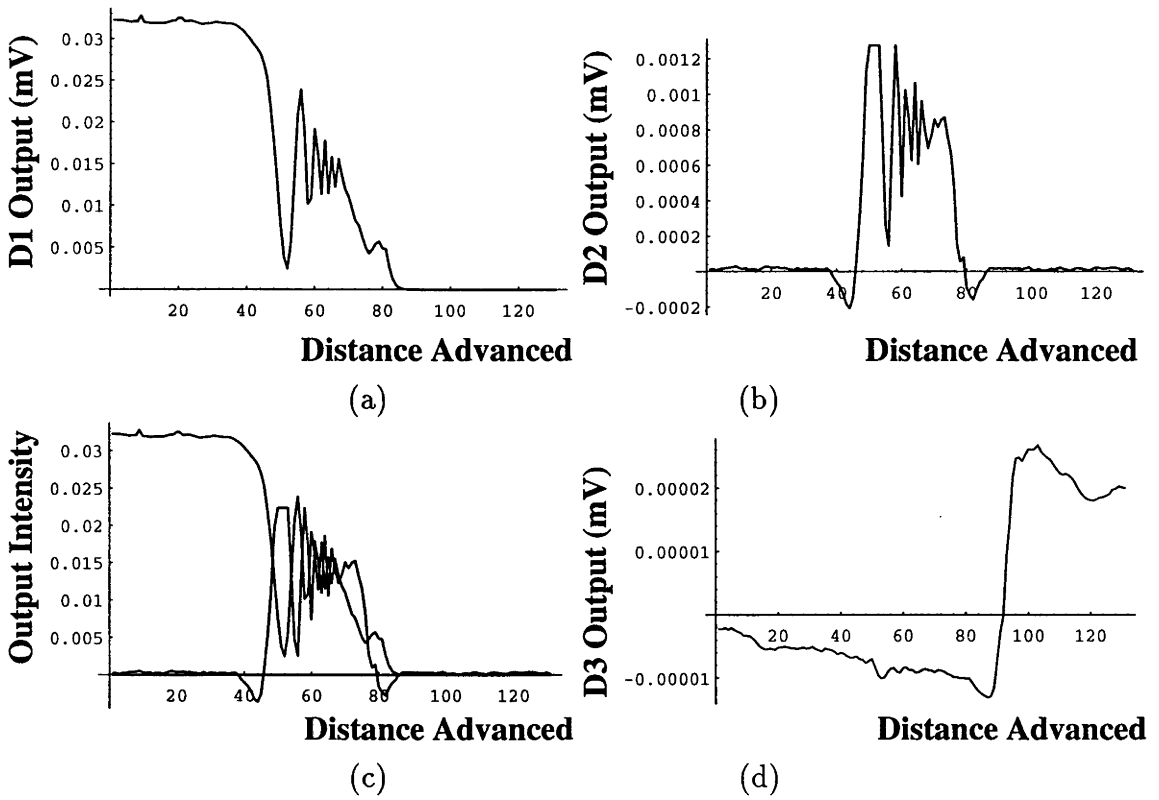

Figure 3.6: Typical signals from a coupler drawing experiment; horizontal axes normalised *(a)* D1 signal *(b)* D2 signal; *(c)* D1 & D2 signals superimposed and scaled for equal effective detector sensitivity *(d)* reflexion signal; *Horizontal axes:* one unit equivalent to 25μm advance.

Experiment Number	Waist Width (μm)	D3 Output for Unit Input (V)	D3 Signal (μV) after: drawing	clamp release	index matching	Final dB Reflexion
1	50.0	15.6	43.0	43.0	6.0	-56.3
2	48.0	13.3	26.6	26.8	13.1	-59.9
3	33.0	6.6	66.0	7.1	-0.46	-60.5
4	30.0	5.5	22.8	-105.7	-162.4	-49.8
5	24.0	5.5	35.1	31.0	-152.2	-44.7
6	20.0	5.5	39.0	-80.0	-148.0	-49.0
7	6.0	5.5	2.9	3.6	0.1	-61.9
8	2.0	7.4	55.0	96.7	-20.0	-48.0

Table 3.2: Reflexions from couplers of various tapering degrees

There is not the strong correlation between the degree of tapering and the reflexion level predicted by the findings of §3.2.2 (Fig-3.7), especially given the small reflexion from the well-tapered coupler number 7. The Spearman Co-efficient of Rank Correlation between the waist-width / reflexion data pairs is 0.24; *i.e.* statistically insignificant[Walpole and Meyers, 1978]. Even if the most outlying result is removed (coupler 7), the Spearman co-efficient is only 0.64; again, insignificant. These experimental results therefore provide reasonable evidence that the major reflexions from couplers do not arise from any of the effects discussed in §§-3.2.1, 3.2.2 or 3.2.3. It should be noted that if the coupler was so highly tapered as to break, the back reflexion increased dramatically (to as much as about -20dB) owing to the high Fresnel reflexion from the broken end.

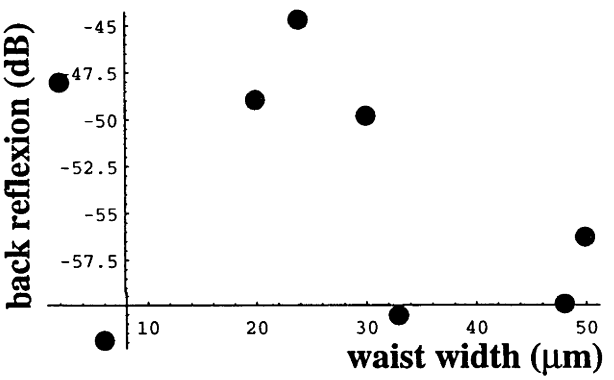

Figure 3.7: Reflexion as a function of waist width, being an indication of degree of tapering

3.5.3 Coherence Experiments

A second experiment was now undertaken to try to observe the dependence of the back reflexions on the source coherence length. The back-reflexion from three commercial fused biconic 50 : 50 couplers was measured both with the DFB laser and the LED sources. Given the curves in Fig-3.3, the DFB laser should be equivalent to a source of infinite coherence length.

With the DFB laser source, three sample couplers return -62dB, -58dB and -52dB back-reflected power relative to the source power. With the quartz-iodide lamp through the monochromator, these figures become -66dB, -60dB and -51dB,

respectively. If the linewidth $\Delta\lambda$ of $G(\nu)$ in (3.32) is taken to be the difference between the two wavelengths where $G(\nu)$ is half its peak value, then $\Delta\lambda \approx \lambda^2/(\pi l_c n_{cl})$. Thus, for the LED source, $l_c \approx 1.54^2/(1.5 \times \pi \times 0.04) \approx 13\mu$m. For a Lorentzian lineshape, Fig-3.3*(a)* shows that this is short enough to give an appreciable increase in back-reflexion over the perfectly coherent case, thus the lack of difference between the DFB and LED results means either *(i)* that the reflexions do not arise from distributed regions, *i.e.* L_c is short and the reflexions are Fresnel-like or *(ii)* $B(\nu)$ is non-Lorentzian, possibly Gaussian.

3.6 Conclusions

This Chapter has presented a range of theories, to explain the source of the back reflexions observed from fused-biconic couplers. To evaluate these theories' predictions for a specific example, the coupler's cross-section was taken to be circular and the even and odd modes are then the $HE_{1,1}$ and $HE_{2,1}$ modes of a multimode fibre. The motivations for this choice are *(i)* that it is analytically tractible and *(ii)* that the coupling in a fused biconic coupler takes place in its most highly drawn-down regions, where the cross-section is very nearly circular. Since coupling coefficients are weighted overlap integrals between modes and since the modal shapes are not highly sensitive functions of the cross-section, it seems reasonable to expect that the results of the analyses in this Chapter would not change greatly if the real coupler's shape were somewhat distorted from that assumed.

It was found in general that most perturbations/imperfections/tapers present in fibre couplers are far too small to be the origin of those observed because, aside from the Fresnel case, reflexions arise from a distributed set of points rather than a single point and, unless the waveguide varies with z at the correct Bragg wavelength, the components of the distributed reflexion suffer destructive interference. Thus, the observed reflexions must arise either from *(i)* abrupt changes and transverse interfaces within the guide; or *(ii)* perturbations varying at a spatial frequency corresponding to the correct Bragg wavelength; or *(iii)* extremely large coupling co-efficients, of the order of 10^4m^{-1}.

Owing to the smooth drawing process, abrupt changes within the coupler are

unlikely. By steeping different parts of the coupler in index-matching fluid, it was observed that the back reflexions were probably not localised to regions of less than a millimetre in length. Hence, this experimental result would seem to support the assertion that there are no abrupt waveguide changes.

Surface roughness on the cladding-air interface may have significant spatial spectral content at the correct Bragg spatial frequencies; however, if surface roughness is the main reflexion source, the results of §3.2.3 predict an extremely strong dependence of the reflected power on the degree of tapering, whereas no statistically significant correlation between these two parameters was experimentally observed. Hence, surface roughness is almost certainly not responsible for the main reflexions observed. The same comments apply to any reflexion arising from the cladding-air tapered interface.

Of all the candidate effects examined, only the stress-optic effect produces large enough coupling co-efficients to give distributed reflexions of the order of those observed from practical fused biconic couplers, *i.e.* the analysis suggests it to be the most likely explanation of the back-reflexions from practical fused-biconic couplers. The readily observable influence that the supporting clamps in Fig-3.4 have on the back reflexions lends substantial weight to this theory. Reflexion-producing stress in practical couplers may arise from the knots at either end of the coupling region or from the anchor points securing the coupler inside its housing.

Finally, the experimental use of sources of different coherence lengths did not lead to the marked increase in reflected power with decreasing source coherence length foreseen in §3.4. However, this theory is strongly dependent on the statistics governing the longitudinal coupling co-efficient variation, hence the lack of an observed power increase for low-coherence sources means that either *(i)* the back reflexions are Fresnel-like and arise from abrupt interfaces within the coupler or *(ii)* the autocorrelation function describing the longitudinal coupling co-efficient variation is non-Lorentzian. Given that above results suggest the reflexion sources are not confined to concentrated regions within the coupler, the latter alternative would seem more likely.

3.7 Appendix: Pipe Co-ordinate Coupled Mode Equations

3.7.1 Orthogonal Pipe Co-ordinates

Pipe co-ordinates are familiar in the Theory of Elasticity[Landau and Lifschitz, 1970] and the scalar wave equation has already been cast into them[Kath and Kriegsmann, 1988][Ladouceur, 1992, Ch-8] with the aim of calculating loss from bends. Likewise, we cast the Ampère and Faraday Laws into pipe co-ordinates and then the discussion in [Snyder and Love, 1983, §31-14] yields the coupling co-efficients arising from bends and twists.

Beginning with the Frenet-Serret co-ordinates, let $\mathbf{r}$ be the position vector of a point in the waveguide cross-section and let the arclength s be the distance along the waveguide. The mutually orthogonal *tangent, normal and binormal vectors* $\hat{\mathbf{t}}$, $\hat{\mathbf{n}}$, $\hat{\mathbf{b}}$, respectively, are defined by:

$$\hat{\mathbf{t}} = \frac{\frac{d\mathbf{r}}{ds}}{\left|\frac{d\mathbf{r}}{ds}\right|}; \quad \hat{\mathbf{n}} = \frac{\frac{d\hat{\mathbf{t}}}{ds}}{\left|\frac{d\hat{\mathbf{t}}}{ds}\right|}; \quad \hat{\mathbf{b}} = \hat{\mathbf{t}} \times \hat{\mathbf{n}} \tag{3.33}$$

and fulfill the Frenet-Serret formulas:

$$\frac{d\hat{\mathbf{n}}}{ds} = \tau\hat{\mathbf{b}} - \kappa\hat{\mathbf{t}}; \quad \frac{d\hat{\mathbf{b}}}{ds} = -\tau\hat{\mathbf{n}}; \quad \frac{d\hat{\mathbf{t}}}{ds} = \kappa\hat{\mathbf{n}}; \tag{3.34}$$

where the scalars τ and κ, with dimensions of reciprocal length, are called the torsion and curvature, respectively.

The Frenet-Serret co-ordinates, defined by expressing the position vector of a point within a cross-section as $n\hat{\mathbf{n}} + b\hat{\mathbf{b}}$, is *not* an orthogonal system. As s increases, a point with constant co-ordinates (n, b) traces out a thread whose tangent, by (3.34), is $n\tau\hat{\mathbf{b}} - n\kappa\hat{\mathbf{t}} - b\tau\hat{\mathbf{n}}$, *i.e. is not* parallel to $\hat{\mathbf{t}}$ and therefore the thread does not in general intersect any cross-section $s = s_0$ at right angles. To find unit vectors $\hat{\mathbf{u}} = a(s)\hat{\mathbf{n}} + b(s)\hat{\mathbf{b}}$ and $\hat{\mathbf{v}}$ (orthogonal to $\hat{\mathbf{u}}$) whose heads move parallel to the tangent $\hat{\mathbf{t}}$ as s increases, we require the $\hat{\mathbf{n}}$ and $\hat{\mathbf{b}}$ components of $d\hat{\mathbf{u}}/ds$ to vanish and simplify the resulting expressions with (3.33):

$$\frac{da(s)}{ds} - \tau b(s) = 0; \quad \frac{db(s)}{ds} + \tau a(s) = 0 \tag{3.35}$$

If $(a(s), b(s)$ is a solution of (3.35), so is $(-b(s), a(s))$, whence the required orthonormal vectors:

$$\hat{\mathbf{u}} = \frac{a(s)\hat{\mathbf{n}} + b(s)\hat{\mathbf{b}}}{\sqrt{a(s)^2 + b(s)^2}}; \quad \hat{\mathbf{v}} = \frac{-b(s)\hat{\mathbf{n}} + a(s)\hat{\mathbf{b}}}{\sqrt{a(s)^2 + b(s)^2}} \tag{3.36}$$

which, together with the tangent $\hat{\mathbf{t}}$, define an orthogonal curvillinear co-ordinate system. Any solution of (3.35) will define an orthogonal system and also shows that the co-ordinate axes defined by $\hat{\mathbf{u}}$ and $\hat{\mathbf{v}}$ rotate with a spatial angular frequency of τ radians per unit length with respect to $\hat{\mathbf{b}}$ and $\hat{\mathbf{n}}$. A particular solution of (3.35) is $(a(s), b(s)) = (\cos(\tau s), \sin(\tau s))$, whence:

$$\frac{d\hat{\mathbf{u}}}{ds} = -\kappa\cos(\tau s)\hat{\mathbf{t}}; \quad \frac{d\hat{\mathbf{v}}}{ds} = \kappa\sin(\tau s)\hat{\mathbf{t}}; \quad \frac{d\hat{\mathbf{t}}}{ds} = \kappa\left(\cos(\tau s)\hat{\mathbf{u}} - \sin(\tau s)\hat{\mathbf{v}}\right); \tag{3.37}$$

The co-ordinate systems defined by the Frenet-Serret and pipe co-ordinates are *not* single-valued, for any two planes $s = s_1$ and $s = s_2$ in general intersect, thus the points on the intersection have at least two possible co-ordinate representations.

The line of intersection between the planes $s = s_0$ and $s = s_0 + \delta s$ as $\delta s \to 0$ can be readily calculated to be given by $\mathbf{K}.\mathbf{r}_a = 1$, where $\mathbf{r}_a = u_a\hat{\mathbf{u}} + v_a\hat{\mathbf{v}}$ is the position vector of any point on the intersection line and the *curvature vector* $\mathbf{K} = \kappa\hat{\mathbf{n}}$ is orthogonal to the intersection line, *i.e.* points directly to the point on the intersection line nearest to the waveguide's axis at $(0, 0, s_0)$. The minimum distance from the waveguide's axis to the intersection line is $R = 1/\kappa$, the radius of curvature, and the waveguide's cross-section rotates about an instant axis, contained in the cross-section, though κ radians per unit arclength.

Note that, for most practical waveguides, the fields at a distance R from the waveguides are utterly negligible, so we can safely do usual vector analysis in the pipe co-ordinate system without fear of multiple-valuedness invalidating our procedures.

3.7.2 Maxwell's Equations in Pipe Co-ordinates

At a point $\mathbf{r} = u\hat{\mathbf{u}} + v\hat{\mathbf{v}}$ on a particular cross-section, the *scale factors* or *metric weights* for the orthogonal pipe co-ordinate system[Spiegel, 1974, Ch-7] are $h_u = |\partial\mathbf{r}/\partial u|$, $h_v = |\partial\mathbf{r}/\partial v|$ and $h_s = |\partial\mathbf{r}/\partial s|$. By (3.37), $d\mathbf{r} = \hat{\mathbf{u}}du + \hat{\mathbf{v}}dv + (1 - \mathbf{K}.\mathbf{r})\hat{\mathbf{t}}$, so that:

$$h_u = h_v = 1; \quad h_s = \eta = 1 - \mathbf{K}.\mathbf{r} = 1 - \kappa u\cos(\tau s) + \kappa v \sin(\tau s) \tag{3.38}$$

For $\mathbf{E} = E_u\hat{\mathbf{u}} + E_v\hat{\mathbf{v}} + E_s\hat{\mathbf{t}}$:

$$\nabla \times \mathbf{E} = \frac{1}{h_u h_v h_s}\begin{vmatrix} h_u\hat{\mathbf{u}} & h_v\hat{\mathbf{v}} & h_s\hat{\mathbf{t}} \\ \frac{\partial}{\partial u} & \frac{\partial}{\partial v} & \frac{\partial}{\partial s} \\ h_u E_u & h_v E_v & h_s E_s \end{vmatrix} \tag{3.39}$$

(3.39) can be used to write down the Ampère and Faraday Laws in pipe co-ordinates. Simplification of the result to eliminate all axial field components yields:

$$\begin{aligned} \frac{1}{\eta}\hat{\mathbf{t}} \times D_s(\mathbf{E}_\perp) + \bar{\nabla}_\perp \times \left(\frac{\bar{\nabla}_\perp \times \mathbf{H}_\perp}{i\omega\epsilon}\right) - \frac{1}{i\omega\epsilon\eta}\mathbf{K} \times (\bar{\nabla}_\perp \times \mathbf{H}_\perp) &= -i\omega\mu\mathbf{H}_\perp \\ \frac{1}{\eta}\hat{\mathbf{t}} \times D_s(\mathbf{H}_\perp) - \bar{\nabla}_\perp \times \left(\frac{\bar{\nabla}_\perp \times \mathbf{E}_\perp}{i\omega\mu}\right) + \frac{1}{i\omega\mu\eta}\mathbf{K} \times (\bar{\nabla}_\perp \times \mathbf{E}_\perp) &= i\omega\epsilon\mathbf{E}_\perp \end{aligned} \tag{3.40}$$

where:

$$D_s(\mathbf{E}_\perp) = \frac{\partial E_u}{\partial s}\hat{\mathbf{u}} + \frac{\partial E_v}{\partial s}\hat{\mathbf{v}}; \quad \bar{\nabla}_\perp \times \mathbf{E}_\perp = \left(\frac{\partial E_v}{\partial u} - \frac{\partial E_u}{\partial v}\right)\hat{\mathbf{t}} \tag{3.41}$$

i.e. D_s and $\bar{\nabla}_\perp$ *would be* the s-derivative and transverse component of the curl *were* the co-ordinate system rectangular, *i.e.* $\kappa = 0$. In the above, the relationship $\nabla\eta = -\mathbf{K}$ has been used.

The axial field components are given by:

$$\frac{\partial E_v}{\partial u} - \frac{\partial E_u}{\partial v} = -i\omega\mu H_s; \quad \frac{\partial H_v}{\partial u} - \frac{\partial H_u}{\partial v} = i\omega\epsilon E_s \tag{3.42}$$

3.7.3 The Coupled Mode Equations in Pipe Co-ordinates

We reproduce the reasoning in [Snyder and Love, 1983, §31-14] for pipe co-ordinates using the local modal fields $\{\hat{\mathbf{e}}_j, \hat{\mathbf{h}}_j\}$. Since these fields are modes of a translationally-invariant waveguide with the same cross-section as the bent one at the plane $s = s_0$ in question, they obey (3.40) when $h_s = \eta = 1$ and $\mathbf{K} = \mathbf{0}$. Therefore:

$$\begin{aligned} i\beta_j\hat{\mathbf{t}} \times \hat{\mathbf{e}}_{j\perp} + \bar{\nabla}_\perp \times \left(\frac{\bar{\nabla}_\perp \times \hat{\mathbf{h}}_{j\perp}}{i\omega\epsilon}\right) &= -i\omega\mu\hat{\mathbf{h}}_{j\perp} \\ i\beta_j\hat{\mathbf{t}} \times \hat{\mathbf{h}}_{j\perp} - \bar{\nabla}_\perp \times \left(\frac{\bar{\nabla}_\perp \times \hat{\mathbf{e}}_{j\perp}}{i\omega\mu}\right) &= i\omega\epsilon\hat{\mathbf{e}}_{j\perp} \end{aligned} \tag{3.43}$$

The transverse electromagnetic field can be written:

$$\mathbf{E}_\perp = \sum_j \left(b_{+j}(s) + b_{-j}(s)\right) \hat{\mathbf{e}}_{j\perp}; \quad \mathbf{H}_\perp = \sum_j \left(b_{+j}(s) - b_{-j}(s)\right) \hat{\mathbf{h}}_{j\perp} \tag{3.44}$$

(3.44) is substituted into (3.40), simplified with (3.43) and then the reasoning of [Snyder and Love, 1983, §13-14] is applied almost without modification. After (3.42) is used to eliminate the $\bar{\nabla}_\perp \times \hat{\mathbf{e}}$ and $\bar{\nabla}_\perp \times \hat{\mathbf{h}}$ terms, this leaves:

$$\begin{aligned} 4C_{-j,+k} = &- \int_{A_\infty} \hat{\mathbf{t}}. \left(\hat{\mathbf{h}}_{j\perp} \times \frac{\partial \hat{\mathbf{e}}_{k\perp}}{\partial s} + \hat{\mathbf{e}}_{j\perp} \times \frac{\partial \hat{\mathbf{h}}_{k\perp}}{\partial s} \right) dA + \\ & i\beta_k \mathbf{K}. \int_{A_\infty} \mathbf{r}\, \hat{\mathbf{t}}. \left(\hat{\mathbf{e}}_{k\perp} \times \hat{\mathbf{h}}_{j\perp} - \hat{\mathbf{e}}_{j\perp} \times \hat{\mathbf{h}}_{k\perp} \right) dA - \mathbf{K}. \int_{A_\infty} \hat{\mathbf{t}} \times \left(\hat{e}_{ks} \hat{\mathbf{h}}_{j\perp} + \hat{h}_{ks} \hat{\mathbf{e}}_{j\perp} \right) dA \end{aligned} \tag{3.45}$$

and the remaining coupling co-efficients $C_{+j,+k}$, $C_{+j,-k}$ and $C_{-j,-k}$ follow from (3.3) and (3.45) by using [Snyder and Love, 1983, Eq-(11-7)], *i.e.* with $\beta_{-j} = -\beta_j$, $\hat{\mathbf{e}}_{-j\perp} = \hat{\mathbf{e}}_{j\perp}$ and $\hat{\mathbf{h}}_{-j\perp} = -\hat{\mathbf{h}}_{j\perp}$.

The first term in (3.45) is real for lossless waveguides and is the same as the coupling co-efficient in (3.4). It is thus nonzero for tapers or fibres with surface roughness. It is also nonzero as the result of any effect where the electromagnetic field spins relative to the vectors $\hat{\mathbf{u}}$ and $\hat{\mathbf{v}}$, *e.g.* when a birefringent fibre is twisted or in a spun birefringent fibre.

The second and third terms arise from waveguide bending, vanish if and only if $\mathbf{K} = \mathbf{0}$ and are purely imaginary for a lossless waveguide. It is useful to examine $C_{j,j}$, whose second term in (3.45) dwarfs the third in the weak guidance case, when all fields are almost transverse. $C_{j,j}$ adds to the propagation constant β_j and if ψ_j is the normalised scalar wavefunction, then (3.45) gives the effective propagation constant for a bend of curvature κ as:

$$\beta_{j,eff} = \beta_j + iC_{+j,+j} = \beta_j \left(1 + \kappa \int_{A_\infty} r \cos(\theta) \psi^2 dA\right) \tag{3.46}$$

The methods of [Snyder and Love, 1983, §36-14] analyse a bend by replacing it with an effective index at the point with polar co-ordinates (r, θ) in the fibre's cross-section given by:

$$n_{eff}^2 = n_{cl}^2 (1 + 2\kappa r \cos(\theta)) \tag{3.47}$$

and such an index profile can be shown, with perturbation theory, to produce an effective propagation constant as given by (3.46). Thus, the coupling co-efficients agree with the results of the effective index profile method.

Chapter 4

Loss-Reduction in Fused-Biconic Couplers

4.1 Introduction

In this Chapter we briefly examine possibilities for the redesign of fused-biconic couplers with the aims of *(i)* the further reduction of their already low-loss characteristics and *(ii)* device shortening and compaction. Data from a commercial coupler will be used and, to uphold confidentiality, the study's quantitative results cannot be disclosed. Instead, the study's methods are summarised and a qualitative description of its findings is given.

The fused biconic process is currently by far the most widely used production technique for commercially-produced optical couplers, notwithstanding the growing research effort and commercial development in planar technology. The limited means of controlling the internal dimensions of a fused biconic coupler, whose production was outlined in §3.5, are *(i)* the furnace temperature profile, *(ii)* the drawing speed and *(iii)* the tension in the fibres. A method[Birks and Li, 1992] has recently been proposed for finely controlling the taper shape and involves heating the fibres with a small flame swept back and forth along the coupling region. The relative proportion of time spent by the flame at each position along the fibre is adjustable and controls the heat power input and therefore the effective temperature and glass viscosity as a function of longitudinal position. By solving the viscous flow equations, one can calculate the required sweeping to produce the desired internal coupler dimensions.

Embellishments of the fused biconic process include *(i)* the pretapering of one of the coupler's fibres to introduce an asymmetry to the cross-section, thus improving the wavelength-independence of the coupler's behaviour[Mortimore, 1985] and *(ii)* the threading of the coupled fibres through vicor tubing, which then maintains specific cross-sectional geometries[Mortimore, 1989] throughout the drawing process.

The design of tapers for the practical manufacture of couplers has hitherto been an almost wholly experimental procedure, choosing different furnace and drawing speed configurations by trial and error. However, as optical fibre networks become commonplace and performance requirements on the components become steadily more demanding, the need to optimise component designs will become overwhelming. Given that internal coupler dimensions can now be coarsely controlled[Birks and Li, 1992], it would now seem worthwhile to appraise and improve contemporary coupler designs with the physically-based adiabaticity delineation criteria and computer design tools, such as the beam propagation method (BPM).

4.2 Simulations of Tapered Couplers

4.2.1 Geometric Coupler Model

Dimension data were taken from a practical wavelength-flattened asymmetric coupler sliced at representative transverse cross-sections. The defining parameters measured were the two fibre diameters, a and b, and the separation, d, between the fibre centres, as defined in Fig-4.1. Note that $b < a$, since one of the fibres is pretapered to achieve a better (weaker) splitting ratio dependence on wavelength.

It will be shown that coupling between the fibres takes place only over a very short length near the waist, so that the coupling ratio will be highly sensitive to coupler measurement uncertainty in this region. However, owing to the waist region's small size, one can only measure very few cross-sections in practice. Given this coarseness of measurement, and other uncertainties, it is important to use a reasonable geometric model to filter noise from the data. Even so, the theoretical coupling ratio predictions are not expected to be very accurate.

With one fibre pretapered, the two lengths of fibre have the characteristic shapes shown in Fig-4.2*(a)*. A plot of the ratio b/a against axial distance z would have the

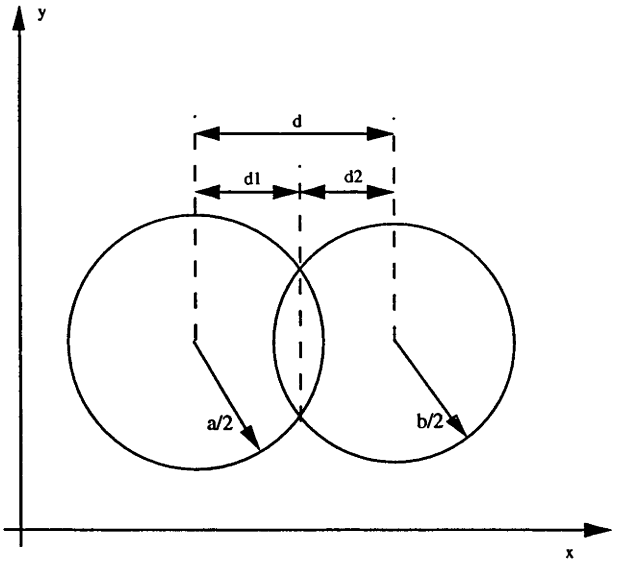

Figure 4.1: Measured cross-sectional dimensions

smooth general shape typified in Fig-4.2*(b)*. Fourier series were fitted to the data to express a, b and d as low-pass filtered functions of z. The number of terms was chosen so that the series fitted the measured data reasonably well whilst the ratio of low-pass b to low-pass a resembled Fig-4.2*(b)*.

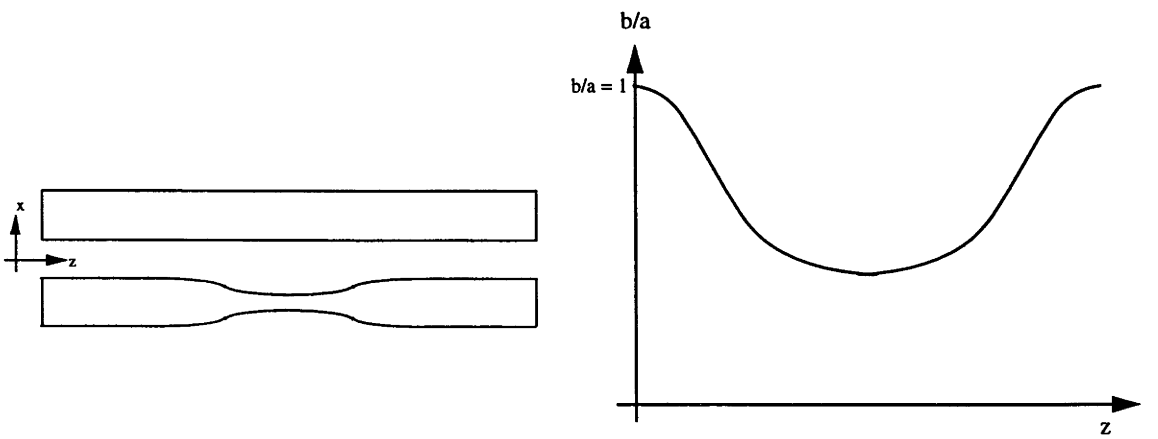

(a) (b)

Figure 4.2: *(a)* Typical fibre shapes after pretapering yet before fusion; *(b)* Typical ratio of coupler fibre radii as a function of axial distance

4.2.2 Accuracy and Limitations of the BPM

The hardware used for the numerical analysis was a Thinking Machines Corporation model CM-2 Connection Machine parallel supercomputer, with 16384 32-bit processors. The standard Fourier-transform implementation of the BPM[Feit and Fleck, 1978] was used in our studies because the processor connexion topology is ideal for calculating the many fast Fourier transforms (FFTs) needed. However, despite the increased speed, there is the restriction that the numerical cross-sectional grid must be regularly spaced, as well as all the problems peculiar to the FFT described in §2.1.

The Fourier, inverse Fourier and, for lossless media, lens correction operators constituting one axial step of the BPM are all unitary, *i.e.* they conserve the optical power of the input wavefront. Note that radiation does not appear as a loss because we are analysing an infinite periodic array, as discussed in §2.1, hence radiated power passes into neighbouring cells and is not accounted for by the method; only when lossy radiation-absorbing regions are introduced can the loss be observed. Numerical roundoff error grows linearly with axial distance because the power of roundoff errors at one step is roughly conserved and added to the power of subsequent roundoff errors.

Practical couplers are usually extremely long compared to the idealised devices often modelled by the BPM. Typically, fifty thousand axial steps are needed in a realistic simulation. Another problem peculiar to their modelling is that the cross-section is detailed over large as well as small length scales. The fibre cores are small compared to the fibres themselves and both the core-cladding and cladding-air interfaces strongly influence the coupler's behaviour. As we must represent the coupler's cross-section by a *regular* numerical grid for the FFT BPM, typically 512×512 points are needed for enough detail to be included. The finite-difference BPM implementation is not constrained to a regular grid and so could be used to concentrate the detail around the coupler's interfaces where needed, but is much slower than the Fourier implementation on the hardware used.

A simple numerical experiment found the roundoff error growth rate for our computer hardware to be such that there would be roughly a $\pm 5\%$ power uncertainty in the output powers computed by a fifty-thousand step BPM simulation

in single-precision arithmetic. This experiment entailed the BPM-analysis of a translationally-invariant, circular step refractive index profile waveguide and subsequent comparison of the results with those from an analytical analysis.

Note that, by the time the studies to be documented in Chapters-6, 7, 8 and 10 were undertaken, the Connection Machine Supercomputer used for the numerical simulations in this chapter had been upgraded to run double precision calculations, so the simulations of these later chapters will not be hindered by the 5% uncertainty referred to above.

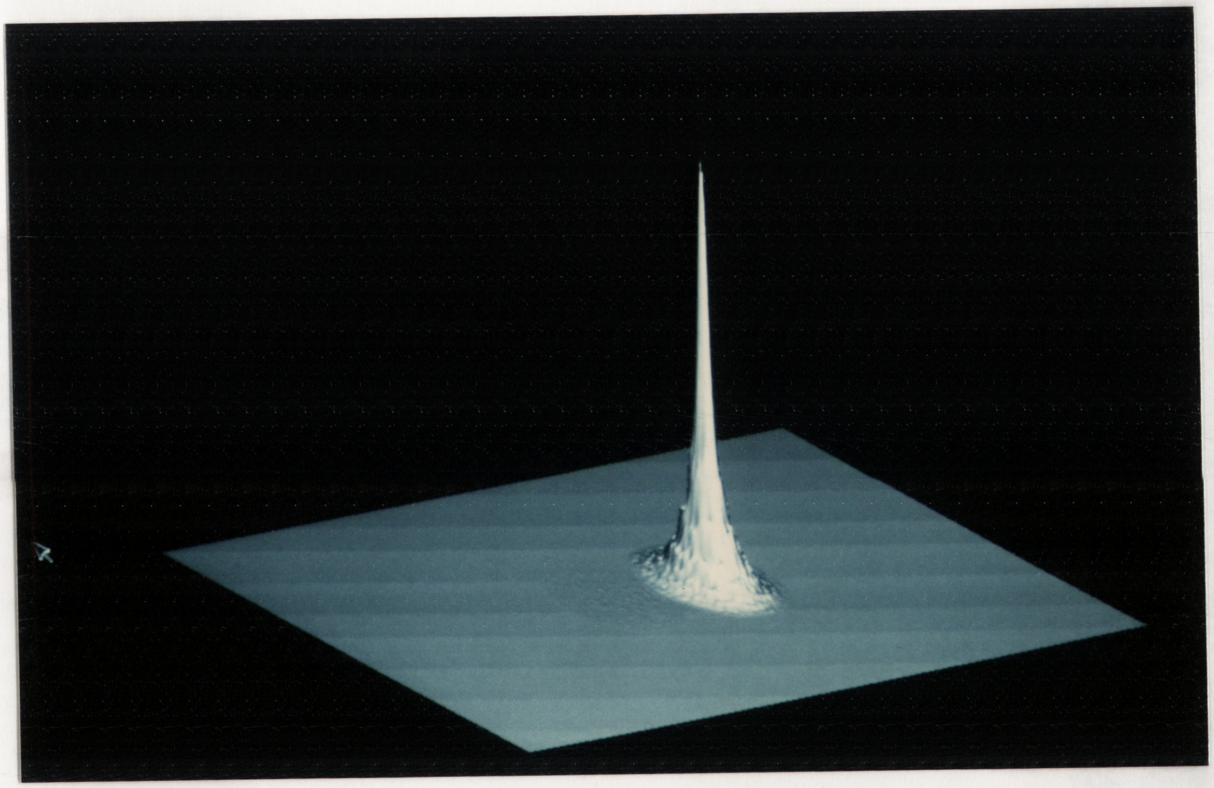

Figure 4.3: Intensity at the beginning of the coupling region, where the cladding-air interface provides all guidance.

4.2.3 BPM Simulations

For the simulations described throughout this Chapter, all axial lengths are normalised so that the coupler is one unit long, all fibre diameters and radii normalised so that the initial radius of the *undrawn* fibre is one unit and all taper angles are normalised so that a radius/diameter change of one normalised unit over one normalised unit axial length corresponds to unit taper angle.

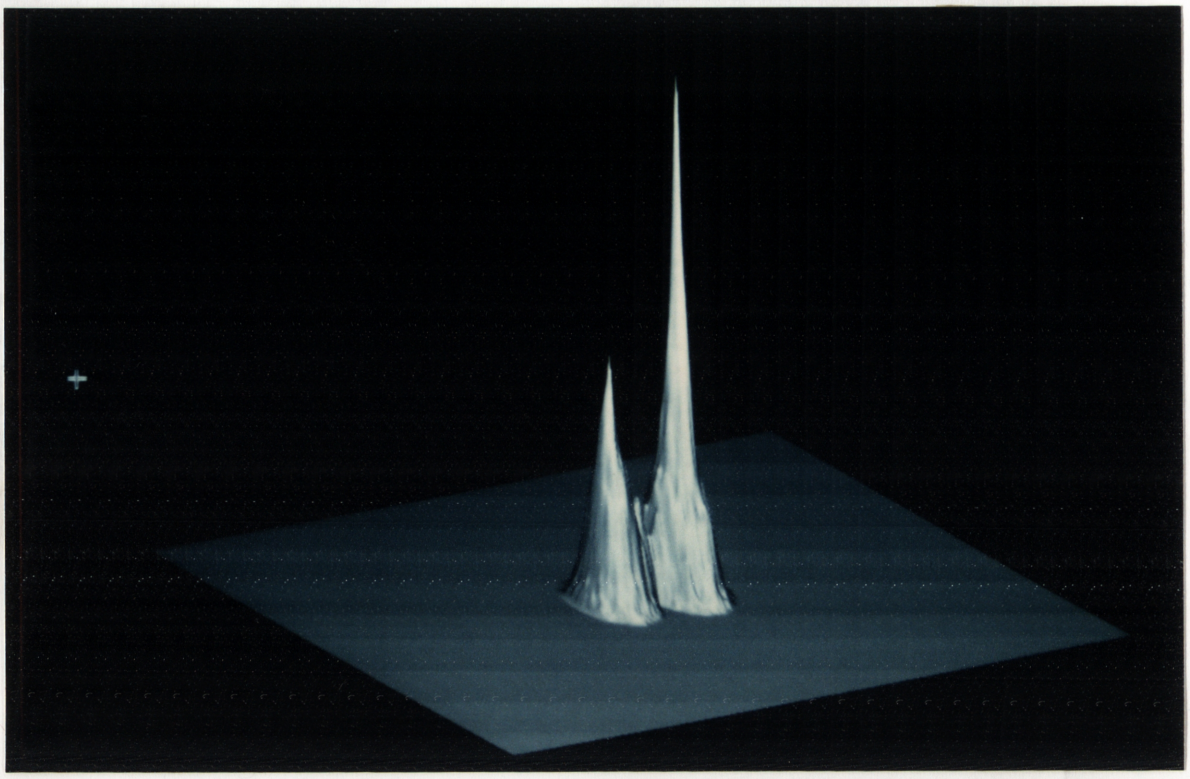

Figure 4.4: Intensity halfway through the coupler

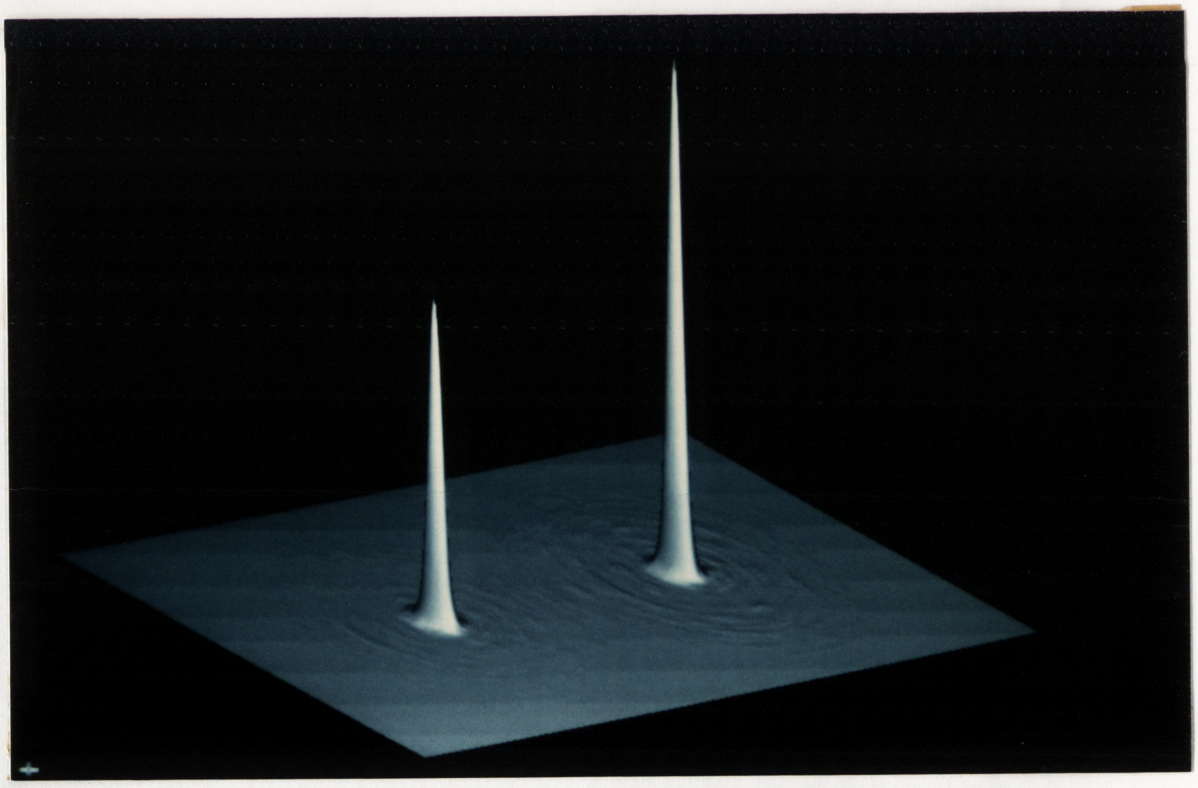

Figure 4.5: Intensity just after field leaves coupling region ($z = 0.62$)

The coupler simulation was undertaken at the manufacturer's intended working wavelength and gave the following qualitative results: *(i)* The core region loses its guidance as the fibres are tapered down so much that the core waveguide parameter $V < 1$ and guiding is then almost wholly provided by the cladding-air interface. *(ii)* Almost all the power transfer from the driven to coupled fibre takes place where $V < 1$. *(iii)* The computed coupling ratio and excess loss were quite consistent with the manufacturer's specifications given the quoted uncertainty on this figure, and also given the high uncertainty inherent in the BPM simulation of practical couplers, as discussed in §4.2.1. Thus, the BPM simulation would seem to model the practical coupler at least accurately enough to give a good qualitative indication of its behaviour.

The plots of Figs-4.3, 4.4 and 4.5 show the scalar field intensities, as found by the BPM, at several representative cross-sections of the practical coupler.

4.3 Delineation Criteria

In this Section the tapering control needed for lower coupler excess loss and short coupler lengths is discussed. The concept of the delineation curve, which distinguishes low- from high-loss tapers, is introduced and the practical coupler's performance is appraised using this curve.

Owing to the coupler's changing cross-section, energy is necessarily transferred between local supermodes. Energy loss from the coupler's bound supermodes to higher-order cladding modes, whose power is then normally dissipated in the jacket of the coupler's fibre leads, is included in such a transfer, which has been thoroughly studied[Love *et al.*, 1991] for a single, one-moded fibre taper. In the following, we apply the results of this study to a fused taper coupler, even though the coupler's cross-section and that of a taper differ.

The study derives delineation curves by two methods, the first of which considers the beat length between a single-mode taper's bound mode, with propagation constant β_1, and the cladding mode[1] with the same symmetry and whose propaga-

[1] *i.e.* when the finite cladding of a single-mode fibre is accounted for, many higher order *cladding* modes are also bound. However, being in contact with the fibre's lossy jacket, they are quickly attenuated as they propagate.

tion constant, β_2, is nearest to β_1, so that most of the excess loss arises from power transfer between these two modes. It is intuitive that the loss will be small if z_b, the beatlength, or power transfer period, between these two modes, is far greater than a length z_t over which the taper's cross-section changes significantly. A measure of z_t is taken to be the length of taper that would shrink the given cross-section down to a point if the tapering angle were held constant at its value at the cross-section in question. Thus $z_t = \rho/\Omega$, where ρ is the local core radius and Ω the local core taper angle. An approximate delineating curve between low and high-loss tapers is taken to be given by $z_t = z_b$ or:

$$\Omega = \frac{\rho(\beta_1 - \beta_2)}{2\pi} \tag{4.1}$$

which defines the local core taper angle wholly as a function of the core radius and wavelength when ρ is the core radius. By replacing ρ by the outer cladding radius, (4.1) determines the corresponding cladding taper angle.

A more accurate delineation curve can be derived more rigorously as follows. As above, the bound mode is most likely to couple to the cladding mode with the same azimuthal symmetry and whose propagation constant is nearest to that of the bound mode. In a tapered circular fibre, the fundamental eigenfield is the HE_{11} mode. Although the TE_{01} mode has the nearest propagation constant, its azimuthal symmetry is such that there can be no coupling from the HE_{11} to this mode. Hence, the fundamental bound mode will suffer loss mostly to the HE_{12} mode. From coupled local mode theory, an expression is found for the HE_{12} mode amplitude, whence the delineation criterion[Love *et al.*, 1991]:

$$Cz_b = 1 \tag{4.2}$$

where $C \; \alpha \; \Omega$ is the coupling co-efficient between the HE_{11} and HE_{12} modes. In a taper fulfilling this criterion, power oscillates sinusoidally between the fundamental and cladding modes (*c.f.* §§10.2.3, 10.2.4 and 10.3.1) so that the maximum loss to the latter is $1/\pi^2$, or roughly one tenth of the bound power. In practice, for step index fibres, this criterion gives delineation curves very similar to those given by (4.1). Thus, the more comprehensive, yet computationally costly analysis[2], needed

[2]To calculate the delineation curve exactly for the coupler by a method analogous to the rigorous

to calculate the delineation curves by this more rigorous method can be avoided and (4.1) will hereafter be used together with the following slight modification:

$$\Omega = \frac{\rho(\beta_1 - \beta_2)}{2\pi^2} \tag{4.3}$$

Since power loss is proportional to the square of Ω, the delineation curve defined by (4.3) can be used to describe a taper that loses about 1% of its bound power over each coupling period.

All the curves calculated from (4.3) show that when the core waveguide-parameter $V \approx 0.84$, corresponding to the transition from core to cladding guidance, the maximum tolerable taper angle is smallest so that even reasonably small taper angles can give rise to large excess losses. The maximum allowable taper angle is particularly shallow when $0.6 < V_{core} < 1.2$.

Fig-4.6 shows the local taper angle, $\Omega = d\rho/dz$, plotted as a function of $\rho = a(z)/2$ for the coupler. This curve is a closed loop since the taper assumes each value of ρ twice, once in the downtaper and once in the uptaper. Overlaid on the curve is the curve (4.3) calculated at the coupler's intended working wavelength, together with its image reflected in the ρ axis. If the Ω against ρ curve breaches the shaded region in as it does in Fig-4.6, then significant excess loss can be expected.

In the practical coupler, the taper angle is shallow when the constituent fibre radii are high, exactly where the steepest taper angles can be tolerated. The appraisal summarised in Fig-4.6 therefore suggests that the practical coupler can be considerably shortened with the appropriate taper shape.

4.4 Optimally Short Taper Design

For a small taper angle, $\Omega \approx d\rho(z)/dz$ and (4.3) is a differential equation defining a taper $\rho(z)$. Clearly, the one satisfying (4.3) has the most steeply tapering $\rho(z)$ that does not cross the shaded regions in Fig-4.6 and it is the shortest possible taper that

method in [Love *et al.*, 1991], one would have to find the coupler's local modal field at each axial step with the Fourier Decomposition Method[Henry and Shani, 1991], a computationally forbidding task even with the Connection Machine, whereas the curves described by (4.1) and (4.3) can be calculated with a personal computer. The rigorous use of delineation curves is demonstrated in §§10.2.3, 10.2.4 and 10.3.1.

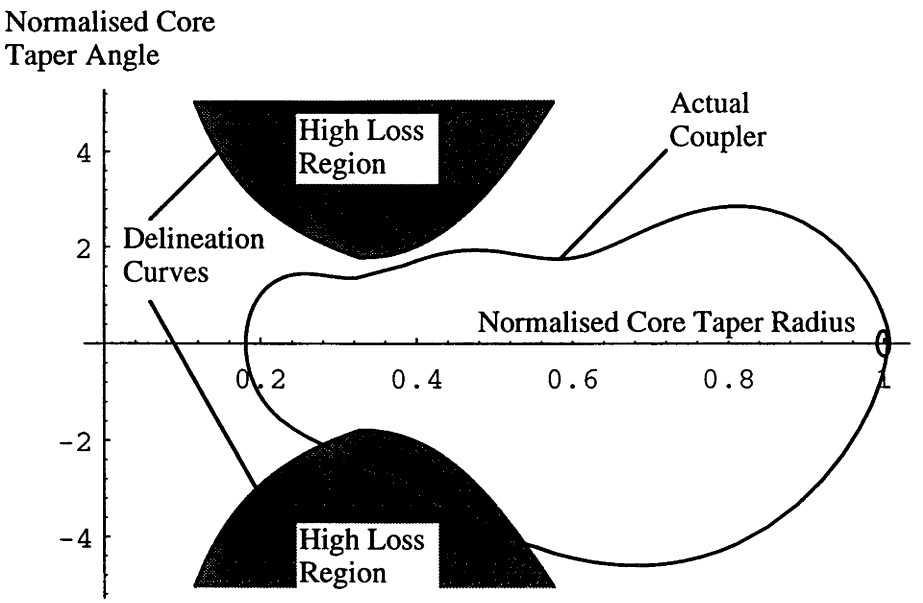

Figure 4.6: Appraisal by 1% loss delinenation curve (4.3): couplers whose defining trajectories remain outside the high loss region induce less than 1% excess loss for each 2π phase lag imposed by the coupler on the even mode relative to the odd mode.

transforms the fibre radius from the given initial to final values whilst keeping loss to within roughly 1%. A single fibre taper satisfying (4.3) is shown in Fig-4.7.

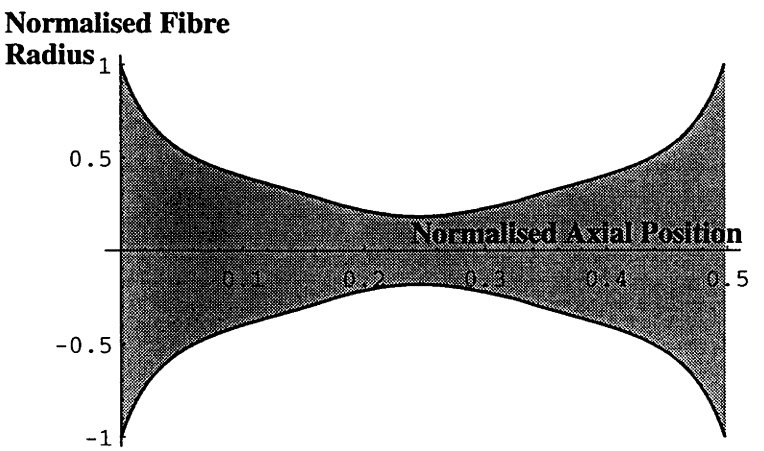

Figure 4.7: Normalised optimally-short taper shape

It must be emphasised that the shortened coupler is only optimally short at the wavelength it is designed for and BPM simulations of both the practical and length-optimised couplers based on the taper of Fig-4.7 shows the latter's excess loss to

increase to unacceptable levels when the source wavelength deviates even slightly from the intended value. The optimised taper's shortened length is bought at the price of a marked worsening of the device's loss performance and a more sensitive dependence on wavelength. Whereas the actual coupler's wavelength response is very flat and the excess loss remains reasonable within the whole band studied, the coupler optimised for wavelengths at the lower end of this band is so lossy at the upper end as to be unusable.

The optimised coupler's excess loss, computed to be 10% at its intended working wavelength, is greater than predicted by the considerations in 4.3 and the prediction error can arise from the following. *(i)* The coupler's eigenfields differ from those of a single-fibre taper, thus leading to inaccuracies in the calculation of the coupling co-efficient C in (4.2). *(ii)* The coupler's cross-section is not circularly symmetric, therefore small coupling can arise between the HE_{11} and TE_{01} modes. This coupling, although not accounted for in the derivation of (4.2), may be comparable to the coupling to the HE_{12} mode. Lastly *(iii)* The intuitive criterion (4.3) describes the delineation curves only approximately.

The optimally-short coupler's performance was now compared with that of one shortened by a simple length scaling. The latter was a version of the actual coupler scaled to be the same length as the optimised device and its excess loss performance was far inferior to that of the optimised one. Indeed, its excess loss was so great as to render the scaled device unusable.

4.5 Conclusions

In this Chapter we have demonstrated a successful modelling of and underlined the modelling problems peculiar to practical couplers. An optimally short coupler was designed whose taper angle at all positions is the maximum allowable for a given maximum power transfer between the HE_{11} and HE_{12} modes. BPM analyses of the optimised coupler and of a coupler shortened by simple scaling shows the latter's performance to be far inferior to the former's, thus showing the delineation criterion to be a useful design guide. However, a study of wavelength performance shows the optimised designs to suffer markedly worsened wavelength response and thus there

is a design trade-off between the goals of shortened device length and wide device bandwidth.

Although the exact manufacture of the optimally short taper would not be easy, significant shortening of couplers could be achieved by increasing tapering angles where the constituent fibre radii are large and by ensuring shallow taper angles in the critical region where $0.6 < V_{core} < 1.2$.

Chapter 5

Optimal Erbium Amplifier Tapers

5.1 Background

Although very early work on rare-earth doped fibre amplifiers[Snitzer, 1961; Stone, 1974] had been forgotten for many years, the development history of the erbium-doped fibre amplifier (EDFA) is truly remarkable in that there were only three years between between its first research announcement in 1987[Mears *et al.*, 1987] and the appearance of commercial EDFA systems in 1990[Payne, 1992]. In the two years immediately beforehand[Poole *et al.*, 1985; Mears *et al.*, 1985], the Modified Chemical Vapour Deposition Method (MCVD) had been enhanced to allow the incorporation of rare-earth dopants, such as Nd^{3+} and Er^{3+}, into single-moded optical fibres. Compounds based on these dopants had hitherto been unusable owing to their high melting-points.

In the few years since the EDFA's conception, the research effort on it has concentrated on a basic understanding of its physics and its design[Bjarklev *et al.*, 1989; Giles and Desurvire, 1991b; Pedersen *et al.*, 1991] and led to some outstandingly high quality, wide bandwidth devices achieving extremely high gains at close to the quantum noise limit[Laming *et al.*, 1992]. These are, of course, highly compatible with contemporary fibre systems. The research topics that, at this time (February 1994), seem important to the future development of rare-earth doped amplifiers include:

- The development of rare-earth doped fibres operating in the 1300nm optical communications band;

- The overcoming of the concentration quenching; and

- The investigation of various co-dopants (Al_2O_3, Yt^{3+}) for many novel uses, notably the "sensitisation" of an amplifying ion to light of an otherwise unusable wavelength[Townsend *et al.*, 1991; Townsend *et al.*, 1987]).

The EDFA operates at 1530nm, whereas most contemporary optical fibre communication systems operate in the 1300nm band, hence the great interest in praseodymium (Pr^{3+}) doped amplifiers (PDFAs) operating in this latter band[Ankiewicz and Rühl, 1994]. Concentration quenching is a phenomenon peculiar to erbium whereby the dopant's quantum efficiency is severely lessened for Er^{3+} concentrations greater than about 300ppm[Payne, 1992]; hence a minimum contemporary EDFA length must be about a metre, for worthwhile gains to be achieved with low Er^{3+} concentrations. Clearly, this problem must be overcome if rare-earth doped fibres are to be useful in planar integrated optics technology.

In this Chapter, we shall be studying the usefulness of EDFA tapering for the achievement of lower noise figures, higher gains and higher saturation powers. When we began our research into EDFA tapering (July 1992), many effects, *e.g.* erbium concentration, fibre numerical aperture, fibre length and background loss, had been thoroughly studied for their relevance to EDFA design and the effect of tapering seemed to be a scantily-investigated research realm. Some preliminary work[Bjarklev *et al.*, 1992] had suggested that tapering might lead to worthwhile improvements in EDFA noise performance and inspired us to undertake the research discussed here.

Unfortunately, it will be shown that, except in nontypical examples of little practical use, EDFA tapering has little effect on *what* happens within a fibre amplifier concerning noise, signal and pump powers. However, it will be seen that tapering has a considerable effect on *where* in a rare-earth doped fibre these noise, signal and pump levels are reached, and may thus be useful in future planar systems for the matching of amplifying system components that would otherwise be length-incompatible. In making our study, we shall further the approach in [Peroni and Tamburrini, 1989], where the position co-ordinate z is eliminated from system dynamic equations, and thus develop a state-space model for the EDFA.

Before discussing our study, we briefly examine the basic theory of optical am-

plification.

5.2 Basic Optical Amplifier Theory

5.2.1 Stimulated Emission and Gain Media

The underlying mechanism of an optical gain medium is that of stimulated emission[Ghatak and Thyagarajan, 1989], first predicted by Albert Einstein in 1917. In such a gain medium, the constituent atoms have several energy states and normally almost all atoms are in their lowest, or *ground* state. There are also two *lasing states* such that:

- Downward transitions between them are radiative; and
- The upper state is sufficiently long lived that a *population inversion*, where more atoms are in the upper rather than lower state, can be established.

Any energy input into the system, from electric arc discharge, chemical reaction, incoming light or many other sources, may give rise to the inversion. If an incoming light photon has energy equal to the difference between the lasing state energies, the photon may interact with an upper lasing state atom, which then falls to the lower state by emitting a photon of the same frequency, phase and direction as the incoming photon. It may also raise a lower lasing state atom to the upper state, thus undergoing *stimulated absorption* and yielding its energy to the medium. As the probabilities of each interaction are proportional to the respective energy state populations, an incoming lightbeam undergoes a net amplification when and only when there is a population inversion.

The incoming light's frequency does not have to be *exactly* equal to that corresponding to the lasing-level difference to cause stimulated emission or absorption. Many processes in the medium blur the energy levels; for example, lattice vibrations may Doppler-shift the lasing levels so that upper lasing state atoms can interact with photons whose energies differ slightly from the lasing-level difference. Clearly, the greater the imbalance between the incoming photon energy and the lasing-level difference, the less likely it will be that mechanisms such as the above will shift energy

levels enough for stimulated emission. Therefore, fewer stimulated photons will be emitted/ absorbed as the incoming light's frequency deviates more from that corresponding to the atomic energy level difference, thus giving rise to the *emission and absorption spectra*[Giles and Desurvire, 1991a].

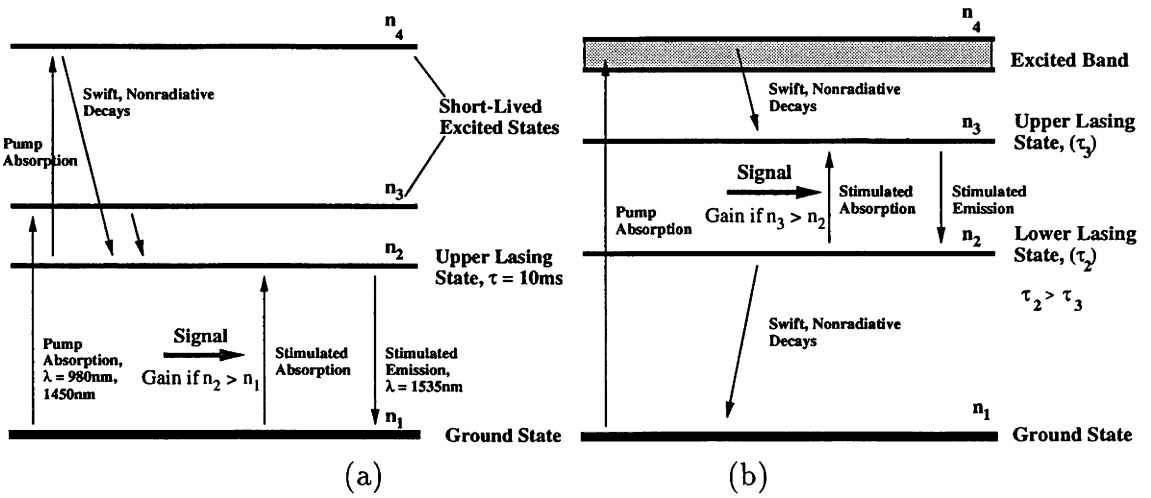

Figure 5.1: Optical Amplifier Energy Diagrams: *(a)* Main EDFA energy levels; *(b)* Schematic energy levels for four-level amplification system.

There are four important energy levels in the erbium gain medium (Fig-5.1): the ground state, which is the lower lasing state, the upper lasing state and two short-lived higher energy states[Bjarklev *et al.*, 1989, §2]. A pump beam, typically at 980nm or 1480nm, can raise ground state atoms to the third state or upper lasing state atoms to the fourth energy state. The third and fourth states are extremely short-lived and atoms in them decay swiftly by non-radiative processes to the upper lasing state, whose lifetime, τ_{21}, of about eleven milliseconds, is long enough to establish a population inversion. Note that since the lower lasing and ground states are the same, more than half of *all* the system's lasing atoms must be raised to the upper lasing state to yield a population inversion. Amplifiers with co-inciding lower lasing and ground states are called three-level lasers (even though there are really many levels) because there are ground and upper lasing states and a short-lived energy band (in the erbium amplifier comprising levels three and four), which a pump can excite ground state atoms to.

The erbium amplifier contrasts where a so-called four-level amplifier, whose lower lasing state is not the ground state but an excited one[Ghatak and Thyagarajan, 1989] and the gain material is such that the lower lasing level is much shorter lived than the upper level. Atoms raised to the fourth state quickly decay to, and tend to accumulate in, the upper lasing state, which is long lived. When they at last decay to the lower lasing level, they quickly fall to the ground level, thus establishing a population inversion with most atoms still in the ground state. The pump power needed for population inversion in a four-level amplifier is typically many thousandfold less than a corresponding three-level system, so, in this sense, the erbium amplifier is quite pump-inefficient. So far, no research has produced a suitable four-level replacement for the EDFA.

5.2.2 State Transition Defining Parameters

We now consider a sliver of gain medium, sliced along planes orthogonal to the incoming light propagation direction. Each sliver is so thin that there are no erbium ions hidden directly behind other ions from the incoming light; *i.e.* all the ions are *equally* likely to interact with the light. We consider a unit surface area: in unit time, the number of photons crossing this unit area is $I/(hf)$ where I is the light's intensity, f its frequency and h is Plank's constant. If the erbium ion concentration is n and the sliver's thickness δz, the number of ions per unit area is $n\delta z$. Let each erbium ion present an effective cross-sectional area σ to the incoming light. Then, the number of interactions per unit time per unit area of the sliver is:

$$\frac{\sigma I n \delta z}{hf} \tag{5.1}$$

Since the ion-light interaction probability is strongly frequency-dependent, so is σ.

If the interaction is a stimulated emission, the above quantity is the time-rate of photon addition to the incoming light. It is also the time-rate of ion loss from the upper to the lower lasing level. For stimulated absorption of the signal, the obvious absorption and transition rate analogies apply; for stimulated pump absorption, (5.1) is the time rate of increase of pump band ion concentration. However, ions in this band are assumed to fall instantaneously to the upper lasing level by nonradiative processes, namely the addition of vibrational energy to the gain medium's

lattice. Thus for *both* pump and signal absorption, (5.1) is the time rate of increase of upper lasing level ion concentration. Note that an ion's effective area differs for each separate transition, owing to differing physical parameters describing each transition, and the effective cross sectional-area for the transition from state a to state b is written σ_{ab}.

An ion can also decay from a higher to a lower state spontaneously, with a constant probability per unit time, independently of the particular stimulated processes taking place around it. The only important spontaneous change in erbium is from the upper lasing to the ground state and the time rate per unit volume of this change is $n_2\tau_{21}$, where n_2 is the concentration of upper lasing state ions and τ_{21} the mean time for an upper lasing state ion to decay after it has been observed in the upper lasing state. If an ion is observed in the upper lasing state, the probability that it will still be there after time t is:

$$p(t) = \frac{1}{\tau_{21}} \exp\left(-\frac{t}{\tau_{21}}\right) \tag{5.2}$$

5.3 System Dynamics

5.3.1 Basic Equations

The above considerations now lead simply, as shown in the abundant literature on EDFA dynamic analysis[Giles and Desurvire, 1991b; Giles and Desurvire, 1991a; Pedersen *et al.*, 1991; Peroni and Tamburrini, 1989; Bjarklev *et al.*, 1989], to the basic system dynamic equations. We describe all positions within the fibre using cylindrical polar co-ordinates (r, ϕ, z); thus, the signal and pump intensities within the fibre are respectively $P_s\hat{\psi}_s^2(r,\phi,z)$ and $P_p\hat{\psi}_p^2(r,\phi,z)$, with $\hat{\psi}_s$ and $\hat{\psi}_p$ the normalised fundamental (LP_{01}) fibre eigenfields at the appropriate wavelength. Throughout this Chapter, the subscript s stands for the signal and the subscript p the pump.

Consider a unit area of a slice of thickness δz. In unit time, the pump raises from the ground state (state 1) to the pump band (state 3) $\sigma_{13}P_p\hat{\psi}_p^2 n_1 \delta z/(hf_p)$ ions, which then decay straight away to state 2. Likewise, the signal raises $\sigma_{12}P_s\hat{\psi}_s^2 n_1 \delta z/(hf_s)$ straight from the ground state to state 2, for signal and pump frequencies f_s and f_p respectively. The signal also causes $\sigma_{21}P_s\hat{\psi}_s^2 n_2 \delta z/(hf_s)$ stimulated emissions back

from state 2 to 1. Meanwhile, $n_2\tau_{21}$ ions in state 2 decay spontaneously, giving rise to photons with the same frequency as, yet uncorrelated with, the signal. These propagate in both directions through the fibre and, if they contribute to the guided fundamental signal mode, are amplified as though a signal, thus giving rise to the forward and backward *amplified spontaneous emission* (ASE) powers P^+_{ASE} and P^-_{ASE}, respectively. By convention, the forward (positive) direction is the signal propagation direction. Therefore, in all the above rate terms, P_s must be replaced with $P_s + P^+_{ASE} + P^-_{ASE}$.

The total time derivative of the number of upper lasing state ions within a unit sliver area is $dn_2/dt\ \delta z$, whence:

$$\frac{dn_2}{dt} = \frac{\sigma_{13}P_p\hat{\psi}_p^2 n_1}{hf_p} + \frac{\sigma_{12}(P_s + P^+_{ASE} + P^-_{ASE})\hat{\psi}_s^2 n_1}{hf_s} - \frac{\sigma_{21}(P_s + P^+_{ASE} + P^-_{ASE})\hat{\psi}_s^2 n_2}{hf_s} - \frac{n_2}{\tau_{21}} \tag{5.3}$$

The ground state rate equation for dn_1/dt is wholly analogous. Steady state conditions are now assumed so that $dn_1/dt = -dn_2/dt = 0$, whence the *excited ion fraction* (or proportion of ions in the upper lasing state):

$$x(P_s, P_p, P^+_{ASE}, P^-_{ASE}, r, \phi, z) = \frac{\frac{\sigma_{13}P_p\hat{\psi}_p^2}{hf_p} + \frac{\sigma_{12}(P_s+P^+_{ASE}+P^-_{ASE})\hat{\psi}_s^2}{hf_s}}{\frac{\sigma_{13}P_p\hat{\psi}_p^2}{hf_p} + \frac{(\sigma_{12}+\sigma_{21})(P_s+P^+_{ASE}+P^-_{ASE})\hat{\psi}_s^2}{hf_s} + \frac{1}{\tau_{12}}} \tag{5.4}$$

Note that the upper and lower lasing state ion concentrations are given by $n_2 = x\rho$, $n_1 = (1-x)\rho$, where ρ is the total ion concentration.

The signal's energy is augmented (*resp.* diminished) by hf_s for each stimulated emission (*resp.* absorption). Using the calculation results above for the number of ion transitions both upwards and downwards between the various states per unit time in a unit area sliver of length δz, integrating these results over the fibre cross-section at position z and multiplying the result by the energy change per transition hf_s (or hf_p for the pump), the system dynamic equations describing signal, pump and ASE evolution are found[Bjarklev *et al.*, 1989]:

$$\frac{dP_p}{dz} = P_p g_p \left(P_s, P_p, P^+_{ASE}, P^-_{ASE}, z\right)$$

$$\frac{dP_s}{dz} = P_s g_s \left(P_s, P_p, P^+_{ASE}, P^-_{ASE}, z\right)$$

$$\frac{dP^\pm_{ASE}}{dz} = \pm P^\pm_{ASE} g_s \left(P_s, P_p, P^+_{ASE}, P^-_{ASE}, z\right) \pm B\ h\ f_s a \left(P_s, P_p, P^+_{ASE}, P^-_{ASE}, z\right) \tag{5.5}$$

where

$$g_p \left(P_s, P_p, P^+_{ASE}, P^-_{ASE}, z\right) =$$
$$-H \int_0^\infty \int_0^{2\pi} \hat{\psi}_p^2(r,\phi,z) \left(\sigma_{24} n_2(P_s, P_p, P^+_{ASE}, P^-_{ASE}, r, \phi, z) + \right.$$
$$\left. \sigma_{13} n_1(P_s, P_p, P^+_{ASE}, P^-_{ASE}, r, \phi, z)\right) r dr d\phi$$

$$g_s \left(P_s, P_p, P^+_{ASE}, P^-_{ASE}, z\right) = a(P_s, P_p, P^+_{ASE}, P^-_{ASE}, z) - b(P_s, P_p, P^+_{ASE}, P^-_{ASE}, z))$$

$$a(P_s, P_p, P^+_{ASE}, P^-_{ASE}, z) = \sigma_{21} \int_0^\infty \int_0^{2\pi} \hat{\psi}_s^2(r,\phi,z) n_2(P_s, P_p, P^+_{ASE}, P^-_{ASE}, r, \phi, z) r dr d\phi$$

$$b(P_s, P_p, z) = \sigma_{12} \int_0^\infty \int_0^{2\pi} \hat{\psi}_s^2(r,\phi,z) n_1(P_s, P_p, P^+_{ASE}, P^-_{ASE}, r, \phi, z) r dr d\phi \tag{5.6}$$

Here H is the pump's heading: $H = +1$ for a co-propagating signal pump (pump in same direction as the signal) and $H = -1$ for a counterpropagating pump. B is the detector's bandwidth and the Bhf_s term's derivation is not straightforward from the above discussion (the reader is referred to [Shimoda *et al.*, 1957, §6]). Note also that usually $\sigma_{12} = \sigma_{21}$ and we shall hereafter be assuming this.

A function that will be important in the following is:

$$f(z) = a(z) + b(z) \tag{5.7}$$

Note that f is *independent* of P_s, P_p and ASE since the total ion concentration, $n_1 + n_2$, is also independent of these powers.

EDFA analysis is greatly complicated by the full account of the ASE terms and we make one of two approximations, as stated in the relevant Section:

- Neglect the ASE terms altogether, **or**

- Account for them fully in the solution of the dynamic equations 5.5, whilst neglecting them for the concurrent calculation of the tapering strategies.

The first approximation will be valid in *e.g.* large signal, co-propagating pump systems, such as the example shown in [Bjarklev *et al.*, 1989, Fig-3]. Here, the amplified spontaneous emission is very small compared to the signal except along the first fifth of the amplifier's length, where the backward propagating amplified spontaneous emission is between 0dB and 20dB higher than the signal. However, in these very early amplifier stages, the pump dwarfs both the signal and amplified spontaneous emission and is by far the dominant term in (5.4). The ASE influences the system dynamics by affecting the excited ion fraction, x, but in [Bjarklev *et al.*, 1989] this influence is utterly negligible owing to the dominance of both signal and pump. This approximation will be used in §§5.4 and 5.7.

The second approximation will be used in §5.5 and its validity will be appraised in each individual case.

The usual outcome from neglect of ASE is that the excited ion fraction, and therefore amplifier gain, are overestimated (see (5.4)). Eq. (5.8) (below) shows the system noise figure to be a weighted average (along the amplifier's length) of the reciprocal of the signal power, hence ASE neglect leads to noise underestimation. These outcomes are illustrated by Fig-5.2, which shows the calculated system noise figure and gain as a function of EDFA length for the 20m-long, counterpropagating pump, untapered EDFA studied in §5.6 with ASE both included and neglected.

5.3.2 Noise Considerations

The output noise in an erbium amplifier arises wholly from the quantum nature of the interactions taking place between the signal light and the erbium ions. If the system really were described by the continuous, deterministic equations of the foregoing section, then, for a given input, the output would always be exactly the same. Even the amplified spontaneous emission, which has nothing whatsoever to do with the signal, would not, in any way, be noise, because it would always be exactly known at the output and its effect could be exactly accounted for. However, the events within the gain medium are probabalistic; the per-unit-time number of spontaneous,

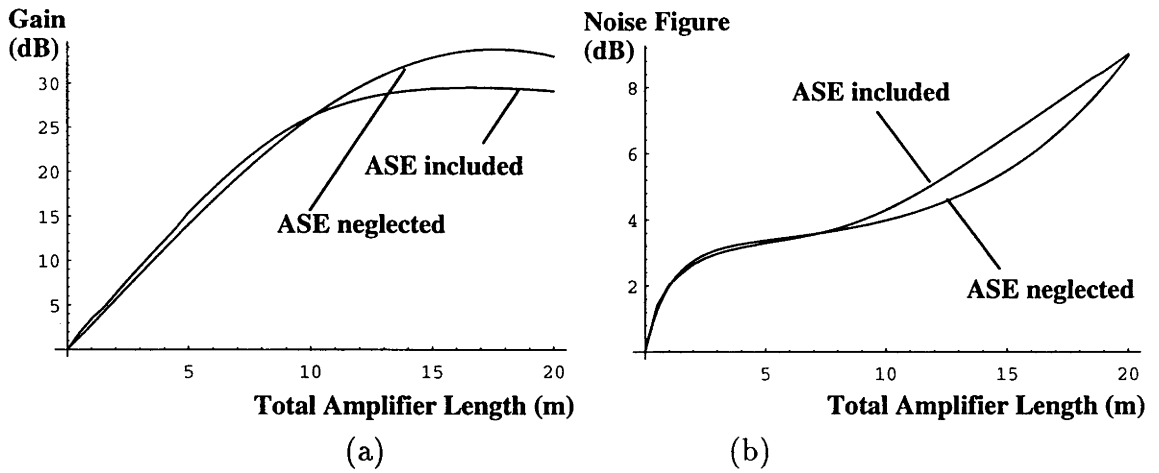

Figure 5.2: Comparison of gain and noise figure calculations with and without account for ASE for a 20m long EDFA with a counterpropagating, 150mW pump, 0.1mW signal input and all other physical parameters as described in [Bjarklev *et al.*, 1989]: *(a)* predicted gain and *(b)* noise figure.

stimulated emissions and so on waver around their mean values. This problem is addressed in [Shimoda *et al.*, 1957], wherein the differential equation describing the evolution of signal power along the fibre is replaced by an equation for the evolution of probability distributions of the number of signal photons. Appendix-5.13 presents a summary of this probabilistic approach, which leads to the following expression for the *noise figure* (*i.e.* ratio of output to input noise-to-signal ratios):

$$F(L) = P_s(0) \int_0^L \frac{f(z)}{P_s(z)} dz + 1 \tag{5.8}$$

The signal P_s is smallest near the input, so it is clear that it is beneficial to have high gain in the early amplifier stages. This lessens overall noise, in analogy with the well-known principle in the theory of amplifiers that the least noisy amplifier should be placed first in an amplifier cascade.

5.3.3 Elimination of the Axial Co-ordinate

In the following, we shall analyse the use of tapering to produce an EDFA whose core radius, R, is a specific function of the axial distance, z. The right hand sides of (5.7) and (5.4) and the gains g_p and g_s depend on R, but not explicitly on z. In

§5.5 we shall be seeking a *drawing control strategy* $R(z)$ to maximise the amplifier's signal-to-noise ratio. Following the analysis in [Peroni and Tamburrini, 1989], we can eliminate z from all equations and suppose the drawing control strategy to be no longer formulated as a function of z but rather of P_s. Thus we can specify $R = R(P_s)$ and (5.5) will yield a unique solution, given an input *system state* $(P_s, P_p, P^+_{ASE}, P^-_{ASE})$. The specifications $R(z)$ and $R(P_s)$ are thus equivalent and we can write:

$$\begin{aligned} \frac{dP_p}{dP_s} &= \frac{P_p g_p\left(P_s, P_p, P^+_{ASE}, P^-_{ASE}, R\right)}{P_s g_s\left(P_s, P_p, P^+_{ASE}, P^-_{ASE}, R\right)} \\ \frac{dP^{\pm}_{ASE}}{dP_s} &= \pm\frac{P^{\pm}_{ASE}}{P_s} \pm \frac{B\ h\ \nu\ a(Ps, P_p, P^+_{ASE}, P^-_{ASE}, R)}{P_s g_s(P_s, P_p, P^+_{ASE}, P^-_{ASE}, R)} \end{aligned} \tag{5.9}$$

Conceptually, we might imagine monitoring the output pump, signal and ASE powers and using these measurements for closed-loop control of the drawing process. In practice, the taper shape $R(z)$ would be fully calculated from $R(P_s)$ before drawing and implemented open-loop without monitoring any powers.

z is also readily removed from the noise figure by noting that $dP_s/dz = P_s g_s$:

$$F(P_{so}) = 1 + P_{si}\int_{P_{si}}^{P_{so}} \frac{f(R)}{g_s(P_s, P_p, P^+_{ASE}, P^-_{ASE}, R(P_s))P_s^2} dP_s \tag{5.10}$$

where P_{si} and P_{so} are the input and output signal powers, respectively. We shall be seeking a strategy $R(P_s)$ to minimise the cost function:

$$C(P_{si}, P_{so}) = \int_{P_{si}}^{P_{so}} \frac{f(R)}{g_s(P_s, P_p, P^+_{ASE}, P^-_{ASE}, R)P_s^2} dP_s \tag{5.11}$$

which increases monotonically with the output noise figure. We shall also be studying strategies to maximise the system gain for a given pump power, to maximise the output saturation power and to minimise the EDFA length for a given gain. This minimum-length taper will be relevant for length savings in future planar integrated amplifiers.

The elimination of the axial co-ordinate and subsequent use of the signal power as the independent variable is of great benefit to the noise minimisation problem. For, if the axial co-ordinate were present, we would have to minimise the integral:

$$\int_0^L \frac{f(u)\,du}{P_s(u)} \tag{5.12}$$

subject to the constraint that the output signal power be constant. This constraint would have to be accommodated by deriving the change in output signal $\delta P_s(L)$ as a linear functional of the perturbation, $\delta R(z)$, in the tapering strategy (analogously to δP_p as a linear functional of δR below (in 5.15, but with the axial co-ordinate included) and then minimising (5.12) subject to $\delta P_s(L) = 0$ with a Lagrange multiplier method. The use of P_s as the independent variable means that the constancy of output signal power is no longer an explicit constraint, but simply the upper endpoint.

5.4 State-Space Description of the Erbium Amplifier

Throughout this Section, all ASE terms will be dropped from all equations, thus the discussion will be only be strictly valid for large-signal systems, such as in [Bjarklev *et al.*, 1989]. In Appendix-5.12, a brief description of a full state-space model including ASE will be outlined.

Under these conditions, if P_p is known at *any* value of P_s, (5.9) completely defines P_p for all values of P_s. The point (P_s, P_p) is thus a *system state*[Anderson, 1979]. The (P_s, P_p) plane is then a system state space, and the amplifier's behaviour is fully defined by trajectories satisfying (5.9). We therefore examine the trajectories in state-space more fully.

Suppose that the system begins at point A in Fig-5.3 and consider firstly a copropagating pump-beam. The pump gain g_p is always negative as the pump is always being depleted, so, with g_s positive, the state trajectory has negative slope (equal to $P_p g_p/(g_s P_s)$). This slope never vanishes and indeed becomes infinite as the signal gain falls to zero, when the trajectory is parallel to the P_p axis at point Z. As the pump is further depleted, the signal gain becomes a signal loss as signal-stimulated absorptions outweigh signal-stimulated emissions. The trajectory slope is then positive (ZF') and a typical trajectory is as shown in Fig-5.3.

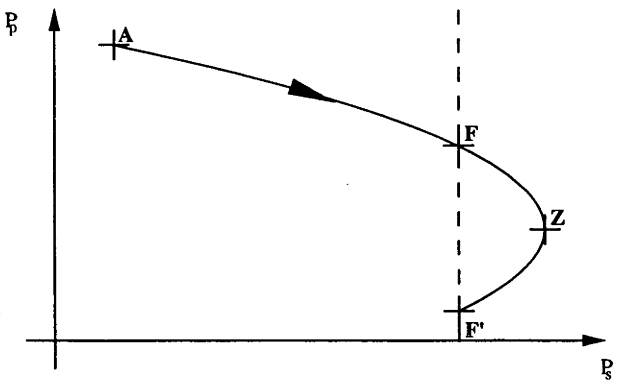

Figure 5.3: Typical state space trajectory for an erbium-doped fibre amplifier

Thus, the trajectory slope can only become positive by passing through a vertical slope. Now, there is no benefit in allowing the system state to proceed from state F to state F' in Fig-5.3 because the final signal power is the same in both cases yet the cost function C is greater at state F' than at state F. It can readily be shown that all erbium-doped fibre devices, whether amplifying or lossy (owing to an over-depleted pump), worsen the output signal-to-noise ratio as the cost of travelling in the state space is always positive. Therefore, trajectories proceeding beyond the point Z (where they become vertical) will not be further considered. The point Z corresponds to the Rühl optimal length[Rühl, 1991], where the local (incremental) gain vanishes.

We see therefore that all trajectories of useful fibre amplifiers are given by $P_p = P_p(P_s)$, *where* P_p *is a monotonically decreasing function of* P_s, *when the pump and beam are copropagating. Likewise, it is readily shown that for useful amplifiers with a counterpropagating pump,* P_p *is a monotonically increasing function of* P_s.

Trajectories can move along vertical lines in state-space if R is always chosen to annul the signal gain. This condition, $g_s(P_s, P_p, R) = 0$, defines the strategy $R(P_s, P_p)$ implicitly. However, again, such a device is not useful as it worsens the output signal-to-noise ratio and returns no gain.

We now consider the set of *reachable* states when the output signal must reach a specified goal and where a maximum input pump power is given (Fig-5.4). That is,

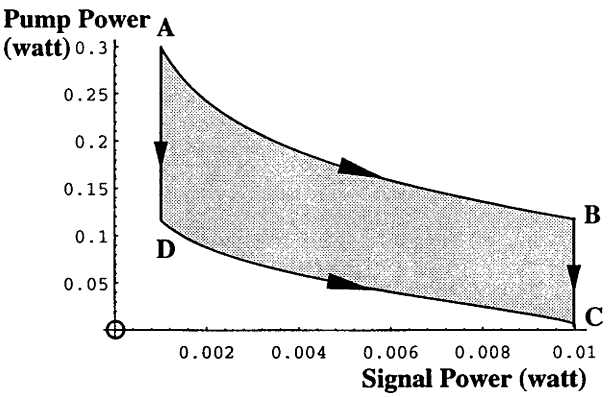

Figure 5.4: Typical set of all reachable states for an erbium doped fibre amplifier

we consider all points that lie on some trajectory taking the system state from some point along the line $P_s = P_{si}$ with $P_p < P_{p\,max}$ to some point on the line $P_s = P_{so}$, where P_{si} is the input signal power, P_{so} the specified output power to be reached and $P_{p\,max}$ the maximum possible input pump power.

We now calculate the reachable set's boundaries. If the system begins at point A in Fig-5.4 and moves to a new signal power, we seek the maximum value of the pump power at the new signal power. Otherwise put, we look for the minimum pump depletion for any given signal output. Suppose that a drawing strategy $R(P_s)$ is chosen and that the resulting pump power is $P_p(P_s)$. We now perturb this strategy by a function $\delta R(P_s) = \epsilon \tilde{R}(P_s)$, where $\tilde{R}$ is a valid function as discussed below. The resulting change in pump power as a function of P_s is found as follows: if $\epsilon \to 0$ then (5.9) can be linearised about the point (P_s, P_p) on the unperturbed trajectory and about the unperturbed radius R:

$$\frac{d\,\delta P_p}{dP_s} = \mathcal{A}\delta P_p + \mathcal{B}\delta R \tag{5.13}$$

where

$$\mathcal{A}(P_s) = \frac{\partial}{\partial P_p}\left(\frac{P_p g_p(P_s, P_p, R)}{P_s g_s(P_s, P_p, R)}\right); \quad \mathcal{B}(P_s) = \frac{\partial}{\partial R}\left(\frac{P_p g_p(P_s, P_p, R)}{P_s g_s(P_s, P_p, R)}\right) \tag{5.14}$$

$\mathcal{A}$ and $\mathcal{B}$ are written as functions of P_s only since R has already been chosen; hence, given the input P_p, (5.9) *wholly* determines P_p as a function of P_s.

The linear equation is solved to express $\delta P_p(P_s)$ as a linear functional of $\delta R(P_s)$:

$$\delta P_p(P_s) = \exp\left(\int_{P_{si}}^{P_s} \mathcal{A}(u)du\right) \int_{P_{si}}^{P_s} \exp\left(-\int_{P_{si}}^{u} \mathcal{A}(v)dv\right) \mathcal{B}(u)\delta R(u)du \qquad (5.15)$$

(5.15) is easier to understand if given a geometrical interpretation by writing[1]:

$$\delta P_p(P_s) = \epsilon \left\langle G, \tilde{R} \right\rangle$$

where

$$G(u) = \exp\left(\int_{P_{si}}^{P_{so}} \mathcal{A}(w)dw\right) \exp\left(-\int_{P_{si}}^{u} \mathcal{A}(v)dv\right) \mathcal{B}(u) \qquad (5.16)$$

and

$$< X, Y > \stackrel{def}{=} \int_{P_{si}}^{P_{so}} X(u)Y^*(u)du$$

If the trajectory in phase space is one of least pump power loss[2], then $G(u) = 0$ for *all* $u \in [P_{si}, P_s]$ and, since the exponential term cannot vanish[3]:

$$\mathcal{B}(u) = 0 \ \ \forall u \in [P_{si}, P_s] \qquad (5.17)$$

The condition that $\mathcal{B} = 0$ defines R implicitly as a function of P_s and P_p. If we solve (5.9) with (5.17) and with the initial condition given by point A in the phase-space, then we can derive the trajectory of least pump power loss (boundary AB in Fig-5.4).

We now consider the lower boundary, DC, of the reachable set. This corresponds to the minimum input pump power allowing the signal power to reach the target value P_{so}. If a state trajectory barely reaches the line BC in Fig-5.4, then clearly $g_s = 0$ exactly when the signal power reaches P_{so}, otherwise the amplifier could further amplify the signal. The point C therefore corresponds to the Rühl optimal

[1] We consider[Michel and Herget, 1981, §7.3][Royden, 1968, §7.3] the functions G and $\tilde{R}$ to be vectors in the Hilbert space, $\mathbf{L}_2$, of square Lebesgue-integrable functions on the interval $[P_{si}, P_s]$ where $<,>$ is this space's inner product

[2] Then $\delta P_p(P_s)$ vanishes for *all* $\delta R \in \mathbf{L}_2$; in particular, it must do so if δR is proportional to $G(u)$.

[3] (5.17) was derived for arbitrary perturbations $\epsilon\tilde{R}$, not only perturbations such that $P_p + \delta P_p$ was monotonically decreasing. However, since δP_p is a continuous functional of δR we can choose ϵ small enough that $P_p + \delta P_p$ is monotonic for $\tilde{R} = G$ and all the above reasoning will still hold, even given the monotonicity of P_p as a constraint.

length. The core-radius R is set so that the pump power corresponding to C is the minimum possible pump power corresponding to $g_s = 0$. That is, as the pump is drained and $g_s \to 0$, we can adjust R to keep $g_s > 0$, thus forestalling the onset of signal loss for as long as possible. Eventually (point C), no further adjustment of R will keep g_s positive.

The reachable set's lower boundary is then clearly a minimum pump power loss curve (found from (5.17) and (5.9)) passing through the point C. Thus we can calculate the minimum pump power, corresponding to the point D, needed to raise the signal power to P_{so}. Numerical calculation of the curve DC is extremely difficult, as the slope becomes infinite at C, so a point slightly above C must be chosen.

The reachable set is then the shaded region $ABCD$ in Fig-5.4. The example shown was calculated for a maximum input pump power of $0.3W$. An amplifier with all physical parameters set to the values given in [Bjarklev *et al.*, 1989], a step refractive index profile such that $V = 2.2$ when the core radius is 5μm, a uniform erbium ion concentration of $1.8 \times 10^{24}\text{m}^{-3}$ in the core and with no erbium ions in the cladding was assumed. The signal freespace wavelength is 1530nm and that of the pump 980nm.

5.5 Optimal Taper Shapes

In this Section, we shall assume that we solve the system dynamic equations (5.5) to fully account for ASE. However, the concurrent calculation of the optimal fibre radius R from the solutions to these equations will neglect the ASE terms, as stated in the Introduction.

Using the state-space description, as introduced in the foregoing section, we shall now consider:

Given P_{si}, P_{so} and that $P_p < P_{p\,max}$, what strategy $R(P_s)$ minimises the cost function C at the output?

Owing to a well-known example from electronic amplifier design, it is intuitively reasonable to hope that there is such an optimum. If we concatenate several amplifier

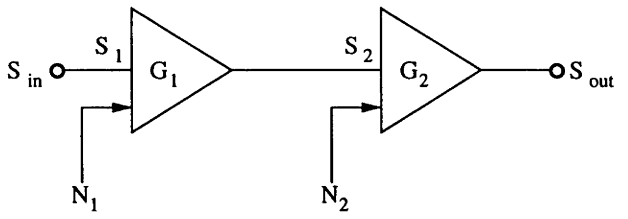

Figure 5.5: Cascaded Generalised Amplifiers

stages (Fig-5.5) with infinite input impedances and zero output impedances, we shall achieve the same gain whatever the stage cascading order. However, the output signal-to-noise ratio:

$$\left(\frac{S}{N}\right)_{total} = \frac{1}{\left(\frac{S_1}{N_1}\right)^{-1} + \left(\frac{S_2}{N_2}\right)^{-1}} \tag{5.18}$$

is order-dependent and well-known to be highest when the higher-gain, lower noise-figure stages are placed early in the cascade. Likewise, by inspection of the cost function in (5.11), it is readily seen that the output signal-to-noise can be improved by amplifying the signal more in the erbium amplifier's initial rather than later stages.

The following discussion may be supplemented with the discussion in Appendix-5.14 of the various kinds of optima.

5.5.1 First Derivation

We now derive a differential equation defining such a strategy. Suppose that we perturb a drawing strategy by a function $\delta R(P_s)$. The cost function perturbation is found from (5.11) to be:

$$\delta C = \int_{P_{si}}^{P_{so}} \left(\frac{1}{P_s^2} \frac{\partial}{\partial R} \frac{f(R)}{g_s} \delta R - \frac{f(R)}{P_s^2 g_s^2} \frac{\partial g_s}{\partial P_p} \delta P_p \right) dP_s \tag{5.19}$$

Note that we have neglected the perturbation arising from the change in ASE powers. For the optimal taper, $\delta C = 0$ for all $\delta R \in \mathbf{L}_2$. By expressing δP_p in terms of δR with (5.15), the optimality condition can be written in the form $< M, \delta R >= 0$. This leads to (Appendix-5.15):

$$\frac{1}{P_s^2}\frac{\partial}{\partial R}\left(\frac{f}{g_s}\right) - \int_{P_s}^{P_{so}} \mathcal{D}(u)I(u)^{-1}du\; I(P_s)\mathcal{B}(P_s) = 0$$

where

$$I(P_s) = \exp\left(-\int_{P_{si}}^{P_s} \mathcal{A}(v)dv\right) \tag{5.20}$$

$$\mathcal{D}(P_s) = \frac{f(R(P_s))}{P_s^2 g_s^2(P_s, P_p(P_s), P_{ASE}^+(P_s), P_{ASE}^-(P_s), R(P_s))}\frac{\partial g_s}{\partial P_p}$$

Upon division through by $I\,\mathcal{B}$ and differentiation with respect to P_s, the following differential equation is found:

$$\frac{\mathcal{A}}{P_s^2\mathcal{B}}\frac{\partial}{\partial R}\left(\frac{f}{g_s}\right) + \frac{d}{dP_s}\left(\frac{\frac{\partial}{\partial R}\left(\frac{f}{g_s}\right)}{P_s^2\mathcal{B}}\right) = -H\frac{f}{P_s^2 g_s^2}\frac{\partial g_s}{\partial P_p} \tag{5.21}$$

Here, the pump heading H indicates how the optimal taper equation differs in the co- and counterpropagating pump cases. To make the differential equation equivalent to (5.20) the following boundary condition must be fulfilled:

$$\frac{\partial}{\partial R}\left(\frac{f}{g_s}\right) = 0 \tag{5.22}$$

for $P_s = P_{so}$ in the case of copropagating pump system and for $P_s = P_{si}$ for the case of a counterpropagating pump system. The meaning of a simultaneous solution of (5.9) and (5.21) without heed of the boundary condition is discussed in §5.5.3.

A brief discussion, accounting fully for ASE, of the exact optimal taper equation will be given in Appendix-5.12.

5.5.2 Second Derivation

We now consider an alternative drawing strategy specification and rederive the equations above. We consider any monotonically decreasing trajectory passing through the reachable set and then find the drawing strategy yielding this trajectory. That is, we begin with a monotonically decreasing $P_p(P_s)$ and differentiate it to find $g_p/g_s = dP_p/dP_s$ at all points on the trajectory. Thus, the drawing strategy $R(P_s, P_p, P_p')$, where $P_p' = dP_p/dP_s$, is implicitly defined with P_s, P_p and $g_p(P_s, P_p, R)/g_s(P_s, P_p, R)$ known at all points on the trajectory.

The cost function then becomes:

$$C = \int_{P_{sb}}^{P_{se}} \mathcal{F}(P_s, P_p, P_p')dP_s$$

where : (5.23)

$$\mathcal{F}(P_s, P_p, P_p') = \frac{f(R(P_s, P_p, P_p'))}{P_s^2 g_s(P_s, P_p, R(P_s, P_p, P_p'))}$$

(5.23) is in the form dealt with by the classic formulation of the Calculus of Variations. The stationary trajectories are then defined by the Euler-Lagrange equation:

$$\frac{d}{dP_s}\left(\frac{\partial \mathcal{F}}{\partial P_p'}\right) - \frac{\partial \mathcal{F}}{\partial P_p} = 0 \tag{5.24}$$

Now, if we set:

$$\tilde{g}_p(P_s, P_p, R) \stackrel{def}{=} \frac{g_p(P_s, P_p, R)}{g_s(P_s, P_p, R)}$$

then (5.9) becomes $P_p' = \tilde{g}_p(P_s, P_p, R)$. Now we return to the Euler-Lagrange equation wherein P_s, P_p and P_p' are the independent variables. Hence:

$$\begin{aligned} 0 = \frac{\partial P_p'}{\partial P_s} &= \frac{\partial \tilde{g}_p}{\partial P_s} + \frac{\partial \tilde{g}_p}{\partial R}\frac{\partial R}{\partial P_s} \\ 0 = \frac{\partial P_p'}{\partial P_p} &= \frac{\partial \tilde{g}_p}{\partial P_p} + \frac{\partial \tilde{g}_p}{\partial R}\frac{\partial R}{\partial P_p} \\ 1 = \frac{\partial P_p'}{\partial P_p'} &= \frac{\partial \tilde{g}_p}{\partial R}\frac{\partial R}{\partial P_p'} \end{aligned} \tag{5.25}$$

So that:

$$\begin{aligned} \frac{\partial \mathcal{F}}{\partial P_p} &= \left(\frac{f\frac{\partial g_s}{\partial R}}{P_s^2 g_s^2} - \frac{f'(R)}{P_s^2 g_s}\right)\frac{\frac{\partial \tilde{g}_p}{\partial P_p}}{\frac{\partial \tilde{g}_p}{\partial R}} - \frac{f}{P_s^2 g_s^2}\frac{\partial g_s}{\partial P_p} \\ \frac{\partial \mathcal{F}}{\partial P_p'} &= \left(\frac{f'(R)}{P_s^2 g_s} - \frac{f\frac{\partial g_s}{\partial R}}{P_s^2 g_s^2}\right)\frac{1}{\frac{\partial \tilde{g}_p}{\partial R}} \end{aligned} \tag{5.26}$$

The Euler-Lagrange Equation then becomes:

$$-\frac{d}{dP_s}\left(\frac{f(R)\frac{\partial g_s}{\partial R} - f'(R)g_s}{P_s^2 g_s^2\, \mathcal{B}}\right) = \frac{f(R)\frac{\partial g_s}{\partial R} - f'(R)g_s}{P_s^2 g_s^2\, \mathcal{B}}\mathcal{A} - \frac{f}{P_s^2 g_s^2}\frac{\partial g_s}{\partial P_p} \tag{5.27}$$

where $\mathcal{A}$ and $\mathcal{B}$ are as defined in (5.13). It is now readily shown that (5.27) is the same as (5.21) where I is as defined in (5.20).

5.5.3 Boundary Conditions

The usual Euler-Lagrange equation applies to trajectories whose two endpoints are fixed. In our case one or two of the end points can float, *i.e.* one seldom cares what the final pump power is and so we shall allow any final state along the line BC in the reachable set (Fig-5.4). From the Calculus of Variations, the floating endpoint is equivalent to the imposition of the boundary condition:

$$\left.\frac{\partial \mathcal{F}}{\partial P_p'}\right|_{P_s=P_{se}} = 0 \tag{5.28}$$

which, by (5.26), is readily shown to lead to the same boundary condition as that given in (5.22).

The dropping of the boundary condition (5.22) therefore corresponds to the fixing of the output pump power. Hence, if (5.9) and (5.21) are solved simultaneously with $R(P_{sb}) = R_0$ without heed of (5.22) and if the resulting output pump power is P_{pe}, then the trajectory found will be optimal over the class of trajectories fulfilling the constraint that the output pump power should be P_{pe}.

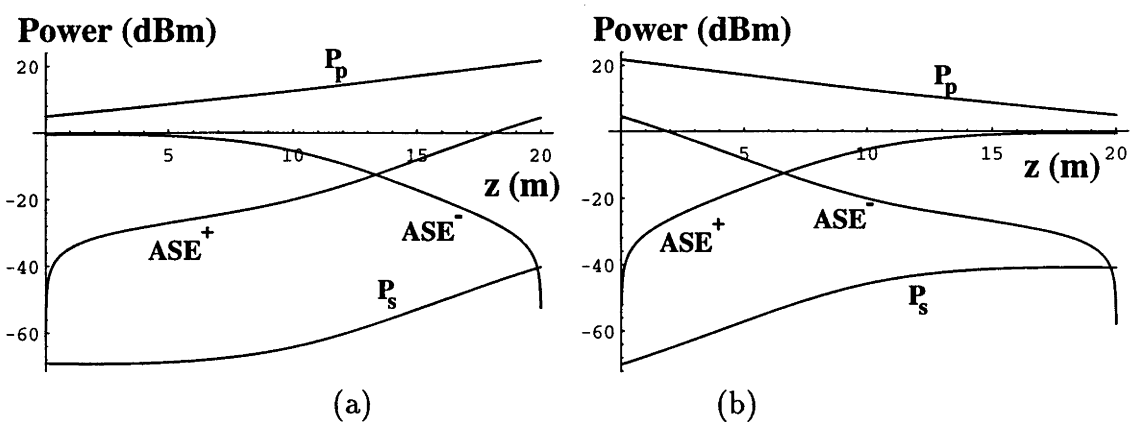

Figure 5.6: Signal, pump and ASE evolution in untapered EDFA: *(a)* counter- and *(b)* copropagating pump.

5.6 Comparison of Linear and Optimal Tapers

We now refer to [Bjarklev *et al.*, 1992], wherein it is claimed that a linearly-tapered erbium amplifier can achieve a better noise figure than an untapered one. Here

we reproduce these results and discuss them more fully. We also investigate the performance of optimal tapers fulfilling (5.21).

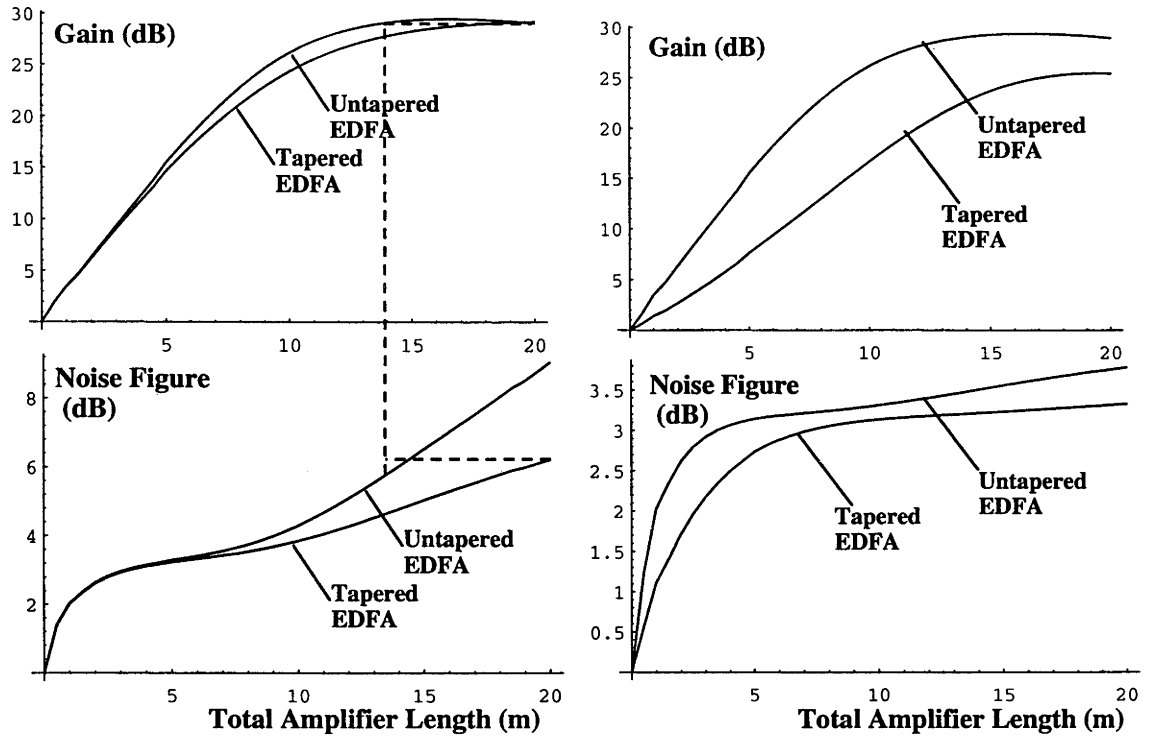

Figure 5.7: Gains and noise figures for straight and linearly tapered EDFAs: *(left)* counter- and *(right)* copropagating pump.

Figs-5.6 and 5.7 summarise our reproduction. Although not all the information needed to reproduce the results can be gleaned from [Bjarklev *et al.*, 1992], very similar results can be obtained by making reasonable guesses of the unknown physical parameters; we take the input P_p and output P_s to be 150mW and 0.1mW respectively, with all other physical parameters as given in [Bjarklev *et al.*, 1989]. The full dynamic equations (5.5) were solved numerically (see Appendix-5.11) to find the total gains and noise figures for separate amplifiers of different lengths L, and these results are plotted in Fig-5.7 for both the untapered and tapered EDFAs described in [Bjarklev *et al.*, 1992].

It must first be said that the claim that the linear taper has a considerably improved noise performance could be somewhat misleading. If Fig-2 of [Bjarklev *et al.*, 1992] had used fibre length normalised with respect to the Rühl optimal length as the horizontal axis, then the noise figure improvement for the tapered fibre would be seen to be rather small. At first glance, our Fig-5.7 suggests that the linear taper

achieves a handsome 3dB noise figure improvement over the untapered fibre in the counterpropagating pump case and a 0.5dB improvement for the copropagating case. However, in the counterpropagating pump case, note that the tapered fibre's gain is 29.2dB at its output and its noise figure is 6.21dB. As the total fibre length of the untapered EDFA is increased, its total gain first reaches 29.2dB for $L = 14.3$m, when its noise figure is 6.20dB. As the EDFA length increases further, the rate of increase of gain with L dwindles very quickly and the noise figure quickly worsens with increasing L owing to serious pump depletion near the untapered amplifier's input. An untapered fibre shortened from $20m$ to $14.3m$ would achieve the same gain and as good a noise figure as the linear taper. From this viewpoint, it is seen that there is very little noise improvement from amplifier tapering. Results almost as good can be achieved by carefully choosing the amplifier length to reduce pump depletion; thus, an amplifier longer than the Rühl optimal length should never be used. In practice, the amplifier should be significantly shorter than the optimal length because significant pump depletion, and therefore significant noise figure degradation, occur in the last few metres of an optimal length fibre whilst yielding very small further gain.

This discussion is further exemplified by Fig-5.8, where the amplifier noise figures are plotted as a function of the total amplifier gain. Fig-5.8*(a)* shows results for both the tapered and untapered EDFAs with counterpropagating pump, and the two plots are nearly the same. Fig-5.8*(b)* shows the difference ΔF between the noise figures for the two different EDFAs; these improvements are very small and indeed tapering *worsens* noise figures for systems working near maximum gain. Figs-5.8*(c)* and 5.8*(d)* show corresponding curves for copropagating pump EDFAs.

We now examine some solutions of the optimal taper equation (5.21). The d/dP_s term in (5.5) is expanded:

$$\frac{d}{dP_s}\left(\frac{\frac{\partial}{\partial R}\left(\frac{f}{g_s}\right)}{P_s^2\mathcal{B}}\right) = \left(\frac{\partial}{\partial P_s} + \frac{P_p g_p}{P_s g_s}\frac{\partial}{\partial P_p} + \frac{P_{ASE}^+ - P_{ASE}^-}{P_s}\frac{\partial}{\partial P_{ASE}^+} + \frac{dR}{dP_s}\frac{\partial}{\partial R}\right)\left(\frac{\frac{\partial}{\partial R}\left(\frac{f}{g_s}\right)}{P_s^2\mathcal{B}}\right) \tag{5.29}$$

Thus (5.21) can be used to give the local radius as the full equations (5.5) are solved. A solution to such a system of equations is found for a counterpropagating pump EDFA with an output P_s of -10dBm, an input P_s of -40dBm (*i.e.* 30dB EDFA gain),

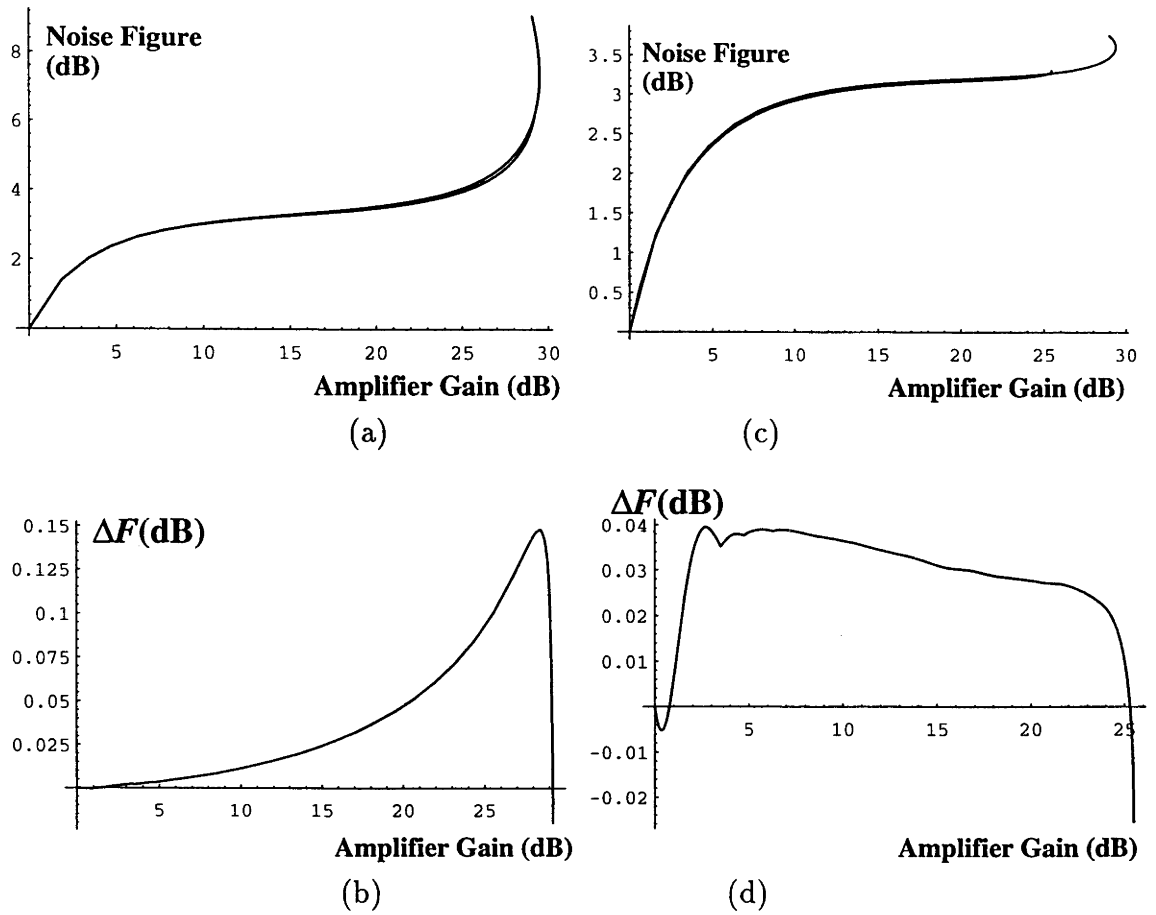

Figure 5.8: Noise figures as functions of gain: (*a. top left*) Straight and linearly tapered counterpropagating pump EDFAs; (*b. bottom left*) Difference between noise figures for straight and tapered EDFAs; (*c. & d. right*) Corresponding curves for copropagating pump EDFAs.

an input P_p of 150mW, all other physical EDFA parameters as in [Bjarklev *et al.*, 1989] and a final fibre radius of 3.4μm. It is very time consuming to find solutions to (5.21), and even more so to find a solution fulfilling the condition (5.22) exactly. Here, (5.22) approximately holds, hence the taper shown in Fig-5.9*(a)* is very nearly the overall optimal EDFA for the input power, gain and physical EDFA parameters given. So far, no solutions to (5.21) have been found for the copropagating pump case.

Fig-5.9*(b)* plots the evolution of the EDFA noise figure with P_s for the optimal taper and for the straight and linearly-tapered EDFAs of [Bjarklev *et al.*, 1992]. The plot for the linear taper pertains to a 20m long EDFA as in [Bjarklev *et al.*,

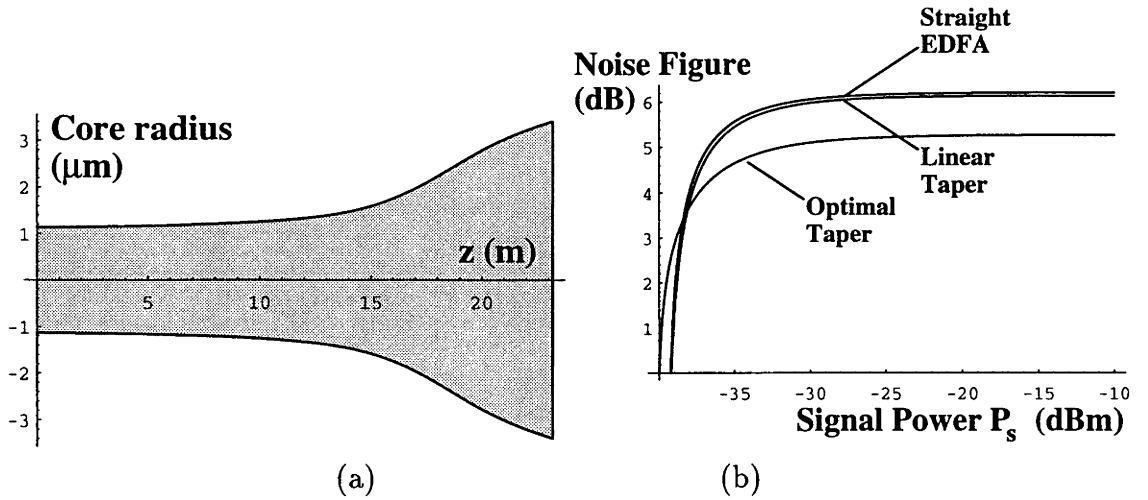

Figure 5.9: Optimal Noise Performance: *(a)* Optimal taper shape for minimum noise; *(b)* Noise figure evolution for optimal, linear and straight tapers.

1992], while the plot for the straight EDFA pertains to one 14.3m long, so that, as discussed above, it has the same gain as the linearly-tapered EDFA, yet is shorter than its optimal length so as not to suffer the severe pump depletion and poor noise performance of its 20m-long counterpart in [Bjarklev *et al.*, 1992]. The optimal taper has a slightly higher gain (30dB rather than 29.2dB) than the other two, so that the comparison in Fig-5.9*(b)* unfairly handicaps the optimal taper, which, nonetheless, still achieves about a 1dB noise figure improvement over the other two EDFAs.

It is interesting to note the effect of tapering on the excited ion fraction. Fig-5.10*(a)* plots the weighted average excited ion fraction:

$$x_{av}(P_s, P_p, P^+_{ASE}, P^-_{ASE}, R) = \int_{r=0}^{R}\int_{\phi=0}^{2\pi} x(P_s, P_p, P^+_{ASE}, P^-_{ASE}, r, \phi)\hat{\psi}_s^2(r,\phi) r \; d\phi \; dr \tag{5.30}$$

as a function of the amplifier signal power. It can clearly be seen that the optimal strategy strives to uphold the highest excited ion fraction for as long as possible as the pump becomes severely depleted towards the EDFA's input. To achieve this, a lower degree of inversion near the output is allowed than is present near the outputs of the other EDFAs, thus ensuring a higher P_p near the input (Fig-5.10*(b)*). The overall result is that the weighted average excited ion fraction as a function of either P_s or the axial distance z is much more flattened relative to the corresponding

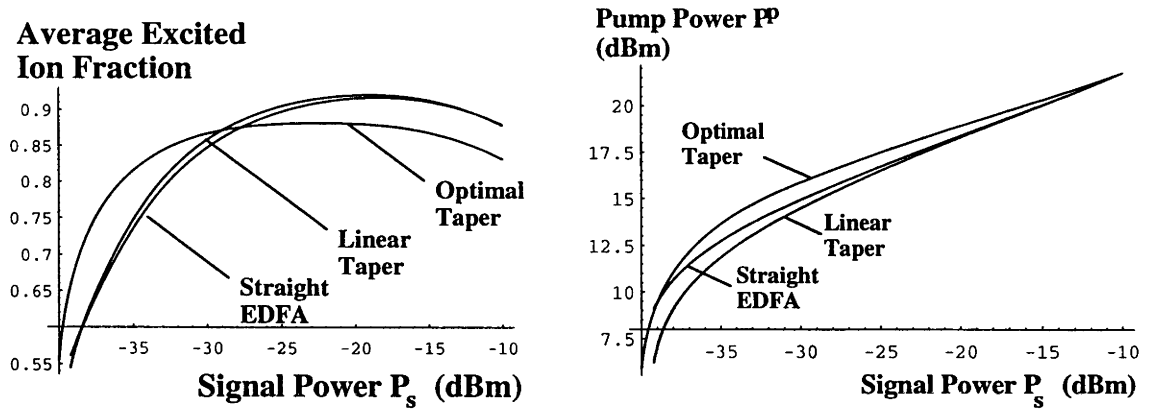

Figure 5.10: Effect of tapering on internal EDFA dynamics: *(a)* Weighted average excited ion fraction and *(b)* Pump power as function of signal power for optimal, linear and straight tapers.

functions for the other EDFAs.

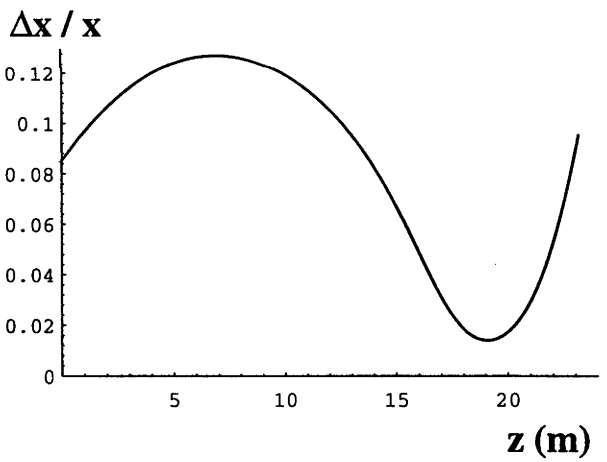

Figure 5.11: Excited ion fraction error from neglect of ASE

Also calculated for the optimal taper, is the function (Fig-5.11):

$$\frac{x_{av}(P_s, P_p, P^+_{ASE}, P^-_{ASE}, R) - x_{av}(P_s, P_p, 0, 0, R)}{x_{av}(P_s, P_p, 0, 0, R)}$$

i.e. the fractional difference between the weighted average excited ion fraction calculated with ASE and with ASE neglected. This measures how significant the ASE is compared to P_s and P_p in determining the excited ion fraction. At all points

along the optimal taper, the ASE was found to account for at most one eight (typically 0.05) of the ion excitation and therefore our approximation of dropping it from the optimal taper equations would seem to be reasonable, at least as a first approximation.

In closing this discussion, it must be emphasised that for examples where a noise figure improvement can be brought about by tapering (*e.g.* the examples of this Section together with those in [Grunnet-Jepsen *et al.*, 1992]), one begins with unusually noisy EDFAs achieving far worse than the 3dB noise figure theoretical lower limit. For the examples studied above, the poor noise performance arises directly from excessive pump depletion and careful avoidance of this, *e.g.* by fibre shortening, is a much simpler solution than tapering and is almost as effective. It is possible[Laming and Payne, 1990] to achieve close to the 3dB quantum noise limit with *untapered* EDFAs yielding almost as much gain as those discussed here and both near optimal (3.1dB) noise figure and extremely high gain (54dB) can be achieved by untapered EDFAs with the use of an optical isolator to quell ASE[Laming *et al.*, 1992]. Thus, tapering is of little use in a system whose physical parameters and working environment are well-chosen. Furthermore, for the time being, it would also seem that the EDFA itself is a relatively minor source of noise since the best reported noise figure for a complete preamplifier/receiver system is 8.6dB[Payne, 1992]. It would therefore be more productive to concentrate on eliminating other sources of EDFA system noise rather than to improve the EDFA itself slightly through tapering, especially since at least one end of a tapered EDFA is the wrong size to splice onto standard fibre components, thus giving possible splice loss.

5.7 Tapering for Optimal Signal Power Output

In §5.4, it was shown that an amplifier tapered to fulfill (5.17) will achieve minimum pump depletion for a given signal power gain, if the effect of ASE can be neglected, which will be assumed true in the following. The state-trajectory for such an amplifier is the upper boundary of the set of reachable states in the (P_s, P_p) state space. Clearly, for an amplifier to achieve maximum signal gain for a given pump power, it must follow this minimum pump depletion trajectory. We shall now

investigate the attainable gain increase from tapering; an experimental study of the gain improvement wrought by tapering is to be found in [Grunnet-Jepsen *et al.*, 1992].

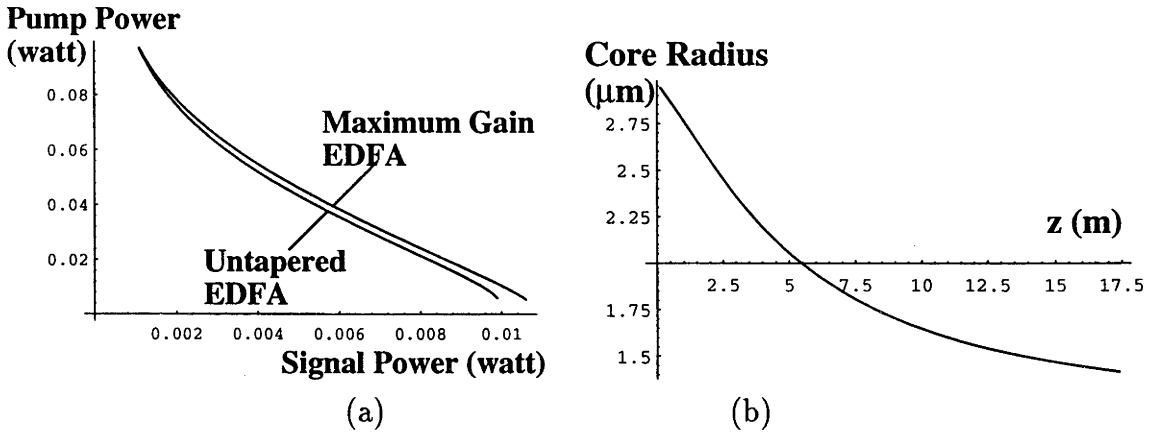

Figure 5.12: Tapering for maximum EDFA signal gain: *(a)* Comparison of tapered and untapered EDFAs; *(b)* Maximum gain taper.

In the following we neglect ASE completely. An amplifier was investigated with a copropagating pump beam and with all physical constants as in the foregoing section. The input pump power was 100mW and the input signal power 1mW. It can be seen from Fig-5.12*(a)* that amplifier tapering can only slightly increase the signal gain obtainable for the given pump power. For all of the other cases that we have studied numerically, the gain increase was, as here, about five percent. The maximum gain taper for the present example is shown in Fig-5.12*(b)*.

5.8 Tapering for Minimum EDFA Length

Although tapering has only a weak effect on what signal power, pump power and noise are attained within an EDFA, it has a powerful effect on *where* these powers and noise are attained. For example, even though the 14.3m-long tapered EDFA yielding 29.2dB gain of §5.6 has the same noise performance as the 29.2dB, 20m-long untapered EDFA, the tapering achieves a 29% EDFA length saving. Such length savings may be useful:

- To produce small cost savings through reduced doped fibre usage in EDFA production; or
- In the future, if the problem of concentration quenching is overcome, length savings in planar integrated optic EDFAs will be extremely useful for system compactification.

We therefore now seek the taper shape yielding the minimum length EDFA for a given gain. After our study of noise-optimal tapers, this is an easy problem to solve because, with the axial co-ordinate eliminated and the state-space model (5.9) used, the EDFA length is given by:

$$L = \int_{P_{si}}^{P_{so}} \frac{dz}{dP_s} dP_s = \int_{P_{si}}^{P_{so}} \frac{dP_s}{P_s g_s} \tag{5.31}$$

Clearly, the minimisation of this integral would be exactly the same as the minimisation of system noise figure if $f(z)$ were constant, hence, the shortest taper fulfills (5.21) (or (5.47) if ASE cannot be neglected for the taper calculation) with $f(R)$ set to 1. As in Sec-5.5.3, the solution of (5.21) without heed of (5.22) is equivalent to finding the shortest possible taper subject to the constraint that the output pump power should be constant. Fig-5.13*(a)* shows the solution of (5.21) fulfilling boundary condition (5.22) for a 150mW counterpropagating pump EDFA boosting a 1mW signal to 10mW and all physical constants as in [Bjarklev *et al.*, 1989]. Its length is 5.096m.

Also shown in Fig-5.13*(b)* is a plot of the length required for a *constant radius* EDFA to attain the stated gain with a 150mW counterpropagating pump. As can be seen, although EDFA radius control has a strong effect on EDFA length, an appropriate (3.3μm) constant radius EDFA achieves almost as short a length (5.139m) as the overall-optimal taper in Fig-5.13*(a)*. Moreover, the constant radius EDFA's noise figure is 5.126dB, whereas that of the optimal taper is 4.917dB, so that the noise performance advantage from tapering is only slight.

Fig-5.14 shows that the above comments also hold for a copropagating pump EDFA, where the 5.964m-long overall-optimal taper's noise figure (Fig-5.14*(a)*) is 4.576dB, whereas that of the shortest (6.013m-long) constant radius (3.1μm) EDFA is 4.586dB.

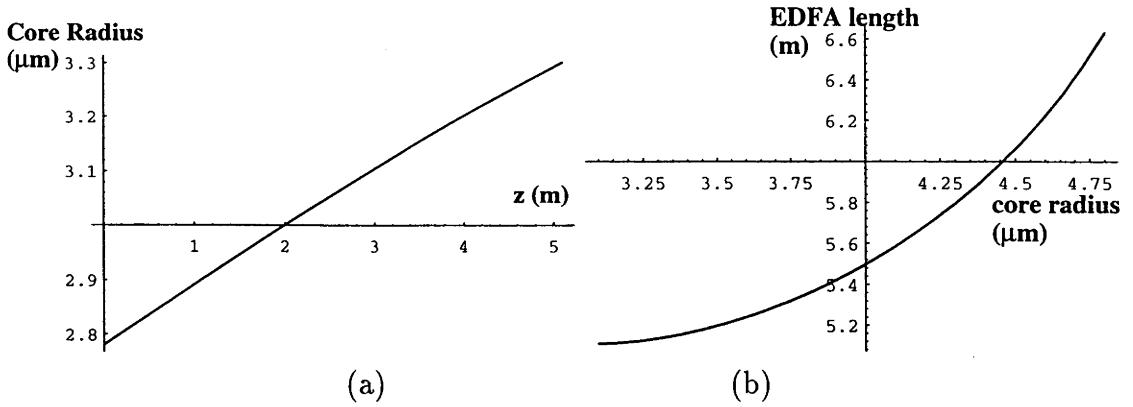

Figure 5.13: Tapering for minimum counterpropagating pump EDFA length *(a)* Taper for overall minimum length; *(b)* Untapered EDFA length as a function of core radius.

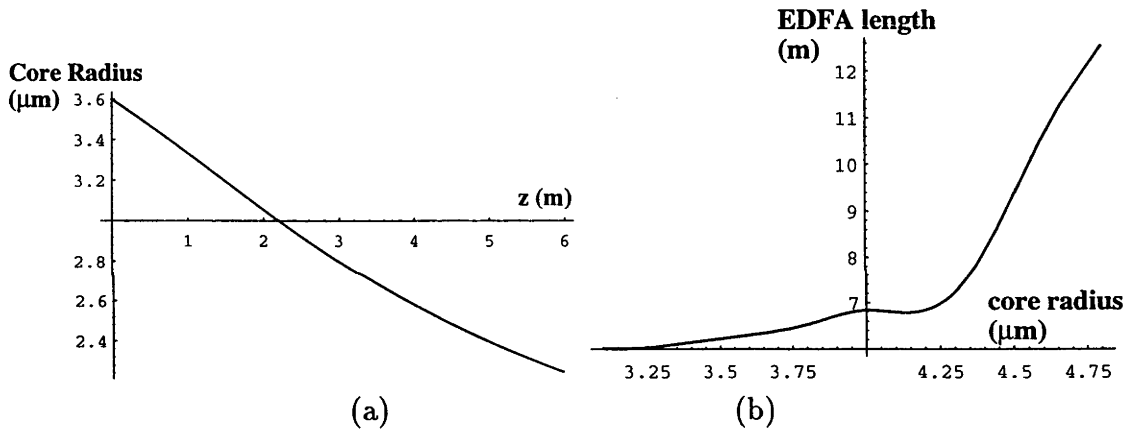

Figure 5.14: Tapering for minimum copropagating pump EDFA length: *(a)* Taper for overall minimum length; *(b)* Untapered EDFA length as a function of core radius.

5.9 Taper Control for Maximum Saturation Power

Finally, we consider a tapering strategy to yield the maximum saturation power for a given pump-power and EDFA length. The phenomenon of saturation is the dwindling of small-signal gain (*i.e.* the output signal power increase divided by the small input power increase producing it) with increasing input power. The plot in Fig-5.15 demonstrating saturation was made for a counterpropagating 100mW pump, 2μm core-radius EDFA with all other physical constants as in [Bjarklev *et al.*, 1989]. From (5.4), the excited ion fraction in a saturated EDFA ($P_s \to \infty$)

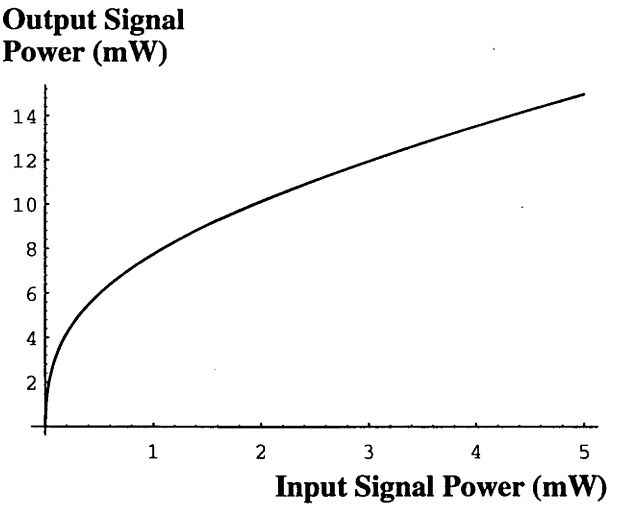

Figure 5.15: Saturation in EDFA output power

approaches 1/2 and there is barely a population inversion. For $\sigma_{12} = \sigma_{21}$, the signal gain can be written:

$$g_s = \sigma_{12}\rho \int_{r=0}^{R}\int_{\phi=0}^{2\pi}(2x-1)\hat{\psi}_s^2 r\,d\phi\,dr \tag{5.32}$$

and, when $P_s \to \infty$:

$$2x - 1 \to \frac{\frac{\sigma_{13}\hat{\psi}_p^2 P_p f_s}{f_p} - \frac{hf_s}{\tau_{12}}}{2\sigma_{12}\hat{\psi}_s^2 P_s} \tag{5.33}$$

so that

$$P_s g_s \to \frac{hf_s\rho}{2}\int_{r=0}^{R}\int_{\phi=0}^{2\pi}\left(\frac{\sigma_{13}P_p\hat{\psi}_p^2}{hf_p} - \frac{1}{\tau_{12}}\right) r\,d\phi\,dr = \frac{f_s\rho}{2}\left(\frac{\sigma_{13}P_p\eta_p(R)}{f_p} - \frac{h\pi R^2}{\tau_{12}}\right) \tag{5.34}$$

where $\eta_p(R)$ is the fraction of the fundamental pump eigenfield power within the core radius R. The fibre is taken to be uniformly doped with a concentration of ρ erbium ions per unit volume in its core and to be undoped in its cladding. Likewise for the pump we have:

$$P_p g_p \to -H\frac{\sigma_{24}+\sigma_{13}}{2}\rho\eta_p(R)P_p \tag{5.35}$$

Hence, the system dynamic equations become:

$$\begin{aligned}\frac{dP_s}{dz} &= P_s g_s = -\frac{H\sigma_{13} f_s}{f_p(\sigma_{13}+\sigma_{24})}\frac{dP_p}{dz} - \frac{h f_s \rho \pi R^2}{2\tau_{12}} \\ \frac{dP_p}{dz} &= -H\frac{\sigma_{13}+\sigma_{24}}{2}\rho\eta_p(R)P_p\end{aligned} \tag{5.36}$$

and, dwarfed by the high signal level, ASE has no effect on the system output power. The following analysis assumes a copropagating pump and the analysis for the counterpropagating case is wholly analogous. The saturated case dynamic equations are linear and readily solved, assuming pump and signal powers of $P_p(0)$ and $P_s(0)$ respectively at $z = 0$:

$$\begin{aligned}P_p(z) &= P_p(0)\exp\left(-\frac{\sigma_{13}+\sigma_{24}}{2}\rho\int_0^z \eta_p(R(u))du\right) \\ P_s(z) &= P_s(0) - \frac{\sigma_{13} f_s}{f_p(\sigma_{13}+\sigma_{24})}(P_p(z) - P_p(0)) - \frac{\pi h f_s \rho}{2\tau_{12}}\int_0^z R^2(u)du\end{aligned} \tag{5.37}$$

Now, we seek the tapering strategy to maximise the output signal power, $P_s(L)$, where L is the taper length. Suppose that the tapering strategy is perturbed by $\delta R(z)$; then, by noting that $\delta P_p(0) = 0$, the change in output power $\delta P_s(L)$ resulting from the strategy change is readily calculated from (5.37) and set to nought to give the condition for the the optimal taper:

$$\begin{aligned}0 = &-\frac{\sigma_{13}\tau_{12}}{\pi h f_p \rho(\sigma_{13}+\sigma_{24})}\delta P_p(L) - \int_0^L R(u)\delta R(u)du = \\ &\int_0^L \left(\frac{\sigma_{13}P_p(0)\tau_{12}}{2\pi h f_p}\exp\left(-\frac{\sigma_{13}+\sigma_{24}}{2}\rho\int_0^L \eta_p(R(u))du\right)\frac{d\eta_p(R)}{dR} - R(u)\right)\delta R(u)du\end{aligned} \tag{5.38}$$

whence

$$\eta_p'(R)\frac{\sigma_{13}\tau_{12}P_p(0)}{2\pi h f_p}\exp\left(-\frac{\sigma_{13}+\sigma_{24}}{2}\int_0^L \eta_p(R(u))du\right) = R \tag{5.39}$$

Since the quantity $\int_0^L \eta_p(R(u))du$ is a property of the whole taper and independent of the axial position, z, (5.39) is an *algebraic* equation in R which is independent of both the system state (P_s, P_p) and z. Hence, the sought optimal taper is, in fact, a fibre of constant radius, which obeys:

$$\eta_p'(R)\sigma_{13}\tau_{12}P_p(0)\exp\left(-\frac{\sigma_{13}+\sigma_{24}}{2}L\eta_p(R)\right) = 2\pi R h f_p \tag{5.40}$$

The above reasoning applied to the counterpropagating pump case yields the same equation as (5.40) with $P_p(0)$ replaced by $P_p(L)$, *i.e.* the system pump-power input.

When the fibre radius is constant, the following simple expression for the output signal power holds in the co-propagating pump case:

$$P_s(L) = P_s(0) + \frac{f_s P_p(0)\sigma_{13}}{f_p(\sigma_{13}+\sigma_{24})}\left(1 - \exp\left(-\eta_p(R)\frac{L}{2}\rho(\sigma_{13}+\sigma_{24})\right)\right) - \frac{hf_s L\rho\pi R^2}{2\tau_{12}} \tag{5.41}$$

Again, replacement of $P_p(0)$ by $P_p(L)$ yields the analogous equation for the counter-propagating pump case. (5.40) is now seen to be simply the solution of $\partial P_s(L)/\partial R = 0$.

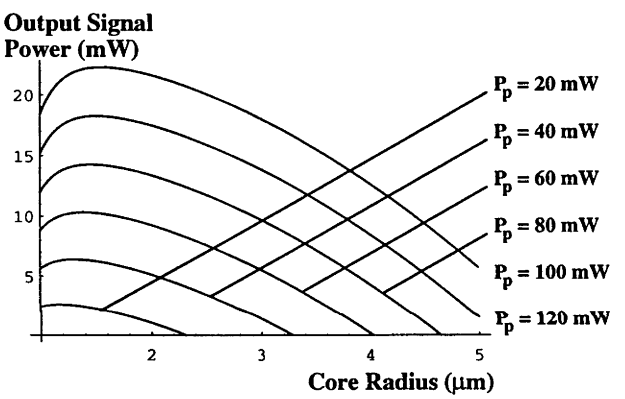

Figure 5.16: Output saturation power as a function of core radius

Fig-5.16 plots the output signal powers (neglecting the $P_s(0)$ term in (5.41) as a function of fibre radius for a co-propagating pump EDFA with all physical constants as in [Bjarklev *et al.*, 1989] and a length of 20m for various pump power levels. Fig-5.17*(a)* plots the maximum output signal, determined by (5.40), as a function EDFA length for various pump levels. Fig-5.17*(b)* shows the corresponding EDFA radii needed to achieve these maximum outputs. In each case, there is seen to be an optimal length yielding the maximum saturation output power possible for the given pump input and erbium ion concentration given by:

$$L_{opt} = -\frac{2}{\eta_p(R)\rho(\sigma_{13}+\sigma_{24})}\log\left(\frac{hf_p\pi R^2}{\tau_{12}\sigma_{13}P_p\eta_p(R)}\right) \tag{5.42}$$

The simultaneous solution of (5.42) and (5.40) yields:

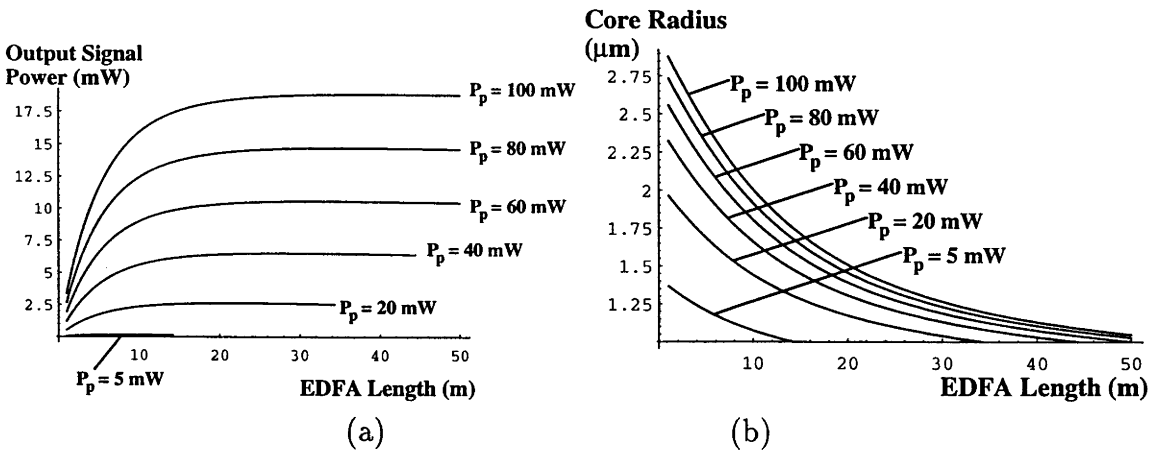

Figure 5.17: Untapered EDFAs for maximum saturation power: *(a)* Maximum saturation power for given pump power as a function of EDFA length; *(b)* Corresponding core radii needed for maximum saturation power.

$$R\eta_p'(R) = 2\eta_p(R) \tag{5.43}$$

which is an equation for R independent of P_p and L, *i.e.* the taper radius yielding the overall-maximum output saturation power is a universal constant for a given erbium doping concentration. In the present case, it is 1.135103μm. Using this result, the optimal length is found and the maximum output power possible for a given P_p is plotted in Fig-5.18 as a function of P_p. Clearly, in practice, a taper considerably shorter than the optimal length would be used since, to attain the last few tenths of a milliwatt attainable for a given P_p, the EDFA must be lengthened by the order of ten metres or more.

5.10 Conclusions

In many ways the studies described in this Chapter have drawn to a somewhat disappointing conclusion: that the tapering of erbium doped fibre amplifiers has only a very slight effect on *what* happens within an EDFA, although there can be a major effect on *where* it happens. This marked shift in the position at which the EDFA attains given signal gains and noise figures may yield useful length savings in future, integrated optic EDFA devices. However, as stated in the Introduction,

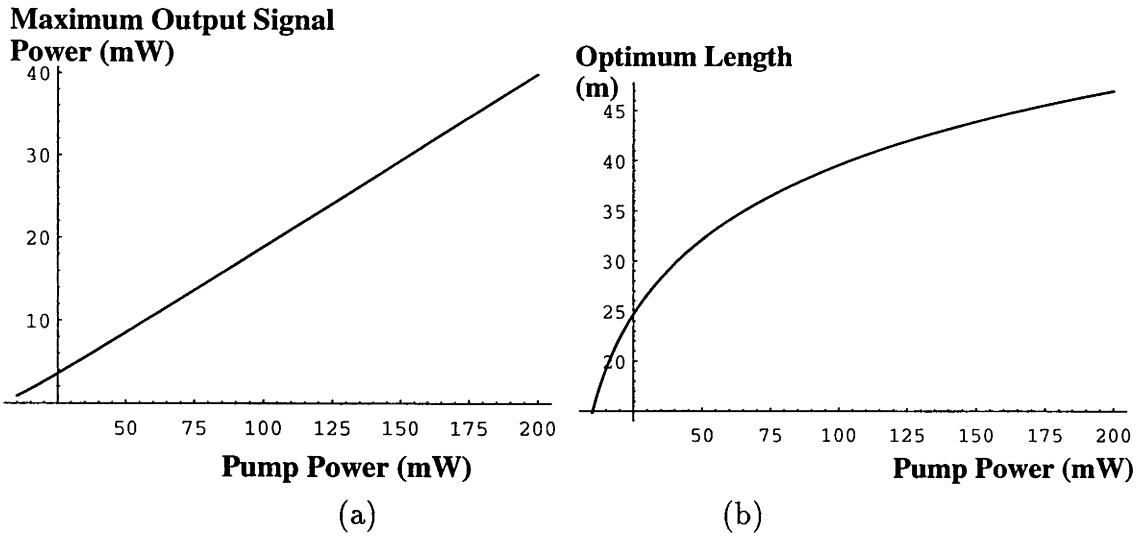

Figure 5.18: Overall-maximum achievable saturation power: *(a)* Overall-maximum saturation power; *(b)* Corresponding 1.135103μm-core-EDFA length.

such future EDFA development depends on the solution of the basic concentration-quenching problem. Moreover, the use of appropriate constant fibre radii can achieve length savings almost as great as those observed for tapered EDFAs, at least for the examples studied in this Chapter.

Evidence was also presented suggesting that the tapering of an erbium doped fibre amplifier will yield only slight (< 1dB) benefits to the noise performance. There are good reasons to suspect that this statement is generally true:

- We have carried out many simulations like those presented here and the conclusions were the same in each case.

- A useful small signal amplifier must not be allowed to suffer significant pump depletion, otherwise the noise performance will be severely degraded. Therefore, the pump power must always be large. However, in such cases the fraction of excited ions is close to 1, and then the noise performance is only slightly influenced by fibre tapering.

Finally, the signal gain attained for a given input pump power can be modestly increased by tapering; typically 5% (0.2dB) improvements can be achieved.

Perhaps the most important result of this study was the introduction of state-space and control system analysis methods to the subject of EDFA design. Although the EDFA's description (Equations (5.5) and (5.9)) is simple in concept, there are far too many terms within the equations for a designer to readily visualise the outcome of a given choice of design parameters. The state-space approach presented here, especially with the ASE neglected, is the simplest approach we could find to solve our problems and it is to be hoped that similar approaches may be used to simplify future EDFA design problems.

5.11 Appendix: Basic Numerical Techniques

The two numerical problems to be solved in the study of EDFA dynamics are:

- The calculation of the signal and pump eigenfields for an EDFA of a given core radius and;
- The subsequent integration of the dynamic equations (5.5) and (5.9).

For the first problem, a weak-guidance approximation was made and the scalar wave equation solved using the eigenvalue equation of Table-14.3 in [Snyder and Love, 1983]. This transcendental equation was solved by a simple bisection method [Press *et al.*, 1990, §9.1]. This method, although slow, was chosen for its famous, stalwart reliability, which is especially important for the solution of eigenvalue equations of extremely weakly guided fibres or ones with many roots. Subsequent substitution of the roots into the field expressions of Table-14.3 yielded the eigenfields. Many, much simpler, analytical approximations for the eigenfields are possible but are only applicable for a limited V-value range. The standard Gaussian approximation[Snyder and Love, 1983, Ch-15] fails as $V \rightarrow 1$ whereas the modified Gaussian approach[Peng and Ankiewicz, 1991] overcomes this drawback yet is inaccurate at high V-values. The tapers studied in this Chapter assume an extremely wide range of V-values, making the these methods unsuitable for many of them. In theory the Generalised Gaussian approach[Ankiewicz and Peng, 1992] overcomes these shortcomings, but was not used.

The basic technique used for the integration of the system dynamic equations was the Runge-Kutta Method[Press *et al.*, 1990, §15.1]. When integrating (5.9), the EDFA length and noise figure were calculated by integrating the equations $dF/dP_s = f/(P_s^2 g_s)$ and $dz/dP_s = 1/(P_s g_s)$ by the Runge-Kutta method alongside the other dynamic equations. It was not found necessary to use adaptive stepsize control.

To solve fully for the ASE, a shooting technique was used. This entails putting the Runge-Kutta dynamic equation integration under the control of the Bisection method. For example, for a co-propagating pump EDFA, the integration is begun at the system output. Here, clearly, $P_{ASE}^- = 0$, whereas P_{ASE}^+ is unknown. The latter is therefore guessed, the equations integrated and the sign of the calculated P_{ASE}^+ at the fibre input is used by the bisection method to repeat the simulation with different output P_{ASE}^+ values until the right value is found to make $P_{ASE}^- = 0$ at the fibre input, to within the desired accuracy.

5.12 Appendix: Full State Space EDFA Description

When ASE terms cannot be neglected, the full dynamic equations (5.9) must be solved. These equations constitute a three-dimensional state-space model and, to wholly specify the system's state for all values of P_s, it suffices to know the three-component state vector $(P_p, P_{ASE}^+, P_{ASE}^-)$ at any one particular value of P_s. The reachable set will then be a four-dimensional volume rather than a two-dimensional region as in Fig-5.4. Of course, the reachable set's description will be much more complicated than for the simplified model of §5.4. We stress that the following derivation is made only to show that, *in principle*, an optimal tapering strategy taking full account of ASE can be made; in practice, the equation to be described together with its boundary conditions would be extremely onerous to solve computationally. The following derivation applies for a copropagating pump case; the reasoning for the couterpropagating pump case is wholly analogous.

In §5.4, (5.9) was linearised, in the absence of ASE, about a state trajectory to express the perturbation δP_p as a linear functional of any perturbation δR made to the drawing strategy (5.15). This procedure, when repeated for the full Eqs. (5.9)

including the ASE terms, yields an equation:

$$\frac{d\delta\mathbf{P}}{dP_s} = \mathbf{A}\delta\mathbf{P} + \mathbf{B}\delta R \tag{5.44}$$

analogous to (5.13). Here $\delta\mathbf{P} = (\delta P_p, \delta P^+_{ASE}, \delta P^-_{ASE})^T$, $\mathbf{A}$ and $\mathbf{B}$ are now 3×3 and 3×1 matrices respectively and (5.44) is a state-space model for the evolution of small P_p and ASE perturbations in response to small taper changes. This model leads to a matrix analogy of (5.20), with $\mathcal{D}$ replaced by the 1×3 vector:

$$\mathbf{D} = \frac{f}{P_s^2 g_s^2}\left(\frac{\partial g_s}{\partial P_p}, \frac{\partial g_s}{\partial P^+_{ASE}}, \frac{\partial g_s}{\partial P^-_{ASE}}\right) \tag{5.45}$$

and the integrating factor $I(P_s)$ replaced by a 3×3 *state transition matrix* $\mathbf{\Phi}(P_s)$ obeying:

$$\frac{d\mathbf{\Phi}}{dP_s} = -\mathbf{\Phi}\mathbf{A} \tag{5.46}$$

The matrix analogy of (5.20) is thrice differentiated to yield:

$$\begin{aligned}
&\frac{1}{P_s^2}\frac{\partial}{\partial R}\left(\frac{f}{g_s}\right) - \int_{P_s}^{P_{so}} \mathbf{D}(u)\mathbf{\Phi}^{-1}(u)du\ \mathbf{\Phi}(P_s)\mathbf{B} = 0 \\
&\frac{d}{dP_s}\left(\frac{1}{P_s^2}\frac{\partial}{\partial R}\left(\frac{f}{g_s}\right)\right) + \mathbf{DB} + \int_{P_s}^{P_{so}} \mathbf{D}(u)\mathbf{\Phi}^{-1}(u)du\ \mathbf{\Phi}(P_s)\mathbf{AB} = 0 \\
&\frac{d^2}{dP_s^2}\left(\frac{1}{P_s^2}\frac{\partial}{\partial R}\left(\frac{f}{g_s}\right)\right) + \frac{d}{dP_s}(\mathbf{DB}) - \mathbf{DAB} - \int_{P_s}^{P_{so}} \mathbf{D}(u)\mathbf{\Phi}^{-1}(u)du\ \mathbf{\Phi}(P_s)\mathbf{A}^2\mathbf{B} = 0 \\
&\frac{d^3}{dP_s^3}\left(\frac{1}{P_s^3}\frac{\partial}{\partial R}\left(\frac{f}{g_s}\right)\right) \\
&\qquad + \frac{d^2}{dP_s^2}(\mathbf{DB}) - \frac{d}{dP_s}(\mathbf{DAB}) + \mathbf{DA}^2\mathbf{B} + \int_{P_s}^{P_{so}} \mathbf{D}(u)\mathbf{\Phi}^{-1}(u)du\ \mathbf{\Phi}(P_s)\mathbf{A}^3\mathbf{B} = 0
\end{aligned} \tag{5.47}$$

Now, by the Cayley-Hamilton theorem [Michel and Herget, 1981, 4.5] $\mathbf{A}$ fulfills a characteristic equation of the form:

$$p_0(P_S)\mathbf{I} + p_1(P_s)\mathbf{A} + p_2(P_s)\mathbf{A}^2 + p_3(P_s)\mathbf{A}^3 = \mathbf{0} \tag{5.48}$$

so that the set (5.47) can be linearly combined and simplified with (5.48) to yield:

$$\left(-p_0 + p_1\frac{d}{dP_s} - p_2\frac{d^2}{dP_s^2} + p_3\frac{d^3}{dP_s^3}\right)\left(\frac{1}{P_s^2}\frac{\partial}{\partial R}\left(\frac{f}{g_s}\right)\right)$$
$$-H\left(p_0\mathbf{DA}^{-1}\mathbf{B} + p_2\frac{d}{dP_s}(\mathbf{DB}) - p_3\frac{d^2}{dP_s^2}(\mathbf{DB}) + p_3\frac{d}{dP_s}(\mathbf{DAB})\right) = 0 \tag{5.49}$$

whence, by expanding the total derivatives as in (5.29), a third order ODE for the local taper radius is found. Here, H generalises the above result to both co- and counterpropagating EDFAs.

As well as (5.22), the following further three boundary conditions must be fulfilled at the output (*resp.* input) end for a co- (*resp* counter-) propagating pump EDFA:

$$\begin{aligned}
&\frac{d}{dP_s}\left(\frac{1}{P_s^2}\frac{\partial}{\partial R}\left(\frac{f}{g_s}\right)\right) + \mathbf{DB} = 0\\
&\frac{d^2}{dP_s^2}\left(\frac{1}{P_s^2}\frac{\partial}{\partial R}\left(\frac{f}{g_s}\right)\right) + \frac{d}{dP_s}(\mathbf{DB}) - \mathbf{DAB} = 0\\
&\frac{d^3}{dP_s^3}\left(\frac{1}{P_s^3}\frac{\partial}{\partial R}\left(\frac{f}{g_s}\right)\right) + \frac{d^2}{dP_s^2}(\mathbf{DB}) - \frac{d}{dP_s}(\mathbf{DAB}) + \mathbf{DA}^2\mathbf{B} = 0
\end{aligned} \tag{5.50}$$

5.13 Appendix: Quantum EDFA Noise

The following is a discussion of the results derived in [Shimoda *et al.*, 1957] and adapted for fibre amplifiers in [Pedersen *et al.*, 1991]. Note, however, that the final step below in the derivation of (5.8) is the assumption that the arrival of input signal photons follows a Poisson process, and this is not made clear in [Pedersen *et al.*, 1991]. The evolution of photon number mean and variance calculations detailed below are not explicit in either paper.

Let $P(m,z)$ be the probability distribution of the number of signal photons entering an infinitesimal sliver a distance z along the fibre. For such a sliver, the probability of the number of photons changing by one overwhelms the probability of its changing by more than one. Thus we need only to consider the following changes arising in the sliver:

- The number of photons increases by one.

- The number of photons is lessened by one.

- The number of photons remains the same.

The probability of a photon addition by stimulated emission is proportional to the sliver's thickness and to the number of incoming photons. Clearly, if the number of photons increases by a fraction δn in a length δz then the lightbeam's power also rises by the same fraction. Therefore[Bjarklev *et al.*, 1989, Eq-(16)], the constant of proportionality is the constant $a(z)$ of (5.5). As well as stimulated emission, there is spontaneous emission, whose probability is independent of the incoming photon number and proportional to the amplifier length. From (5.5), the probability is $c(z) = Ba(z)$. The probability of a photon subtraction by absorption is proportional to the sliver's thickness and to the number of incoming photons with $b(z)$ as the constant of proportionality. The probability that the number of photons does not change is then one minus the foregoing two probabilities, since the three events addition, subtraction and constancy comprise all possibilities.

Given the above event probabilities, $P(m, z + \delta z)$ can be evaluated in terms of $P(m, z)$:

$$\begin{array}{c} P(m,z+\delta z) = P(m,z)(1-(a+b)m\delta z - c\delta z) + \\ P(m+1,z)b(m+1)\delta z + \\ P(m-1,z)(a(m-1)+c)\delta z \end{array} \tag{5.51}$$

Hence[Shimoda *et al.*, 1957]

$$\frac{dP(m,z)}{dz} = -((a+b)m+c)P(m,z)+(m+1)bP(m+1,z)+(a(m-1)+c)P(m-1,z) \tag{5.52}$$

The output noise to signal ratio is now the output photon number variance divided by the squared mean photon number at the output, since these quantities are proportional to the noise and signal powers arising at the detector output. They can be derived from the definitions of output signal power $< N >^2$ and variance V:

$$
\begin{aligned}
&< N >= \mathcal{E}(m,z) = \sum_{m=1}^{\infty} mP(m,z) \\
&V = \mathcal{E}\left(m^2,z\right) - < N >^2 \\
&\mathcal{E}\left(m^2,z\right) = \sum_{m=1}^{\infty} m^2 P(m,z)
\end{aligned}
\tag{5.53}
$$

where $\mathcal{E}(Q,z)$ is the expectation of quantity Q at the axial position z. On differentiating the system-5.53 and simplifying with 5.52, it is found that:

$$
\begin{aligned}
&\frac{dV}{dz} = 2(a-b)V + (a+b) < N > +c \\
&\frac{d < N >}{dz} = (a-b) < N > +c
\end{aligned}
\tag{5.54}
$$

The spontaneous emission term is usually neglected because the signal is inside a narrow band about the signal frequency whereas the spontaneous emission is broadband, hence most of it can be bandpass filtered out of the signal. The system noise performance is measured by the *noise figure* $F(z)$, defined to be the ratio of the noise-to-signal ratio $V/(< N >^2)$ at position z to its value at the input, $z = 0$. Upon dropping the c terms in (5.53), using (5.54) to simplify the expression for $(d/dz)(V/ < N >^2)$ and integrating, $F(z)$ is found to be:

$$
F(z) = 1 + \frac{< N(0) >}{V(0)} \int_0^z (a(u) + b(u)) \frac{< N(0) >}{< N(u) >} du \tag{5.55}
$$

At the amplifier's input, we assume that the number of signal photons arriving per unit time is described by a *Poisson process*[Walpole and Meyers, 1978, §3.5][Saleh and Teich, 1991, §11.2C], whose the mean and the variance are equal, *i.e.* $< N(0) > /V(0) = 1$. Moreover, since the signal's power is proportional to the number of photons it comprises, $< N(0) > / < N(z) >= P_s(0)/P_s(z)$. These considerations and (5.7) applied to (5.55) yield the noise figure expression in (5.8).

(5.8) can be used to derive the *quantum noise limit.* As $f(z)$ depends only on the core radius, a lower bound on $F(z)$ can be obtained by using an upper bound for $P_s(z)$; clearly, we shall overestimate $P(z)$ if we assume $x = 1$ at all points within the amplifier. In this case, $g_s = f$ and:

$$F(P_{so}) = 1 + P_{si}\int_{P_{si}}^{P_{so}} \frac{f\, dP_s}{P_s^2 f} = 2 - \frac{P_{si}}{P_{so}} \tag{5.56}$$

This lower bound approaches 2, *i.e.* about 3dB, as the EDFA gain becomes large.

5.14 Appendix: Different Classes of Optima

Here, to further validate the variational approaches used in this Chapter, we discuss different kinds of optima in the context of the noise-figure-minimisation problem.

A stationary point is an optimum is found by the methods of the Calculus of Variations and is the most directly derived kind. The change in output signal-to-noise ratio is derived as a functional of a small perturbation to the drawing strategy $R(P_s)$. Then, equations for the optimal strategy result from the imposition of the condition that the signal-to-noise change, to first order, should vanish for strategy perturbations belonging to a suitable class of allowable functions $\epsilon\tilde{R}(P_s, P_p)$. Such a method yields a *local* optimum, that is, the resulting strategy $R_{loc}^{opt}(P_s, P_p)$ will give the greatest output signal-to-noise ratio for strategies belonging to some small neighbourhood:

$$\left\{R \mid \left\langle R - R_{loc}^{opt}, R - R_{loc}^{opt}\right\rangle < d\right\} \tag{5.57}$$

for some small distance d. Here the inner product $<,>$ is as defined in §5.4.

The global optimum, that is, the monotonically decreasing trajectory contained within the reachable set that yields the least output noise may be partly or wholly a trajectory along the reachable set's boundary. It is readily shown that if the overall-optimal strategy is not a stationary point, then it must be a boundary trajectory (either curve AB or DC in Fig-5.4) or a trajectory that follows a boundary for some of its history and elsewhere follows a stationary trajectory. Suppose that for $P_1 < P_s < P_2$, the optimal strategy does not follow the reachable set's boundary. Here $P_{si} < P_1 < P_2 < P_{so}$ and P_1 and P_2 are two intermediate powers. Then we can find a neighbourhood $\mathcal{N}_{ss}$ of state-space trajectories about the optimal trajectory interior to the reachable set. Since the mapping of a drawing strategy to the resulting state-space trajectory is continuous, we can find a neighbourhood $\mathcal{N}_d$ of the optimal drawing strategy with the form (5.57) whose image is contained in $\mathcal{N}_{ss}$. The cost

function change arising from a perturbation $\epsilon\tilde{R}(P_s)$ is a functional of the form[4] $< \mathcal{H}, \tilde{R} >$, where the inner product is an integral over the interval $[P_1, P_2]$. If the optimal strategy is not stationary, then $\mathcal{H} \neq 0$ and we can choose a perturbation such that $\tilde{R}$ is proportional to $-\mathcal{H}$, thus the perturbation in the cost function is strictly negative, contradicting the assumption that the optimal strategy was not stationary.

Thus, the global optimum may be wholly a boundary, wholly a stationary trajectory or a hybrid thereof.

5.15 Appendix: Details of Perturbation Calculation

The perturbation arising from the δP_p term in (5.19) can be written $\epsilon < M(P_s), \mathcal{L}\tilde{R} >$ where $\mathcal{L}$ is a linear operator, defined by (5.15), mapping δR to δPp. Here,

$$M(P_s) = -\frac{f\left(R(P_s)\right)}{P_s^2 g_s(P_p(P_s), P_p, R(P_s))^2} \frac{\partial g_s}{\partial P_p}$$

For the Hilbert space $\mathbf{L}_2[P_{sb}, P_{se}]$, we can always calculate $\bar{M} \in \mathbf{L}_2$ where[5] $< \bar{M}, \delta R >=< M, \mathcal{L}\delta R >$. The following *ad hoc* procedure calculates $\bar{M} = \mathcal{L}^\dagger M$ in this case:

$$\begin{aligned}
&\int_{P_{si}}^{P_{so}} M(P_s)\delta P_p(P_s) dP_s = \\
&\int_{P_{si}}^{P_{so}} M(P_s) I^{-1}(P_s) \int_{P_{si}}^{P_s} I(u)\mathcal{B}(u)\delta R(u) du \, dP_s = \\
&\int_{P_{si}}^{P_{so}} \int_{P_{si}}^{P_{so}} M(P_s) I^{-1}(P_s)\mathcal{U}(P_s - u) I(u)\mathcal{B}(u)\delta R(u) du \, dP_s
\end{aligned} \tag{5.58}$$

where $\mathcal{U}$ is the Heaviside step function and $I(P_s)$ is as defined in (5.20). By swapping the roles of the dummy-variables u and P_s in the above, we find:

[4] In a Hilbert space, *every* linear functional can be written in this form, where each and every linear functional has a one-to-one correspondence to a unique Hilbert space element $\mathcal{H}$; this well-known Riesz Representation Theorem [Michel and Herget, 1981, §§6.11, 6.14] is a direct consequence of the space's *completeness*.

[5] Again, this follows by the Riesz Representation Theorem, since $< M, \mathcal{L}\delta R >$ is a linear functional of δR. Furthermore, it is straightforwardly shown that $\bar{M}$ is a linear functional $\mathcal{L}^\dagger M$ of M, where $\mathcal{L}^\dagger$ is known as the *adjoint* operator to $\mathcal{L}$.

$$< M, \mathcal{L}\delta R >=< \mathcal{L}^{\dagger} M, \delta R >= \int_{P_{si}}^{P_{so}} \int_{P_s}^{P_{so}} M(u) I^{-1}(u) I(P_s) \mathcal{B}(P_s) \delta R(P_s) du \, dP_s \tag{5.59}$$

The total cost perturbation is now readily expressed in the form:

$$\delta C = \left\langle N(P_s) + \mathcal{L}^{\dagger} M(P_s), \delta R(P_s) \right\rangle = 0 \tag{5.60}$$

whence (5.20) readily follows.

Chapter 6

Planar Emulation of 3×3 Fibre Couplers

6.1 Introduction

6.1.1 Basic Goal

In this and the next two Chapters, we address the problem that, whereas many useful optical couplers comprise waveguides configured in *non*planar arrangements, only *planar* waveguide arrangements can be readily manufactured as integrated optics devices.

Our basic goal will be the derivation of a design procedure, based on the concatenation of a finite number of elementary building-block couplers, to yield a planar coupler with identical behaviour to any desired nonplanar waveguide array.

The underlying mathematical basis for the existence of a planar coupler equivalent to any nonplanar waveguide array is to be found in the theory of matrix Lie groups. Furthermore, quantified examples of devices are given with a view to eventual fabrication using the plasma etching/deposition process in Plasma Research Laboratory at the Australian National University.

The inspiration for this work is twofold: *(i)* we seek a planar emulation of the symmetric 3×3 fibre coupler, an inherently nonplanar device crucial to an elegant

interferometric fading compensation scheme[Sheem, 1981] and *(ii)* the corresponding problem of unrealisability of nonplanar networks arises in integrated electronics and has often been overcome by emulations of passive nonplanar networks by planar active operational amplifier networks. In the planar optical couplers of this and the following two Chapters, it is the precise control of the internal waveguide dimensions, formerly unavailable in fused biconic technology, that overcomes the planar constraint.

6.1.2 Planar Integrated Optics Technology

To date, planar integrated optics technology is unique in enabling precise control of internal waveguide dimensions. This is in stark contrast to fused biconic technology, wherein there is almost no fine dimension control and correct device working is achieved by closed-loop control of the manufacturing process from device output measurements (see Chapters-3, 4). A further exciting possibility with integrated optics is the manufacture of optical, electronic and optoelectronic circuits on the one chip. This allows, for example, for an optical system with its semiconductor source laser on-chip. Another interesting integrated electro-optic possibility is a phased optical antenna array switch[Heaton *et al.*, 1992]. Here, different control delays are imposed optoelectronically on a large array of lithium-niobate waveguides, thus allowing an almost-arbitrary phasing of the output optical field. Such a device can be used to quickly steer an optical beam and thus switch it at rates of about 1GHz between different output waveguides frequency with an electrical control signal.

For these reasons, *i.e.* the tight dimension control and electro-optic possibilities, there is great current interest (*e.g.* [Lerminiaux, 1992]) in planar integrated optics technology. At the time of writing, the Ion Exchange Process, is the maturest and least lossy integrated optics technology, producing waveguides with propagation losses of a few hundredths of a dB per centimetre. An alternative is the buried channel waveguide approach, as practised in the Plasma Research Laboratory at the Australian National University[Giroult-Matlakowski *et al.*, 1992]. Here the waveguide layers of differing refractive index are laid down using plasma-enhanced chemical vapour deposition (PECVD) and the best reported loss is comparable to that of ion-exchange devices[Adar *et al.*, 1991] but more typically about a tenth of a dB

per centimetre[Ladouceur, 1992, §7.3]. A more novel variation of the buried channel technology entails the depositing of layers by PECVD followed by bombardment of the cladding regions with low-energy electrons[Lewandowski *et al.*, 1991] to realise the core-cladding refractive index difference. This action leads to the expansion and therefore decrease in both the cladding's mass density and refractive index. It is unknown whether the expansion and therefore the waveguide are permanent and the technology is, as yet, of rather high loss, being about 1dB per centimetre.

6.1.3 Outline of Techniques

This Chapter discusses two planar realisations of the symmetric 3×3 fibre coupler. The designs are makeshift and specialised to the particular problem at hand, but they lead to a general discussion of the emulation of nonplanar couplers by planar ones in Chapter-7. It is proven that, in a restricted sense, a planar coupler can mimic any nonplanar coupled waveguide array. The mathematical tool for this discussion is the theory of matrix Lie groups, which will be presented in a concise form most applicable to the design of optical waveguides. Next, a general design procedure is presented to realise a coupler by a finite concatenation of elementary building blocks and the procedure is proven capable of deriving a finite planar mimic for *any* nonplanar coupler. The design procedure is illustrated in the 2×2 coupler case, where the Poincaré sphere yields vivid geometric insight. Finally, in Chapter-8, the general design procedure is applied in detail to the design of planar mimics for the symmetric 5×5, 4×4 and 3×3 fibre couplers and the designs are appraised by Beam Propagation Method simulations. A further, *ad hoc*, planar realisation of the 3×3 fibre coupler is also presented.

6.1.4 Microwave Coupler Design

Before proceeding, it is useful to refer to corresponding work in the field of microwave coupler design and compare it to the present research. A transfer matrix notation for microwave devices is described in [Carroll and Rigg, 1980] and the definitions in §6.2 are simply generalisations of the *forward scattering matrix* in (5) of [Herscher and Carroll, 1982], which considers the problem of designing a microwave waveguide so

that, for excitation by *one* input waveguide *alone*, any desired output distribution of powers can be obtained and is reasonably constant over a specified frequency band. Thus, in effect, the designer seeks to set *one* column only of the forward transfer matrix regardless of the other elements. This same problem was also considered in a less general way in [Gunton, 1978] and [Rigg and Carroll, 1980]. In [Islam and Carroll, 1986], the same problem was approached by arranging that the single input excitation is, in fact, a local modal excitation which is evolved adiabatically into the desired output power distribution. This, so-called, *warped mode coupler* is the microwave analogue of the adiabatic devices considered in [Yajima, 1973; Burns and Milton, 1980; Shani *et al.*, 1991] and developed in Chapter-10. At the same time, various six-port microwave devices were investigated for the measurement of both amplitude and phase in reflectometers and network analysers[Luff *et al.*, 1984; Engen and Hoer, 1984]; such devices solve the same measurement problems as the Sheem interferometers in this Chapter.

Our present work differs from the design procedures in [Herscher and Carroll, 1982] in that *(i)* we seek to implement both the amplitude *and* phase of *all* the transfer matrix elements, not just one column; and *(ii)* there is no optical analogue for the comb-line couplers nor the capacitive coupling within them used to implement the above microwave designs.

It is interesting to note that a bulk-optics analogue of the symmetric 4 × 4 fibre coupler was investigated[Walker and Carroll, 1984] and was probably the first optical demonstration of the microwave six-port techniques for fail-safe phase measurement. Sheem proposed a scheme based on the symmetric 3 × 3 fibre coupler in 1981, but the idea could not be tested experimentally as such devices were unavailable then.

6.1.5 Basic Motivating System

The basic system to be cast into a planar form is the modified Mach-Zehnder interferometer, using a 3 × 3 coupler as the beam-recombiner as illustrated in Fig-6.1. A modified Sagnac interferometer, presented by Sheem[Sheem, 1981] and also shown in Fig-6.1, is especially useful in optical fibre gyroscope systems. Practical implementations of this system have hitherto used the symmetric 3 × 3 fibre coupler, an inherently nonplanar device comprising three identical fibres coupled together in an

equilateral triangular arrangement, as shown in Fig-6.2.

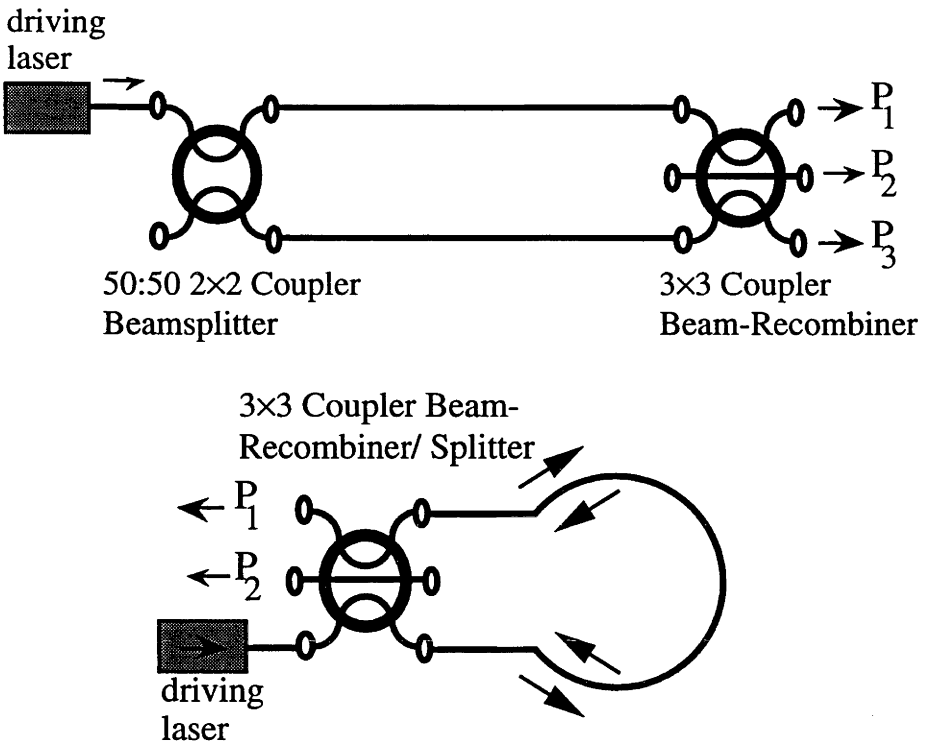

Figure 6.1: *top* Modified Mach-Zehnder and *bottom* Sagnac Interferometers

The three output powers, P_j, as functions of the relative phase delay, ϕ, between the two interferometer arms are given by:

$$\begin{aligned} P_1 &= \tfrac{1}{3}\left(1 - \cos\left(\phi\right)\right) \\ P_2 &= \tfrac{1}{3}\left(1 - \cos\left(\phi + \tfrac{2\pi}{3}\right)\right) \\ P_3 &= \tfrac{1}{3}\left(1 - \cos\left(\phi + \tfrac{4\pi}{3}\right)\right) \end{aligned} \tag{6.1}$$

with unit power input to the system. The behaviour embodied in (6.1) allows the Sheem Interferometer to overcome most of the problems faced by interferometric systems:

- The three output power measurements can be combined to yield an estimator of ϕ whose sensitivity to small changes in ϕ is independent of ϕ, whereas, with a 2×2 coupler as the beam recombiner, the system's small-signal sensitivity can fade altogether as the large-signal ϕ drifts owing to thermal and other environmental effects;

- The correct quadrant of ϕ can be determined; and

- Fringe-counting can be performed so that the system can measure arbitrarily large phase angle changes whereas neither fringe-counting nor quadrant inference is possible for the conventional Mach-Zehnder interferometer.

An evocative geometric interpretation of the realisation of these goals by the 3 × 3 coupler is given in [Travis and Carroll, 1989] and outlined in §8.2.

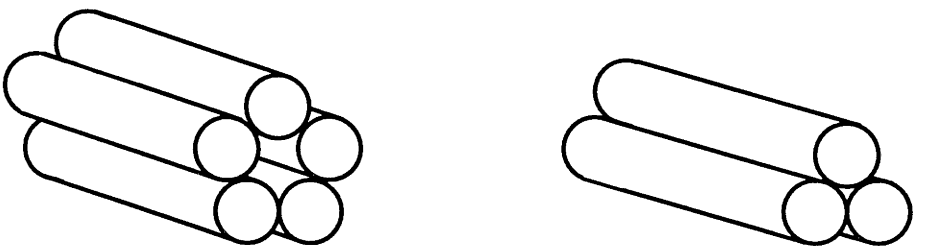

Figure 6.2: Waveguide arrangements for symmetric *left* 5 × 5 and *right* 3 × 3 fibre couplers

In the following discussion, we give a full design of a planar emulation of the Sheem interferometer system. The design procedure is based on coupling and forward transfer matrices and assumes that *(i)* the waveguide cores are very weakly coupled and *(ii)* that, for varying cross-section devices, the propagation is adiabatic[Shani *et al.*, 1991]. Notwithstanding these limitations, the transfer matrix method has the advantage of leading to a full engineering specification of the device, since coupling coefficients and propagation constants are directly and individually set by the waveguide widths and separations. In §6.4 we present a design procedure free from these restrictions, but whose practical implementation is much more unwieldy.

6.2 Transfer Matrix Notation

We describe all couplers by their *forward transfer matrices*, U. If the coupler's constituent waveguides are weakly enough coupled, its bound field is accurately described by linear superpositions of the eigenfields of the cores in isolation. Hence, if an $N \times N$ coupler's waveguides are all single-moded when in isolation, the coupler's input and output electromagnetic fields are wholly defined by vectors of N complex numbers, each number representing the phase and magnitude of the field on each

waveguide. U is then the matrix of the coupler's linear mapping between the input and output field-defining vectors. More generally, let $\left\{\psi_j^{in}\right\}$ be a basis for the bound field at the coupler's input, that is, the input can be written as a linear superposition of the ψ_j^{in} (in practice, this need only be true to a reasonable approximation). The basis need not be the set of isolated core eigenfields as in [Pietzsch, 1989; Carroll and Rigg, 1980]; it could be the set of local supermodal fields (as in §6.4) or indeed *any* other complete set. If $\left\{\psi_j^{out}\right\}$ is a basis for the output fields, then the linear coupler's action is defined by a linear, homogeneous mapping between the input and output weights defining the input and output fields as superpositions of the $\left\{\psi_j^{in}\right\}$ and $\left\{\psi_j^{out}\right\}$. The matrix U of this mapping is the coupler's transfer matrix.

In many cases of practical interest, the input and output basis fields are orthonormal, *i.e.* the total field's propagating power is the sum of the squared magnitudes of the complex weights in the superposition representing the field. Such is the case if normalised local modal fields are used or if the isolated waveguide eigenfields are used *and* the overlap between them is negligible. In such a case, the system is lossless if and only if the transfer matrix is unitary[Pietzsch, 1989][Haus, 1984, §§3.2, 3.3]. In the rest of this thesis, unless otherwise stated, all bases are orthonormal, the couplers will be lossless and therefore their transfer matrices will be unitary.

With the isolated core eigenfields as basis, U, considered as a function of the axial distance, z, along the coupler, is the solution of the differential equation[Snyder and Love, 1983, Ch-29]:

$$\frac{dU(z)}{dz} = iK(z)U(z) \tag{6.2}$$

where[1] $K(z)$ is the matrix of coupling coefficients, the off-diagonal elements at (j,k) are the coupling coefficients $C_{jk}(z)$ between cores j and k and the diagonal elements are the core propagation constant $\beta_j(z)$. We describe the difference between planar and more general devices in terms of these elements as follows: a planar coupler is one whose waveguides can be numbered so that guide m is a nearest neighbour to guides

[1] If the basis fields are orthonormal, the rate of change of propagating power is $d(x^\dagger U^\dagger U x)/dz = ix^\dagger U^\dagger(-K^\dagger + K)Ux$ for the input x. Since U is invertible, an input can be chosen to make Ux arbitrary, so that power is conserved if and only if $K = K^\dagger$ *i.e.* the coupling matrix is Hermitian. Energy conservation, unitarity of U and Hermitian symmetry of K are equivalent statements with orthonormal basis fields.

$m \pm 1$ for all m *and* whose is K matrix with this numbering is tridiagonal *i.e.* has nonzero elements only along the leading diagonal and the two neighbouring stripes, since $C_{jk} = 0$ if guides j and k are not nearest neighbours. In almost all practical coupled waveguide devices the electromagnetic fields are highly concentrated about the waveguide cores and so coupling between non-nearest neighbours is negligible.

If the waveguide system is translationally invariant, the solution to (6.2) is $U = \exp(iKz)$ and the set of U-matrices realisable by planar devices is clearly far more restricted than the set realisable by general devices, since the general K-matrix is not necessarily tridiagonal. More generally, if K is constrained to vary so that its eigenvectors are constants, then:

$$U = \exp\left(i \int_0^z K(v)dv\right) \tag{6.3}$$

However, if we allow K to vary arbitrarily, then the set of planar-realisable U matrices is much broader and will be shown, in the next Chapter, to be essentially the same as the set of all generally-realisable U-matrices. Thus, in theory, planar technology can mimic *any* coupled waveguide system. The tridiagonal matrix elements can be complex (as long as the matrix is Hermitian); the physical meanings of negative and complex coupling coefficients and propagation constants are explained in §8.4.2.

6.3 3×3 Coupler Design by Transfer Matrix

6.3.1 Design Specification

The cross-section of a planar 3×3 coupler is shown in Fig-6.3 and the core widths $w_j(z)$ and separations $d_j(z)$ can be fairly arbitrary functions of the z, and they are directly controlled by the planar photomask. In the following designs, the coupling coefficients $k_{13}(z)$ and $k_{31}(z)$ between waveguides 1 and 3 vanish to ensure tridiagonality and hence planar-realisability.

Throughout §6.3, we assume the system eigenfields are well-approximated by linear superpositions of the isolated core eigenfields, taken as basis fields, and the coupled guide description (6.2) holds. Furthermore, the overlap between the core

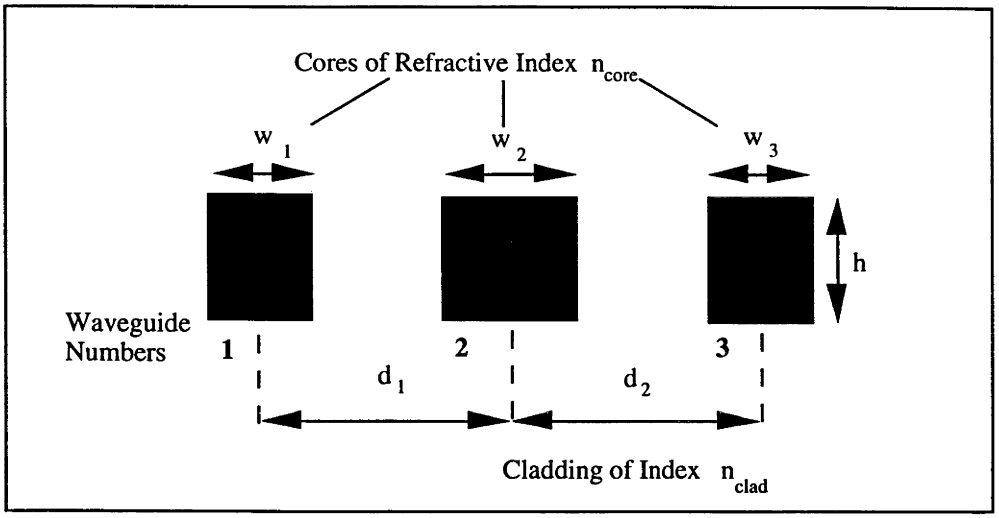

Figure 6.3: Planar coupler cross-section dimension definitions

fields is assumed small for the purposes of power calculations, *i.e.* the total power travelling along the coupled waveguide system is approximately the sum of the powers borne by each core. Consequently, the coupler's input and output powers are the squared lengths of the column vectors describing the input and output fields, and energy conservation is equivalent to unitarity of U when the core eigenfields are suitably normalised. Since the overlap $\langle \psi_j, \psi_k \rangle << 1$, and if the difference between propagation constant pairs is comparable to the coupling coefficients (which will be shown true for the systems considered here), then $(C_{jk} - C_{kj})/C_{jk} << 1$, by (A9) in [Snyder and Ankiewicz, 1988]. Hence, the K matrix is symmetric and so is the U matrix for systems that are invariant to a swap of the roles of their input and output ports[2].

The Sheem interferometer cannot be realised by three identical coupled waveguides with equal coupling between neighbours (when $w_1 = w_2 = w_3$ and $d_1 = d_2$ so that $\beta_1 = \beta_2$ in (6.8) below), for straightforward analysis shows that the eigenvectors of K are constant and given by $(1, 0, -1)^T$, $(1, \pm\sqrt{2}, 1)^T$ and that:

$$U = \frac{\exp(i\eta_1)}{2} \begin{pmatrix} \cos(\eta_2) + 1 & \sqrt{2}i\sin(\eta_2) & cos(\eta_2) - 1 \\ \sqrt{2}i\sin(\eta_2) & 2\cos(\eta_2) & \sqrt{2}i\sin(\eta_2) \\ \cos(\eta_2) - 1 & \sqrt{2}i\sin(\eta_2) & cos(\eta_2) + 1 \end{pmatrix} \tag{6.4}$$

[2]The forward transfer matrix U_f is then the same as the backward transfer matrix U_b (*i.e.* the forward transfer matrix when the roles of the input and output are swapped), but the relationship $U_f = U_b^T$ is general (see Appendix-6.6 or [Pietzsch, 1989]), whence $U = U^T$.

where

$$\eta_1 = \int_0^z \beta(v)dv, \quad \eta_2 = \sqrt{2}\int_0^z C(v)dv \tag{6.5}$$

It is readily shown that an interferometer with a recombiner described by (6.4) does *not* obey (6.1).

If $w_1 = w_3$ in Fig-6.3, the waveguide's symmetry, together with the basic U and K-matrix symmetries, requires $U_{11} = U_{33}$, $U_{12} = U_{21} = U_{23} = U_{32}$ and $U_{13} = U_{31}$. If, in Fig-6.1, the interferometer's arms are input to the two outer waveguides, the magnitudes and relative phases of the output powers as functions of ϕ are those of $U_{11}\ U_{13}^*$, $U_{12}\ U_{12}^*$ and $U_{13}\ U_{11}^*$, respectively. Therefore, if the system obeys (6.1), $U_{11}\ U_{13}^* = a\ U_{12}\ U_{12}^* = a^2\ U_{13}\ U_{11}^*$, where $a = \exp\left(\pm\frac{2\pi\, i}{3}\right)$. The most general unitary U fulfilling all of the above conditions is readily shown to be:

$$U = \frac{1}{\sqrt{3}} \begin{pmatrix} \exp(i\theta) & 1 & \exp\left(i\left(\theta + \frac{4\pi}{3}\right)\right) \\ 1 & \exp\left(i\left(\frac{4\pi}{3} - \theta\right)\right) & 1 \\ \exp\left(i\left(\theta + \frac{4\pi}{3}\right)\right) & 1 & \exp(i\theta) \end{pmatrix} \tag{6.6}$$

where θ is an arbitrary real angle. This can be repeated using the middle and one outer waveguide as inputs and the corresponding U-matrix is:

$$U = \frac{1}{\sqrt{3}} \begin{pmatrix} \exp(i\left(\frac{2\pi}{3} - \theta\right)) & 1 & \exp\left(i\left(\frac{4\pi}{3} - \theta\right)\right) \\ 1 & \exp(i\theta) & 1 \\ \exp\left(i\left(\frac{4\pi}{3} - \theta\right)\right) & 1 & \exp\left(i\left(\frac{2\pi}{3} - \theta\right)\right) \end{pmatrix} \tag{6.7}$$

It must be emphasised that, so far, we have said nothing about the coupler's being *planar*, we have merely derived the most general U-matrices for the desired interferometer behaviour. From (6.3), a direct computation of the matrix logarithm[3]

[3]Diagonalise U to find $U = P\exp(-i\Lambda)P^{-1}$ where:

$$P = \begin{pmatrix} 1 & 1 & 1 \\ 0 & \alpha^+(\theta) & \alpha^-(\theta) \\ -1 & 1 & 1 \end{pmatrix} \quad \Lambda = \mathrm{diag}\left(\frac{\pi}{2} - \theta + 2n_1\pi, \xi(\theta) + 2n_2\pi, (2n_3+1)\pi - \xi(\theta)\right)$$

$$\alpha^{\pm}(\theta) = \cos(\theta) \pm \sqrt{2 + \cos^2(\theta)} \qquad \xi(\theta) = \pm\arctan\left(\frac{\sin(\theta)}{\sqrt{2+\cos^2(\theta)}}\right)$$

by diagonalisation[4] of U gives an expression for $k_{13}(\theta) = k_{31}(\theta)$. We then impose a *planar* 3×3 array by choosing θ such that $k_{13} = 0$. Thus, if the coupling matrix has the form:

$$K(z) = \begin{pmatrix} \beta_1(z) & C(z) & 0 \\ C(z) & \beta_2(z) & C(z) \\ 0 & C(z) & \beta_1(z) \end{pmatrix} \tag{6.8}$$

$$C(z) = 0.759741\,(\beta_2(z) - \beta_1(z)) \tag{6.9}$$

then we obtain the U matrix of (6.6) (aside from an inconsequential phase-delay) provided:

$$\int_0^z (\beta_2(u) - \beta_1(u))\,du = 1.70495 \tag{6.10}$$

or:

$$\int_0^z (\beta_{e1}(u) + \beta_{e2}(u) - 2\beta_o(u))\,du = 1.70495 \tag{6.11}$$

where β_{e1}, β_{e2} and β_o are the propagation constants of the couplers first even, second even and first odd supermodes, respectively. In the weakly coupled case, they are

---

whence $K = P\Lambda P^{-1}$ and the required expression

$$k_{31}(\theta) = -\frac{1}{2(5+\cos(2\theta))}\left(4\theta + 4n\pi + 2\cos^2(\theta)(\theta - n\pi) + \cos(\theta)\sqrt{2+\cos^2(\theta)}((2n+4m+1)\pi - 2\xi(\theta))\right)$$

where n_1, n_2, n_3, $n = n_2 + n_3 - 2n_1$ and $m = n_1 - n_2$ are arbitrary integers depending on the branch of the matrix logarithm taken. $k_{31} = 0$ can clearly be solved for any pair (n, m), since k_{31} is everywhere a continuous function of θ and $k_{31} \to \pm\infty$ for $\theta \to \pm\infty$.

[4]In diagonalising U, note that there must be one eigenvector of the form $(1, 0, -1)^T$ and two of the form $(1, \alpha, 1)^T$. This follows because the eigenfields can *always* be chosen to have either even or odd symmetry about any plane of mirror symmetry of the waveguide's cross-section. For let $\mathcal{R}$ be a reflexion about this plane of symmetry; then it is readily shown that, if ψ and β are an eigenfield and propagation constant fulfilling the scalar wave equation $(\nabla^2 + k^2n^2 - \beta^2)\psi = 0$ then $\mathcal{R}\psi$ and therefore $\psi_e = \psi + \mathcal{R}\psi$ and $\psi_o = \psi - \mathcal{R}\psi$ are also eigenfields with the same propagation constant. Then, trivially, $\mathcal{R}\psi_e = \psi_e$ and $\mathcal{R}\psi_o = -\psi_o$ since $\mathcal{R}^2 = 1$ and $\mathcal{R}$ is linear *i.e.* ψ_e and ψ_o have even and odd symmetry about the cross-sectional plane of symmetry. The set of all even-symmetric eigenfields spans the vector space of all even-symmetric fields, and likewise for the odd eigenfields and odd-symmetric fields. The two vector spaces are orthogonal complements and direct-sum to the space of all bound waveguide fields. Any input field with either even or odd symmetry about a plane of reflexional symmetry of the waveguide retains its symmetry as it propagates.

given by the K-matrix's eigenvalues. If $(\beta_1-\beta_2)/C$ is constant, as in (6.9), the matrix of eigenvectors of K is constant. Otherwise, (6.2) cannot be solved as the K matrices at different cross-sections do not commute with one another, thus invalidating a solution of the simple form in (6.3). If the guides become tightly coupled, so that $C_{jk} \neq C_{kj}$ (Appendix-6.6), the K-matrix's eigenvectors *must* vary since they are necessarily orthogonal when $K = K^T$ and necessarily not orthogonal when $K \neq K^T$. Hence, the reason for the failure of the present design in tightly coupled systems.

6.3.2 Photomask Design

A photomask was designed with $w_1(z) = w_3(z) = 2w(z)$ (*i.e.* $w(z)$ denotes the outer core halfwidth) and $d_1(z) = d_2(z) = d(z)$ (Fig-6.3) chosen to satisfy (6.9). For simplicity, the middle waveguide's width w_2 is kept constant. The waveguide depth must be the same for all three waveguides for fabrication in contemporary planar technology. Beginning with w, the eigenfields for the middle and outer waveguides can be calculated using the Fourier Decomposition Method (FDM)[Henry and Shani, 1991]. The FDM is very accurate and, moreover, the coupling coefficient between any two eigenfields can be calculated *analytically* in terms of separation, d, as the Fourier cosine transform (using d as the transform variable) of an array comprising simple functions of the spatial Fourier components (output from the FDM) defining the eigenfields. Thus, a Fourier transform yields $C(d)$ (Fig-6.4) in one computational step and d can be chosen to satisfy (6.9). This procedure is repeated many times for different w values and the $w(d)$ curve defined by (6.9) is calculated (Fig-6.5).

Next, a slowly-varying trajectory (defined by $d(z)$) is chosen for the outer waveguide so as not to lose device adiabaticity and $w(z)$ is derived from the $w(d)$ curve. Lastly, the appropriate length of constant cross-section coupling region is inserted into the device to satisfy (6.9).

An example using the above method uses a freespace wavelength $\lambda = 1500$nm and a cladding refractive index of 1.5. The middle core is a $8\mu\text{m} \times 8\mu\text{m}$ square cross-section and the core refractive index n_{co} is such that $V_{mid} = \pi w_2\sqrt{n_{co}^2 - n_{cl}^2}/\lambda = 2$, where w_2 is as in Fig-6.3. Consider, for example, a cross-section where the outer core's halfwidth is $w_1 = w_3 = 2w = 7\mu$m. The FDM gives β_1 (outer core propagation constant) $= 6.292791 \times 10^6\text{m}^{-1}$ and β_2 (middle core propagation constant)

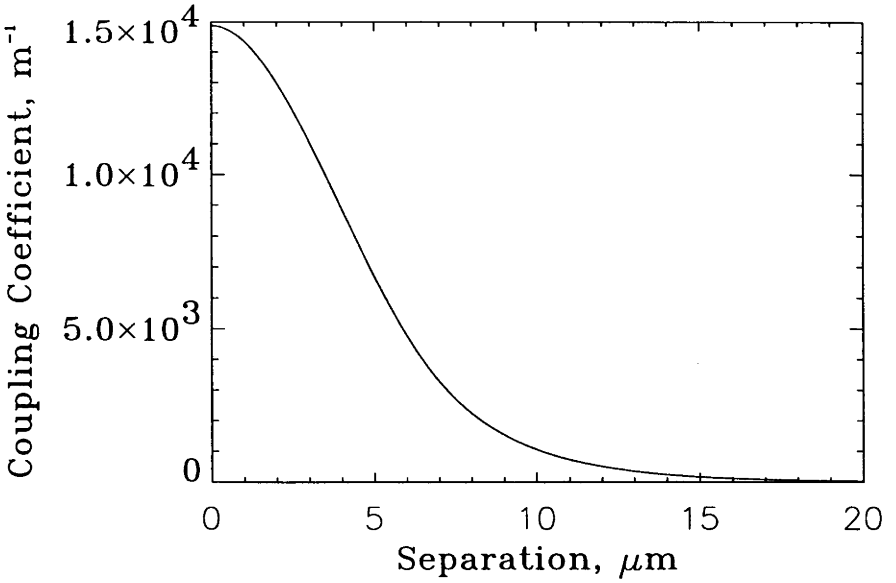

Figure 6.4: Coupling coefficient as a function of centre-to-centre separation, $d = d_1 = d_2$, when $w_2 = 8\mu$m and $w_1 = w_3 = w/2 = 3.5\mu$m in Figure-6.3.

$= 6.291941 \times 10^6 \text{m}^{-1}$. Therefore, by (6.9), d must be chosen so that $C = 645.78\text{m}^{-1}$ and, from Fig-6.4, the separation required is $d = 11.34\mu$m. Repetition of this procedure for various w generates the $w(d)$ curve in Fig-6.5.

To check how closely spaced the cores can be without invalidating this procedure, the overlap between the cores is plotted in Fig-6.6 as a function of separation. The core widths are chosen in accordance with the $w(d)$ curve (Fig-6.5) and then the overlap between the two cores is calculated from the spatial Fourier components without the need to reconstruct the fields themselves.

As a further check on the procedure's soundness, the exact propagation constants for several cross-sections on the $w(d)$ curve were calculated. In Fig-6.7, these are compared with the eigenvalues of the K-matrix. One reason for the discrepancies revealed is that, for weak coupling, $C_{jk} = C_{kj}$, which does not hold when overlap between the fields is significant. From these two plots, the smallest outer core halfwidth for which the present design method is sound is about 3.5μm (corresponding to a core-to-core separation of 11.34μm). Accordingly, a photomask was designed to taper the cores so that d decreased linearly from 16.12μm (when the

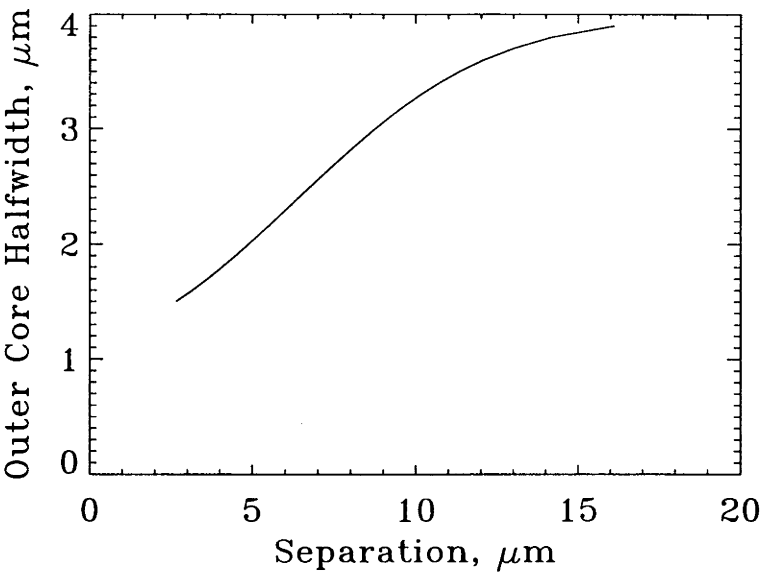

Figure 6.5: Outer waveguide halfwidth, w, as a function of d required to fulfill (6.9)

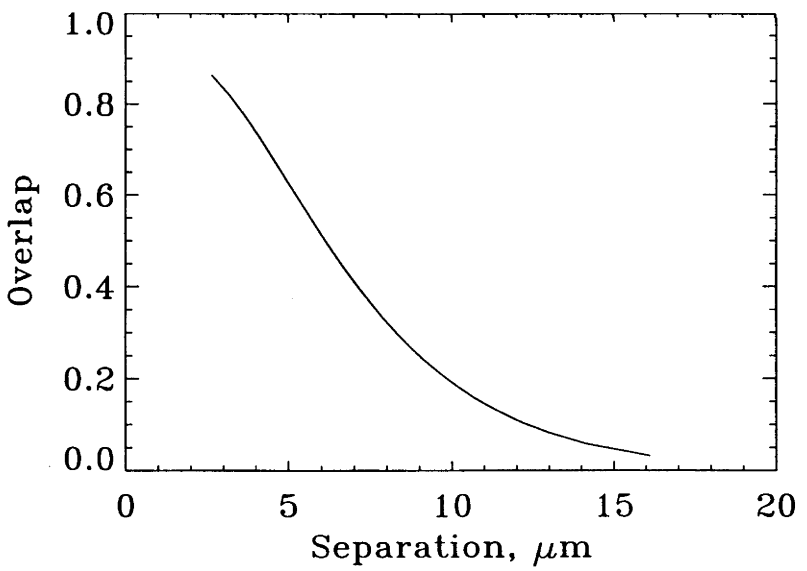

Figure 6.6: Core-to-core overlap as a function of core-to-core separation $d_1 = d_2 = d$

outer core halfwidth is, by (6.9), 3.9μm) down to 11.34μm (outer core halfwidth is 3.5μm) along an axial distance of 500μm. The outer core halfwidth is given by $w(d)$

and, for this downtaper:

$$\int_0^{500\mu m} (\beta_2 - \beta_1) dz = 0.206495 \text{ radian} \tag{6.12}$$

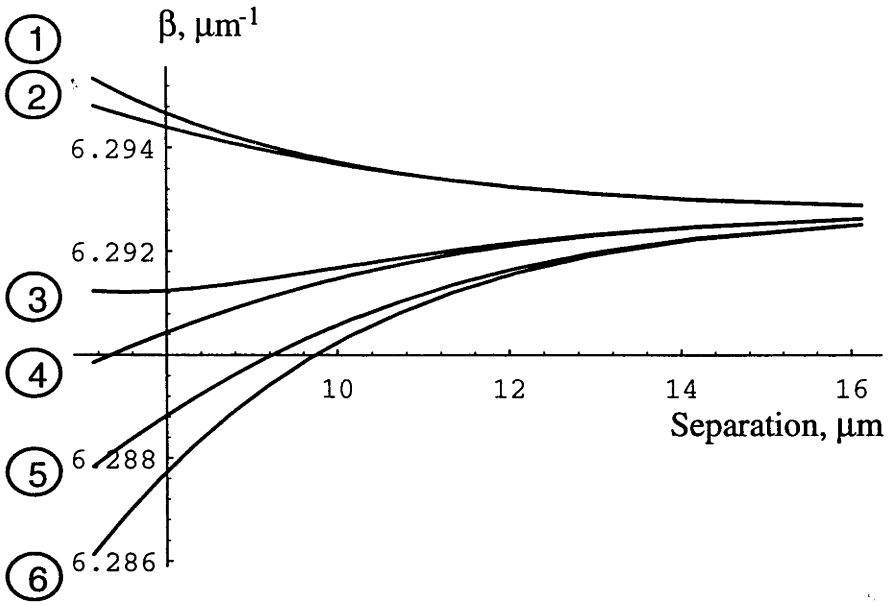

Key:

1: Fundamental even eigenfield, exact FDM calculation
2: Fundamental even eigenfield, K-matrix theory
3: Odd eigenfield, exact FDM calculation
4: Odd eigenfield, K-matrix theory
5: Second even eigenfield, K-matrix theory
6: Second even eigenfield, exact FDM calculation

Figure 6.7: Propagation constants from K-matrix and FDM calculations

The whole coupler is the present downtaper, followed by a translationally-invariant coupler with the same cross-section as the downtaper's output and of length, L, yet to be found, followed by an uptaper identical to the downtaper. Reciprocity (Appendix-6.6) requires the uptaper's transfer matrix with respect to the local supermodes to be the transpose of that of the downtaper.

6.3.3 Beam Propagation Analysis

Three separate BPM simulations of the coupler downtaper were undertaken, one for each local supermode (as calculated exactly by the FDM) input into the $d = 16.12\mu m$

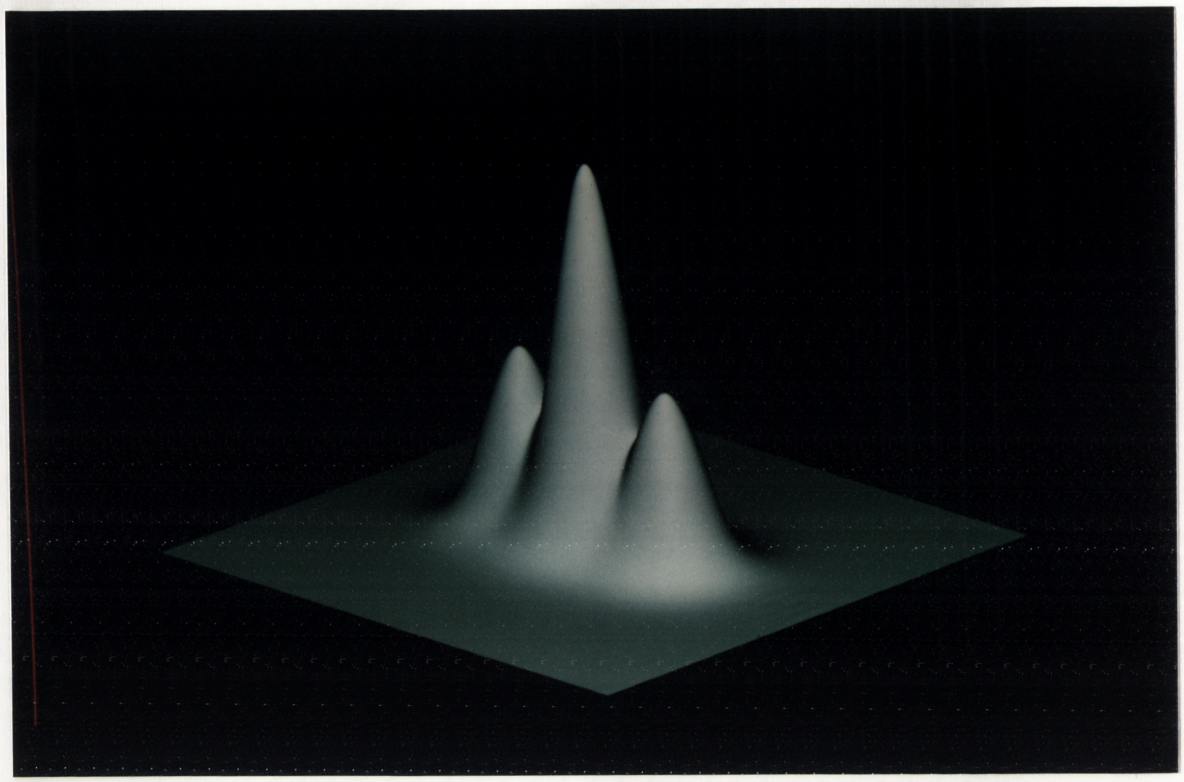

Figure 6.8: Fundamental eigenfield of the central coupling region. Note the even symmetry about the waveguide cross-section's plane of reflexional symmetry

side of the taper. The overlaps between the taper's outputs and the local supermodes (again calculated by the FDM—see the field amplitude plots in Figs-6.8, 6.9, 6.10)[5] were calculated and the results are summarised in the transfer matrix with respect to the local supermodes:

$$U_{taper} = \begin{pmatrix} -0.325758 + 0.938193i & 0.00100569 - 0.00539975i & 0.0261106 + 0.0867151i \\ -0.000409456 - 0.005228i & 0.0898486 - 0.975139i & 0.000234841 - 0.00729506i \\ -0.0435583 + 0.0752248i & -0.00417461 + 0.00588145i & -0.129076 - 0.981447i \end{pmatrix} \tag{6.13}$$

Here the fundamental even eigenfield is mode 1, the odd eigenfield mode 2 and the second even eigenfield mode 3. The leading diagonal magnitudes are close to

[5]Note that the eigenfields have either even or odd symmetry about the waveguide cross-section's plane of reflexional symmetry, see the previous footnote.

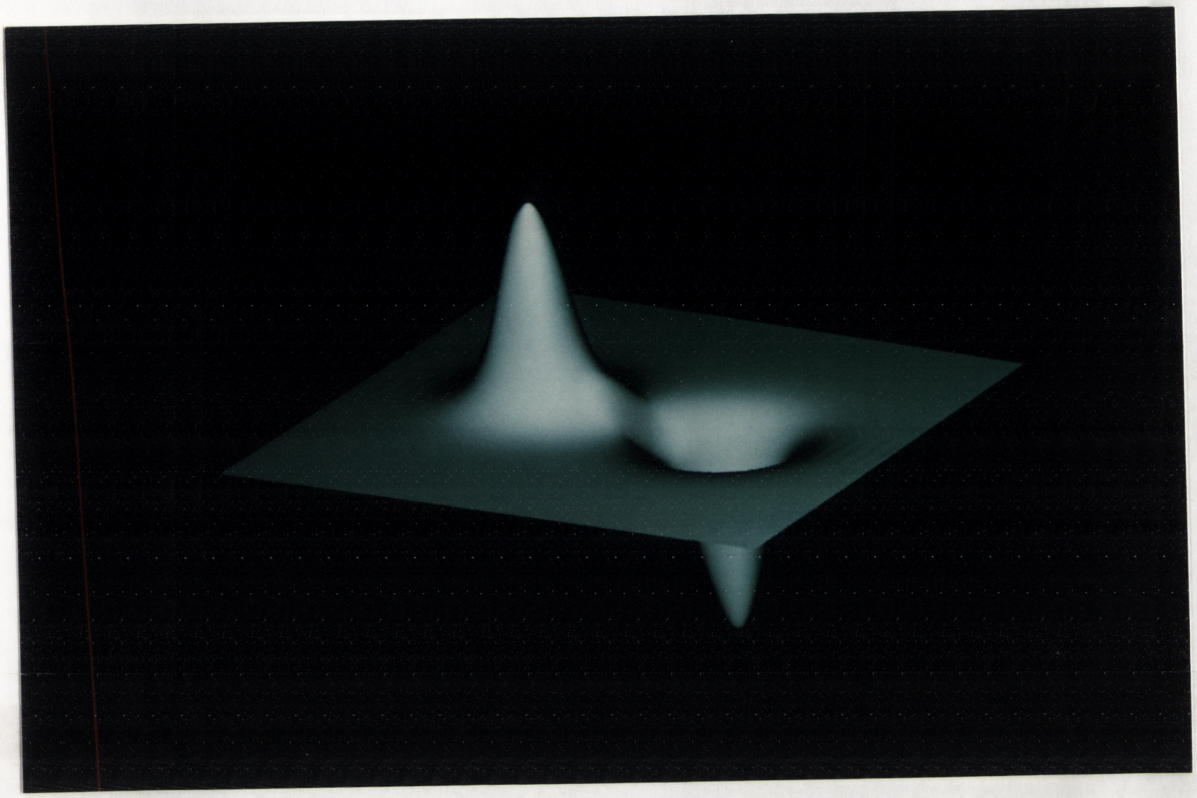

Figure 6.9: Second eigenfield *i.e.* first odd eigenfield of the central coupling region

1 and the off-diagonal elements (whose squared magnitudes are the supermode-to-supermode extinction ratios, see Chapter-10) are about -20dB, showing that the taper is approximately adiabatic.

Since the downtaper and uptaper contribute $2 \times 0.206495 = 0.41299$ radian (6.12) to the integral in (6.10), this equation gives $L = 1.525$mm, when the core propagation constants are used, and $L = 2.336$mm for the FDM-calculated supermode propagation constants. Clearly, with even the fairly small overlap in this case, there is considerable discrepancy between FDM and K-matrix theory. However, simulations show that the coupler would approximate (6.1) with reasonable accuracy for *every* L in the range $1525\mu\text{m} < L < 2400\mu\text{m}$ (see below), indicating that the device is quite tolerant to manufacturing errors. The optimal value is $L \approx 2250\mu$m, so that the FDM clearly gives the more accurate value of coupling length.

The propagation through the translationally invariant section is most conveniently analysed by the FDM. The forward transfer matrix with respect to the local supermodes is:

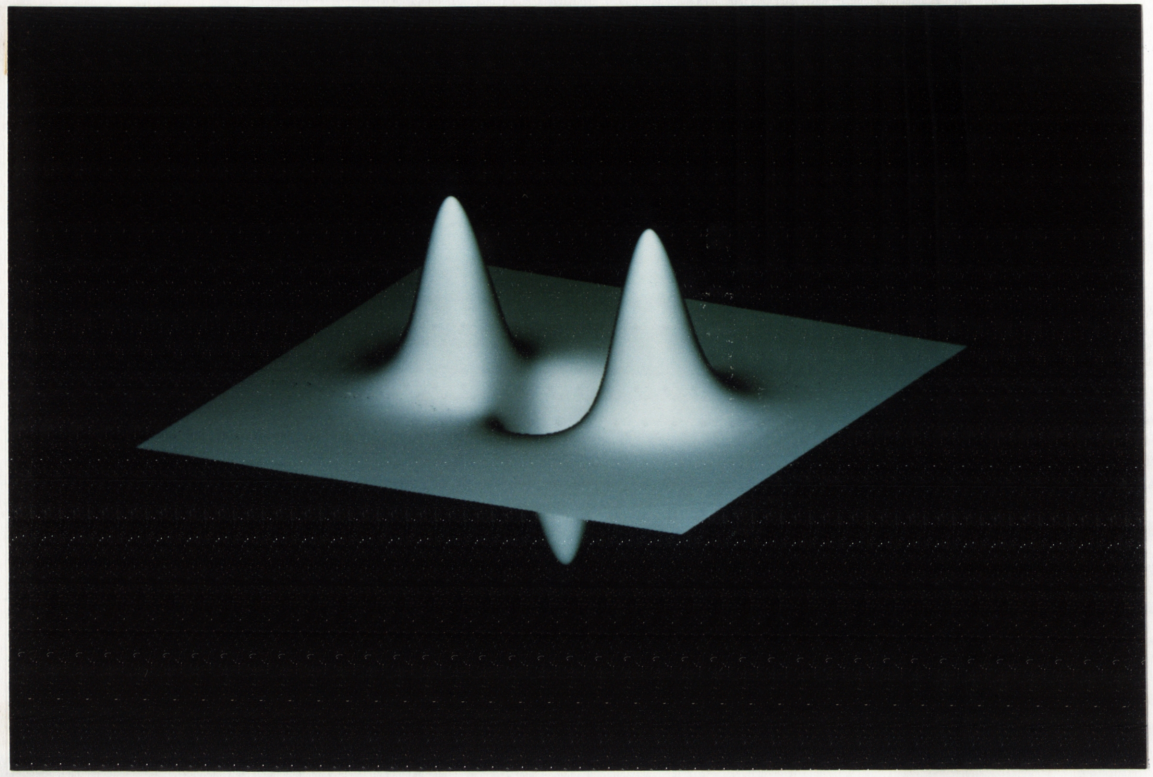

Figure 6.10: Third eigenfield *i.e.* second odd eigenfield of the central coupling region

$$\Lambda = \text{diag}\left[\ \exp(-i\beta_{e1}L),\ \ \exp(-i\beta_{o}L),\ \ \exp(-i\beta_{e2}L)\ \right] \tag{6.14}$$

where β_{e1}, β_{e2} and β_o are the propagation constants of the first even, second even and the first odd supermodes, respectively. The product $U_{taper}^{T}\Lambda U_{taper}$ is the system transfer matrix with the local supermodal fields as the basis at the input and output; this can be converted to the transfer matrix with the isolated core eigenfields as basis by using the matrix P of core-to-supermode overlaps: $P_{j,k} = \left\langle \hat{\phi}_j, \hat{\psi}_k \right\rangle$, where the $\hat{\phi}_j$ are the normalised isolated core eigenfields and $\hat{\psi}_j$ are the normalised local supermodes at the input and output. Thus, the BPM and FDM predict that the coupler's forward transfer matrix, with respect to the isolated core eigenfields, is:

$$U = P^{-1} U_{taper}^{T} \Lambda U_{taper} P =$$

$$\begin{pmatrix} -0.524502 + 0.143701i & -0.541978 - 0.0613173i & 0.117034 - 0.574846i \\ -0.570616 - 0.066266i & 0.515826 - 0.322285i & -0.560606 - 0.0819363i \\ 0.116365 - 0.575621i & -0.52996 - 0.0793975i & -0.528222 + 0.128423i \end{pmatrix} \tag{6.15}$$

when $L = 2250\mu$m. If the relative phase between the interferometer's arms in Fig-6.1 is ϕ, then the output powers are the squared component magnitudes of $U\left(\exp(i\phi/2), 0, \exp(-i\phi/2)\right)^T/\sqrt{2}$ with the arms input into the two outer waveguides. With the arms input into the middle and one outer guide, the output powers are the squared component magnitudes of $U\left(\exp(i\phi/2), \exp(-i\phi/), 0\right)^T/\sqrt{2}$. These results are plotted in Fig-6.11.

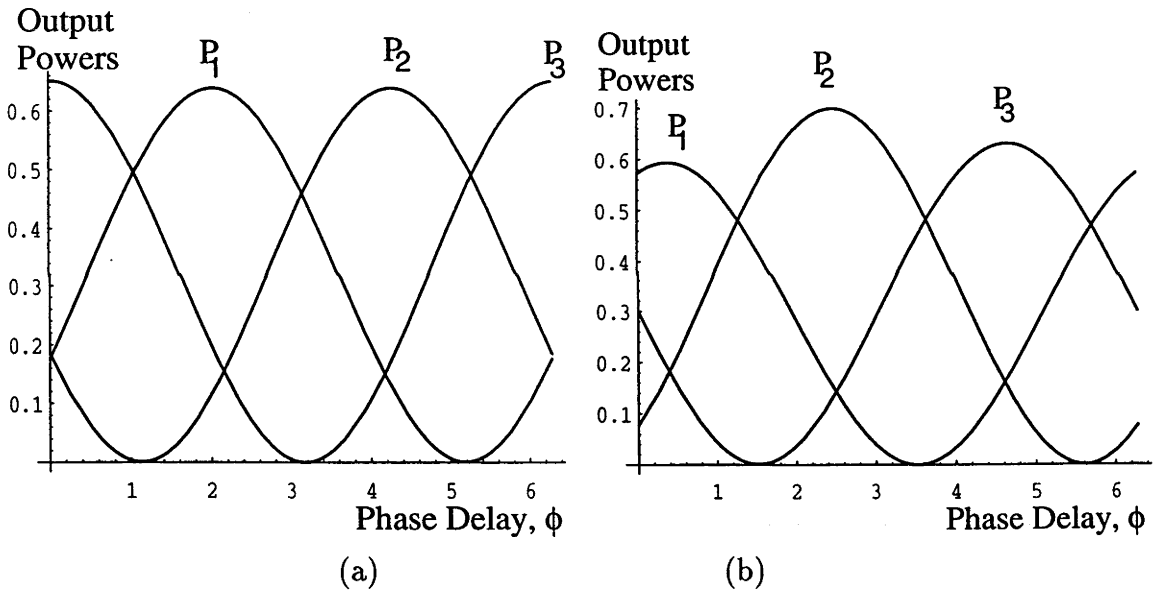

Figure 6.11: Interferometer output intensities as a function of relative phase between the interferometer branches. Results for input into the *(a)* two outer; *(b)* one outer and one inner waveguides.

For this device, the coupling coefficients are very small for cores separated by more than about 16μm, so the error arising from the connexion of the coupler to tapers linking it elsewhere can be assumed negligible. One could extend the design by using the FDM method to calculate d and w for the tapers for much larger separations. However, the Fourier Decomposition Method has one important

drawback — Fourier sine and cosine terms do not represent the fields far from the core well, where they decay exponentially with distance from the core, unless the Fourier series include many terms. Hence, the calculation of coupling coefficients by the FDM in the case where the fields are very weakly coupled may give rise to significant error.

6.4 Supermode Based Design

We can remove the approximations inherent in the coupled guide design procedure by using a supermode analysis. This allows more tightly coupled structures, whose required eigenfield delays occur over shorter coupling lengths, and thus leads to more compact and therefore more temperature-insensitive devices. The procedure is also more physically meaningful, using the coupled structure's normal modes rather than eigenfields of the waveguides in isolation. However, the new design procedure is far more unwieldy than the transfer matrix approach, from an engineering point of view, for neither the coupling coefficients between the supermodes nor their propagation constants can be changed individually. Instead, any cross-sectional change strongly influences all these quantities simultaneously and it is difficult to set up the coupling coefficient/propagation constant combination needed for a given device.

6.4.1 Coupler Description

In the following design, slab waveguides are considered for simplicity. The photomask is shown schematically in Fig-6.12 and comprises a symmetric downtaper, uptaper and a central supermode coupling region, which is a simple, three-moded slab waveguide. The control bars introduce further degrees of freedom to the central coupling region design, as discussed at the end of §6.4.3. They are not used for the design in this Chapter, but they may be useful for similar systems as long as they do not lead to excessive loss.

The basis fields for this system's analysis are the local supermodes. At the device's input and output, the isolated core eigenfields, at 55μm separation, are so weakly coupled that they can be considered, for all practical purposes, to be orthogonal system supermodes. *Any* reasonably lossless downtaper/uptaper can be chosen;

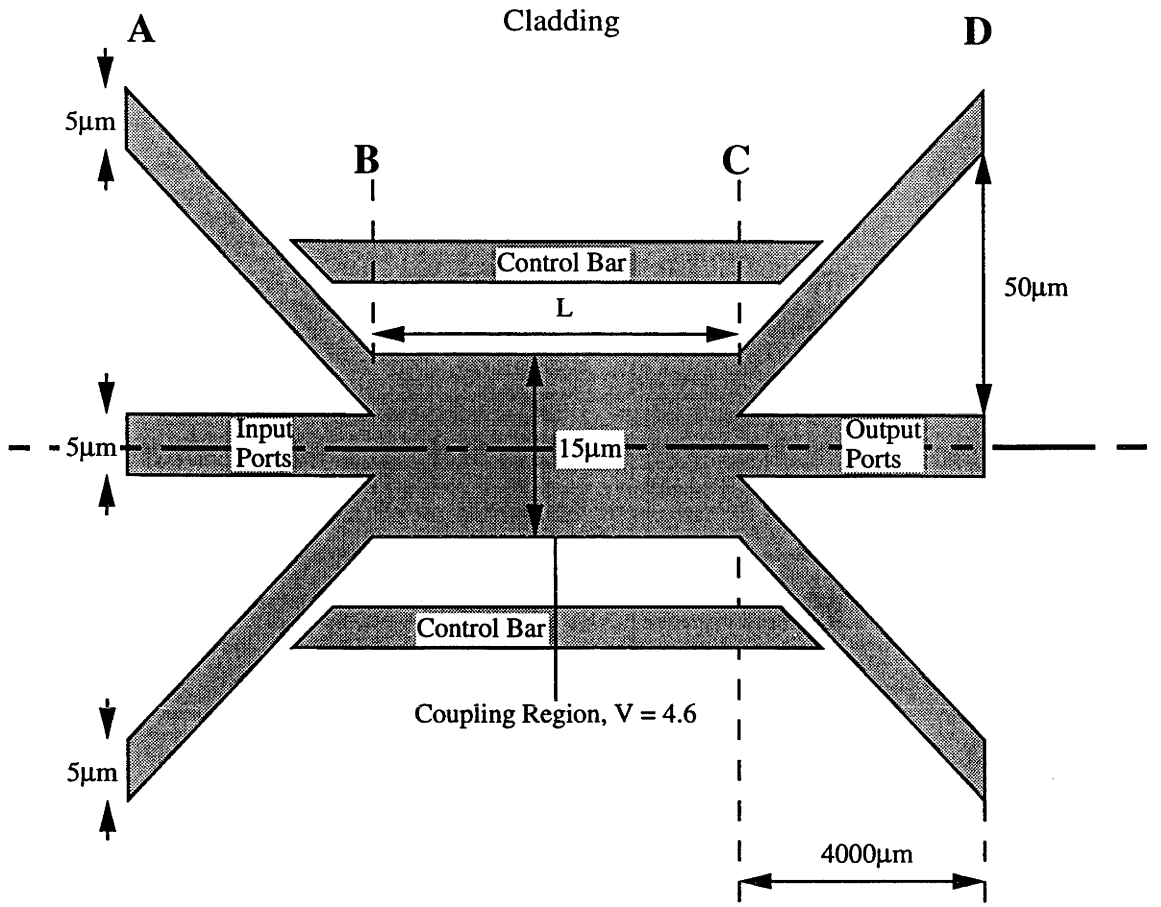

Figure 6.12: Photomask schematic for a strongly-coupled 3×3 Coupler

the tapers do not have to be adiabatic (*i.e.* each local supermode having constant power) and, indeed, the design is facilitated if they are not. A BPM simulation gives the transfer matrices of the up- and downtapers. Using these matrices together with the design goal (6.6) or (6.7), the coupling between supermodes is calculated.

The coupler's working freespace wavelength is taken to be 1500nm with a cladding refractive index of 1.5. The slab waveguide in section BC is a single slab of width 15μm and the core refractive index for the whole device is such that $V = 4.6$ in BC. Thus the central coupling region has three bound modes: the fundamental even mode, the first odd mode and the second even mode, in order of decreasing propagation constant. The whole device has even symmetry about the centreline drawn in Fig-6.12.

6.4.2 Coupling Region

If U_{taper} is the transfer matrix of the taper AB, its structure can be inferred from symmetry. Any input to the middle waveguide has even symmetry about the centreline and *cannot* excite the odd supermode. Excitation of both even supermodes from input to one outer waveguide is exactly the same as for the other outer waveguide. The odd-supermode excitation arising from input to one outer waveguide is the same as that arising from input to the other outer waveguide but with opposite sign. Moreover, U_{taper} is unitary and the most general U_{taper} fulfilling all of these conditions is:

$$U_{taper} = \begin{pmatrix} p & \sqrt{1-2p^2}e^{i\phi_1} & p \\ \frac{1}{\sqrt{2}}e^{i\phi_3} & 0 & -\frac{1}{\sqrt{2}}e^{i\phi_3} \\ \frac{\sqrt{1-2p^2}}{\sqrt{2}}e^{i\phi_2} & -\sqrt{2}pe^{i(\phi_1+\phi_2)} & \frac{1}{\sqrt{2}}\sqrt{1-2p^2}e^{i\phi_2} \end{pmatrix} \tag{6.16}$$

where the ϕ_j are arbitrary real angles and $p \leq 1/\sqrt{2}$ is real. For the coupler shown in Fig-6.12, a one-dimensional BPM analysis shows that the downtaper AB is defined by the above matrix with $p = 0.485392$, $\phi_1 = -2.265559$, $\phi_2 = 0.0778898$ and $\phi_3 = -1.474127$. The forward transfer matrix of the uptaper CD is, by reciprocity, U_{taper}^T. Thus $U = U_{taper}^T U_c U_{taper}$ or $U_c = U_{taper}^* U U_{taper}^\dagger$, where U_c is the transfer matrix of the central coupling region BC and U is the design goal of (6.6) or (6.7). Hence:

$$U_c = \begin{pmatrix} U_{11}^c & 0 & U_{13}^c \\ 0 & U_{22}^c & 0 \\ U_{13}^c & 0 & U_{33}^c \end{pmatrix}$$

where

$$\begin{aligned} U_{11}^c &= \frac{e^{-i\phi_1}}{\sqrt{3}}\left(4p\sqrt{1-2p^2} - \exp\left(-i\left(\phi_1+\theta+\frac{\pi}{3}\right)\right) + 4p^2\cos\left(\phi_1+\theta+\frac{\pi}{3}\right)\right) \\ U_{22}^c &= \exp\left(i\left(\theta-\frac{\pi}{6}\right)\right) \\ U_{13}^c &= \sqrt{\frac{2}{3}}\left(1-4p^2+2p\sqrt{1-2p^2}\cos\left(\phi_1+\theta+\frac{\pi}{3}\right)\right) \end{aligned} \tag{6.17}$$

and

$$U_{33}^c = -(U_{11}^c)^* \frac{U_{13}^c}{(U_{13}^c)^*}; \quad |U_{11}^c|^2 + |U_{13}^c|^2 = 1; \quad |U_{33}^c|^2 + |U_{13}^c|^2 = 1; \quad |U_{22}^c|^2 = 1 \tag{6.18}$$

describe the unitarity of U^c.

To achieve our design goal we require coupling between the supermodes as described by (6.17). We can use the free parameter θ in (6.6) or (6.7) to simplify the device design. By setting $\theta = 2.870811$, we have $U^c_{13} = 0$ and the coupling region does not couple the supermodes, but imposes phase-delays U^c_{11}, U^c_{22} and U^c_{33} on the individual supermodes. If the now-diagonal U^c is multiplied by $e^{i\omega}$, where ω is any real number, the device's working will not be changed. Thus, only the ratios $U^c_{11}/U^c_{22} = \exp(3.866404i)$ and $U^c_{22}/U^c_{33} = \exp(0.65722i)$ are important. Nevertheless, it is still not clear how to satisfy these phase conditions. If we use a constant cross-section slab for the coupling region, there is only one degree of freedom, the waveguide's length L, to vary, and we must satisfy the simultaneous conditions:

$$\begin{aligned} (-(\beta_{e1} - \beta_o)L) \bmod 2\pi &= -6.852 \times 10^{-3}\, L \bmod 2\pi = 3.866403 \\ (-(\beta_o - \beta_{e2})L) \bmod 2\pi &= -1.0717 \times 10^{-2}\, L \bmod 2\pi = 0.65722 \end{aligned} \tag{6.19}$$

which is not possible. However, we can satisfy (6.19) to within an arbitrary accuracy with a long-enough coupling region.

Consider a plot of $\theta_2 = (\beta_o - \beta_{e2})L$ against $\theta_1 = (\beta_{e1} - \beta_o)L$. We are only interested in these angles' values modulo 2π, hence we can break the $\theta_1 - \theta_2$ plane up into unit cells of sidelength 2π — one unit cell is shown in Fig-6.13, *i.e.* the ordered pairs (θ_1, θ_2) for $0 \leq \theta_j < 2\pi$ can be mapped one-to-one and onto the Cartesian product of two circles, namely, a torus. The torus is equivalent to the unit cell in Fig-6.13 if the sides TU and WV are identified (imagined pasted together) such that points T and W become one point as do U and V. One now has a cylinder, which can be bent to bring the two ends together as a torus, *i.e.* the sides VU and WT are identified.

If we follow the trajectory of the point (θ_1, θ_2) on the torus and the unit cell as L increases, it begins at A and threads the central hole to arrive at B (note the two B-points in Fig-6.13*(a)* are identified to become one point B in Fig-6.13*(b)*), likewise to points C, D, E, F, G and H. If $\beta_{e2} - \beta_o$ is not an integer multiple of $\beta_o - \beta_{e1}$, the the trajectory does not close but instead progresses to I through H' and now winds another full θ_1-cycle around the torus. It is readily shown that the

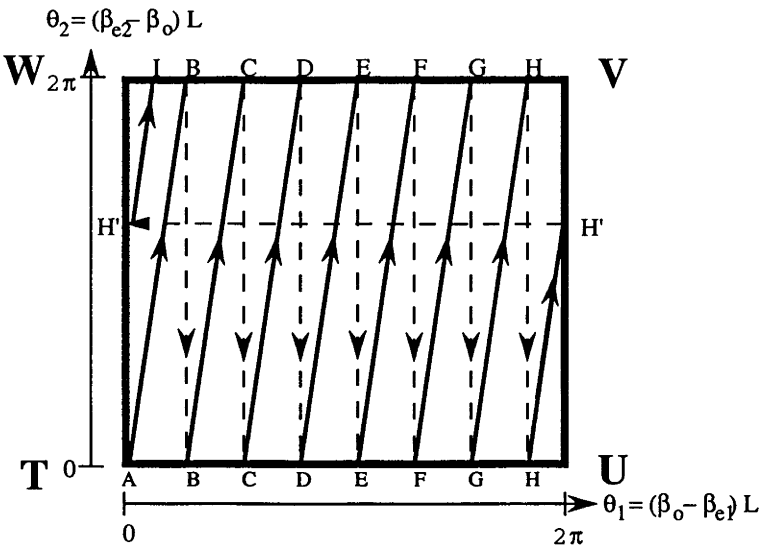

(a)

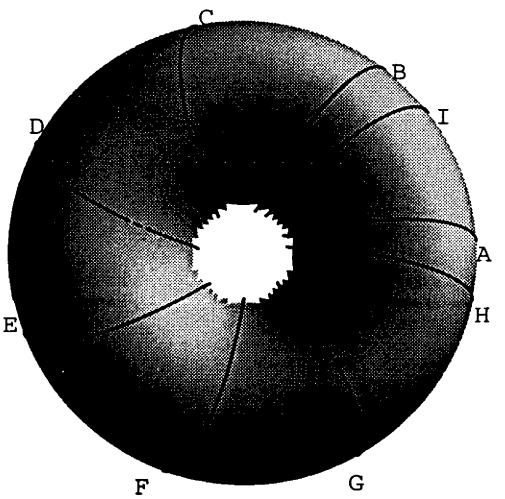

(b)

Figure 6.13: *(a)* Unit cell of (θ_1, θ_2) plot and *(b)* (θ_1, θ_2)-trajectory on a torus

trajectory will only link with itself if and only if its gradient is a rational number, *i.e.* $\beta_{e2} - \beta_o$ and $\beta_o - \beta_{e1}$ are rationally related. Otherwise[Bröckner and Dieck, 1985, Theorem 4.13] the trajectory is then *dense on the torus's surface*, *i.e.*, passes *arbitrarily near* to *every* pair of phase angles, even though there are infinitely many (*e.g.* any rationally-related pair) that it does not pass through. Thus, with a long enough coupling region, *any* pair (θ_1, θ_2) can be satisfied to arbitrary accuracy.

There is a practical limitation, however; some pairs may require an excessively long coupling region, violating the requirement of device compactness needed for good temperature and mechanical stability.

6.4.3 Results

In our case, we find that for $L = 4021\mu$m, $\theta_1 = 3.8664$ and $\theta_2 = 0.8929$, so θ_2 is matched to within 0.23 radian or 13 degrees and the device's transfer matrix is:

$$U = U_{taper}^T \exp\left(i \,\mathrm{diag}\left[\begin{array}{ccc} 3.866, & 0, & -0.8929 \end{array}\right]\right) U_{taper} =$$

$$\left(\begin{array}{ccc} -0.471313 - 0.429997i & 0.338965 + 0.401666i & 0.510055 - 0.237861i \\ 0.338965 + 0.401666i & 0.664866 + 0.0740843i & 0.338965 + 0.401666i \\ 0.510055 - 0.237861i & 0.338965 + 0.401666i & -0.471313 - 0.429997i \end{array}\right) \tag{6.20}$$

where U_{taper} is the matrix in (6.16) with parameters determined by the BPM simulation of the taper. A BPM analysis of the whole device (rather than of the taper only, with the whole device's behaviour then inferred from reciprocity, as above) fully confirms this result. The device's performance, when incorporated into the interferometer of Fig-6.1, is summarised in Fig-6.14 and would be adequate for this application.

If we examine a graphical representation of the full BPM analysis, Fig-6.15 shows the intensities within the device when a unit power eigenfield is input to the middle guide, the field propagating from right to left in this figure. Note that the beating in the central coupling region is very regular since, with the input to the middle core, there is only beating between the two even supermodes. This contrasts with Fig-6.16, which shows the field evolution after unit power is input to the outer waveguide at the top right-hand corner of the figure, with the field propagating right to left. In this case, all three supermodes are present in the coupling region, and the beating there is complicated.

Finally, the control bars illustrated in Fig-6.12 may refine the design. If placed far enough away from the device's centreline, so as to influence only the second even supermode (the other supermodes being too concentrated about the central core to feel their effect), a second degree of freedom can be introduced into (6.19) to allow

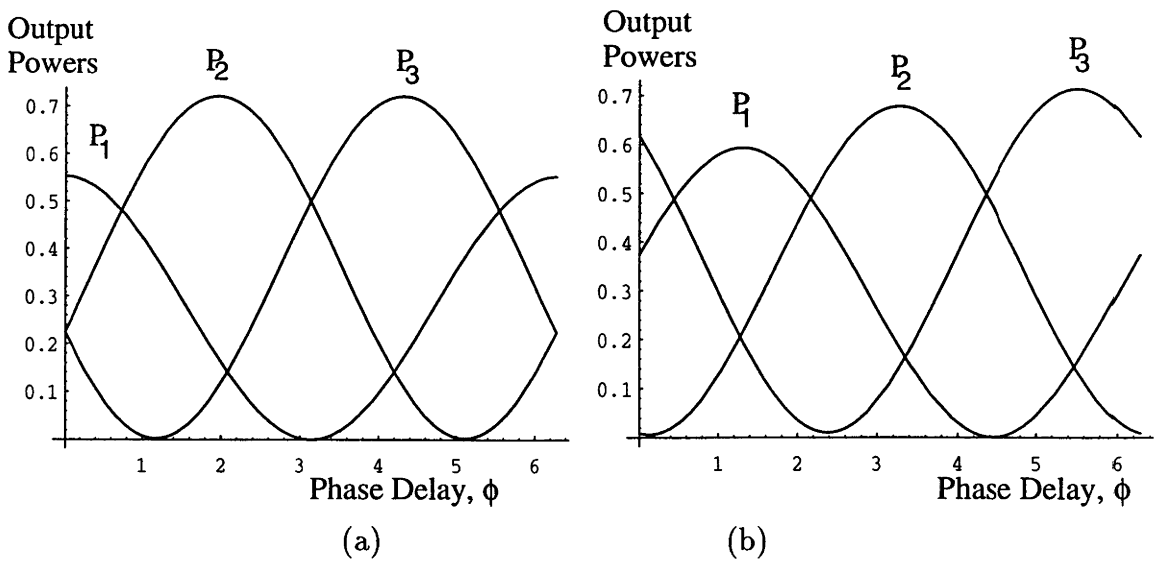

Figure 6.14: Interferometer output intensities as a function of relative phase between the interferometer branches. Results for input into the *(a)* two outer waveguides and *(b)* one outer and one inner waveguide.

the phase condition, in theory, to be satisfied exactly. However, if the bars are far enough from the core to influence the second even supermode only, their effect is too small to improve phase matching significantly. If the bars are closer to the core, their design becomes extremely difficult as they influence all the supermodes. In the present case, the device is adequate without the bars but the principle may well be useful in other cases.

6.5 Conclusions

We have presented two design procedures producing a 3×3 planar coupler to mimic the nonplanar symmetric 3×3 fibre coupler, and have shown, by numerical simulation, that they achieve their design goals adequately. The first procedure has the advantage that it specifies isolated core propagation constants and coupling coefficients, which are directly and *individually* controllable by core widths and separations. Thus, the procedure is simple to implement. However, the procedure is only valid for weakly coupled guides. The second design procedure is valid however tightly coupled the constituent waveguides may be; indeed, in our example, the three

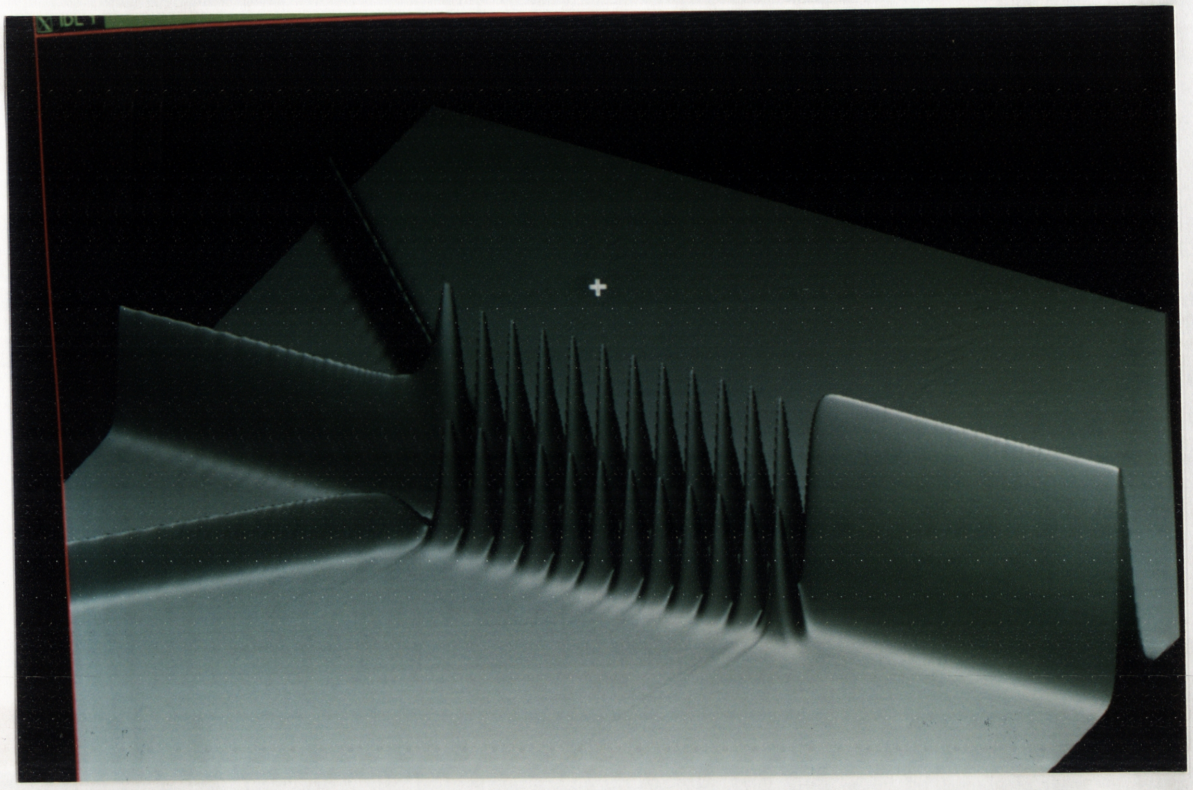

Figure 6.15: Propagation within strongly coupled device after excitation through middle input waveguide

coupled waveguides merge into one. Furthermore, the procedure is grounded on the physically more meaningful concept of coupled waveguide supermodes. However, the procedure is unwieldy and its success depends more on trial-and-error because any change made to the coupler's cross-section influences all the supermodes together. There is no simple way to design a waveguide's cross-section so that specified phase delays and couplings can be imposed on *individual* supermodes and supermode pairs.

We shall address the shortcomings of these *ad hoc* methods in the next two Chapters.

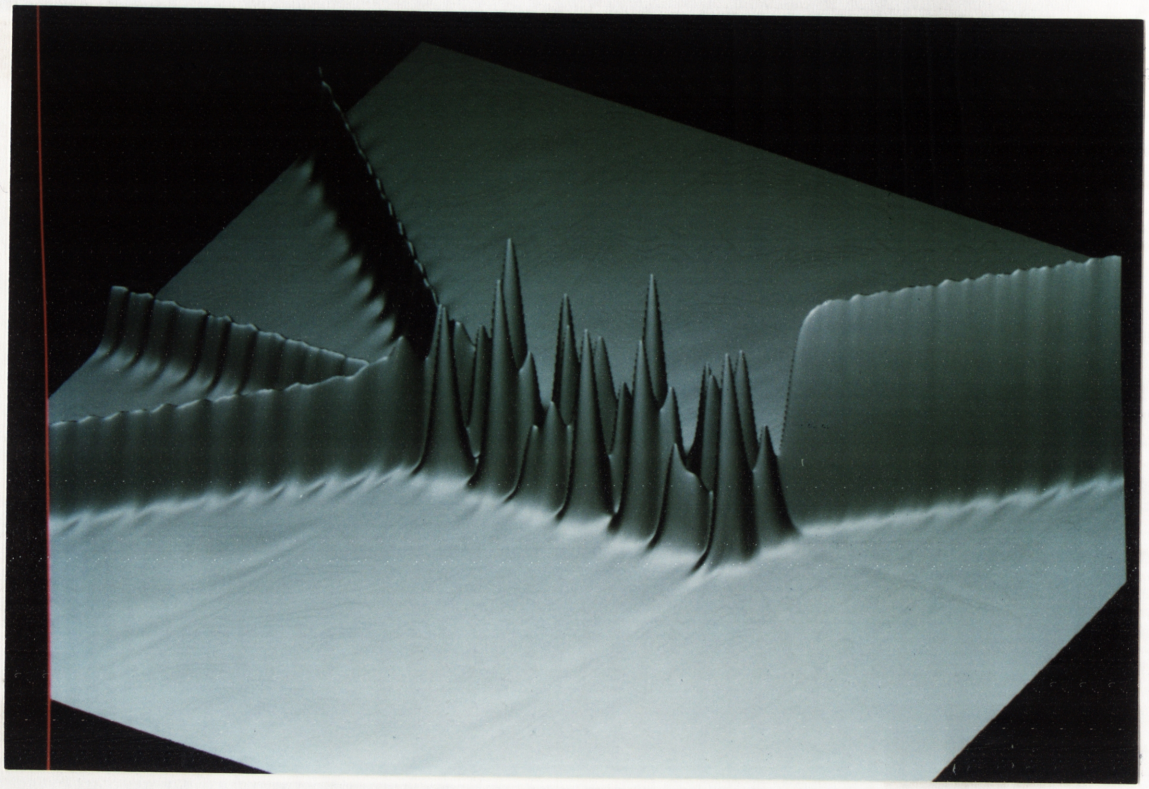

Figure 6.16: Propagation within strongly coupled device after excitation through outer input waveguide

6.6 Appendix: Matrix Reciprocity and Conservation Laws

6.6.1 General Case

When waveguides are coupled so that overlaps between them cannot be neglected for power calculation purposes, the Reciprocity Law shows that the K matrix *cannot* have translationally invariant eigenvectors. Hence, the first design procedure presented in this Chapter will fail.

We consider the general waveguide section (not necessarily translationally invariant) in Fig-6.17. Let the transverse electric fields at cross-section A be expressible by a superposition of complete basis fields $\left\{\hat{\psi}_j^A\right\}$, those at section B by fields from basis $\left\{\hat{\psi}_j^B\right\}$. Let $(\mathbf{E}_1', \mathbf{H}_1')$ be the field output from section B after the input of $(\mathbf{E}_1, \mathbf{H}_1)$ into section A; likewise let $(\mathbf{E}_2', \mathbf{H}_2')$ be the output from section A as a result of the input of $(\mathbf{E}_2, \mathbf{H}_2)$ into section B. The Poynting vectors $\mathbf{S}_j$ show the propagation

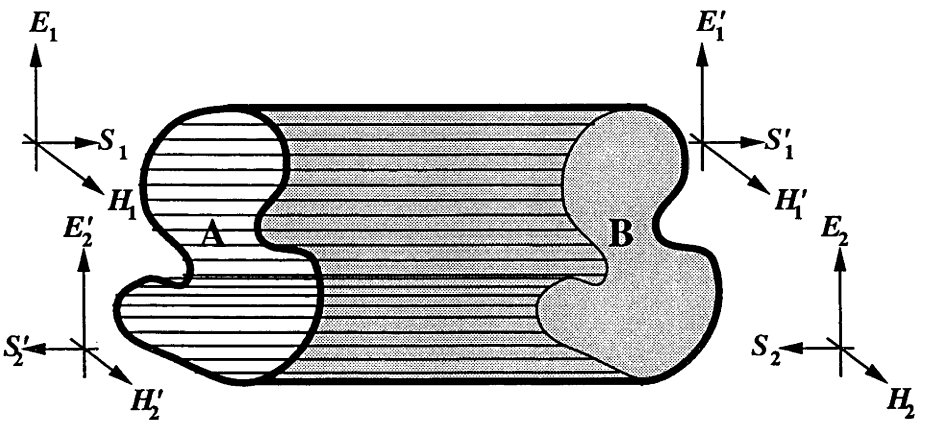

Figure 6.17: Notation for the matrix form of the Reciprocity Law

directions. The electric fields are expressible as:

$$\begin{aligned}
\mathbf{E}_1 &= \sum_j E_{1j}\, \hat{\psi}_j^A\, \hat{\mathbf{x}} \\
\mathbf{E}'_1 &= \sum_j \sum_k U_{jk}^f\, E_{1j}\, \hat{\psi}_j^B\, \hat{\mathbf{x}} \\
\mathbf{E}_2 &= \sum_j E_{2j}\, \hat{\psi}_j^B\, \hat{\mathbf{x}} \\
\mathbf{E}'_2 &= \sum_j \sum_k U_{jk}^b\, E_{2j}\, \hat{\psi}_j^A\, \hat{\mathbf{x}}
\end{aligned} \tag{6.21}$$

where the E_{1j} and E_{2j} are the complex weights in the linear superpositions representing the fields and U_{jk}^f and U_{jk}^b are the elements of the forward and backward transfer matrices, respectively. Since the system is linear, the weights in the input (unprimed) field superpositions are mapped to those in the output (primed) field superpositions by linear maps whose matrices are U^f and U^b. If we assume that the incidence of the input fields does not give rise to reflexions, then substitution of (6.21) into the unconjugated reciprocity law[Snyder and Love, 1983, §31-2] (the fields with subscript 1 are written for the unbarred field, those with subscript 2 for the barred field) followed by integration of [Snyder and Love, 1983, Eq-(31-8)] over the surface shown in Fig-6.17 yields:

$$(U^b)^T V_A = V_B U^f \tag{6.22}$$

where $(V_A)_{jk} = \left\langle \hat{\psi}_j^A, \hat{\psi}_k^A \right\rangle$ and $(V_B)_{jk} = \left\langle \hat{\psi}_j^B, \hat{\psi}_k^B \right\rangle$ define the matrices of overlap

integrals between the basis fields.

6.6.2 Special Cases

The matrix reciprocity law (6.22) gives the following special cases:

- For a waveguide of length δz whose basis fields are the isolated core eigenfields, $U^f \approx U^b \approx \exp(iK\,\delta z)$ and, by taking the limit as $\delta z \to 0$, (6.22) is found to be exactly equivalent to $K^T V = VK$;
- If the overlaps between the cores are negligible then $K^T = K$,
- If the waveguide is made of non-absorbing dielectric, then K must be real (as are the isolated core eigenfields) and $U^* = U^{-1}$. This can be used to show that $U^\dagger V U = V$, which becomes $U^\dagger U = I$ (U is unitary) when overlaps between the isolated cores can be neglected;
- If the basis fields are the *local supermodal fields*, which are *always* orthogonal, then $U^b = (U^f)^T$ and U^b and U^f are unitary (by energy conservation, if the fields are normalised) however tightly coupled the system may be; and
- If we consider a general 2×2 coupler with isolated core eigenfields as basis, then we find $(\beta_1 - \beta_2)\langle\psi_1, \psi_2\rangle = (K_{21} - K_{12})$, that is, (A9) in [Snyder and Ankiewicz, 1988] is a special case of $K^T V = VK$.

We note in passing that U^f and U^b are the off-diagonal partitions of the complete scattering matrix[Pietzsch, 1989] $\mathcal{S}$ and the usual matrix statement of the reciprocity law is $\mathcal{S} = \mathcal{S}^T$. We see that the matrix reciprocity and energy conservation laws take their simplest form when the basis fields used are the local supermodes. Then (6.2) is replaced with a system of coupled local mode equations[Snyder and Love, 1983, §31-14] and K is replaced with the Hermitian matrix of local modal coupling coefficients, whose eigenvectors are orthogonal however tightly coupled the cores may be.

Note also that $K^T V = VK$ implies that, since $K = K^T$ in weakly coupled systems and $K \neq K^T$ in tightly coupled ones, the eigenvectors are necessarily orthogonal in the former case and necessarily not orthogonal in the latter. Hence,

the procedure of §6.3, assuming translationally-invariant eigenvectors, must fail in a system whose waveguides become too tightly coupled.

Chapter 7

Lie Theory Applied to Planar Coupler Design

7.1 Introduction

We have seen in the foregoing Chapter that, with the isolated core eigenfields as basis and with the weak-coupling assumptions stipulated in §6.2, the planar constraint restricts possible coupling matrices, K, to being *real, symmetric* and *tridiagonal.* Clearly, if the waveguide is translationally invariant, the coupler's forward transfer matrix $U = \exp(iKz)$ is far more restricted than it would be in the general, nonplanar case where K can have nonzero elements at any position. In particular, a cyclic[1] K matrix is not possible in the planar case so that a translationally-invariant planar coupler cannot realise a cyclic transfer matrix. Cyclic symmetry will be shown to play an essential role in the realisation of the symmetric 3×3 and 5×5 couplers in the next Chapter.

It is an altogether different matter if the K-matrix can vary with distance, z along the coupler. The variation can be exploited to overcome at least some of the planar constraint, as the following simple example shows. Consider the planar realisations of the symmetric 5×5 coupler to be discussed in §8.4.2; here we have $U_{goal} = \exp(iK_1)\exp(iK_2)$, where, although K_1 and K_2 are tridiagonal, the planar coupler's transfer matrix U_{goal} is cyclic, a situation not possible if a single translationally-invariant planar section $\exp(iK_1)$ were used. The question naturally

[1] *i.e.* One whose rows are cyclic shifts of one-another.

arises as to just how well the planar constraint can be overcome by exploiting a variable $K(z)$. Can a variable $K(z)$ be used to realise, in planar technology, *any* transfer matrix realisable by more general, nonplanar couplers? Or, whilst clearly broader than the class of transfer matrices realisable by translationally-invariant planar couplers as shown by the simple example, is the class of planar-realisable couplers truly more restricted than the more general nonplanar coupler? More generally, we consider:

Suppose a manufacturing constraint restricts the class of all possible coupling matrices to come from a certain possible set. Given a complete specification of this manufacturing constraint (tantamount to a full definition of the coupling matrix set), we seek a full characterisation of the set of all realisable transfer matrices

In the first half of this Chapter we shall show that, in a certain restricted sense, planar couplers can indeed realise *any* transfer matrix realisable by a nonplanar coupler. The restriction is that there may be some transfer matrices unrealisable exactly by planar couplers but, by making the coupler long enough, these outlying transfer matrices can be realised to within any desired accuracy. The situation will be akin to the strongly-coupled device of §6.4; there, we could not match the phase-condition (6.19) exactly, but we could come as close as we liked to doing so if we allowed a long-enough coupling region.

Clearly, such realisations are not always practical. However, in the second half of this Chapter, we shall introduce a design procedure, based on generalised Mach-Zehnder interferometers, that is *guaranteed* to realise *any* possible $N \times N$ unitary transfer matrix by a *finite* number of fundamental planar building-blocks, provided that we can find N basic planar N-waveguide couplers fulfilling a simple condition. This second procedure will be introduced by a simple 2×2 coupler example, where the problem can be fully visualised by rotations of the Poincaré sphere.

The basic mathematical tool of this Chapter is the theory of matrix Lie groups. This is a difficult weapon to wield and not all of its intricate machinery is needed for the problem at hand. This Chapter therefore seeks a presentation of Lie theory readily comprehensible to optical engineers by *defining* Lie groups and Lie algebras

in terms of the physical concepts of sets of transfer matrices realisable by coupled optical waveguides.

7.2 Lie Groups Defined by Linear Couplers

7.2.1 Reachable Group and its Closure

As in the foregoing Chapter, we shall describe all couplers by their forwards transfer and coupling matrices. However, we shall use an approach that does not directly refer to (6.2). Instead, one begins with translationally-invariant coupler building-blocks and couplers comprising concatenations of such blocks as the basic concepts. This corresponds to a piecewise-constant $K(z)$ in (6.2). If we consider the concatenation of two translationally-invariant couplers of lengths z_1 and z_2 and with the same cross-section, and if $U(z)$ defines the transfer matrix of a guide of this cross-section and length z, then it follows immediately that $U(z_1 + z_2) = U(z_1)U(z_2)$ and $U(z) = \exp(hz)$ for some constant h characterising the cross-section, by definition of the exponential and without appeal to (6.2). In the following, it will be convenient to use h rather than iK and absorb the coupling region lengths into the coupling matrices themselves. Hence, we write $\exp(h)$ for a translationally-invariant coupler's transfer matrix and call h the coupling matrix, noting that it includes the coupling region length and that the notation differs from the standard literature on coupled waveguide theory. Energy conservation, for orthonormal basis fields at the system's input and output, is equivalent to skew-Hermitian symmetry of h, *i.e.* $h = -h^\dagger$, where $\dagger$ denotes the complex-conjugate transpose of a matrix.

We define a *manufacturing constraint* to be a complete specification of the set $\mathbf{h}_0$ of all coupling matrices h realisable by a given manufacturing process. For example, if only planar, weakly-coupled, lossless $N \times N$ couplers can be made and if the basis fields are the isolated waveguide modes, $\mathbf{h}_0$ is the set of all tridiagonal, skew-hermitian, purely imaginary $N \times N$ matrices. For all manufacturing constraints, we assume that, if h is realisable, so is ht for all real t (even $t < 0$), *i.e.* coupler sections of any length can be built and the methods of §8.4.2 show the physical significance of negative coupling co-efficients. Also note that the design procedure of §7.4 yields $\exp(-h)$ extremely simply if it can yield $\exp(h)$.

We study the set $\mathbf{H}$ of all transfer matrices realisable subject to a given manufacturing constraint. $\mathbf{H}$ is then the set of all finite products of the form:

$$\mathbf{H} = \{\exp(h_1)\exp(h_2)...\exp(h_n)|h_1,...,h_n \in \mathrm{h}_0\} \tag{7.1}$$

It is clear that $\mathbf{H}$ is a group, since if $U_1, U_2 \in \mathbf{H}$ then $U_1U_2 \in \mathbf{H}$ (corresponding physically to the concatenation of two couplers) and $U^{-1} \in \mathbf{H}$ whenever $U \in \mathbf{H}$, since if $U = \exp(h_1)\exp(h_2)...\exp(h_n)$, $U^{-1} = \exp(-h_n)\exp(-h_{n-1})...\exp(-h_1)$. Furthermore, let us define the *effective coupling matrix* $h_e = h_e(h_1, h_2, ..., h_n)$ of the concatenation $U_c = \exp(h_1)...\exp(h_n)$ as the matrix with the smallest norm giving $\exp(h_e) = U_c$. For obvious reasons, let $\mathbf{H}$ be called the *reachable group.*

For reasons given below, we consider the closure[2] $\bar{\mathbf{H}}$ of $\mathbf{H}$ and the closures of the sets of all transfer matrices obtained from *(i)* piecewise-constant, *(ii)* continuous or *(iii)* analytic $h(z)$ are readily proven to be the same by showing a limit point of any one set is also a limit point of the other two. Hence, our restriction to piecewise-constant $h(z) = iK(z)$ in (6.2) does not restrict the definition of $\bar{\mathbf{H}}$. An important fact is that $\bar{\mathbf{H}}$ is a group, which can be proven by showing that the products and inverses of limit points of $\mathbf{H}$ are also limit points of $\mathbf{H}$, analogously to [Sagle and Walde, 1973, §3.2]. One good physical reason for considering $\bar{\mathbf{H}}$ is that if a matrix *arbitrarily* close to a particular design goal can be realised, then it seems reasonable to say that the design goal has been achieved. If the discussion were not restricted to the closure of the set of realisable matrices, we should have to specify exact limits on *e.g.* the greatest allowable rate of change of $K(z)$, the greatest allowable coupling length *etc.*, thus complicating our analysis.

7.2.2 Lie Algebra $\mathfrak{h}$

We now *define* the concepts of Lie groups and algebras in terms of sets of transfer and coupling matrices as the most expedient way of presenting the theory and these definitions will be reconciled with standard ones in §7.2.5.

[2]To consider questions about closure and other topological aspects, we use the metric space defined by any suitable matrix norm, *e.g.* the spectral or trace norms, and the topology induced by this metric.

Let $\mathbf{h}_n$ be the set of all matrices derivable from members of $\mathbf{h}_0$ in n operations of the form:

- For two matrices h_1 and h_2 form the matrix $t_1 h_1 + t_2 h_2$, for any real t_1 and t_2;
- For h_1, h_2 form $t[h_1, h_2]$, for any real t.

where $[h_1, h_2] = h_1 h_2 - h_2 h_1$ is the Lie product between h_1 and h_2. It is readily shown by induction that $\exp(h) \in \bar{\mathbf{H}}$ if $h \in \mathbf{h}_n$ for all integer n as follows: let h_1, $h_2 \in \mathbf{h}_n$ and assume it has already been proven that $\exp(\mathbf{h}_n) \subseteq \bar{\mathbf{H}}$. Consider (*c.f.* the construction of [Ise and Takeuchi, 1990, Ch-1]) the sequence whose m^{th} member is:

$$\left(\exp(h_1)\exp\left(\frac{h_2 t}{m}\right)\exp(-h_1)\exp\left(\frac{-h_2 t}{m}\right)\right)^m = \exp(h_{3,m}) \tag{7.2}$$

where

$$h_{3,m} = t[h_1, h_2] + O\left(\frac{t^2}{m^2}\right)$$

by the exponential's Taylor series. Since $\bar{\mathbf{H}}$ is a group, $\exp(h_{3,m}) \in \bar{\mathbf{H}}$ and $\bar{\mathbf{H}}$ is closed, so the sequence limit $[h_1, h_2]t \in \bar{\mathbf{H}}$ for all real t. Likewise, $\exp(t_1 h_1 + t_2 h_2)$ can be shown to belong to $\bar{\mathbf{H}}$ for any real t_1, t_2 by considering the sequence whose m^{th} member is $(\exp(t_1 h_1/m)\exp(t_2 h_2/m))^m$. Hence, since $\exp(\mathbf{h}_0) \subseteq \bar{\mathbf{H}}$, the induction is complete.

Thus, if $\mathfrak{h}$ is the union of all the $\mathbf{h}_n$, *i.e.* the set of all matrices derivable from $\mathbf{h}_0$ by a finite number of linear superpositions and Lie-products, then, by the above:

$$\mathbf{H} \subseteq \exp(\mathfrak{h}) \subseteq \bar{\mathbf{H}} \tag{7.3}$$

Being closed under the Lie product and also a vector space over the reals (since $t_1\, h_1 + t_2\, h_2 \in \mathfrak{h}$ if $h_1, h_2 \in \mathfrak{h}$ for all real t_1, t_2), $\mathfrak{h}$ is a Lie algebra[Varadarajan, 1974, §2.2] and, by (7.3), members of the reachable group can realise any $\exp(h)$ for $h \in \mathfrak{h}$ to within an arbitrary accuracy.

7.2.3 Lie Group $\mathfrak{H}$

Consider the neighbourhood:

$$\mathfrak{h}_\delta = \{h : \ h \in \mathfrak{h} \text{ and } |h| < \delta\} \tag{7.4}$$

of $\mathbf{0}$ in $\mathfrak{h}$. Then, let the *coupler group* $\mathfrak{H}$ *subject to the manufacturing constraint specified by* $\mathbf{h}_0$ be defined as the group of all finite products of members of the neighbourhood[3] $\exp(\mathfrak{h}_\delta)$. By (7.3), it then follows that:

$$\mathbf{H} \subseteq \mathfrak{H} \subseteq \bar{\mathbf{H}} \tag{7.5}$$

and therefore that all the coupler group's members can be realised to within an arbitrary accuracy. This construction is standard[Ise and Takeuchi, 1990, Lemma 1.3][Sagle and Walde, 1973, Ch-6] and it can be shown that $\exp(\mathcal{N})$ is a neighbourhood of the identity in $\mathfrak{H}$ whenever $\mathcal{N}$ is a neighbourhood of $\mathbf{0}$ in $\mathfrak{h}$. Thus, all matrices H in $\mathfrak{H}$ fulfilling $\|H - I\| < \epsilon$ for some nonzero $\epsilon > 0$ can be represented as an $\exp(h)$ for $h \in \mathfrak{h}$ and multiplication of matrices sufficiently close to the identity is fully defined[4] by the Lie algebra $\mathfrak{h}$.

$\mathfrak{h}$ will be called *the* Lie algebra of the coupler group and is the smallest Lie algebra, as defined in §7.2.5, containing $\mathbf{h}_0$. $\mathfrak{h}$ is also a vector field over the reals. $\mathfrak{H}$ is the smallest Lie group, as defined in [Varadarajan, 1974, §2.1], containing $\mathbf{H}$.

---

[3]In the following, we shall use the obvious notation that, if A is a set, $\exp(A) = \{y \mid y = \exp(x) \text{ for some } x \in A\}$. Likewise, if A and B are subsets of a matrix group then we write $AB = \{x \mid x = yz \text{ for some } y \in A \ z \in B\}$

[4]The *Baker-Campbell-Hausdorff* theorem shows that, if $\|h_1\|$, $\|h_2\|$ are small enough, then $\exp(h_2)\exp(h_1) = \exp(h_3)$ where:

$$h_3 = h_1 + h_2 + \frac{[h_1, h_2]}{2} + \frac{[[h_1, h_2], h_2] - [[h_1, h_2], h_1]}{12} - \frac{[h_2, [h_1, [h_1, h_2]]] - [h_1, [h_2, [h_1, h_2]]]}{48} + \ldots \tag{7.6}$$

The co-efficients in the series are not expressible simply, and their exact values are irrelevant to the present discussion. What is important is that, if h_1, h_2 belong to $\mathfrak{h}$, so do all the partial sums of the series in (7.6), since they are derived from h_1, h_2 by linear superpositions and Lie products and $\mathfrak{h}$ is a Lie algebra. The same is true *for the partial sum limit*, since $\mathfrak{h}$ is closed[Michel and Herget, 1981, §6.6]. Hence, $h_3 \in \mathfrak{h}$. In the coupler group, the theorem thus guarantees, sufficiently near the identity matrix, *all* elements are of the form $\exp(h)$ where $h \in \mathfrak{h}$.

There is a further formula, universally valid, which can be proven directly from the Taylor series definition of the exponential function, namely (7.31) in Appendix-7.8.

7.2.4 Advantages of Lie Algebra

As seen above, the coupler group can be generated from any neighbourhood of the **0** in the Lie algebra and[Sagle and Walde, 1973, Ch-3] is *uniquely defined.* Conversely, as in §7.2.5, the Lie algebra is uniquely defined by the group; there is thus a one-to-one correspondence between Lie algebras and coupler groups and so two manufacturing constraints lead to the same coupler group if and only if they lead to the same Lie algebra. Intuitively the algebra and group contain precisely the same information[5].

The advantages of using the Lie algebra are that:

- Lie algebra computations are much simpler than those in the Lie group. In §7.3, the proof that the coupler group for lossless planar, weakly coupled $N \times N$ couplers is the whole unitary group would be impossible by multiplicative computations with transfer matrices.

- The Lie algebra is a *vector space over the reals*, thus a test of whether or not a matrix belongs to the Lie algebra is a simple *linear test* of whether it is expressible as a linear superposition of basis matrices.

- In contrast, the test for Lie group membership is nonlinear, *e.g.* for the group $\mathfrak{U}(N)$ of unitary[6] matrices, one must test whether $UU^\dagger = I$.

7.2.5 Conventional Definitions

The conventional definition of a Lie group and its Lie algebra is as follows. A *Lie group* $\mathfrak{H}$ is a group whose members can be locally parameterised in some way such that multiplication in the group is defined by analytic functions of the co-ordinates,

[5] In general, the correspondence between Lie groups and algebras is many-to-one. However, here the coupler group's construction yields the *smallest* connected group with a given algebra, thus making the correspondence one-to-one.

[6] Notation: Upper-case Fraktur characters denote a Lie group and the corresponding lower-case letters the corresponding Lie algebra. *E.g.* $\mathfrak{U}(N)$, the group of $N \times N$ unitary matrices; $\mathfrak{u}(N)$, the corresponding algebra of $N \times N$ skew-Hermitian matrices; $\mathfrak{SU}(N)$ (special unitary), the group of $N \times N$ unitary, unimodular (determinant = 1) matrices; $\mathfrak{su}(N)$, the corresponding algebra of $N \times N$ traceless, skew-Hermitian matrices.

i.e., if $H_a = H(a_1, a_2, ...)$ and $H_b = H(b_1, b_2, ...)$ are two group members with local co-ordinates $(a_1, a_2, ...)$ and $(b_1, b_2, ...)$ and if $H_c = H(c_1, c_2, ...) = H_a H_b$ is their product, then the c_j are analytic functions of the a_j and the b_j. Owing to the parameterisations presented in (7.9) or (7.10), the coupler group discussed in §7.2.3 is clearly a Lie group and indeed is the smallest Lie group containing $\exp(\mathfrak{h})$.

To construct the Lie algebra from the coupler group, we suppose that the group co-ordinates x_j are all analytic real functions of a single real variable t, *i.e.* $H = H(x_1(t), ..., x_n(t))$ and t defines a one-dimensional path (or *integral curve*) through the Lie group. Consider a *tangent vector* at a given point H_0:

$$\sum_j \dot{x}_j(t) \left.\frac{\partial H}{\partial x_j}\right|_{H=H_0}$$

Then[Sagle and Walde, 1973, §2.4][Normand, 1980, Appendix C.5.3.3][Varadarajan, 1974, §1.1] the *tangent space* of all possible vectors tangent to some integral curve is clearly a vector space over the reals spanned by the vectors $\partial H/\partial x_j$ and its dimension can be shown to be independent of the group co-ordinates used. The Lie algebra is then the tangent space to the group's identity matrix.

The tangent space to an element H of the group is found as follows. If a co-ordinate x varies, then

$$\lim_{\delta x \to 0} \frac{H(x+\delta x) - H(x)}{\delta x} = \lim_{\delta x \to 0} \frac{H(x+\delta x)H^{-1}(x) - I}{\delta x} H(x) \qquad (7.7)$$

is a tangent vector. By definition of the Lie group, the group co-ordinates of $H(x + \delta x)H^{-1}(x)$ are analytic functions of δx, so $\lim_{\delta x \to 0}(H(x+\delta)H^{-1}(x) - I)/\delta x$ belongs to the tangent space to the identity, *i.e.* the tangent space at H is $H\mathfrak{h}$, thus tangent spaces transform linearly (*c.f.* definitions of tensors in terms of transformation laws[Spiegel, 1974, Ch-8]).

Consider now a *vector field* assigning to each group element H a tangent of the form hH, where $h \in \mathfrak{h}$ is a constant Lie-algebra member. Vector fields expressible in this form are *right-invariant*, thus the Lie-algebra can be mapped one-to-one onto the set of all right-invariant[7] fields. If we consider the curve in the Lie group passing through the identity with hH as its tangent, it is describable in the form

[7] Left-invariant fields, assigning Hh to H can be used in a wholly analogous way.

$dH/dt = hH$ (*c.f.* (6.2)) and $\exp(ht) \in \mathfrak{H}$ for all real t. Thus, yet another definition for the Lie algebra is the set:

$$\mathfrak{h} = \{x \mid \exp(tx) \in \mathfrak{H} \text{ for all real t}\} \tag{7.8}$$

Let $h_1, h_2 \in \mathfrak{h}$ and because $\mathfrak{H}$ is a Lie group, $\exp(h_1)\exp(h_2 t)\exp(-h_1)\exp(-h_2 t) \in \mathfrak{H}$ for all real t and the tangent to the path traced by this element at $t = 0$ is readily shown to be $[h_1, h_2]$. Thus, the group's Lie algebra is closed under the Lie product and the nomenclature "Lie algebra" is justified.

7.2.6 Canonical Co-ordinates

We here present two co-ordinate systems parameterising a suitable neighbourhood of a Lie group's identity, the second of which is of great importance to the practical design procedures of §7.4.

Let $\mathfrak{h}_\delta$ be a neighbourhood of $\mathbf{0}$ in the Lie algebra and suppose that $\{X_1, X_2, ..., X_m\}$ is a basis for $\mathfrak{h}$. Then, for δ small enough, all members H of the neighbourhood $\exp(\mathfrak{h}_\delta)$ can be written in the form:

$$H(x_1, x_2, ..., x_m) = \exp\left(\sum_j x_j X_j\right) \tag{7.9}$$

where the x_j are unique for a given basis and known as the *canonical co-ordinates of the first kind*[Ise and Takeuchi, 1990, Theorem 1.2] for the neighbourhood.

It can be also shown[Ise and Takeuchi, 1990, Example-1.5][Varadarajan, 1974, §2.10][Wei and Norman, 1963; Wei and Norman, 1964] that there is some $\delta > 0$ such that all members of $\exp(\mathfrak{h}_\delta)$ can be uniquely represented as:

$$H(\omega_1, \omega_2, ...\omega_m) = \exp(\omega_1 X_1)\exp(\omega_2 X_2)...\exp(\omega_m X_m) \tag{7.10}$$

and the ω_j are known as *canonical co-ordinates of the second kind.*

For any member H of the coupler group, the function $Y \rightarrow HY$ is one-to-one, onto and continuous, hence the neighbourhood $\exp(\mathfrak{h}_\delta)$ can be mapped onto a neighbourhood $\exp(\mathfrak{h}_\delta)H$ of H by multiplication by H and this neighbourhood can be parameterised in the same way as above.

7.3 Lie-Theoretic Study of the Planar Constraint

7.3.1 Inductive Proof

We now apply a Lie-theoretic investigation to determine the set of *all* possible transfer matrices realisable by planar, lossless, weakly-coupled waveguide devices. Under the conditions stated in §6.2, the planar constraint is tantamount to restricting the set of possible coupling matrices $h = iK$ to be the set $\mathbf{h}_0$ of purely imaginary, symmetric ($h = h^T$, *i.e.* $h^\dagger = -h$), tridiagonal matrices. By the foregoing discussion, the set of all planar-realisable transfer matrices is the coupler group corresponding to the *smallest* Lie algebra containing $\mathbf{h}_0$. We prove below that this smallest Lie algebra must contain the *whole* set $\mathfrak{u}$ of skew-Hermitian matrices. However, since $\mathfrak{u}$ is a Lie algebra *containing* $\mathbf{h}_0$, it must be the required smallest Lie algebra. $\mathfrak{u}$ is also the Lie algebra corresponding to the unitary group $\mathfrak{U}$ of all coupling matrices realisable by general, *non*planar, lossless couplers, hence, *in theory*, by appropriate control of the coupling matrix variation with z:

Any transfer matrix realisable by a nonplanar lossless linear coupler is also realisable, to within an arbitrarily high accuracy, by a planar lossless linear coupler.

We effect the proof by mathematical induction on N, the number of waveguides, and assume that it has already been proven that *any* $(N-1)\times(N-1)$ skew-Hermitian matrix belongs to the Lie algebra generated by the set of $(N-1)\times(N-1)$ matrices of the form iK_{N-1} where K is real, self transpose and tridiagonal. Thus the following matrices belong to the Lie algebra generated by the set of $N \times N$ matrices of the form iK_N, K_N real, self transpose and tridiagonal:

$$\left(\begin{array}{c|cccc} \mathrm{i}\,\beta_1 & ic_1 & 0 & 0 & \ldots \\ \hline ic_1 & & & & \\ 0 & & & & \\ 0 & & M_1 & & \\ \ldots & & & & \end{array}\right) \quad \text{and} \quad \left(\begin{array}{c|cccc} \mathrm{i}\,\beta_2 & ic_2 & 0 & 0 & \ldots \\ \hline ic_2 & & & & \\ 0 & & & & \\ 0 & & M_2 & & \\ \ldots & & & & \end{array}\right) \tag{7.11}$$

where M_1 and M_2 are arbitrary $(N-1)\times(N-1)$ skew-Hermitian matrices and we have partitioned the above matrices in the obvious way. β_1, β_2, c_1 and c_2 are all real. The Lie product of these two matrices is:

$$\left(\begin{array}{c|c} 0 & -P_{21}^{\dagger} \\ \hline P_{21} & [M_1, M_2] \end{array}\right) \tag{7.12}$$

where

$$P_{21} = \begin{pmatrix} c_2\beta_1 - c_1\beta_2 \\ 0 \\ 0 \\ .... \end{pmatrix} + iM_1 \begin{pmatrix} c_2 \\ 0 \\ 0 \\ .... \end{pmatrix} - iM_2 \begin{pmatrix} c_1 \\ 0 \\ 0 \\ .... \end{pmatrix}$$

Using the fact that M_1 and M_2 are arbitrary $(N-1) \times (N-1)$ skew-Hermitian matrices, we can achieve an arbitrary $N \times N$ skew-Hermitian matrix if we subtract the partition $[M_1, M_2]$, add in its place M_3, an arbitrary $(N-1) \times (N-1)$ skew-Hermitian matrix, and finally add a matrix of the form:

$$\begin{pmatrix} i\beta_3 & ic_3 & 0 & 0 & ... \\ ic_3 & 0 & 0 & 0 & ... \\ 0 & 0 & 0 & 0 & ... \\ 0 & 0 & 0 & 0 & ... \\ ... & ... & ... & ... & ... \end{pmatrix}$$

for β_3 and c_3 real. The resulting matrix still belongs to the same Lie algebra, thus the induction step is proven. For $N = 1$, the result is trivially true, thus the mathematical induction is complete and therefore *the set of realisable matrices is the group* $\mathfrak{U}$ *of all* $N \times N$ *unitary matrices.*

7.3.2 Former Relevant Works

The previous investigations most relevant to the present problem were the studies of Lie-algebraic solutions of linear differential equations of the form of (6.2) made by Magnus, Wei and Norman[Magnus, 1954; Wei and Norman, 1963; Wei and Norman, 1964], where $h(z)$ belongs to some Lie algebra. However, these works were concerned with the local representation of solutions of (6.2) given a specification of $h(z)$, whereas we are concerned with the inverse problem of either *(i)* finding an $h(z)$ to realise a given design goal U, or proving that there is none and *(ii)* characterising the whole set of transfer matrices realisable with $h(z) \in \mathbf{h}_0$. Furthermore, the aforesaid works are only generally applicable to $U(z)$ belonging to some neighbourhood of the identity and we are concerned with the whole[8] set $\mathbf{H}$.

[8]The results of [Magnus, 1954; Wei and Norman, 1963; Wei and Norman, 1964] are sometimes globally applicable, *e.g.* when $h(z)$ belongs to a solvable Lie algebra[Varadarajan, 1974, §3.7].

7.4 Design with Mach-Zehnder Interferometer Cascades

The above discussions lead to specifications and bounds on which transfer matrices can be achieved subject to a given manufacturing constraint. However, they give no inkling as to how a given transfer matrix can be achieved and *exact* realisation of this matrix is not guaranteed, only realisation to within an arbitrary accuracy if one is willing to make the system arbitrarily long. In contrast, the design procedure of this Section is *guaranteed* to realise *any* possible $N \times N$ transfer matrix by a *finite* number of fundamental planar building-blocks fulfilling a simple condition. We outline the procedure and discuss it with reference to a simple 2×2 coupler example, where the problem can be fully visualised by rotations of the Poincaré sphere, before giving a full discussion. The procedure will then be used in the next Chapter to give full finite planar designs of the symmetric 3×3, 4×4 and 5×5 fibre couplers.

The procedure is grounded on the concatenation, as shown in Fig-7.1*(a)*, of fundamental building-block couplers C_j, whose single-moded waveguides are strongly coupled, interspaced by sets of single-moded uncoupled[9] governing optical delay lines δ_j. The basis fields here are the eigenfields of the individual single moded waveguides. Unlike the design procedure of §6.2, the present one makes absolutely no assumption as to the degree of coupling between the waveguides in region C. The coupler down- and up-tapers do not have to be adiabatic, provided there is low loss, so that, for the time being, all transfer matrices are assumed to belong to the group $\mathfrak{U}(N)$ of $N \times N$ unitary matrices. The phase delay imposed by each delay line is individually controllable by at least four methods, each of which changes each line's propagation constant:

- By delay-line width control through the photomask at manufacture, if production is repeatable (§8.3.5).

However, this does not apply to the present problem, as the Lie algebras $\mathfrak{u}(N)$ and $\mathfrak{su}(N)$ used in the following are not solvable. This follows immediately from the commutation relations[Normand, 1980, §4.5] for the Pauli matrices, which span $\mathfrak{su}(2)$.

[9] *i.e.* The transfer matrix of the delay-line set is diagonal and the lines do not interact.

- By ultraviolet light curing[Meltz and Morey, 1991], in germanosilicate technology;
- By a thinning down of the lines with laser trimming (§8.3.5).
- Electro-optically[Tamir, 1990], in lithium niobate technology.

The last three methods can be used to fine-tune the device, possibly under closed loop control based on in-circuit measurements, after basic manufacture. Such tuning principles are widely used for the production of precision integrated electronics[Analog-Devices, 1990]. If the delays are electro-optically controlled, it may even be possible to control the device's behaviour dynamically and use it as a cross-point switch or in adaptive signal processing schemes.

The delay lines must be long enough so that each pair can realise any relative phase between 0 and 2π (§8.3.5). Thus, each delay section δ_j can realise any diagonal unitary transfer matrix of the form $\exp(i\Lambda)$ and, in particular, if $\exp(i\Lambda)$ is realisable, so is $\exp(-i\Lambda)$.

The basic building blocks are concatenated (Fig-7.1 *(b)*) to achieve a system transfer matrix of the form:

$$\exp(i\Lambda_0)U_1\exp(i\Lambda_1)U_2\exp(i\Lambda_2)...U_p\exp(i\Lambda_p) \tag{7.13}$$

If the U_j fulfill the conditions discussed below, then *any* unitary transfer matrix is realisable by a concatenation of a *finite* number of building blocks of the form in Fig-7.1 *(b)*. Such conditions will be discussed below and shown to be both necessary and sufficient. Moreover, the minimum number of such sections needed to realise *any* unitary transfer matrix will be shown to be N, the number of waveguides, and conditions for the number of sections to be minimal will be discussed. Of course, a *particular* design goal may be realisable by fewer than N sections; the conditions to be discussed address a concatenation wherein the U_j are constant and it is required to realise any unitary transfer matrix merely by altering the phase-delays Λ_j.

The coupling regions can be designed almost by trial and error because numerical examples (§8.3) show the conditions of §7.6 to be almost always satisfied. *The detailed system tuning is done by varying the delay regions, thus the need for detailed and complicated design is completely removed from the strongly coupled region and,*

instead, the system transfer matrix is fully controlled by the easily adjusted phase delays.

7.5 2×2 Coupler: Visualisation by Poincaré Sphere

The above ideas can be illustrated with an example of a twin-section 2×2 coupler shown in Fig-7.2. The system comprises two coupling regions[10] C_1, C_2 and three phase delay regions and analysis is simplified if the phase delays in each section sum to zero; thus the top waveguide in the j^{th} section imposes a delay ω_j, the bottom guide $-\omega_j$. Note that the same arbitrary phase ω can be added to all the members of any delay section and the overall system's transfer matrix is merely scaled by $e^{i\omega}$, so that the stated zero-sum phase condition can always be achieved. This corresponds to the forgoing of absolute waveguide phase information and keeping only relative phases. Almost all practical optical systems must be designed so that absolute phase delays are unimportant and the system's behaviour depends only on relative phases, since the latter depend on slight differences between optical delay lines and are little affected by temperature drift if the delay lines are close together whereas the former are strongly temperature dependent.

7.5.1 Poincaré Sphere

If the system is lossless, the system transfer matrices all belong to the special unitary group $\mathfrak{SU}(2)$ of unimodular, unitary 2×2 matrices and the standard homomorphism[Normand, 1980, §4.2] between $\mathfrak{SU}(2)$ and the group of rigid rotations of a sphere $\mathfrak{SO}(3)$ allows the system's working to be visualised in terms of the rigid rotations of the Poincaré sphere. This is a well-used technique in the analysis of 2×2 couplers[Rowland and Love, 1993; Snyder *et al.*, 1991; Daino *et al.*, 1985; Matera and Wabnitz, 1986] as well as polarisation evolution in birefringent media[Born and Wolf, 1980, §1.4.2][Jauch and Rohrlich, 1976, §2.8].

[10]The subsystems of Fig-7.2 are numbered right to left so that, with the device input at the left hand side of Fig-7.2, terms in transfer matrix products can be numbered left to right for convenience.

A simple calculation shows that the system transfer matrix can be written:

$$e^{i\omega_0\sigma_3}U_1e^{i\omega_1\sigma_3}U_2e^{i\omega_2\sigma_3} = U(\omega_0,\omega_1,\omega_2)U_1U_2; \text{ where } U(\omega_0,\omega_1,\omega_2) = \prod_{k=0}^{2} e^{-i\omega_k X_k};$$

$$X_0 = -\sigma_3; \quad X_1 = -U_1\sigma_3U_1^\dagger; \quad X_2 = -U_1U_2\sigma_3U_2^\dagger U_1^\dagger \tag{7.14}$$

where σ_3 is the third Pauli spin matrix[Normand, 1980]:

$$\sigma_0 = I = \begin{pmatrix} 1 & 0 \\ 0 & 1 \end{pmatrix}, \quad \sigma_1 = \begin{pmatrix} 0 & 1 \\ 1 & 0 \end{pmatrix}, \quad \sigma_2 = \begin{pmatrix} 0 & -i \\ i & 0 \end{pmatrix}, \quad \sigma_3 = \begin{pmatrix} 1 & 0 \\ 0 & -1 \end{pmatrix} \tag{7.15}$$

Because the unitary matrix U_1U_2 is invertible, we can study, without loss of information, the set of unitary matrices realisable by the product $U(\omega_0,\omega_1,\omega_2)$ defined in (7.14).

We consider now the transformation that $U(\omega_0,\omega_1,\omega_2)$ induces on the vector $\mathbf{a} = (a_1, a_2) = U_1U_2\tilde{\mathbf{a}}$ where $\tilde{\mathbf{a}}$ is the vector of complex amplitudes of fields on the input waveguides. $\mathbf{a}$ can be defined[Jauch and Rohrlich, 1976, §2.8], via the Pauli spin matrices, in terms of its *Stokes parameters* S_j:

$$S_j = \mathbf{a}^\dagger\sigma_j\mathbf{a} \tag{7.16}$$

whence:

$$\begin{aligned} S_0 &= |a_1|^2 + |a_2|^2 \\ S_1 &= a_1^*a_2 + a_2^*a_1 = 2|a_1||a_2|\cos(\phi_{21}) \\ S_2 &= i(-a_1^*a_2 + a_2^*a_1) = 2|a_1||a_2|\sin(\phi_{21}) \\ S_3 &= |a_1|^2 - |a_2|^2 \end{aligned}$$

where ϕ_{21} is the phase of a_2 relative to that of a_1. Note that this definition of the Stokes parameters is slightly different to that usually given in optics[Born and Wolf, 1980, §1.4]; an unimportant sign change and renumbering has been introduced here. The matrix $U(\omega_0,\omega_1,\omega_2)$ effects a transformation on $\mathbf{a} \rightarrow \mathbf{a}' = U(\omega_0,\omega_1,\omega_2)\mathbf{a}$ and, since $S_1^2 + S_2^2 + S_3^2 = S_0^2$ if the coupler is lossless, S_0 is invariant and the head of the *Stokes vector* $\mathbf{s} = (S_1, S_2, S_3)$ characterising the transformed $\mathbf{a}'$ must follow a path on the surface of the Poincaré sphere $|\mathbf{s}| = const$ as the ϕ_j vary. In fact, (Appendix-7.8), under the action of U, the Poincaré sphere undergoes a rotation whose angle

and rotation axis are found by expressing U in terms of the Pauli spin matrices as follows:

$$U = \exp\left(-\sum_{j=1}^{3}\alpha_j\sigma_j\right) = \exp\left(-\frac{\theta}{2}\sum_{j=1}^{3}\gamma_j\sigma_j\right); \quad \text{where} \quad \sum_{j=1}^{3}\gamma_j^2 = 1 \tag{7.17}$$

The α_j, γ_j and θ are all real and the rotation is through angle θ about an axis with direction cosines $\gamma_1, \gamma_2, \gamma_3$ with respect to the S_1, S_2 and S_3 axes respectively.

The coupler's action can now be visualised (Fig-7.4) on the Poincaré sphere as a composition of rotations about the axes corresponding to the X_j in (7.14).

7.5.2 Subsystem Analysis by BPM

Fig-7.3 defines the dimensions of the building-block couplers, whose waveguides follow cosinusoidal paths, where z in Fig-7.3 is measured from each coupler's input. For simplicity, slab waveguides are used with a cladding refractive index of 1.5, a core refractive index of 1.50185 and a system working wavelength of 1500nm and these conditions ensure single modedness of all the waveguides. The mask of Fig-7.3 was chosen simply because: *(i)* the waveguide trajectories are readily specified in a BPM analysis and (*ii*) the strong coupling between the two waveguides' fields takes place. Aside from these requirements, the choice was almost arbitrary, the aim of the design procedure being to transfer the control of the overall system's behaviour wholly to the interspacing optical delays between the basic building blocks.

C_1 was analysed by the Beam Propagation Method. The transverse grid comprised 16384 points of 8nm spacing arranged so that the midpoint between the two coupled guides' inner edges was at the grid's centre. 5μm thick loss regions of loss tangent 0.005 were used at both edges of the grid and the simulation's axial step-size was 1μm. With these parameters and the 8μm and 10μm thick waveguides numbered 1 and 2, respectively, the forward transfer matrix of C_1 is found to be:

$$U_{1o} = \begin{pmatrix} 0.850696 + 0.205552i & -0.479480 + 0.007793i \\ -0.479482 + 0.007730i & -0.843612 + 0.232451i \end{pmatrix} \tag{7.18}$$

Here the notation "o" in the subscript stands for "observed", *i.e.* the values as found by the BPM. In the following, radiation loss is neglected and all transfer matrices are taken to be unitary. Hence, a nearest unitary matrix U_1 is derived from U_{1o} and

used in all the following calculations by *(i)* taking a matrix logarithm to find h_{1o} where $U_{1o} = \exp(h_{1o})$ and h_{1o} is almost skew Hermitian then *(ii)* finding the nearest skew-Hermitian matrix by averaging h_{1o} and its negative Hermitian conjugate to give $h_1 = (h_{1o} - h_{1o}^\dagger)/2$ then *(iii)* taking the nearest unitary matrix to be $U_1 = \exp(h_1)$:

$$U_1 = \begin{pmatrix} 0.852446 + 0.205914i & -0.480495 + 0.007701i \\ -0.480496 + 0.007638i & -0.845439 + 0.233016i \end{pmatrix} \tag{7.19}$$

The minimum singular value[11] of U_{1o} is 0.9977, thus the maximum excess loss imposed by coupler C_1 is 0.02dB and the use of the unitary matrix U_1 instead of U_{1o} is justified.

Coupler C_2 can be regarded as C_1 with the two waveguides' roles swapped, therefore:

$$U_2 = \begin{pmatrix} -0.845439 + 0.233016i & -0.480496 + 0.007638i \\ -0.480495 + 0.007701i & 0.852446 + 0.205914i \end{pmatrix} \tag{7.20}$$

(7.19) and (7.20) show the matrices X_j in (7.14) to be:

$$\begin{aligned} X_1 &= 0.816049\sigma_1 - 0.210904\sigma_2 - 0.538130\sigma_3 \\ X_2 &= 0.721048\sigma_1 - 0.608260\sigma_2 + 0.331826\sigma_3 \end{aligned} \tag{7.21}$$

The axes X_1 and X_2 are shown in Fig-7.4*(a)* and pierce the sphere at points p_1 and p_2, respectively.

7.5.3 Reachable Transfer Matrices

It is now a simple matter to visualise the set of all transfer matrices realisable by the concatenation of Fig-7.2. From (7.14) and (7.21), the coupler's action can be expressed as a rotation through an angle ω_2 about axis X_2 in Fig-7.4*(a)*, followed by a rotation through ω_1 about axis X_1 followed by a rotation through ω_0 about the S_3 axis. X_1, X_2 and the S_3 axis are linearly independent and this fact guarantees that a *finite* concatenation of systems in Fig-7.2*(a)* can realise *any* unitary 2×2 transfer matrix as will be discussed in §7.6.

[11]The singular values of U are the square-roots of the (real) eigenvalues of $U^\dagger U$. Physically, the maximum and minimum singular values correspond to the maximum and minimum possible Euclidean length of Ux when $|x| = 1$ and thus to the minimum and maximum excess loss incurred by a device with transfer matrix U.

However, it is simple to show that there are some Poincaré sphere rotations that *cannot* be represented as a $U(\omega_0, \omega_1, \omega_2)$ (defined in (7.14)) and this fact proves that, in general, more than two coupler sections are needed to realise some transfer matrices. Note that a rotation of the sphere is uniquely defined by any point not on the rotation axis together with its image under the rotation and that there corresponds a rotation for every pair of points defining initial point and image. Hence, if we take a point on the sphere and can find another point that the former cannot be mapped into by coupler's action, then the result is proven. Consider some point p_3 and the set Ω of its images under rotations about X_2 in Fig-7.4*(a)*. Suppose further that p_3 is close enough to X_2 that Ω is not threaded by the S_3 axis. The images of Ω under a rotation about X_1 is the hoop-shaped region in Fig-7.4*(b)*. Whence, a final rotation about S_3 can reach all points in the shaded region of Fig-7.4*(c)*. It is clear that the points in the cap-shaped unshaded region are unreachable and that the whole sphere would be reachable if and only if a great circle coplanar with the S_3-axis were contained within the hoop-shaped region in Fig-7.4*(b)*.

A composition of three rotations about three linearly independent axes can represent all given Poincaré sphere rotations if and only if the three rotation axes are orthogonal. Orthogonal axes are well-known[Normand, 1980, §4.2.4] to make all rotations realisable as a $U(\omega_0, \omega_1, \omega_2)$; conversely, if the initial point in Fig-7.4 is p_2, then the hoop-shaped region is a circle and it would be a great circle coplanar with S_3 only if X_1, X_2 and S_3 were orthogonal.

This criterion can be restated in terms of the corresponding matrices in the Lie algebra $\mathfrak{su}(2)$: suppose that $U(\omega_0, \omega_1, \omega_2) = \exp(i\omega_0\sigma_3)\exp(i\omega_1 Y_1)\exp(i\omega_2 Y_2)$; then all rotations are realisable as the stated three-term composition about the axes corresponding to Y_1, Y_2 and $Y_3 = \sigma_3$ if and only if the matrices iY_j are linearly independent and orthogonal with respect to the inner product $< a, b >= tr(\Delta_a^\dagger \Delta_b)$:

$$tr(\Delta_{iY_j}^\dagger \Delta_{iY_k}) \begin{cases} = 0 & \text{for } j \neq k; \\ \neq 0 & \text{for } j = k; \end{cases} \tag{7.22}$$

Here Δ_x is the *adjoint* matrix to x (Appendix-7.8). If the rotation axes are orthogonal, the three angles ω_j are then the familiar mechanical *Euler angles* of precession, nutation and proper rotation.

7.6 General $N \times N$ Coupler Case

7.6.1 Reachability of the Whole of $\mathfrak{U}(N)$

We can now address the general $N \times N$ case of Fig-7.1 *(a) & (b)*. The following is a generalisation of the construction, as in §7.2.3, of a Lie group from a neighbourhood of its identity.

As in (7.14), the transfer matrix in (7.13) can be written:

$$\exp(i\Lambda_0)\exp\left(iU_1\Lambda_1U_1^{-1}\right)\exp\left(iU_1U_2\Lambda_2U_2^{-1}U_1^{-1}\right)\exp\left(iU_1U_2U_3\Lambda_3U_3^{-1}U_2^{-1}U_1^{-1}\right)...$$
$$\exp\left(iU_1...U_p\Lambda_pU_p^{-1}...U_1^{-1}\right)U_1U_2...U_p \tag{7.23}$$

Each diagonal element of each Λ_j can be individually varied. Let $D_j = \text{diag}[0,0,...,1,...,0]$ be an $N \times N$ matrix with zeros everywhere except at position (j,j), where there is a 1, *e.g.* for $N = 3$:

$$D_1 = \begin{pmatrix} 1 & 0 & 0 \\ 0 & 0 & 0 \\ 0 & 0 & 0 \end{pmatrix};\ D_2 = \begin{pmatrix} 0 & 0 & 0 \\ 0 & 1 & 0 \\ 0 & 0 & 0 \end{pmatrix};\ D_3 = \begin{pmatrix} 0 & 0 & 0 \\ 0 & 0 & 0 \\ 0 & 0 & 1 \end{pmatrix} \tag{7.24}$$

Hence, the second term of (7.23) can realise the exponential of any of the matrices $iU_1D_jU_1^{-1}$ for $j = 1,...,N$ or any linear combination thereof, the third term can realise the exponential of any linear combination of matrices of the form $iU_1U_2D_jU_2^{-1}U_1^{-1}$ and so on.

Hereafter, suppose that the matrices:

$$\begin{array}{l} iD_j;\ \ j = 1...N \\ iU_1D_jU_1^{\dagger};\ \ j = 1...N \\ iU_1U_2D_jU_2^{\dagger}U_1^{\dagger};\ \ j = 1...N \\ ... \\ iU_1U_2...U_ND_jU_N^{\dagger}...U_2^{\dagger}U_1^{\dagger};\ \ j = 1...N \end{array} \tag{7.25}$$

in (7.23) span the N^2 dimensional Lie algebra u(N) of $N \times N$ skew-Hermitian matrices; numerical simulations show this condition to be readily arranged. At least N basic building blocks are needed to achieve this since the set $\{D_j\}$ gives N linearly independent matrices but the set $\{iU_1D_jU_1^{-1}\}$ and all those following in

(7.25) can only give at most a further $N-1$ linearly independent matrices[12], leaving the required number p of building blocks fulfilling $N + p(N-1) \geq N^2$ or $p \geq N$.

The N building blocks realise the set of matrices:

$$\exp(\mathbf{g_0})\exp(\mathbf{g_1})\exp(\mathbf{g_2})...\exp(\mathbf{g_N})U_1U_2...U_N \tag{7.26}$$

where the vector spaces $\mathbf{g}_j$ are given by:

$$\begin{aligned}\mathbf{g}_j &= \left\{ iU_1...U_j \left(\sum_k x_{jk} D_k \right) U_j^{-1}...U_1^{-1} \;\middle|\; x_{jk} \text{ real} \right\} \\ \mathbf{g}_0 &= \left\{ \sum_k x_{0,k} D_k \;\middle|\; x_{0,k} \text{ real} \right\}\end{aligned} \tag{7.27}$$

$\exp(\mathbf{g}_j)$ is an Abelian Lie group, since all its members have the same matrix of eigenvectors $U_1...U_j$. Therefore, *every* member of this group can be represented as a product of the form $\prod \exp(X_k \omega_k)$, where $\{X_k\}$ is *any* basis of $\mathbf{g}_j$ and, since all the vector spaces $\mathbf{g}_j$ direct-sum to give the whole set of skew-Hermitian matrices, the $(N+1)N$ parameters x_{jk} contain N^2 canonical co-ordinates of the second kind. Therefore, the N coupler sections can realise *any* transfer matrix within a suitably small neighbourhood $\mathcal{B}_\epsilon \mathcal{U}_N$ of $\mathcal{U}_N = U_1U_2...U_N$ with the right choice of x_{jk}. Here $\mathcal{B}_\epsilon$ is an open ball[13] centred on the identity:

$$\mathcal{B}_\epsilon = \{x \mid x \in \mathfrak{U}(N);\;\; \|x - I\| < \epsilon\} \tag{7.28}$$

for some $\epsilon > 0$. If the design goal is not within this set, it may not be realisable by the N-section coupler, as is the case for the unreachable rotations in the 2×2 coupler example of §7.5. When this happens, a further N section coupler is appended to the first. The set realisable by this $2N$-section coupler is:

$$\mathcal{B}_\epsilon \mathcal{U}_N \mathcal{B}_\epsilon \mathcal{U}_N^{-1} \mathcal{U}_N^2$$

[12]Any constant phase delay ϕ can be subtracted from each of the first section's delay lines (corresponding to subtracting ϕ times the identity matrix from Λ_1) and added to each of those of the first section (corresponding to adding ϕI to Λ_0), leaving the product $\exp(i\Lambda_0)\exp\left(iU_1\Lambda_1U_1^{-1}\right)$ unchanged. Hence, any one leading diagonal element of Λ_1 can be arbitrarily set to zero; likewise for $\Lambda_2, ...$

[13]Here $\|x\|$ can be *e.g.* the spectral norm, equal to the maximum singular value of x, or the trace norm $\sqrt{tr(x^\dagger x)}$.

and[14] $\mathcal{B}_\epsilon = \mathcal{U}_N \mathcal{B}_\epsilon \mathcal{U}_N^{-1}$, *i.e.* any transfer matrix within the set $\mathcal{B}_\epsilon^2 \mathcal{U}_N^2$ is realisable. After M repetitions of this process, the set $\mathcal{B}_\epsilon^M \mathcal{U}_N^M$ is realisable. Since *all* members of $\mathfrak{U}(N)$ are expressible in form $\exp(h)$, where $\|h\| \leq N\pi$ (*resp.* $\|h\| \leq \pi$) for the trace (*resp.* spectral) norm, it suffices[15] that $M > N\pi/\log(1+\epsilon)$ (*resp.* $M > \pi/\log(1+\epsilon)$) for the set $\mathcal{B}_\epsilon^M$ to comprise the whole of $\mathfrak{U}(N)$ in the case of the trace (*resp.* spectral) norm, *i.e.*:

Every unitary transfer matrix is realisable by a finite concatenation of the basic building blocks in Fig-7.1(b).

7.6.2 Lossy Systems

The above discussion is readily extended to lossy waveguides and where the system transfer matrices arise from compact Lie groups other than $\mathfrak{U}(N)$. Suppose that the matrices of (7.23) span a Lie algebra $\mathfrak{g}$; then the above reasoning guarantees that a finite concatenation of the form in Fig-7.1*(b)* can realise any transfer matrix in the smallest Lie group $\mathfrak{G}$ with $\mathfrak{g}$ as its Lie algebra, provided that $\|g_1 - g_2\|$ is bounded for all $g_1, g_2 \in \mathfrak{G}$.

7.6.3 Number of Sections Required and Phase-Delay Determination

In the simple numerical example of the 2×2 coupler in §7.5, ω_0, ω_1 and ω_2 in (7.14) indeed form canonical co-ordinates of the second kind, since the matrices $i\sigma_3$, iX_1 and iX_2 are linearly independent and therefore span the Lie algebra $\mathfrak{su}(2)$ of $\mathfrak{SU}(2)$, however we showed that the three-term product of transformations in (7.14) fail to realise some rotations of the Poincaré sphere. Hence, in general, more than N basic sections will be needed to realise any unitary transfer matrix, even though N sections provide enough (N^2) degrees of freedom. The exact number of sections

[14] $\|\mathcal{U}_N u \mathcal{U}_N^{-1} - I\| = \|\mathcal{U}_N(u-I)\mathcal{U}_N^{-1}\| = \|u - I\|$, since $\mathcal{U}_N, \mathcal{U}_N^{-1}$ are isometries with respect to the spectral and trace norms. Hence, $u \in \mathcal{B}_\epsilon$ iff $u \in \mathcal{U}_N \mathcal{B}_\epsilon \mathcal{U}_N^{-1}$.

[15] If $u = \exp(h) \in \mathfrak{U}(N)$, then $u = \exp(h/M)^M$. Now $\|\exp(h/M) - I\| \leq \|h/M\| + \|(h/M)^2/2!\| + \ldots = \exp(\|h\|/M) - 1$.

needed to realise a given goal U_{goal} depends on ϵ, which, in turn, depends on the Lie algebra basis contained in the $X_{jk} = iU_1...U_jD_kU_j^{-1}...U_1$, or, equivalently, the choice of the basic building-block couplers and their cascading order. In special cases the minimum number N of basic sections suffices to realise all unitary matrices and necessary and sufficient conditions were given in §7.5 for this optimal situation to arise in the case of the 2×2 coupler.

It seems reasonable to conjecture that the same conditions would apply to the $N \times N$ lossless coupler case, i.e. that all unitary matrices are realisable by an N-section $N \times N$ coupler of the form in Fig-7.1(b) if and only if the adjoint operators of the linearly independent matrices in (7.23) fulfill (7.22).

The following brief description shows how the ω_j to realise a given transfer matrix U_{goal} and, in principle, ϵ can be found. Let $X_j, j = 1...N^2$ be N^2 linearly independent matrices from (7.25) and α_j be defined from U_j by $\exp(\sum_j \alpha_j X_j) = U_{goal}(U_1U_2...U_N)^{-1}$. If U_{goal} is to be realisable in N sections, then one must find ω_j such that $\prod_j \exp(\omega_j X_j) = \exp(\sum_k \alpha_k X_k)$. Now, consider a path defined by $\exp(t \sum_j \alpha_j X_j)$ leading from the identity matrix, at $t = 0$, to $\exp(\sum_j \alpha_j X_j)$ at $t = 1$. One must then find $\omega_j(t)$ such that $\prod_j \exp(\omega_j(t) X_j) = \exp(t \sum_k \alpha_k X_k)$, and the techniques of [Wei and Norman, 1963] then reduce this to the problem of solving the differential equation:

$$t \begin{pmatrix} \alpha_1 \\ \alpha_2 \\ ... \\ \alpha_N \end{pmatrix} = (\xi_{j,k}(\omega_1, ..., \omega_N)) \frac{d}{dt} \begin{pmatrix} \omega_1 \\ \omega_2 \\ ... \\ \omega_N \end{pmatrix} \tag{7.29}$$

where the $\xi_{j,k}$ are nonlinear functions of the ω_j and the matrix $(\xi_{j,k})$ is the identity at $t = 0$. (7.29) can be integrated so long as the determinant of $(\xi_{j,k})$ is nonzero, which must hold for $t < \delta$ for some $\delta > 0$, since the determinant is an analytic function of t and equal to 1 at $t = 0$. Indeed, this assertion proves[Wei and Norman, 1963] the existence of the canonical co-ordinate system of the second kind.

Thus we see that, to estimate ϵ in §7.6, one could, in theory, derive the $\xi_{j,k}$ as in [Wei and Norman, 1963] for a given X_j and calculate an upper bound on the α_j for which integration of (7.29) is possible for $0 \leq t \leq 1$. In practice, this would be an

intractable problem except in trivial cases. However, the numerical integration of (7.29) is possible and can be used to find the required phase delays, *i.e.* the $\omega_j(1)$. If the determinant of $(\xi_{j,k})$ vanishes during this integration, the procedure fails and the design goal specified by the α_j may require more than N sections to realise. In this thesis (§8.3.4) a randomly-initialised conjugate-gradient method search, rather than integration of (7.29), is used to find the phase delays ω_j.

7.7 Conclusions

This Chapter has presented the minimum Lie group theory relevant to the design of coupled optical waveguides by defining Lie-theoretic concepts in terms of the set of realisable transfer matrices of a coupled waveguide system. This theory allows one to readily characterise the set of transfer matrices that are realisable under a given manufacturing constraint. The Chapter outlined a design procedure for the realisation of unitary transfer matrices based on the concatenation of generalised Mach-Zehnder interferometers. It was shown that the procedure is *guaranteed* to yield an *exact* realisation of any unitary design goal in a *finite number* of Mach-Zehnder sections. The minimum number of sections needed to realise *any* design goal by the method is N, the number of waveguides.

This procedure was applied in detail to a 2×2 coupler example and necessary and sufficient conditions for the number of sections to be minimal were derived. The procedure applied to the lossless $N \times N$ coupler is equivalent to the representation of rigid rotations of an $N^2 - 1$-dimensional Poincaré sphere as a composition of basic rotations about fixed axes. A general condition for the number of coupler sections needed to be minimal has been postulated, but not yet proven.

The procedure based on Mach-Zehnder interferometer concatenation will be further illustrated in the next Chapter when it will be used to provide planar realisations of the symmetric 3×3, 4×4 and 5×5 fibre couplers.

7.8 Appendix: Poincaré Sphere Rotations

We consider the transformation that a unitary transfer matrix U induces on the Poincaré sphere and show it to be a rigid rotation. This is a standard result but the following rederivation yields the simple expressions used in this Chapter for the rotation angles and axes. We note first that it is not immediately obvious that the transformation of the Poincaré sphere is a rotation; it could be some nonlinear deformation of the surface of the sphere onto itself.

U belongs to $\mathfrak{SU}(2)$, the matrices $i\sigma_1, i\sigma_2, i\sigma_3$ form a basis for $\mathfrak{su}(2)$ and U can be written as $U = \exp(-i\sum \alpha_j\sigma_j)$, where the α_j are real. It is convenient to rewrite U as $\exp(-i\theta\sum \gamma_j\sigma_j/2)$, where θ and the γ_j are real and $\sum\gamma_j^2 = 1$. If a 2×2 coupler input is $\mathbf{a}$, then, after transformation by U, its Stokes parameters become, by (7.16):

$$s_k = \mathbf{a}^\dagger U^\dagger \sigma_k U\mathbf{a} = \mathbf{a}^\dagger U^{-1}\sigma_k U\mathbf{a} = -i\mathbf{a}^\dagger \exp\left(i\frac{\theta}{2}\sum_j \gamma_j\sigma_j\right) i\sigma_k \exp\left(-i\frac{\theta}{2}\sum_j \gamma_j\sigma_j\right)\mathbf{a} \tag{7.30}$$

To analyse this transformation, we consider mappings of the form $y \rightarrow e^x y e^{-x}$, where x and y belong to some Lie algebra. The appropriate formula is:

$$e^x y e^{-x} = y + [x,y] + \frac{[x,[x,y]]}{2!} + \frac{[x,[x,[x,y]]]}{3!} + \ldots \tag{7.31}$$

which is derived by direct computation from the exponential series and shown to be convergent for *any* $N\times N$ matrices x and y. It states that, if x and y belong to a Lie algebra, the image of y under $y \rightarrow e^x y e^{-x}$, is still within this same[16] Lie algebra. Consider the two mappings of this Lie algebra induced by x: $y \rightarrow [x,y]$ and $y \rightarrow e^x y e^{-x}$. They are mappings of the Lie algebra onto itself and moreover are linear in y. Hence, if (as in our case) the Lie algebra is finite dimensional, its members can be expressed as components with respect to some basis $\{X_j\}$: $y = (y_1, y_2, \ldots, y_N) = \sum y_j X_j$ and the linear mappings can be fully defined by matrices with respect to this basis. If the matrix of the first mapping is written Δ_x, it immediately follows from (7.31) that the matrix of the second mapping is $\exp(\Delta_x)$. With y expressed as a vector of components, we write $y \rightarrow \Delta_x y$ and $y \rightarrow \exp(\Delta_x)y$ for the two mappings. The operator Δ_x is known as the adjoint matrix to x.

[16] It is this result that plays a crucial role in the derivation of (7.29).

It follows from (7.30) that, under the action of U, the Stokes parameters undergo the *linear* transformation:

$$\mathrm{s} \rightarrow \exp\left(\frac{\theta}{2}\sum_j \gamma_j \Delta_{i\sigma_j}\right)\mathrm{s}, \quad \text{where} \quad \mathrm{s} = \begin{pmatrix} s_1 \\ s_2 \\ s_3 \end{pmatrix} \tag{7.32}$$

which is unexpected since the Stokes parameters are quadratic forms in the vector $\mathbf{a}$, which itself undergoes a linear transformation. Using the basis $\{i\sigma_1, i\sigma_2, i\sigma_3\}$ and[17]:

$$[i\sigma_j, i\sigma_k] = -2i\sum_{r=1}^{3} \epsilon_{j,k,r}\sigma_r \tag{7.33}$$

one gets:

$$\Delta_{i\sigma_1} = 2\begin{pmatrix} 0 & 0 & 0 \\ 0 & 0 & 1 \\ 0 & -1 & 0 \end{pmatrix} \quad \Delta_{i\sigma_2} = 2\begin{pmatrix} 0 & 0 & -1 \\ 0 & 0 & 0 \\ 1 & 0 & 0 \end{pmatrix} \quad \Delta_{i\sigma_3} = 2\begin{pmatrix} 0 & 1 & 0 \\ -1 & 0 & 0 \\ 0 & 0 & 0 \end{pmatrix} \tag{7.34}$$

whence:

$$\mathrm{s} \rightarrow R(\theta;\gamma_1,\gamma_2,\gamma_3)\mathrm{s}, \quad \text{where} \quad R(\theta;\gamma_1,\gamma_2,\gamma_3) = \exp\left[\theta\begin{pmatrix} 0 & \gamma_3 & -\gamma_2 \\ -\gamma_3 & 0 & \gamma_1 \\ \gamma_2 & -\gamma_1 & 0 \end{pmatrix}\right] \tag{7.35}$$

The exponent in the expression for R is real and skew-Hermitian, therefore R is a rigid rotation of the Poincaré sphere. Moreover, R leaves the vector $(\gamma_1, \gamma_2, \gamma_3)$ invariant, which is therefore a unit vector along the axis of rotation, expressed with respect to the S_1, S_2, S_3 axes. The angle of rotation is θ. For every U there is a unique R, conversely for every Poincaré sphere rotation, there is a pair of transfer matrices of the form $\pm U$. Thus, a 2×2 coupler's action is fully defined (modulo an inconsequential phase delay $\exp(i\omega)$) by the rigid rotation it effects on the Poincaré sphere.

We note in passing that the association of a Poincaré sphere rotation to a coupler's forward transfer matrix constitutes precisely the standard homomorphism between the groups $\mathfrak{SU}(2)$ of unimodular unitary transformations and $\mathfrak{SO}(3)$ of 3-dimensional rigid rotations, more generally[Normand, 1980, §§4.2.1, 5.4.2] between

[17] $\epsilon_{j,k,r}$, the standard permutation symbol, is zero if any of j, k and r are equal, $\epsilon_{j,k,r} = 1$ (*resp.* $\epsilon_{j,k,r} = -1$) if (j,k,r) is an even (*resp.* odd) permutation of $(1,2,3)$.

$\mathfrak{SU}(N)$ and $\mathfrak{SO}(N^2-1)$. The action of a lossless $N \times N$ coupler can therefore be fully defined, to within a phase delay, by a rigid rotation of an N^2-1-dimensional Poincaré sphere.

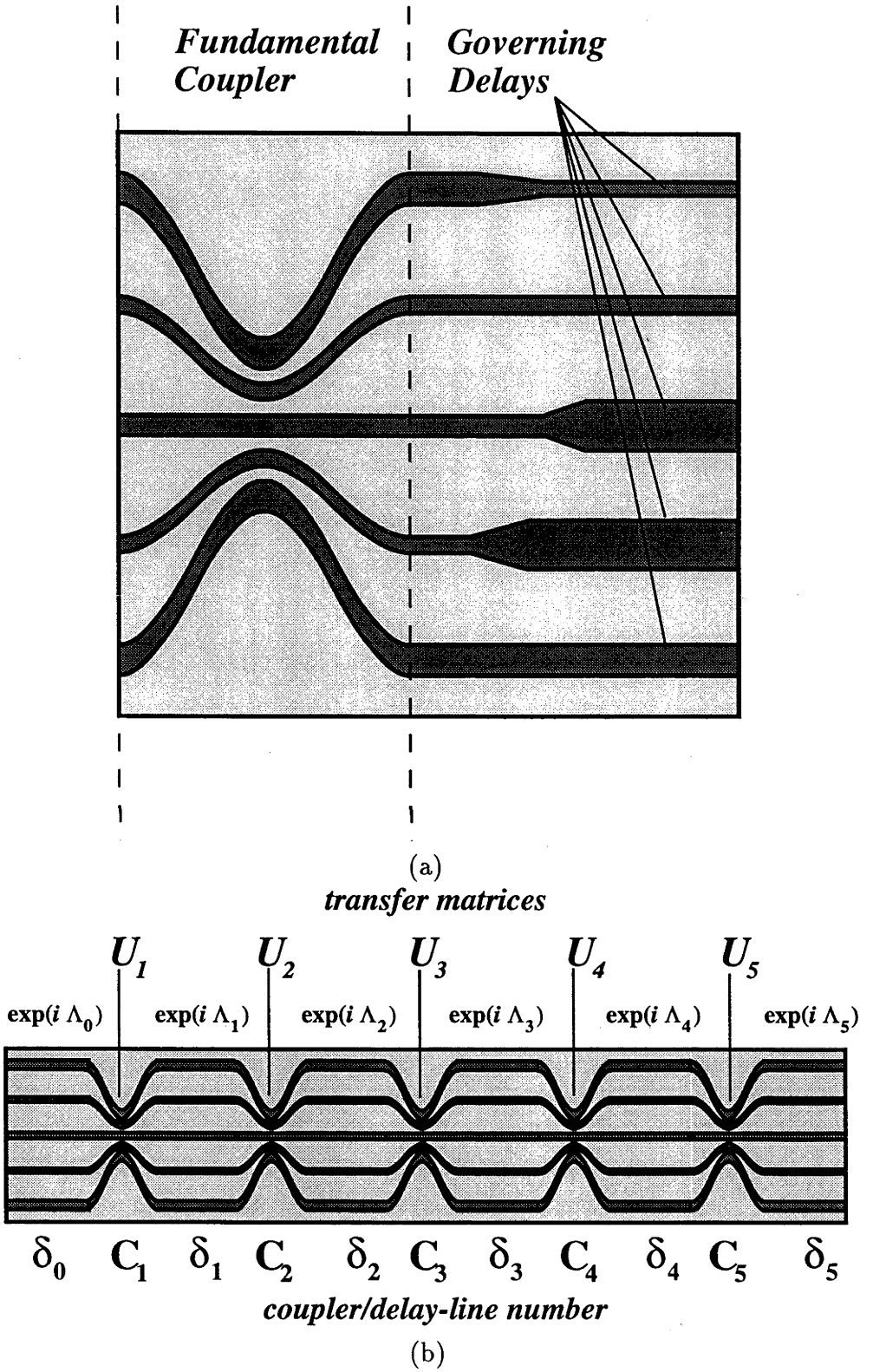

Figure 7.1: *(a)* Basic building-block coupler and *(b)* building block concatenation for the realisation of arbitrary unitary transfer matrices

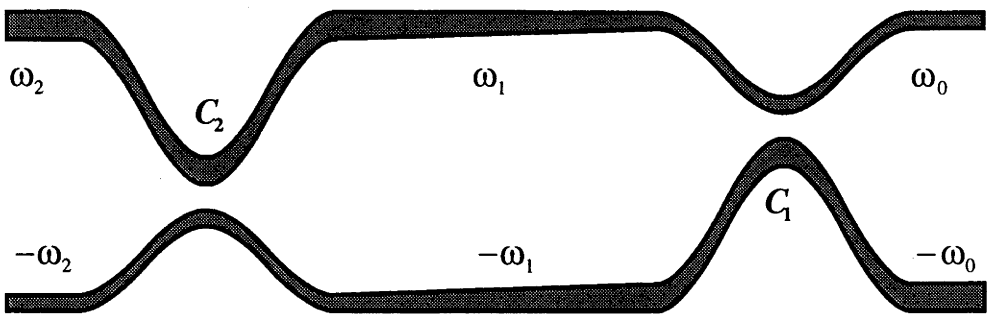

Figure 7.2: Mach-Zehnder Interferometer as Adjustable 2 × 2 Coupler

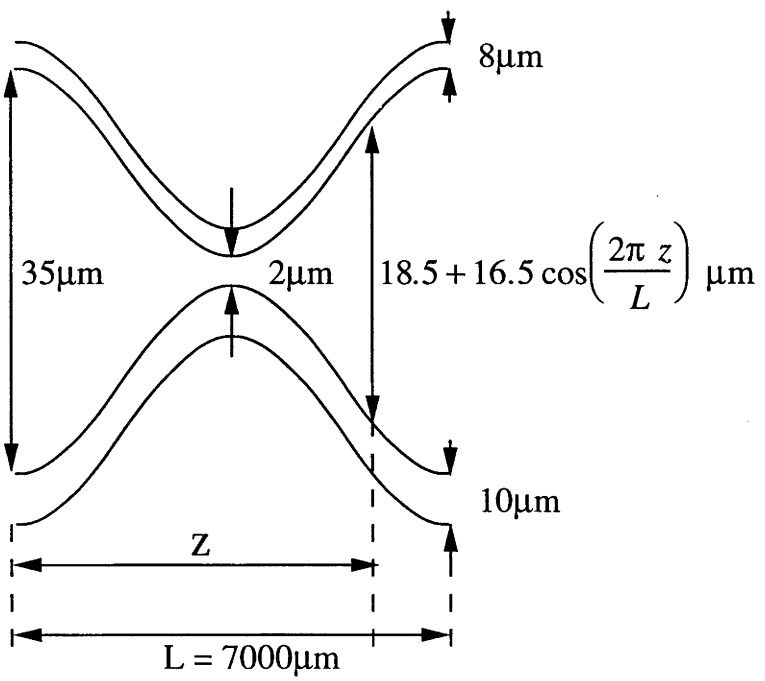

Figure 7.3: Building-Block Coupler Dimensions

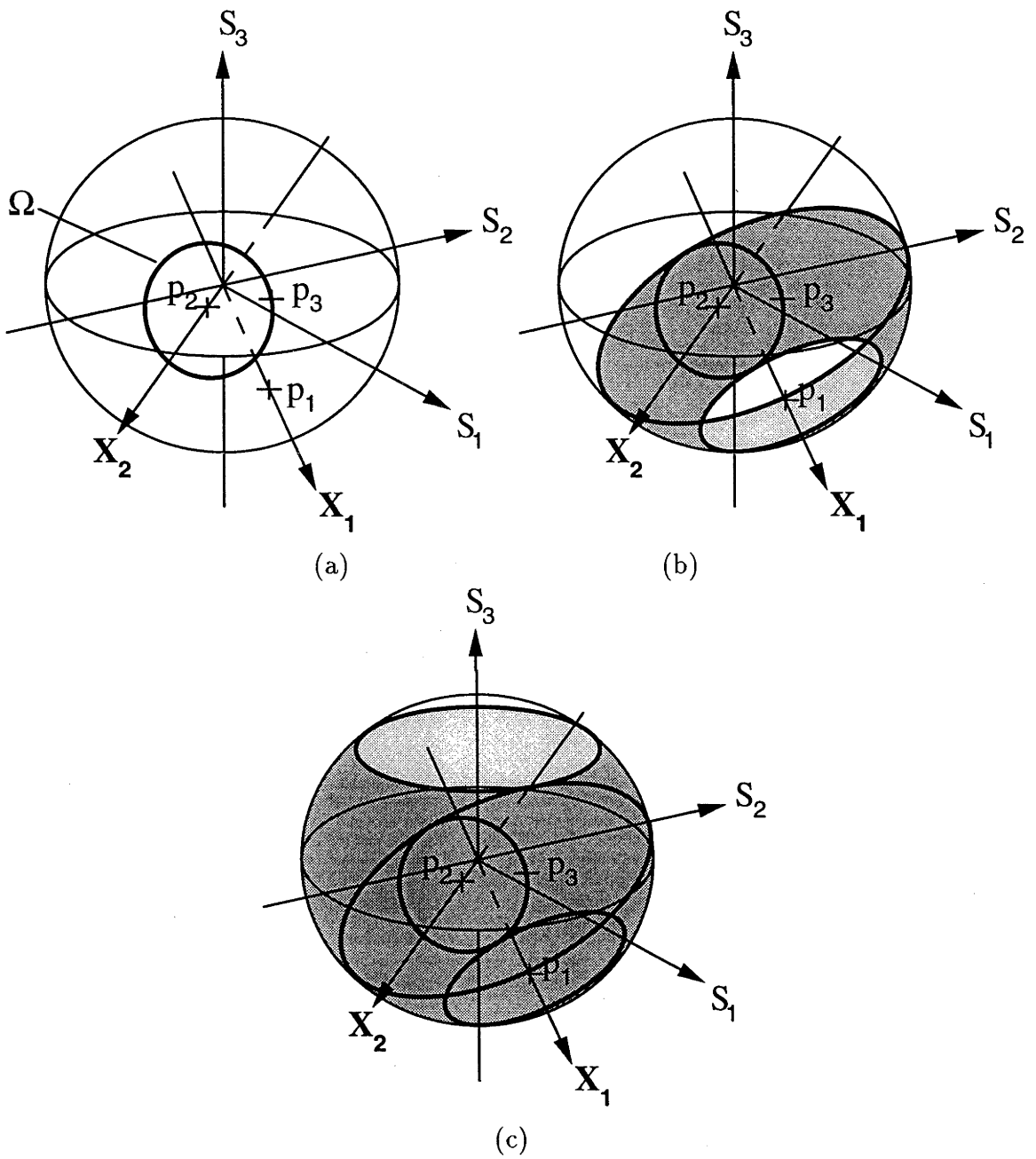

Figure 7.4: Coupler-induced Rotations of the Poincaré Sphere

Chapter 8

Applications of Planar Design Techniques

8.1 Symmetric Fibre Couplers

Symmetric fibre couplers are useful in implementing phase- and polarisation-fading resistant interferometric schemes such as the Sheem interferometer in Chapter-6 and the schemes in [Travis and Carroll, 1989; Travis and Carroll, 1990].

The original 5×5 coupler polarisation diversity scheme[Travis and Carroll, 1989; Travis and Carroll, 1990] was for a polarisation and phase-fading-immune signal demodulation in coherent optical communications systems. Interest in such coherent systems has since waned[Cochrane and Heatly, 1992]; however, the coherent demodulation principles are exactly the same as those in interferometric optical sensing and therefore this scheme is directly applicable to sensing systems.

The designs proposed here can be classified as either *(i)* devices based on the concatenation of generalised planar Mach-Zehnder interferometers as discussed in the last Chapter and applied in §8.3 or *(ii)* devices imposing the fibre coupler's cyclic N-fold symmetry on the geometric structure of a planar device, as in §8.5. The robustness of all designs to temperature drift and source frequency drift is appraised in §8.6, where we find that the Mach-Zehnder interferometer-based schemes are more likely to be practical than the more intuitively understood cyclically-symmetric ones since the former are more resilient to temperature drift and source laser frequency jitter owing to *differential device behaviour.*

8.2 Design Goals

8.2.1 Coherent Detection Schemes

Coherent detection schemes can be thought of as the splitting of a reference beam into N copies, one appearing at each of N system outputs[Travis and Carroll, 1989]. Likewise, the incoming signal beam is split into N copies, one at each output, and the reference-signal copy pairs then individually interfere with one-another. More generally, several references can be used[Travis and Carroll, 1990].

The detection signal-to-noise ratio is maximised if the copies are of equal power and the symmetric $N \times N$ coupler most useful to coherent detection therefore splits the power into any input evenly amongst the N outputs. Furthermore[Travis and Carroll, 1989], the optimal situation, in a signal-processing and fading-immunity sense, is when the phase differences between the signal-reference pairs are $2\pi/N$, $4\pi/N$, ... , $2(N-1)\pi/N$, 2π, not necessarily in that order. These differences correspond to the relative phases between the interferometer output intensities as (sinusoidal) functions of the phase-delay measured by the interferometer.

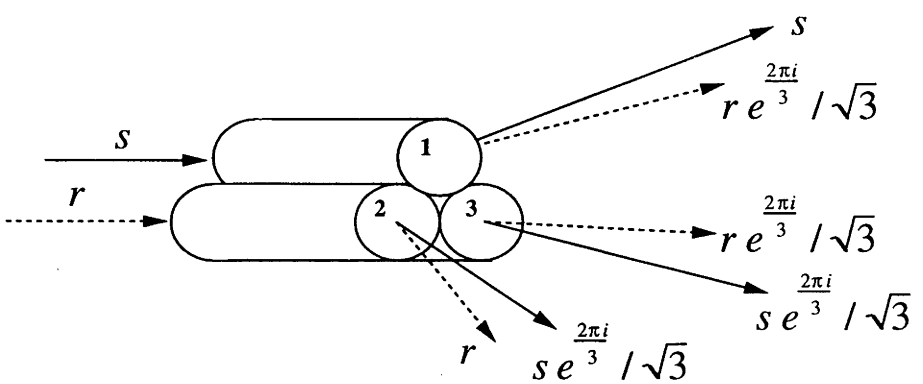

Figure 8.1: Interference Effected by the Symmetric 3×3 Coupler

8.2.2 3×3 Coupler

For the evenly splitting 3×3 coupler in Fig-8.1, the transfer matrix is:

$$U_{3\times3} = \frac{1}{\sqrt{3}} \begin{pmatrix} 1 & a & a \\ a & 1 & a \\ a & a & 1 \end{pmatrix}; \quad \text{where} \quad a = \exp\left(\frac{2\pi\, i}{3}\right) \tag{8.1}$$

which splits the reference r input on waveguide 1 in into copies $r_1 = r$, $r_2 = r\exp(2\pi i/3)$ and $r_3 = r\exp(2\pi i/3)$ at outputs 1, 2 and 3 respectively. Likewise, signal s input on input 2 is split into copies $s_1 = s\exp(2\pi i/3)$, $s_2 = s$, $s_3 = s\exp(2\pi i/3)$. Corresponding pairs of output beams interfere and the interference signals are $2Re(r_j s_j^*) = 2|r||s|\cos(\phi + 2\pi k/3)$ for $k = 1,2,3$. Thus the interference signals have relative phases $0, 2\pi/3, 4\pi/3$ and the scheme is optimal for both signal-to-noise ratio and output signal processing. From the *coherent detection diagram*[Travis and Carroll, 1989], the output interference signals *must* bear this same phase relationship whenever the signal and reference are both split into equal power copies at the output, *i.e.* even power splitting is a sufficient condition for the signal-processing-optimality. The coherent detection diagram's forming a closed loop[Travis and Carroll, 1989] is equivalent to the Energy Conservation Law and the transfer matrix's unitarity.

8.2.3 5×5 Coupler

The symmetric 5×5 fibre coupler can be used to implement an interferometer with immunity to *both* phase fading *and* polarisation fading[Travis and Carroll, 1989; Travis and Carroll, 1990]. However, such a device would seem difficult to build even as a fibre device owing to the difficulties discussed in [Henry, 1991] and to the difficulty of maintaining its cross-sectional symmetry throughout fibre fusing. The device is optimal from a signal-processing standpoint when it has the even power splitting property and its transfer matrix is then:

$$U_{5\times5} = \frac{1}{\sqrt{5}} \begin{pmatrix} 1 & b & b^{-1} & b^{-1} & b \\ b & 1 & b & b^{-1} & b^{-1} \\ b^{-1} & b & 1 & b & b^{-1} \\ b^{-1} & b^{-1} & b & 1 & b \\ b & b^{-1} & b^{-1} & b & 1 \end{pmatrix}; \quad \text{where} \quad b = \exp\left(\pm\frac{2\pi\, i}{5}\right) \tag{8.2}$$

8.3 Mach-Zehnder Interferometer Cascades

8.3.1 5×5 Coupler

In §7.6, it was shown that if the couplers $C_1 ... C_m$ in Fig-7.1*(a)* generate N^2 linearly independent matrices in the array of (7.25), then a concatenation of systems of the

form in Fig-7.1 can realise *any* unitary transfer matrix.

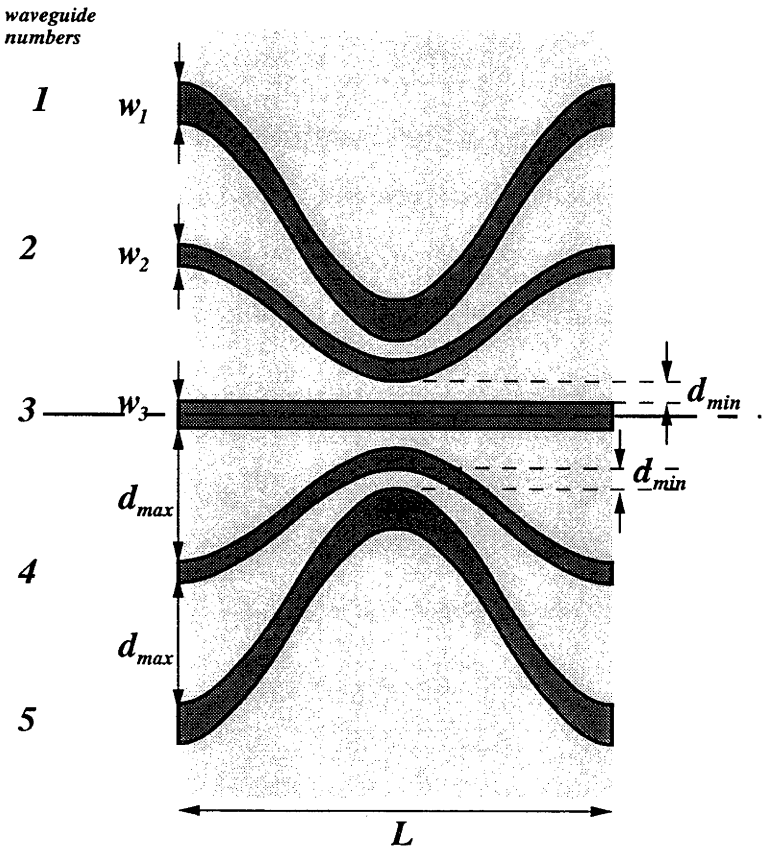

Figure 8.2: Photomask Dimensions of Basic Building-Block Coupler

Given satisfaction of the criterion in §7.6, it is reasonable to hope that the design goal can be realised as a concatenation (Fig-7.1*(b)*) of five[1] fundamental couplers, interspaced by delay lines and with delay lines at the input and output. The transfer matrix of the cascade is:

$$e^{i\Lambda_0}U_1e^{i\Lambda_1}U_2e^{i\Lambda_2}...U_5e^{i\Lambda_5} \tag{8.3}$$

where the real, diagonal matrices $\Lambda_0...\Lambda_5$ define the delay-lines.

8.3.2 Building Block Characterisation

We must first derive couplers implementing suitable U_j. The dimensions defining the basic building-block couplers used are the waveguide widths w_j and the maximum and minimum waveguide separations d_{max} and d_{min} in Fig-8.2. All the waveguides

[1] Although more than five may be needed, analogously to the 2 x 2 coupler example of §7.5.

have uniform width and, aside from the middle waveguide, follow cosinusoidal paths so that the separation between every neighbouring waveguide pair is the same at each cross-section. For simplicity, we study slab waveguides with cladding refractive index of 1.5 and core index 1.501848, *i.e.* the widest (10μm) coupler waveguide has $V = 1.56$ at the 1.5μm working wavelength so that all waveguides are everywhere single-moded. To lessen the number of simulations required to characterise each coupler, mirror symmetry is assumed about the centreline in Fig-8.2.

The first coupler analysed has $L = 7$mm, $d_{max} = 35\mu$m, $d_{min} = 2\mu$m, $w_1 = w_3 = 10\mu$m and $w_2 = 8\mu$m and its behaviour was simulated by a BPM using an axial step-size of 1μm and 16384 transverse points of 0.025μm spacing. The complex amplitudes output from the five waveguides in response to a unit input into waveguide 3 yield u_{13}, u_{23}, u_{33}, u_{43} and u_{53}, *i.e.* the third column of the coupler's transfer matrix. Likewise, the coupler outputs in response to unit input to the second core yield the second U-matrix column. Since the coupler has mirror symmetry, the fourth column follows from $u_{6-j,6-k} = u_{j,k}$. Lastly, outputs in response to a unit input into waveguide 1 yield the first and fifth U-matrix columns. The BPM results are summarised in Table-8.1 along with the results for other four couplers simulated and their defining dimensions. In all five cases, the dimension d_{max} was 35μm and the coupler's length $L = 7$mm.

Owing to small radiation loss, the transfer matrices in Table-8.1 are not exactly unitary. Hereafter, they are replaced by the "nearest" unitary matrices, calculated as follows. Let U_{jo} denote the "observed" transfer matrices, *i.e.* as stated in Table-8.1. The matrix logarithm of U_{jo} yields a matrix h_{jo} where $U_{jo} = \exp(h_{jo})$. Now, h_{jo} *should be* skew-Hermitian and, by symmetry of the structure in Fig-8.2, *should* be invariant to the element permutation defined by $h_{j,k} = h_{6-j,6-k}$ for $j, k = 1, 2, 3$. Let $\tilde{h}_{jo}$ denote the image of h_{jo} under this permutation. Then, the "nearest" unitary matrix U_j with invariance to the state permutation is:

$$U_j = \exp(h_j); \quad \text{where } h_j = \frac{1}{4}\left(h_{jo} - h_{jo}^{\dagger} + \tilde{h}_{jo} - \tilde{h}_{jo}^{\dagger}\right) \tag{8.4}$$

h_j is nearest skew-Hermitian matrix with the stated invariance to h_{jo} in the least-squares sense.

Coupler	C_1	C_2	C_3
$w_1(\mu m)$	10	10	8
$w_2(\mu m)$	8	8	10
$w_3(\mu m)$	10	10	10
$d_{min}(\mu m)$	2	3	2
u_{11}	0.119327-0.072613 i	0.310212-0.173653 i	0.211039+0.574117 i
u_{21}	-0.139928+0.574970 i	-0.018829+0.722123 i	-0.027238+0.408142 i
u_{31}	0.001799-0.454764 i	-0.063814-0.401132 i	-0.368790+0.141884 i
u_{41}	0.511956+0.035883 i	0.359722-0.011516 i	0.293567+0.176155 i
u_{51}	-0.305353+0.211082 i	-0.132813+0.146524 i	0.199011-0.310645 i
u_{12}	-0.139837+0.575009 i	-0.018717+0.722130 i	-0.027263+ 0.408092 i
u_{22}	-0.402463+0.062979 i	-0.098717+0.132962 i	0.391889 + 0.223272 i
u_{32}	-0.015833-0.327313 i	-0.259542-0.237739 i	0.502709 + 0.154335 i
u_{42}	-0.044778-0.306932 i	-0.096457-0.417602 i	-0.464196-0.09252 i
u_{52}	0.511955+0.035825 i	0.359702-0.011565 i	0.293543+0.176162 i
u_{13}	0.001775-0.454762 i	-0.063839-0.401119 i	-0.368801+0.141852 i
u_{23}	-0.015807-0.327319 i	-0.259521-0.237775 i	0.502712+0.154323 i
u_{33}	0.061653-0.598171 i	-0.172455-0.620634 i	0.160418-0.313106 i
u_{43}	-0.015807-0.327319 i	-0.259521-0.237775 i	0.502712+0.154323 i
u_{53}	0.001775-0.454762 i	-0.063839-0.401119 i	-0.368801+0.141852 i

Coupler	C_4	C_5
$w_1(\mu m)$	10	10
$w_2(\mu m)$	10	10
$w_3(\mu m)$	8	8
$d_{min}(\mu m)$	2	3
u_{11}	0.435139+0.059630 i	0.627028-0.162707 i
u_{21}	-0.183034-0.340348 i	-0.279733-0.345042 i
u_{31}	-0.561333+0.179739 i	-0.461692+0.195534 i
u_{41}	-0.323275+0.287658 i	-0.187147+0.213074 i
u_{51}	-0.306429+0.005014 i	-0.153569+0.041557 i
u_{12}	-0.183055-0.340368 i	-0.279755-0.345056 i
u_{22}	0.281997+0.493052 i	0.424505+0.239137 i
u_{32}	-0.122029-0.271759 i	-0.420307-0.222400 i
u_{42}	-0.426875+0.236054 i	-0.387628+0.309745 i
u_{52}	-0.323277+0.287674 i	-0.187154+0.213087 i
u_{13}	-0.561328+0.179820 i	-0.461678+0.195605 i
u_{23}	-0.122092-0.271731 i	-0.420356-0.222336 i
u_{33}	0.123937+0.306440 i	0.033062+0.175464 i
u_{43}	-0.122092-0.271731 i	-0.420356-0.222336 i
u_{53}	-0.561328+0.179820 i	-0.461678+0.195605 i

Table 8.1: BPM-Characterisation of the five building-block 5 × 5 couplers

8.3.3 Building-Block Requirements

It is readily shown numerically that the U_j generate 25 linearly independent matrices in the array of (7.25). Moreover, the couplers C_j were chosen from a set of eleven different candidate couplers and were found, after many random choices of five couplers from the eleven, to be the best set in the following sense. The thirty skew-Hermitian matrices defined by (7.25) were computed for each set. Each is specified by 25 independent real parameters, namely, the imaginary parts of the pure-imaginary leading diagonal elements and the real and imaginary parts of the matrix elements either above or below the leading diagonal. The 25 real parameters for all the matrices were assembled into an array T comprising 30 rows of 25 reals and the singular values of this array, *i.e.* the real eigenvalues of $T^\dagger T$ were computed. The number of linearly independent matrices in the set equals the number of nonzero singular values and the condition number[2] measures "how" linearly independent the corresponding matrices are, *i.e.* small condition numbers signal almost-linearly dependent vectors and thus difficulty in realising certain system transfer matrices. Hence, the couplers described here are the ones whose T array has the highest condition number out of all the coupler sets tried. It should be noted that:

- The coupler order markedly affects the condition number and therefore the workability of the cascade for realising all possible transfer matrices;
- *All* the randomly chosen sets fulfilled the criterion of §7.6 (*i.e.* 25 nonzero singular values in the T-array).

461 out of the possible ${}^{11}P_5 = 55440$ choices of ordered sets of five matrices taken from the eleven were used for this test, and the condition number for all of them was found to exceed 10^{-5}. This indicates that it is very easy to fulfill the criterion merely by trial and error[3].

---

[2] *i.e.* the minimum divided by maximum nonzero singular value.

[3] A run of 461 successes without one failure (in the sense that the T-array's condition number would be less than 10^{-5}) is statistically significant at the 99% confidence level for the Runs test[Walpole and Meyers, 1978, Ch-14], at least for concatenations of five couplers drawn from the eleven candidates. Typically, the T-array's condition number lies between 10^{-3} and 10^{-2}.

8.3.4 Building Block Concatenation

Given that any unitary matrix can be realised by a finite cascade of the couplers C_j defined in §8.3.2 interspaced by delay lines and that five basic sections is the least number required in general, it seems reasonable to hope that the required transfer matrix in (8.2) can be realised as a product of the form (8.3).

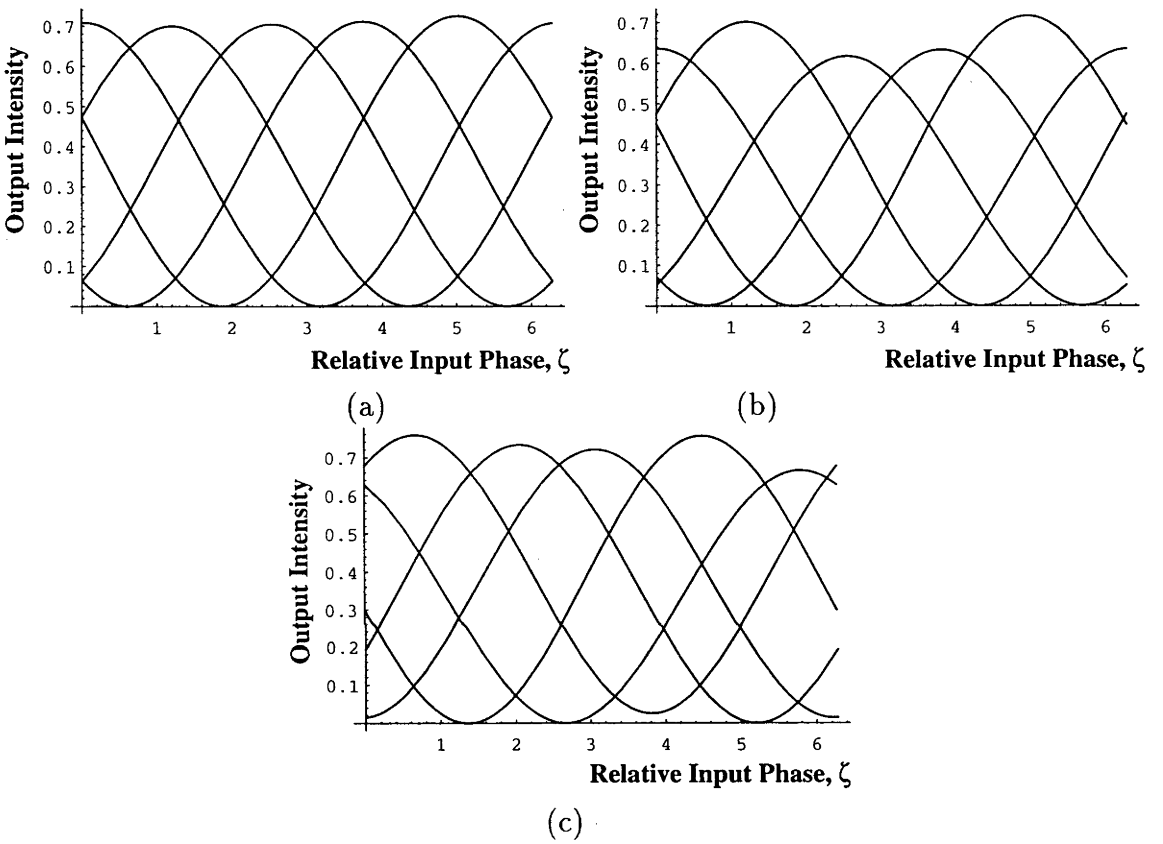

Figure 8.3: *(a)* Nominal Travis-Carroll scheme performance for typical pair of inputs; *(b)* Same for independent random phase perturbations uniformly distributed in $[-0.1, 0.1]$ applied to each phase delay line in the generalised Mach-Zehnder realisation of the symmetric 5×5 fibre coupler; *(c)* Performance for BPM-calculated transfer matrix in Eq-8.7.

The U_j derived from Table-8.1 are substituted into (8.3), the diagonal elements of the Λ_j are randomly initialised and then a simple conjugate-gradient searching method[Press *et al.*, 1990, Ch-10] (*c.f.* [Herscher and Carroll, 1982, §3]) is used to adjust these parameters to minimise the error between the system transfer matrix

in (8.3) in the design goal in (8.2). In this case, we find that the coupler cascade can realise the design goal when:

$$\begin{array}{l}\Lambda_0 = \mathrm{diag}[-0.543185, -0.581059, -3.67651, 1.13161, 0.653338] \\ \Lambda_1 = \mathrm{diag}[0.269921, -1.53459, 0, -0.978497, -0.711886] \\ \Lambda_2 = \mathrm{diag}[-3.18101, -1.42094, 0, 0.640995, 1.60192] \\ \Lambda_3 = \mathrm{diag}[-0.246719, -2.2531, 0, 1.69425, 2.36228] \\ \Lambda_4 = \mathrm{diag}[1.59266, -1.65064, 0, 1.29815, -0.759615] \\ \Lambda_5 = \mathrm{diag}[1.55171, 0.986603, 0, -2.21472, 0.599666]\end{array} \tag{8.5}$$

Fig-8.3*(a)* shows the powers output from the coupler as a function of the phase difference ζ between the reference input into waveguide 1 and a signal input into waveguide 2. The results are very similar for the reference and signal input into any other pair and thus the system would satisfactorily implement the the polarisation diversity scheme in [Travis and Carroll, 1989; Travis and Carroll, 1990]. Fig-8.3*(b)* shows the effect of sizable (up to 0.1 radian) perturbations of the phase delays and thus that the scheme is robust to delay inaccuracy.

8.3.5 Delay Lines

To help assess the scheme's practicality, tapered waveguides were simulated using the BPM to ascertain the delay line length needed to implement any phase delay between 0 and 2π radians. We consider the waveguide designs in Fig-8.4, where the cladding and core refractive indices are as in §8.3.2. The relative phase delay between the guides is controlled by the total length, L, of 8μm guide; since the wider guide has a higher propagation constant, it imposes a greater phase delay. Thus the field propagating through a 10μm wide translationally invariant guide becomes further delayed relative to the other's output as the length of narrowed guide increases. BPM-simulations confirm this relative delay to be approximately a linear function of L, the relationships being:

$$\begin{array}{l}\Delta\theta_a \approx 7.1843 \times 10^{-4} L + 0.3596; \qquad \Delta\theta_b \approx 7.1843 \times 10^{-4}(L_0 - L) + 0.3596 \\ \Delta\theta_c \approx 7.1843 \times 10^{-4} L + 0.1798\end{array} \tag{8.6}$$

radians for designs *(a)*, *(b)* and *(c)*, respectively. Here $7.1843 \times 10^{-4}\mu\mathrm{m}^{-1}$ is the difference between the propagation constants of the 10μm and 8μm guides and 0.1798 is the relative phase delay imposed by one of the 500μm-long tapers. To

Delay Section	δ_1	δ_2	δ_3	δ_4
Guide 1 L (μm)	0.0 *(a)*	6657.5 *(c)*	3631.5 *(c)*	83.1 *(a)*
Guide 2 L (μm)	1488.2 *(b)*	4207.6 *(c)*	6674.5 *(a)*	4597.6 *(a)*
Guide 3 L (μm)	375.7 *(a)*	2480.0 *(a)*	3288.1 *(c)*	2300.0 *(b)*
Guide 4 L (μm)	2262.3 *(b)*	1337.5 *(c)*	1180.1 *(a)*	493.1 *(a)*
Guide 5 L (μm)	1366.6 *(a)*	0.0 *(c)*	0.0 *(c)*	3357.7 *(a)*a
L_0 (μm)	5000.0	7157.5	7674.5	5600.0

Table 8.2: Delayline defining dimensions, bracketted letters showing delay-line design as defined by Fig-8.4

impart any phase difference up to 2π would require delay lines of up to about 9mm long. However, this distance can be reduced by either *(i)* using a larger difference between the waveguide widths (at the risk of increasing unwanted coupling between the delay lines owing to the more spread-out fields associated with low-V waveguides) or *(ii)* using higher-Δ waveguides. In all cases, the excess loss for the delay lines was below 0.006dB, hence the use of delay line tapering can be a practical, loss-free method to set up any desired relative phase between the fields.

Design *(a)* is used to link two 10μm wide coupler ports, design *(b)* to link two 8μm wide ports and *(c)*, a 10μm to an 8μm port. In all three designs, all tapers between the 10μm and 8μm wide sections are 500μm long. The delays are defined by the length L, the length of the 8μm wide section in designs *(a)* and *(c)* and the length of the 10μm long section in design *(b)*. The total delay-line length is L_0. Using (8.6), the necessary delay sections $\delta_1 ... \delta_4$ were designed to connect the basic couplers C_j in the concatenation $C_1\delta_1 C_2\delta_2 C_3\delta_3 C_4\delta_4 C_5$ using the appropriate waveguides of Fig-8.4 and thus to generate the delays in (8.5). In the notations of Figs-8.4*(a)*, *(b)* and *(c)*, the lengths L in μm for each guide were calculated to be as in Table-8.2.

8.3.6 BPM Appraisal

A BPM-simulation of the concatenation of the devices $C_1\delta_1 C_2\delta_2 C_3\delta_3 C_4\delta_4 C_5$, in that order, was now undertaken for a unit power input to waveguide 1 and the results are shown in Fig-8.5. As the delays δ_0 and δ_5 in (8.3) do not affect the schemes of [Travis and Carroll, 1989; Travis and Carroll, 1990], they were not included in the simulation.

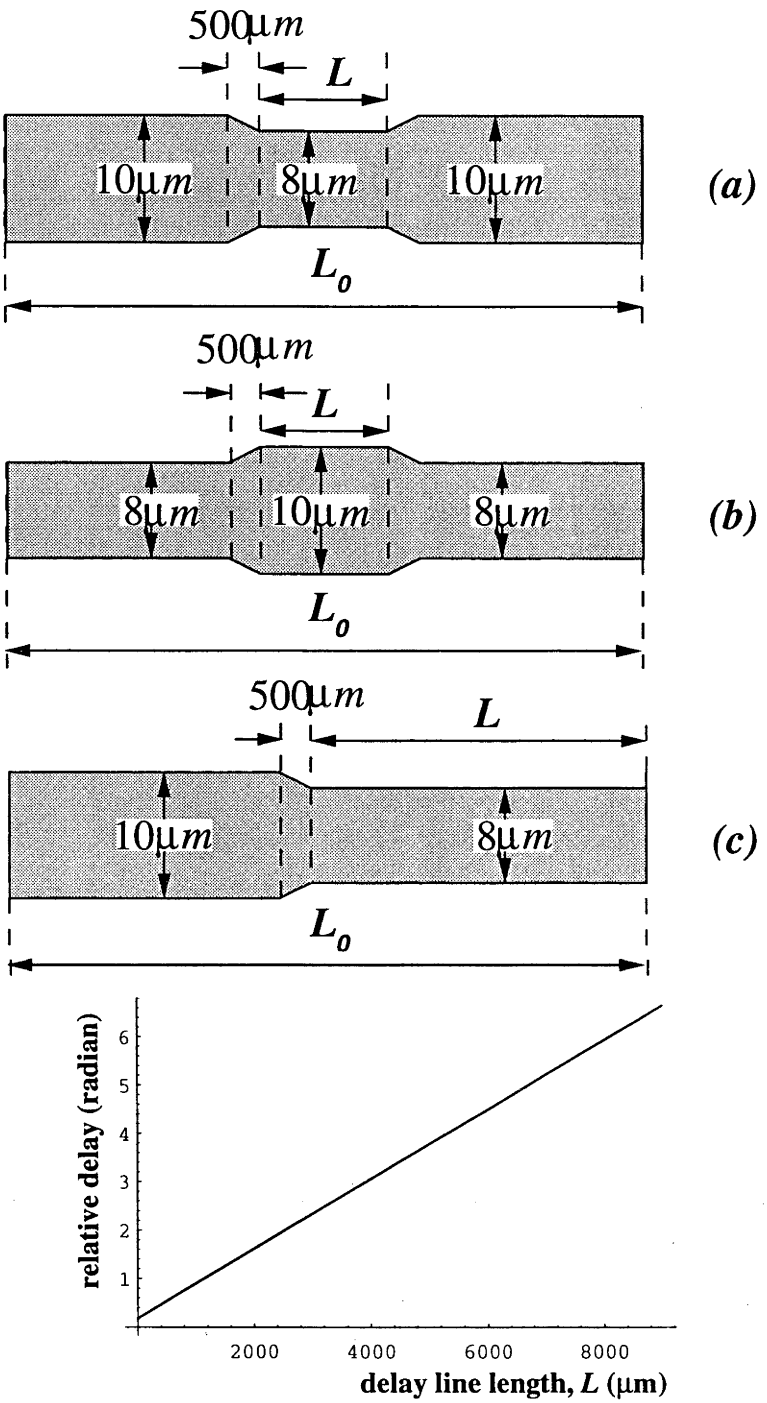

Figure 8.4: Use of tapering to control relative phase delays

As required, the amplitudes of the five output fields are roughly equal, although there is some inaccuracy owing to:

- Slight coupling between the delay line fields;
- Inaccuracy in the simple model (8.6) used to derive the delay line widths.

- Numerical inaccuracy from the 120 000 axial BPM steps required to model the device, whose length is 60.4mm;

- Appreciable attenuation of the outer waveguide fields owing to their overlap with the loss region, since the simulation domain width was limited to 246μm for reasonable computation task size;

The BPM simulation also yields the following system transfer matrix:

$$U = \begin{pmatrix} 0.246928 - 0.267708i & 0.191860 + 0.299707i & 0.291181 - 0.248377i \\ 0.301873 + 0.306820i & 0.430986 + 0.030285i & -0.212043 + 0.321098i \\ 0.103590 + 0.343518i & -0.163388 - 0.455557i & -0.436005 - 0.126069i \\ -0.417325 + 0.280473i & -0.425718 - 0.091520i & 0.415468 + 0.057273i \\ 0.350914 - 0.248091i & -0.333189 - 0.245211i & -0.067462 - 0.481180i \end{pmatrix}$$

$$\begin{pmatrix} -0.052965 + 0.511822i & 0.140395 + 0.468028i \\ -0.225959 + 0.358401i & 0.284534 - 0.334992i \\ 0.143564 + 0.335203i & -0.170236 + 0.392739i \\ -0.000831 + 0.433630i & 0.293096 - 0.186530i \\ -0.397365 - 0.062061i & 0.240887 - 0.274385i \end{pmatrix} \tag{8.7}$$

and Fig-8.3*(c)* shows the powers output from the coupler as a function of the phase difference ζ between the reference input into waveguide 2 and a signal input into waveguide 4. The scheme would still implement the ideas of [Travis and Carroll, 1989], the simulation and delay design inaccuracies notwithstanding.

8.3.7 Shorter Length Devices

For a practical system, the above design is probably too long and could be considerably shortened by using higher-Δ waveguides. The simulated systems used $\Delta n = n_{core} - n_{clad} \approx 8.2 \times 10^{-4}$, far smaller than would be used in practice, to ensure applicability of the BPM and the scalar wave equation, as discussed in Chapter-2. However, it must be stressed that the current design procedure does not depend on a detailed design of the couplers $C_1 ... C_5$, only on a knowledge of their transfer matrices. Hence, the use of extremely high Δ couplers, which could necessitate a

Coupler	C_1	C_2	C_3
$w_1(\mu m)$	10	8	10
$w_2(\mu m)$	8	10	10
$d_{min}(\mu m)$	2	2	2
u_{11}	0.231900+0.142284 i	0.261703+0.010860 i	0.208967-0.158616 i
u_{21}	-0.438034-0.144839 i	-0.284972-0.058030 i	0.551896-0.141914 i
u_{31}	-0.720412+0.430354 i	-0.123211-0.905026 i	-0.771314-0.000274 i
u_{12}	-0.438049-0.144781 i	-0.284981-0.058080 i	0.551903-0.141904 i
u_{22}	0.047095+0.752117 i	0.221778-0.882291 i	0.417467-0.412087 i
u_{32}	-0.438049-0.144781 i	-0.284981-0.058080 i	0.551903-0.141904 i

Table 8.3: 3×3 building-block coupler characterisation.

full vector field analysis, does not hinder our design procedure. The characterisation of $C_1 ... C_5$ could be experimental or numerical and software is available[Geers *et al.*, 1993] for analysing vector field propagation in waveguides.

Using the analysis of [Snyder and Love, 1983, Ch-25] and the curves of [Ladouceur, 1992, Fig-9.4], the minimum waveguide bend radius within a device can be decreased by a factor of about 5 by increasing Δ from 10^{-3} to 10^{-2} if V is constant. If the 5×5 coupler is scaled, the bend radii are proportional to the device length and its therefore plausible that the 5×5 coupler's length can be reduced to less than 10mm.

8.3.8 3×3 Coupler

A three-waveguide system of the form in Fig-7.1 can emulate the symmetric 3×3 fibre coupler[4]. As above, we use fixed building-block couplers interspaced by uncoupled delay lines and, for simplicity, assume mirror symmetry about a central plane. Let w_1 denote the outer waveguide's width and w_2 that of the middle waveguide, all other definitions for the basic couplers are as in Fig-8.2. Several different couplers were simulated and the results are as in Table-8.3. Here $d_{max} = 35\mu$m and $L = 7$mm for each coupler. The BPM simulations all used 16384 points in their transverse grids

[4]It is a subtle point that the couplers studied in §6.2 did *not* realise the symmetric 3×3 fibre coupler, only members of a whole class of 3×3 couplers (see equation (6.6)), any of which can realise the Sheem interferometer scheme. Here, we use the generalised Mach-Zehnder design procedure to realise the cyclically-symmetric 3×3 transfer matrix of the corresponding fibre coupler

spaced by 0.008μm and the axial stepsize was 1.0μm. Refractive indices and the wavelength were the same as for the 5×5 coupler in §8.3.1. When interspaced by delay lines, the system transfer matrix is $e^{i\Lambda_0}U_1e^{i\Lambda_1}...U_3e^{i\Lambda_3}$ and is found to emulate the symmetric 3×3 coupler (transfer matrix in (8.1)) when:

$$\begin{aligned}\Lambda_0 &= \mathrm{diag}[1.52057, 4.89306, 1.52057]; \quad & \Lambda_1 &= \mathrm{diag}[-0.250399, 0, -0.250399] \\ \Lambda_2 &= \mathrm{diag}[-2.11534, 0, -2.11534]; & \Lambda_3 &= \mathrm{diag}[-0.397484, 0, -0.397484]\end{aligned} \tag{8.8}$$

8.4 Simplified Mach-Zehnder Designs

The generalised Mach-Zehnder schemes remove the need for detailed design of the coupled regions and the system transfer matrix is defined by the phase delay lines. Accordingly, the need to solve coupled mode equations is also removed. The coupling regions can be designed almost by trial and error since they only have to satisfy the broad conditions as described above, whereas the procedures of §§6.2, 6.4 required detailed analysis of the coupling region. Moreover, simple coupled equations are convenient for design but inherently inaccurate whereas if the design is generated by a full coupled supermode analysis, the device behaviour prediction is accurate but complexity is sufficient to make design implementation extremely unwieldy except in the simplest cases. The avoidance of coupled mode equations is especially important for high-Δ waveguides, where the vector nature of the fields cannot be neglected. However, to lessen the number of basic building blocks needed, some design of these blocks may be advisable in some cases.

8.4.1 Transfer Matrix Factorisation

A five-section Mach-Zehnder interferometer analogue of the symmetric 5×5 coupler may be too bulky for some applications. A more practical scheme may lie between a design based on coupled mode equations, as in §6.2, and a design based on phase delay tuning, as in §8.3. Thus we use a sectioned system of the form $\exp(iK_1)\exp(iK_2)...$ where the K_j are real, symmetric and tridiagonal matrices, each determined by the techniques of §6.2. Given implementation of the $\exp(iK_j)$, the phase delay lines can be tuned between each section as in §8.3 to help offset the

inherent inaccuracies in the design method of §6.2. To generate 25 independent real parameters, a minimum of three $\exp(h_j)$ terms are needed and the conjugate gradient methods used in the §8.3 show that the equi-splitting, symmetric 5×5 fibre coupler's transfer matrix can be expressed as the product $\exp(i\,K_1)\exp(i\,K_2)\exp(i\,K_3)$ where[5]:

$$K_1 = \begin{pmatrix} 3.33791 & 1.4382 & 0 & 0 & 0 \\ 1.4382 & -1.72917 & -1.07692 & 0 & 0 \\ 0 & -1.07692 & 3.71013 & 1.53476 & 0 \\ 0 & 0 & 1.53476 & 4.14092 & -2.48292 \\ 0 & 0 & 0 & -2.48292 & 1.52859 \end{pmatrix} \tag{8.9}$$

$$K_2 = \begin{pmatrix} 5.71683 & 2.63869 & 0 & 0 & 0 \\ 2.63869 & 3.27886 & 3.41623 & 0 & 0 \\ 0 & 3.41623 & 2.24325 & 2.83231 & 0 \\ 0 & 0 & 2.83231 & 2.92041 & 3.47467 \\ 0 & 0 & 0 & 3.47467 & 5.35115 \end{pmatrix} \tag{8.10}$$

$$K_3 = \begin{pmatrix} 0.495619 & -4.00807 & 0 & 0 & 0 \\ -4.00807 & -1.46454 & -1.14966 & 0 & 0 \\ 0 & -1.14966 & 2.75645 & 3.76958 & 0 \\ 0 & 0 & 3.76958 & -0.1191 & -0.780289 \\ 0 & 0 & 0 & -0.780289 & 5.5318 \end{pmatrix} \tag{8.11}$$

This procedure also yields a transfer matrix factorisation for the symmetric 4×4 coupler[6] transfer matrix:

$$U_{goal} = \frac{1}{2}\begin{pmatrix} 1 & i & -1 & i \\ i & 1 & i & -1 \\ -1 & i & 1 & i \\ i & -1 & 1 & i \end{pmatrix} \tag{8.12}$$

namely, $\exp(i\,K_1)\exp(i\,K_2)$ where:

$$K_1 = \begin{pmatrix} 3.77652 & -2.35618 & 0 & 0 \\ -2.35618 & 3.77653 & 0 & 0 \\ 0 & 0 & 3.77656 & 3.927 \\ 0 & 0 & 3.927 & 3.7765 \end{pmatrix} \tag{8.13}$$

$$K_2 = \begin{pmatrix} 2.50665 & -3.04185 & 0 & 0 \\ -3.04185 & 2.50666 & 1.5708 & 0 \\ 0 & 1.5708 & 2.50664 & -3.04185 \\ 0 & 0 & -3.04185 & 2.50667 \end{pmatrix} \tag{8.14}$$

[5] §8.4.2 explains the meaning of negative coupling co-efficients

[6] A special case of the devices considered in [Mortimore, 1989].

8.4.2 Negative and Complex Coupling Co-efficients

The above design procedures involve negative propagation and coupling coefficients. The same integral multiple of 2π can be added to each of the propagation constants to make all of them positive and the U-matrix will be unaffected. A negative coupling coefficient between two nearest-neighbour waveguides means that the reference phases of the two waveguide fields are exactly out of phase. For example, in the 4×4 coupler (Fig-8.6 & Eqs. (8.13), (8.14)), the coupling co-efficient between waveguides 3 and 4 is positive along section BC and negative along DE. This means that along CD, the reference phase of either waveguide 3 or 4 changes by half a period, *i.e.* a π radian phase delay is imposed on one waveguide alone. Such a delay can be implemented (π-phase-shifter $P2$) by any of the delay methods in §8.3. Likewise, phase-shifters $P1$, $P3$ and $P4$ lead the other negative coefficients and, for the planar case, an analogous method produces any combination of coupling coefficient signs.

The coupling co-efficients can be also complex. Phase-delays of π radians are equivalent to a coupling co-efficient sign-change; more generally, *any* phase delay can be used. Thus, by a conjugate gradient parameter search, the transfer matrix of (8.2) can be expressed as the product $\exp(iK_1)\exp(iK_2)$ where:

$$K_1 = \begin{pmatrix} 6.79538 & 1.54446 - 0.84604i & 0 \\ 1.54446 + 0.84604i & -0.525633 & 1.24655 - 0.702762i \\ 0 & 1.24655 + 0.702762i & -0.173516 \\ 0 & 0 & -2.04206 - 1.14373i \\ 0 & 0 & 0 \end{pmatrix}$$

$$\begin{pmatrix} 0 & 0 \\ 0 & 0 \\ -2.04206 + 1.14373i & 0 \\ 8.57225 & -3.23281 - 1.87977i \\ -3.23281 + 1.87977i & 1.4882 \end{pmatrix} \tag{8.15}$$

$$K_2 = \begin{pmatrix} 2.6142 & 0.421223 - 5.5962i & 0 \\ 0.421223 + 5.5962i & 7.20351 & 2.59604 - 1.60984i \\ 0 & 2.59604 + 1.60984i & 2.3783 \\ 0 & 0 & 6.7224 - 2.52491i \\ 0 & 0 & 0 \end{pmatrix}$$

$$\begin{pmatrix} 0 & 0 \\ 0 & 0 \\ 6.7224 + 2.52491i & 0 \\ 2.95376 & 0.700753 + 1.36314i \\ 0.700753 - 1.36314i & 0.109475 \end{pmatrix}$$

Implementation corresponds to a system such as in Fig-7.1 where a cascade comprises couplers with transfer matrices $\exp(i\tilde{K}_1)$ and $\exp(i\tilde{K}_2)$ and delay-lines before, between and after them. Here $\tilde{K}_1$ and $\tilde{K}_2$ are matrices whose elements are the magnitudes of the corresponding elements in the matrices K_1 and K_2. For example, the coupling co-efficient $1.54446 - 0.84604i$ between waveguides 1 and 2 in the first coupler has a phase of $-28.7°$, *i.e.* between the cascade input and the coupler, delay lines cause the reference phase on waveguide 1 to lag that on guide 2 by $28.7°$. Likewise, the coupling co-efficient $0.421223 - 5.5962i$ between these two guides in coupler 2 has a phase of $-85.7°$, *i.e.* the reference field on guide 1 lags further behind that on guide 2 so that the total lag is $85.7°$. Lastly, delay lines beyond the second coupler give further lag so as to align the reference phases at the output. If the system has only nearest neighbour coupling, the coupling matrices are tridiagonal

and any combination of phases of coupling co-efficients between neighbouring guides can be achieved.

The 5×5 coupler realisation described here is a special case of the procedures of §8.3, but with further design in coupling sections so as to minimise number of sections needed. The reduced complexity is at the cost of reduced system flexibility as the two sections can no longer satisfy the criterion of §7.6. Thus, in general, a given unitary transfer matrix is unreachable by these particular two sections but the aim of the further coupling region design effort is to make the *particular* design goal $U_{5\times5}$ realisable.

8.5 Planar Couplers with Cyclic Symmetry

We now examine schemes achieving cyclic transfer matrix symmetry directly by imposing this symmetry on the physical device's geometry.

8.5.1 Analysis

Fig-8.7 schematically shows a planar six-port resonating ring with 2×2 couplers providing access by the input and output guides to the ring fields. All system waveguides are single-moded, so each input and output can be characterised by single complex numbers a_j and b_j, respectively and the transfer matrix is clearly invariant to a cyclic permutation of the roles of the three inputs and three outputs.

For certain inputs, corresponding to the transfer matrix's eigenvectors and which we shall hereafter call the "*eigeninputs*", the output vector is the input vector scaled by the relevant transfer matrix eigenvalue. For lossless systems, the transfer matrix is unitary and the eigenvalues lie on the unit circle, so that the output is a phase-delayed input when an eigeninput drives the system. The concept of "eigeninputs" is not new, being analogous to the analysis of three-phase power networks by the method of symmetrical components[Bergen, 1986, §-2.3, Ch-13] extended to N rather than three symmetric electric phases. An example of its more recent use is in microwave six-ports[Yeo and Tey, 1989].

We therefore consider the system response to the k^{th} eigeninput using the theory of Appendix-8.8. By (8.24), since the transfer matrix is cyclic, this corresponds to

a complex amplitude of $\exp(2\pi\ i\ k\ j/N)$ input to the j^{th} input port[7].

The output amplitude from the j^{th} port is then $y_k \exp(2\pi\ i\ k\ j/N)$, where y_k is the k^{th} transfer matrix eigenvalue. We fully characterise the system by calculating y_k, since the system transfer matrix is:

$$\mathbf{F}_N \ \mathrm{diag}[y_1, y_2, ...y_N]\ \mathbf{F}_N^{\dagger} \tag{8.17}$$

where $\mathbf{F}_N$ is the N-point discrete Fourier transform. By symmetry, the field at any point rotated by $2\pi/N$ radians about the ring's centre is $\exp(2\pi\ i\ k/N)$ times the initial field at that point. Thus, if the amplitude of ring field at the first coupler's input is z_k, then that at the second coupler is $z_k \exp(2\pi ik/N)$ as in Fig-8.7. If the unitary transfer matrix of each of the 2×2 couplers is $U_{2\times 2} = (u_{j,k})$, then the first coupler's output into the ring is $u_{21} + u_{22}z_k$ and the input to the second coupler from the ring is $\exp(i\phi)(u_{21} + u_{22}z_k)$, where ϕ is the phase delay between neighbouring couplers. Hence $z_k \exp(2\pi ik/N) = \exp(i\phi)(u_{21} + u_{22}z_k)$ and:

$$y_k = u_{11} + u_{12}z_k = \frac{u_{11} - \det(U_{2\times 2}) \exp\left(i\ \phi - \frac{2\pi ik}{N}\right)}{1 - u_{22} \exp\left(i\ \phi - \frac{2\pi ik}{N}\right)} \tag{8.18}$$

Furthermore, as in [Rowland and Love, 1993], we can take the coupler inputs and outputs to be any points where the ring and connecting waveguides are far enough separated as to be effectively uncoupled. Exactly where these points are is unimportant; if they are shifted slightly, extra phase delays are added/removed from the 2×2 transfer matrix and removed/added to the phase delay ϕ, but the system description will be unchanged. Thus, the 2×2 coupler's transfer matrix can be multiplied by any phase delay $\exp(i\omega)$ to be made unimodular[8], hence:

$$\begin{aligned} &|u_{11}| = |u_{22}|;\ \ |u_{21}| = |u_{12}| = \sqrt{1 - |u_{11}|^2} \\ &u_{11}u_{21}^* + u_{12}u_{22}^* = 0;\ \ u_{11}u_{22} - u_{12}u_{21} = 1 \end{aligned} \tag{8.19}$$

[7] *e.g.* For $N = 3$, the first, second and third orthonormal eigeninputs are respectively:

$$\frac{1}{\sqrt{3}}\begin{pmatrix} 1 \\ e^{\frac{2\pi i}{3}} \\ e^{\frac{4\pi i}{3}} \end{pmatrix};\ \frac{1}{\sqrt{3}}\begin{pmatrix} 1 \\ e^{\frac{4\pi i}{3}} \\ e^{\frac{8\pi i}{3}} \end{pmatrix} = \frac{1}{\sqrt{3}}\begin{pmatrix} 1 \\ e^{\frac{4\pi i}{3}} \\ e^{\frac{2\pi i}{3}} \end{pmatrix};\ \text{and}\ \frac{1}{\sqrt{3}}\begin{pmatrix} 1 \\ 1 \\ 1 \end{pmatrix} \tag{8.16}$$

[8] *i.e.* $\det(U_{2\times 2}) = 1$.

These equations can be manipulated to show that if $u_{11} = \gamma e^{i\delta}$, then $u_{22} = \gamma e^{-i\delta}$, where γ, the coupler's splitting ratio, and δ are real and positive. (8.18) and (8.19) then give:

$$y_k = \exp(i\delta)\frac{\gamma - \exp\left(i\,(\phi - \delta) - \frac{2\pi ik}{N}\right)}{1 - \gamma\exp\left(i\,(\phi - \delta) - \frac{2\pi ik}{N}\right)} \tag{8.20}$$

The phase-delay δ can be absorbed into the delay ϕ and also into the phase of the system eigenvalues, hence, without loss of generality, the k^{th} eigenvalue can be written:

$$y_k = \frac{\gamma - \exp\left(i\,\phi - \frac{2\pi ik}{N}\right)}{1 - \gamma\exp\left(i\,\phi - \frac{2\pi ik}{N}\right)} \tag{8.21}$$

This equation holds for the use of any lossless 2×2 couplers, not only symmetric ones, in the system.

After fabrication, some tuning of the delay ϕ may be needed since the waveguide distance between 2×2 couplers may be hundreds of wavelengths, hence, accurate realisation of ϕ at fabrication time may be difficult.

8.5.2 Even Power Splitting

Using (8.17) and (8.21), the system transfer matrix $U(\gamma, \phi)$ can be calculated as a function of γ and ϕ, whence the *splitting error*, η:

$$Y(\gamma,\phi) = U(\gamma,\phi)\begin{pmatrix}1\\0\\0\end{pmatrix};\quad \eta(\gamma,\phi) = \frac{\sqrt{3+\sqrt{3}}}{2}\sqrt{\sum_{j=1}^{3}\left(|Y_j(\gamma,\phi)| - \frac{1}{\sqrt{3}}\right)^2} \tag{8.22}$$

which measures of the power splitting uniformity; $\eta = 0$ if and only if power input to waveguide 1 is split evenly amongst the three outputs and η is maximum ($\eta = 1$) if and only if all power is output in one waveguide only. Fig-8.8 plots η against ϕ for several values of γ and shows that the minimum η (corresponding to maximum splitting uniformity) decreases with increasing γ, *i.e.* as less light escapes from the ring at each recirculation and the ring becomes more resonant. Power splitting can only be precisely uniform when $\gamma = 1$ and the ring's quality factor Q is infinite. However, for high γ, the system is extremely sensitive to small changes in ϕ, and therefore

small temperature drifts, *i.e.* there is a design tradeoff between good splitting uniformity and good temperature stability, see §8.6. A value $\gamma \approx 0.75$ would seem to be the maximum practical value and for $\gamma = 0.7$ (*resp.* 0.8), the highest uniformity occurs when $\phi = 1.87$ (*resp.* 1.96) and $(P_1, P_2, P_3) = (0.333314, 0.447440, 0.219246)$ (*resp.* $(P_1, P_2, P_3) = (0.336324, 0.404681, 0.258996)$).

Fig-8.9 shows the output powers from the coupler in Fig-8.7 when $\gamma = 0.7$ as a function of the phase difference ξ between equal power reference and signal beams. Here, the total power is 1 and the plots are repeated for several ϕ values. Although the output power nonuniformity is appreciable, the phase difference between the powers as sinusoidal functions of ξ remain very close to $2\pi/3$, even though ϕ changes by ± 0.1 radian, thus the device would be usable in the phase diversity schemes of [Sheem, 1981; Travis and Carroll, 1989].

The implementation of an even power splitting 5×5 device can be investigated by recalculating (8.21) for $N = 5$, plotting an analogous quantity to η in (8.22) as a function of γ and ϕ and thus quickly showing that even splitting cannot be achieved, even approximately. This is not surprising, since for even power splitting in the 5×5 device, four phases $\arg(y_1/y_0), ..., \arg(y_4/y_0)$ must be set to certain values with only two variable parameters ϕ and γ, whereas in the 3×3 case, only two phases $\arg(y_1/y_0)$ and $\arg(y_2/y_0)$ need to be prescribed.

8.5.3 Device Compactness

The device must be as small as possible to ensure temperature insensitivity. [Snyder and Love, 1983, Eq-23-23] gives the bending loss for a round cross-section waveguide and, by using this as an estimate in the present problem, the loss for each ring circuit executed by a beam is found to be:

$$L \approx 67\sqrt{R}e^{-0.05R} \text{ decibel} \tag{8.23}$$

for waveguide parameters $V = 2$, $U = 1.528$, $W = 1.29$ and for a profile height $\Delta = 0.07$, which is representative of the most strongly-guiding waveguides in contemporary technology. Here R is the ring radius divided by the waveguide core radius and (8.23) suggests a minimum possible ring radius of about 150μm.

8.6 Temperature & Frequency Stability

8.6.1 Temperature Drift

The distinction made in this Chapter between the cyclically-symmetric schemes of §8.5 and the Mach-Zehnder schemes of §8.3 is important from a temperature and frequency stability point of view. The devices of §8.5 depend on *absolute* optical phase delays and will thus be sensitive to thermal strain in the optical length providing this delay, whereas the schemes of §8.3 depend only on *relative* phase delays between different points on the same cross-section and thus will be sensitive only to *differences* between thermal strains. We illustrate these points by example.

Doped silica for optical waveguide applications has a refractive index that typically changes by 10^{-5} per degree Celsius change and a thermal expansion co-efficient of $10^{-6}\mathrm{K}^{-1}$. The phase delay of a waveguide of length L thus changes by approximately $10^{-5}kn_{eff}L\ \Delta T$ for a temperature change of ΔT, where k is the freespace wavenumber and n_{eff} the guide's effective index. For the high-Δ waveguide example of §8.5.3 with a ring-radius of 200μm, ϕ changes by about $0.018\mathrm{radK}^{-1}$ when $\lambda = 1.5\mu$m and $n_{eff} = 1.5$. Thus, Fig-8.9 suggests the device to be workable over a temperature range of about $\pm 6^{o}$C without device temperature stabilisation.

We now compare these results to the likely results for the devices of §8.3. The suitability of the Mach Zehnder devices for the schemes of [Sheem, 1981; Travis and Carroll, 1989; Travis and Carroll, 1990] are only affected by perturbations to the *relative* phase delays between the system waveguides. The devices are typically less than 100μm wide, so that it is straightforward to arrange for the temperature to be extremely uniform over each cross-section. It would therefore seem reasonable to expect transverse temperature variation to be limited to less than one hundredth of any ambient temperature change. Fig-8.3 shows the 5×5 coupler of §8.3 to adequately implement the schemes of [Sheem, 1981; Travis and Carroll, 1989; Travis and Carroll, 1990] even despite simultaneous random perturbations to all of the phases in (8.5) of up to ± 0.05 radian. The delay lines are of about 5mm length, thus the tolerable temperature drift is ΔT where $\Delta T \times 5 \times 10^{-3} \times 10^{-5}/100 = 0.05 \times 1500 \times 10^{-9}/(2\pi)$ or $\Delta T = \pm 23.9^{o}$C. This figure is achievable with the low-Δ waveguides studied in §8.3; far better temperature stability will be available with

higher-Δ waveguides allowing shorter device lengths and a tolerable temperature range of $\pm 100°C$ is quite conceivable.

8.6.2 Source Frequency Jitter

The effect of source laser frequency instability is like that of temperature drift in that both effects change the effective device dimensions relative to the working wavelength. The phase delay of a waveguide with length L is $2\pi\ L\ f\ n_{eff}/c$, where f is the source frequency and $c \approx 2.998 \times 10^8 \mathrm{ms}^{-1}$ the freespace speed of light, hence a change Δf in source frequency produces a phase delay change[9] of $2\pi\ L\ \Delta f\ n_{eff}/c$. The devices of §8.5, depending on absolute optical delays, will be the most sensitive to source frequency jitter and, by taking a frequency variation of ± 5MHz as an overbound on the normal jitter suffered by contemporary lasers, a waveguide's delay is seen to vary typically by 1.6×10^{-4} radian per millimetre of guide length. Whereas, given this figure, source frequency instability is not a problem for the systems discussed above, one should assess source stability requirements for each intended application. Although source frequency-jitter-induced output change may not affect basic workability, they will give rise to small output intensity variations in interferometric applications. If the jittering occurs at a rate comparable to that of the sensed quantity, serious, irreversible signal contamination may arise.

Because the devices studied in §8.3 depend only on relative delays, they enjoy greatly reduced levels of jitter-induced noise if used as a beam-recombiner and the effect of a ± 5MHz source frequency variation will be negligible for most applications.

8.7 Conclusions

This Chapter analysed several schemes for realising the symmetric 3×3, 4×4 and 5×5 fibre couplers either as *(i)* planar devices with N-fold rotational symmetry whose behaviour depends on absolute optical delays between the N sectors or *(ii)* generalised Mach-Zehnder interferometers, whose working depends on *relative* phase delays between neighbouring waveguides. The schemes based on the generalised Mach-Zehnder interferometer were found to be the most promising, owing

[9] *i.e.* with waveguide and material dispersion[Glodge, 1976] ignored.

to their enhanced resilience to temperature and source frequency variation. This resilience arises because the Mach-Zehnder interferometer's working is a function of the *difference* between rather than the absolute value of optical phase delays. Such differential behaviour is an important system attribute and will be examined in the next Chapter.

8.8 Appendix: Cyclic Transfer Matrices

The symmetric $N \times N$ coupler comprises N equal fibres arranged in an N-sided regular polygonal arrangement as in Fig-8.1. Its structure is unchanged if rotated about a a central axis normal to the cross-section by an integral multiple of $\pm 2\pi/N$, therefore, its analytical description is unchanged if the roles of the fibres are cyclically permuted. Moreover, the cross-section has reflexional symmetry about N planes so that the coupler's forward transfer matrix U is both cyclic and self-transpose.

The theory of matrices with cyclic symmetry, or *circulant matrices*, is well documented[Davis, 1979; Hunt, 1971]. An $N \times N$ matrix $\mathbf{U}$ is circulant if and only if it has the N-point discrete Fourier transform operator $\mathbf{F}_N$ as a matrix of eigenvectors; *i.e.* $\mathbf{F}_N^{-1}\mathbf{U}\mathbf{F}_N = \mathbf{F}_N^{\dagger}\mathbf{U}\mathbf{F}_\mathbf{N}$ is diagonal where:

$$\mathbf{F}_N = \frac{1}{\sqrt{N}} \begin{pmatrix} 1 & 1 & 1 & 1 & \dots & 1 \\ 1 & r^{-1} & r^{-2} & r^{-3} & \dots & r^{-(N-1)} \\ 1 & r^{-2} & r^{-4} & r^{-6} & \dots & r^{-2(N-1)} \\ 1 & r^{-3} & r^{-6} & r^{-9} & \dots & r^{-3(N-1)} \\ \dots & \dots & \dots & \dots & \dots & \dots \end{pmatrix} \quad \text{where } r = \exp\left(\pm i \frac{2\pi}{N}\right) \tag{8.24}$$

If cyclic symmetry applies along a coupler's whole length, the coupling matrix *must* have $\mathbf{F}_N$ as its matrix of eigenvectors and the system's local modes must have the same symmetries as the eigenvectors. That is, a $2\pi/N$ radian rotation of the k^{th} local modal field is equivalent to scaling the modal field by $\exp(2\pi i\ k/N)$ and such symmetry guarantees that coupling co-efficients between different local modes[Snyder *et al.*, 1991, §31-15] must *always* vanish, *i.e.* the coupled local mode equations are completely decoupled and have the solution:

$$U = \mathbf{F}_N \mathrm{diag}\left[\int_0^z \beta_1(u)du, \int_0^z \beta_2(u)du, \dots\right] \mathbf{F}_N^{\dagger} \tag{8.25}$$

however tightly coupled the waveguides may become. Here $\beta_j(z)$ is the j^{th} local mode propagation constant.

The above explains why even approximate formulations of coupled mode theory[10] can be used to predict the symmetric $N \times N$ coupler's behaviour extremely accurately even in tightly coupled systems, *e.g.* a fused biconic symmetric 3×3 fibre coupler. In other cases, such approximate theories become inaccurate for only moderately tightly coupled cases (*c.f.* §6.3.1).

It is also straightforward to show that the vector of eigenvalues and the vector containing the first row of $\mathbf{U}$ are discrete Fourier-transform pairs:

$$u_k = \frac{1}{N} \sum_{j=0}^{N-1} \exp\left(\mp i \frac{2\pi jk}{N}\right) \lambda_j; \quad \lambda_k = \sum_{j=0}^{N-1} \exp\left(\pm i \frac{2\pi jk}{N}\right) u_j \tag{8.26}$$

where the first row of $\mathbf{U}$ is written $(u_0, u_1, ...u_{N-1})$ and the matrix of eigenvalues is diag $[\lambda_0, \lambda_1, ..., \lambda_{N-1}]$. For lossless couplers, $\mathbf{U}$ is unitary and the eigenvalues have unit magnitude, *i.e.* $\lambda_j = \exp(i\theta_j)$ for real θ_j. In the case of the symmetric fibre coupler, the θ_j are given by:

$$\theta_j = \int_0^z \beta_j(u) du \tag{8.27}$$

where $\beta_j(z)$ is the j^{th} supermode propagation constant. Furthermore, $\mathbf{U} = \mathbf{U}^T$, or:

$$U_{j,k} = U_{k,j} \quad \Leftrightarrow \lambda_r = \lambda_{N-r}; \quad r = 1, 2, ..., N-1 \tag{8.28}$$

i.e. the j^{th} and $N - j^{th}$ local modes in the symmetric fibre coupler are degenerate.

This allows the eigenfields of a symmetric fibre coupler to be more simply expressed as follows. Consider the 3×3 fibre coupler and assume that the local modes are linear superpositions of the eigenfields of the constituent fibres in isolation. Then, by the above discussion of circulant matrices, the weights in these modal superpositions are $(1, 1, 1)$, $(1, \exp(2\pi i/3), \exp(4\pi i/3))$ and $(1, \exp(4\pi i/3), \exp(2\pi i/3))$. However, the second and third modes are degenerate, thus any linear superposition of these modes is itself a mode. Therefore, $(0, 1, -1)$ and $(2, 2\cos(2\pi/3), 2\cos(4\pi/3)) = (2, -1, -1)$ can be taken as weights for the second and third modes and this is the more usual choice in the literature.

[10] *e.g.* the coupled guide theory of [Snyder and Love, 1983, Ch-29] where local modes are assumed to be linear superpositions of the eigenfields of the constituent waveguides in isolation.

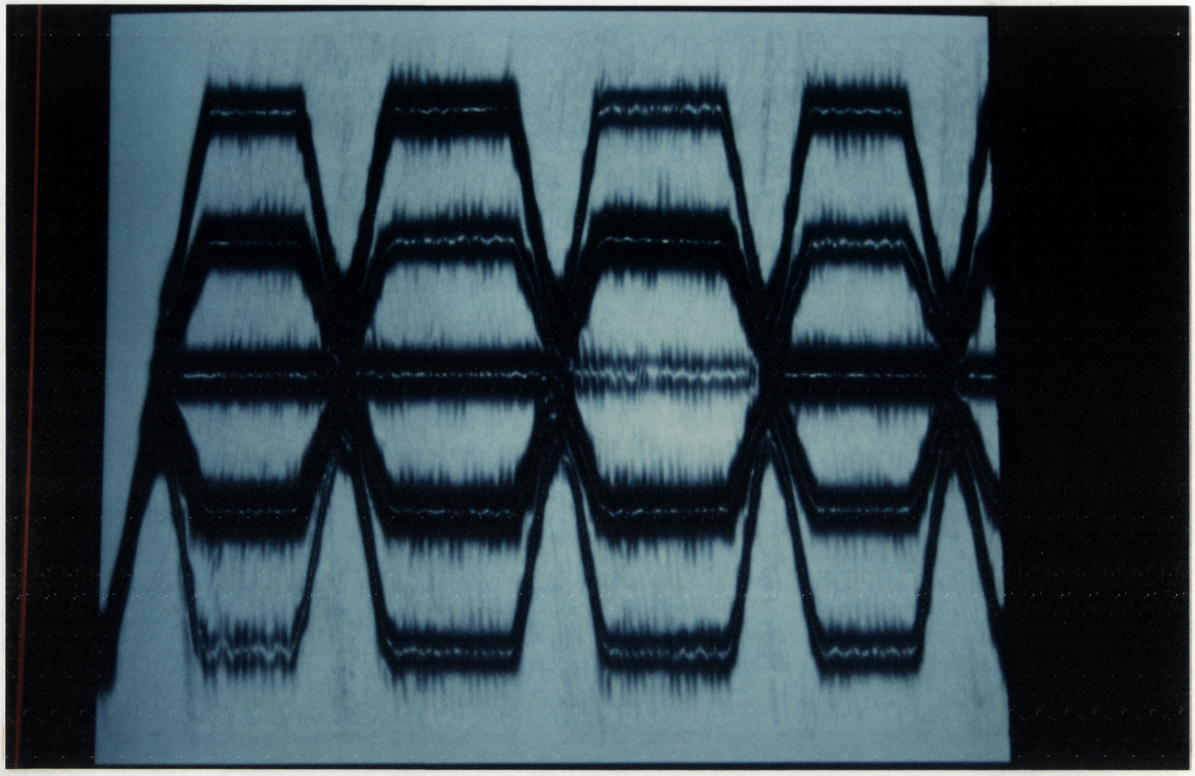

(a)

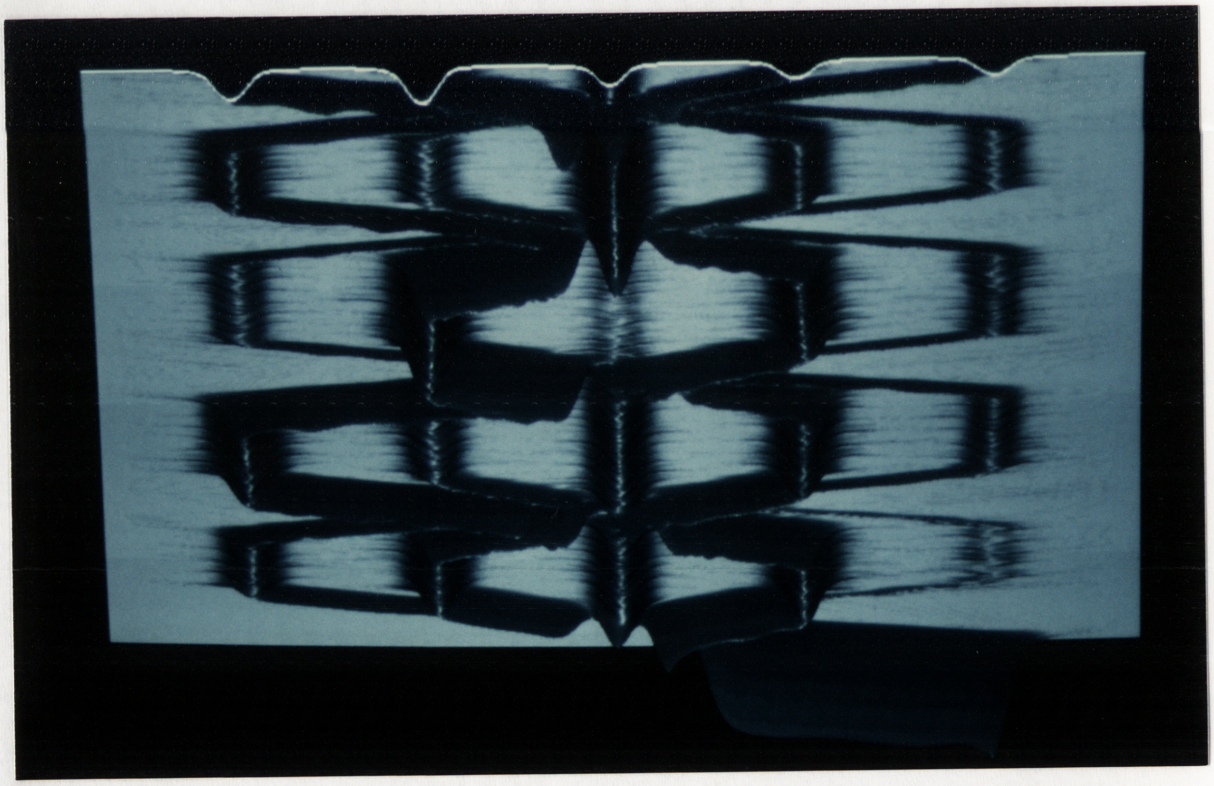

(b)

Figure 8.5: Intensity distribution within planar 5×5 coupler as found by BPM simulation: *(a)* plan view; *(b)* end view.

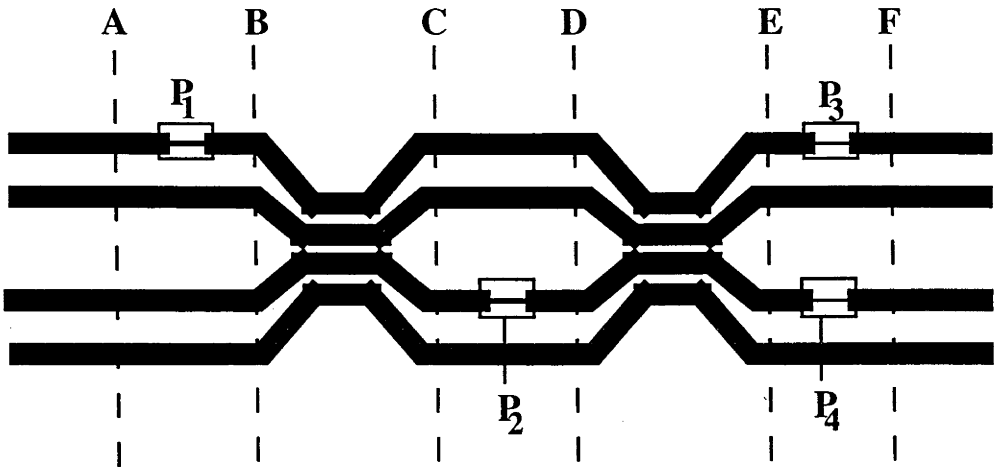

Figure 8.6: Use of delay lines in 4 × 4 coupler to implement negative coupling co-efficients

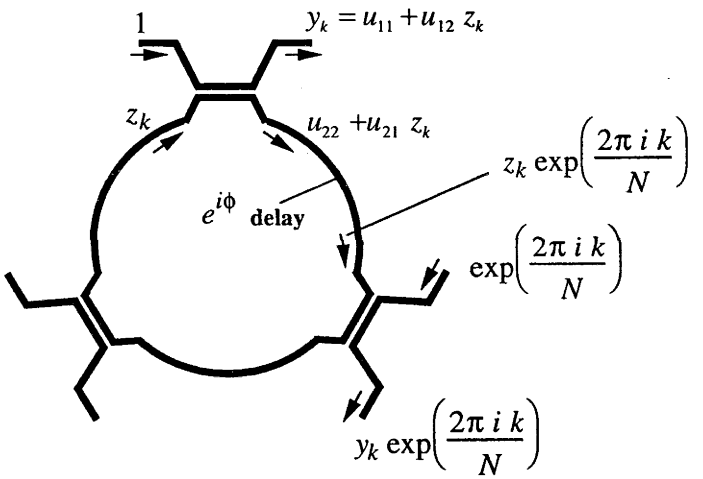

Figure 8.7: Six-port ring field definitions

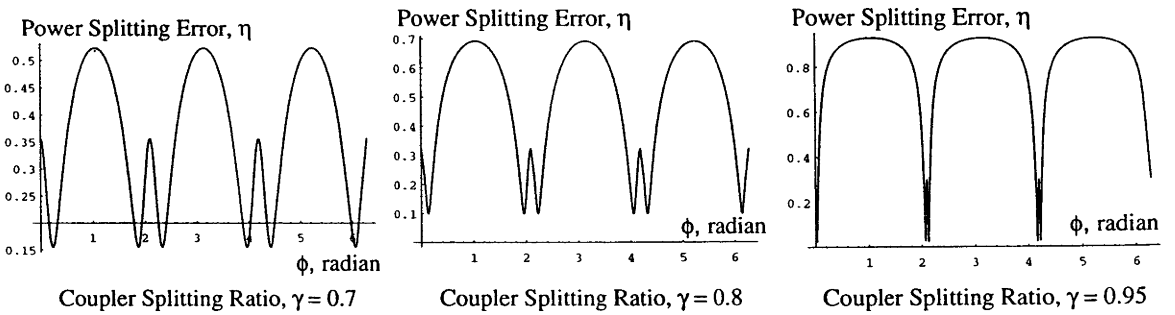

Figure 8.8: Splitting nonuniformity as a function of ring delay for various γ

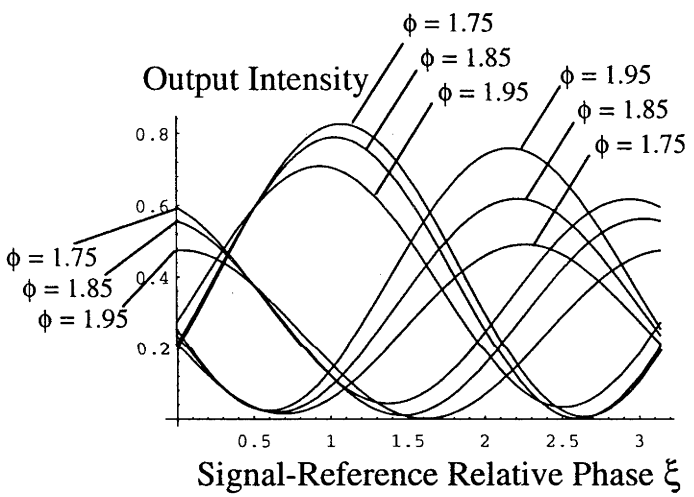

Figure 8.9: Six-port ring performance with ϕ-perturbation

Chapter 9

Differential Behaviour of Linear Systems

9.1 Introduction

The temperature drift and frequency stability considerations in §8.6 of the designs of the foregoing Chapter demonstrate the benefits of differential behaviour in optical systems, *i.e.* when a system's transfer function depends only on the *difference* between two optical pathlengths, rather than the absolute values. This Chapter derives general conditions under which such behaviour arises and is pertinent to interferometry and to the planar designs of this thesis, particularly since the non-differential designs of §8.5 will probably be impracticable unless temperature-stabilised.

The original aim of this work was to improve the sensitivity of interferometric systems with resonant behaviour, whilst retaining differential behaviour with its advantages. Whereas resonant interferometers, such as the Fabry-Pérot cavity or fibre ring-resonator, can have outstanding phase sensitivities[Yue *et al.*, 1988], they have, in most applications, been non-differential and suffer from the drawbacks of the designs in §8.5, *i.e.* poor resilience to temperature drift and source frequency variations compared to those of the less sensitive, two-beam differential interferometers such as the Michelson or Mach-Zehnder. This Chapter investigates whether these latter two are the only kind of differential devices or whether a higher-sensitivity differential scheme may be possible.

Recently, interest has been shown in the use of resonant behaviour to enhance

interferometer sensitivity to extreme levels to detect gravitational waves[Fritschel *et al.*, 1992; Shoemaker *et al.*, 1991]. A resonant interferometer attains high sensitivity by recycling light many times through a sensing optical delay, thus setting up a many-beam interference[Born and Wolf, 1980, §7.6] in contrast to the two-beam interference in Mach-Zehnder or Michelson interferometers. However, this many-beam interference is also highly sensitive to optical frequency shifts and any source laser frequency instability gives rise to high output noise levels. Early attempts to achieve high sensitivity in a fibre ring-resonator were often thwarted; in [Stokes *et al.*, 1983], a resonant ring with a finesse over one hundred was studied, yet the system was only twice as sensitive as the corresponding Mach-Zehnder interferometer owing to high jitter-induced noise. Indeed, the extreme sensitivity of resonators to frequency shifts has led to their main use as laser cavities or sensitive frequency discriminators[Okamura and Iwatsuki, 1990; Chaoyu *et al.*, 1989].

Experience with both Mach-Zehnder and Fabry-Pérot systems suggests the dearth [Jaroszewiz and Pluta, 1990] of practical resonant systems arises from the difficulty of using them. To benefit fully from resonant interferometer behaviour, elaborate steps must be taken to either[Fritschel *et al.*, 1992; Shoemaker *et al.*, 1991] *(i)* frequency-stabilise the source-laser or *(ii)* implement feedback control of the optical sensing delay so as to counteract the effect of source frequency jitter. Such elaboration is often a hindrance in practical systems. In [Vance and Barrow, 1990], an interferometer for magnetic field sensing is required to be fully passive and must detect phase-changes of 10^{-4} radian, for signals between 100Hz and 10kHz. The centre frequency of many contemporary lasers wavers at a rate within this bandwidth, so that the jitter-induced noise is *indistinguishable* [1] from a valid change arising from the sensed magnetic field. The output intensities of the Mach-Zehnder and Michelson interferometers, as functions of the two optical path-lengths L_1 and L_2 are:

$$I = \begin{cases} I_0 \sin^2\left(\frac{\beta}{2}(L_1 - L_2)\right) + I_{res} & (\text{Mach} - \text{Zehnder}) \\ I_0 \sin^2\left(\beta(L_1 - L_2)\right) + I_{res} & (\text{Michelson}) \end{cases} \tag{9.1}$$

where $\beta = 2\pi n_{eff} f/c$ is the propagation constant in the optical paths, c the freespace

[1] *i.e.* being in the band of interest, cannot be bandpass filtered out by signal processing electronics or software.

in §8.5, differential behaviour engenders valuable robustness to temperature drift. Moreover, in interferometry, one is only concerned with a differential length dependence of output intensity; in the applications of Chapter-8, both output intensity *and* relative phase between output fields must be differential functions of lengths. Hence, we show that a Mach-Zehnder or Michelson-like planar systems are the only kinds with such behaviour.

To prove these results, we first set up a general notation for a general interferometric system and illustrate it by formulating a description in §9.4 of a resonant Michelson interferometer with light recycling[Fritschel *et al.*, 1992].

9.3 General Linear Optical Network

We shall study the general optical network schematically shown in Fig-9.1 assuming that:

- The source laser drives the network with a perfectly monochromatic beam a_0 and all beams $a_1, b_1, ..., a_4, b_4$ and b_5 are monochromatic, *i.e.* no frequency shifting takes place within the network;
- There is no feedback of the output b_5 into any part of the network and, in particular, $a_5 = 0$ in this analysis;
- The ports 0 to 5 are single-moded and the field of each is defined by complex amplitudes, a_j and b_j, for the modes incident on and scattered from each port, respectively;
- The network is linear;
- The network is stable; and
- The source laser is unaffected by the scattered component b_0, which therefore need not be evaluated.

No assumption of Reciprocity is needed and the network need not be passive, only stable. It should be noted that the *form* of Fig-9.1 can cope with all feedback of the output into the network despite the assumption otherwise; if there is feedback,

speed of light, n_{eff} the effective refractive index of the two optical paths (assumed equal), f the source laser's frequency and I_{res} is a residual output arising from imperfect fringe visibility ($I_{res} = 0$ for unity visibility). Even for $L_1, L_2 \approx 10$m, the lengths can be matched to within 1 cm, hence, for an interferometer with a required phase resolution $|\Delta\phi| < 10^{-4}$ radian, the largest tolerable frequency jitter, Δf, is:

$$|\Delta f| < \frac{c\,\Delta\phi}{2\pi\, n_{eff}\, |L_1 - L_2|} = 330\text{kHz} \tag{9.2}$$

The ring resonator of [Yue *et al.*, 1988] had a length of 0.6m, so that $|\Delta f| < 5.5$kHz. This performance is beyond all commercially available lasers suitable for sensing in the field.

9.2 Problem Formulation

In differential interferometers, the source frequency instability acts on a length *difference*, which can be extremely small even though the sensing lengths themselves may be extremely long to enhance sensitivity to the sensed quantity. This is not the case for the ring-resonator, wherein source jitter acts on the whole sensing length. It is therefore apparent that an interferometer that would both *(i)* achieve a high sensitivity through resonant behaviour and *(ii)* operate differentially would be a highly desirable interferometric system. For example, the recycling Michelson interferometer in [Fritschel *et al.*, 1992] has separate sensing and reference optical paths and an example of a resonant optical fibre ring resonator with separate sensing and reference paths is found in [Abd-El-Hamid and Davies, 1989]. It is natural to ask whether such systems can be configured to make their outputs wholly differential functions of the sensing and reference lengths. In the following sections, it will be shown that any differential interferometer's output intensity, as a function of path-length difference, has the same form as for the Michelson and Mach-Zehnder interferometers, *i.e.* these classical systems can attain the same phase sensitivities as *any* differential interferometer, so that it is futile to attempt to increase sensitivity through resonant behaviour if differential interferometer operation is essential.

In planar integrated optics devices, the frequency stability problem is not so important as the optical lengths are very much shorter. However, as illustrated

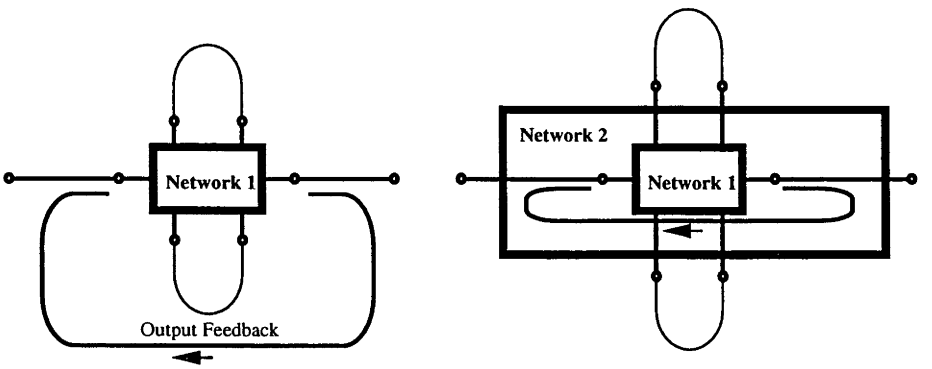

Figure 9.2: System Remodelling to Remove Output Feedback

$$\begin{pmatrix} b_0 \\ b_1 \\ b_2 \\ b_3 \\ b_4 \\ b_5 \end{pmatrix} = \mathbf{S}_6 \begin{pmatrix} a_0 \\ a_1 \\ a_2 \\ a_3 \\ a_4 \\ a_5 \end{pmatrix} \quad \text{or} \quad \left(\begin{array}{c} b_0 \\ \hline \mathbf{b} \\ \hline b_5 \end{array}\right) = \left(\begin{array}{c|c|c} & & \\ \hline \mathbf{D} & \mathbf{S} & \\ \hline \mathrm{F} & \mathbf{G}^T & \end{array}\right) \left(\begin{array}{c} a_0 \\ \hline \mathbf{a} \\ \hline a_5 \end{array}\right) \tag{9.3}$$

where F is a scalar, $\mathbf{D}$ and $\mathbf{G}$ are 4×1 vectors and $\mathbf{S}$ is a 4×4 matrix. $\mathbf{a}$ and $\mathbf{b}$ are respectively the vectors of incident and scattered waves at ports $1, 2, 3$ and 4. The partitions left blank in (9.3) are irrelevant to the following analysis since, by assumption, $a_5 = 0$ and b_0 has no effect on the source laser. Thus, the only relevant equations are:

$$b_5 = F\, a_0 + \mathbf{G}^T\, \mathbf{a}; \quad \mathbf{b} = \mathbf{D}\, a_0 + \mathbf{S}\, \mathbf{a} \tag{9.4}$$

The relevant scattering matrix partitions have the following physical meanings *in the* **absence** *of the links in Fig-9.1.* Namely, F, the *feed-forward constant*, is the ratio of the system output b_5 to input a_0 when there are no waves incident on ports 1 to 4. The *driving vector* $\mathbf{D}$ describes the amplitudes $\mathbf{b} = \mathbf{D}\ a_0$ of the waves launched from ports 1 to 4 in response to the system input a_0. The *gathering vector* $\mathbf{G}$ defines the output $b_5 = \mathbf{G}^T\ \mathbf{a}$ arising from the incidence of waves $\mathbf{a}$ onto ports 1 to 4. Lastly, the reduced scattering matrix $\mathbf{S}$ describes the waves $\mathbf{b} = \mathbf{S}\ \mathbf{a}$ scattered from ports 1 to 4 in response to waves $\mathbf{a}$ incident on these same ports.

The links, of equal propagation constant β and lengths L_1 and L_2, in Fig-9.1 are assumed to satisfy:

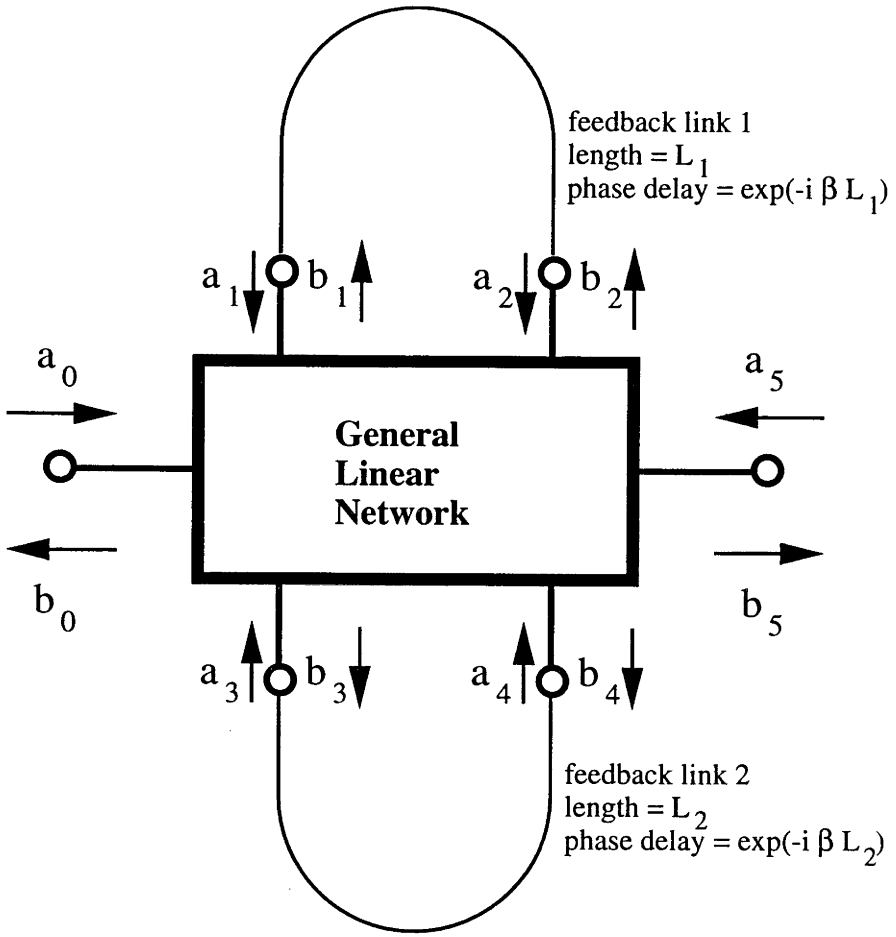

Figure 9.1: Notation for General Linear Interferometer

the boundaries of the general linear six-port in Fig-9.1 can be extended to include its effect inside the "black box", leaving a new output that is not fed back in any way (Fig-9.2). Note that multimoded optical ports can also be accommodated by a simple modification of above notation: for an N-moded port, N separate single-moded ports are assigned in the general model of Fig-9.1 and the field at the n^{th} port is defined by two complex amplitudes describing the incident and scattered n^{th} mode.

In a scattering matrix notation[Haus, 1984, §§3.2, 3.3][Pietzsch, 1989], the 6×6 matrix, S_6 describes the general linear, homogeneous relationship between the incident and scattered waves:

$$T(z_c, z_d) = F + \mathbf{G}^T\,\mathbf{C}(z_d)\,\mathbf{D}\,z_c + \mathbf{G}^T\,\mathbf{C}(z_d)\,\mathbf{S}\,\mathbf{C}(z_d)\,\mathbf{D}\,z_c^2 + \mathbf{G}^T\,(\mathbf{C}(z_d)\,\mathbf{S})^2\,\mathbf{C}(z_d)\,\mathbf{D}\,z_c^3 + \ldots \tag{9.8}$$

If the network is stable, this series converges, otherwise the output power would increase without bound. Practically, the output power would rise until the system were driven out of its linear operation regime and lasing could follow. The condition for stability is that all the eigenvalues of $\mathbf{S}\ \mathbf{C}(z_d)$ should lie within the unit disc. Here, we exclude, as being unattainable in practical systems, the case of *marginal* stability, where the system can be *perfectly* lossless, $\mathbf{S}\ \mathbf{C}(z_d)$ has an eigenvalue *exactly* on the unit circle and thus light recirculates precisely with neither loss nor gain in the links forever.

Under these conditions, the geometric series can be summed and:

$$T(z_c, z_d) = F + \mathbf{G}^T\,(I - z_c\mathbf{C}(z_d)\mathbf{S})^{-1} z_c\,\mathbf{C}(z_d)\,\mathbf{D} \tag{9.9}$$

where I denotes the 4×4 identity matrix. (9.9) can also be derived by a direct solution of (9.4) and (9.6), however, the geometric series (9.8) gives more insight into the system stability and will also be needed in §§9.5.2 and 9.5.4.

9.4 Resonant Michelson Interferometer Example

The general interferometer notation is now applied to the resonant Michelson interferometer in [Fritschel *et al.*, 1992], as shown in Fig-9.3; an optical fibre equivalent is shown in Fig-9.4.

Fabry-Pérot cavities are formed between the pairs of reflectors $m2$ and $m4$, and $m1$ and $m3$. In an optical fibre network, a symmetric 2×2 coupler is equivalent to the half-silvered mirror of the Michelson interferometer and the feedback links are shown as dashed lines. We first derive the F, $\mathbf{D}$, $\mathbf{G}$ and $\mathbf{S}$ matrices by considering the network's behaviour without the links. Let the scattering matrix description of the partially-reflecting mirror $m1$ be:

$$\begin{pmatrix} A_1 \\ b_1 \end{pmatrix} = \begin{pmatrix} r_1 & t_1 \\ t_1 & r_1' \end{pmatrix} \begin{pmatrix} B_1 \\ a_1 \end{pmatrix} \tag{9.10}$$

$$a_1 = \exp(-i\beta L_1)b_2;\ a_2 = \exp(-i\beta L_1)b_1;\ a_3 = \exp(-i\beta L_2)b_4;\ a_4 = \exp(-i\beta L_2)b_3 \tag{9.5}$$

or

$$\mathbf{a} = z_c\, \mathbf{C}(z_d)\, \mathbf{b} \text{ where } \mathbf{C}(z_d) = \begin{pmatrix} 0 & z_d & 0 & 0 \\ z_d & 0 & 0 & 0 \\ 0 & 0 & 0 & z_d^{-1} \\ 0 & 0 & z_d^{-1} & 0 \end{pmatrix} \tag{9.6}$$

and

$$z_c = \exp\left(-i\frac{\beta}{2}(L_1 + L_2)\right);\ z_d = \exp\left(-i\frac{\beta}{2}(L_1 - L_2)\right) \tag{9.7}$$

The notation is taken from the z-transform theory of discrete linear systems, the z-terms corresponding to pure delay lines. The present system resembles a digital filter in many ways and the stability considerations below are similar to those for such filters[Oppenheim and Schafer, 1975].

In analogy to the theory of electronic differential amplifiers, we call z_c and z_d the *common-mode* and *differential-mode* phase delays. If the links are lossless, β is real and z_c and z_d lie on the unit circle. The factors in (9.7) are used instead of $\exp(-i\beta(L_1 + L_2))$ and $\exp(-i\beta(L_1 - L_2))$, since, if the latter were used, the elements of the matrix in (9.6) would be $\sqrt{z_c\, z_d}$ and $\sqrt{z_c/z_d}$ rather than $z_c\, z_d$ and z_c/z_d. The reasoning in §§9.5.2 and 9.5.4 is based on the Laurent series with respect to z_c and z_d of the network transfer function and the square-roots would invalidate this reasoning by introducing branch-points at the origin of the complex plane.

The network can be analysed by a matrix analogy of the derivation of the transfer function for the fibre ring-resonator. In response to a unit input, a wave of amplitude F is immediately output from the system and a vector of waves $\mathbf{D}$ is launched into the links. After these waves travel the links, the vector $z_c\ \mathbf{C}(z_d)\ \mathbf{D}$ is incident on ports 1 to 4, generating a component $z_c\ \mathbf{G}^T\ \mathbf{C}(z_d)\ \mathbf{D}$ at the output and relaunching waves of amplitudes $z_c\ \mathbf{S}\ \mathbf{C}(z_d)\ \mathbf{D}$ into the links. This process leads to an infinite number of light recirculations, the n^{th} recirculation outputting a beam of amplitude $z_c^n\ \mathbf{G}^T\ (\mathbf{S}\ \mathbf{C}(z_d))^n\ \mathbf{C}(z_d)\ \mathbf{D}$. The total system transfer function, $T = b_5/a_0$, is thus:

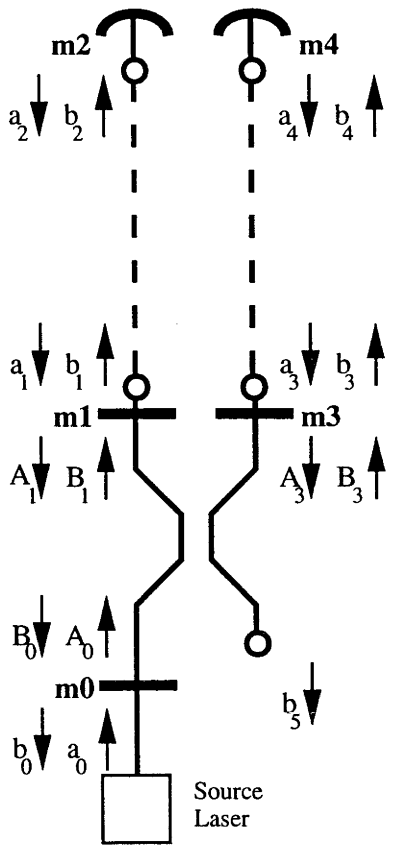

Figure 9.4: Optical Fibre Equivalent

$$\begin{pmatrix} B_1 \\ B_3 \end{pmatrix} = \mathrm{M} \begin{pmatrix} A_0 \\ 0 \end{pmatrix}; \quad \begin{pmatrix} B_0 \\ b_5 \end{pmatrix} = \mathrm{M}^T \begin{pmatrix} A_1 \\ A_3 \end{pmatrix}$$

$$\begin{pmatrix} A_1 \\ A_3 \end{pmatrix} = r \begin{pmatrix} B_1 \\ B_3 \end{pmatrix} + i\sqrt{1-r^2} \begin{pmatrix} a_1 \\ a_3 \end{pmatrix}; \quad \begin{pmatrix} b_1 \\ b_3 \end{pmatrix} = i\sqrt{1-r^2} \begin{pmatrix} B_1 \\ B_3 \end{pmatrix} + r \begin{pmatrix} a_1 \\ a_3 \end{pmatrix}$$

$$A_0 = r_0 B_0 + i\sqrt{1-r_0^2}\, a_0 \tag{9.13}$$

where $r_1 = r_3 = r$ and mirrors $m1$ and $m3$ are identical. On elimination of A_1, B_1, A_3, B_3, A_0 and B_0:

$$\begin{pmatrix} b_1 \\ b_3 \end{pmatrix} = \begin{pmatrix} r - \frac{r_0(1-r^2)}{2} & -i\frac{r_0(1-r^2)}{2} \\ -i\frac{r_0(1-r^2)}{2} & r + \frac{r_0(1-r^2)}{2} \end{pmatrix} \begin{pmatrix} a_1 \\ a_3 \end{pmatrix} - \frac{\sqrt{1-r^2}\sqrt{1-r_0^2}}{\sqrt{2}} \begin{pmatrix} 1 \\ i \end{pmatrix} a_0 \tag{9.14}$$

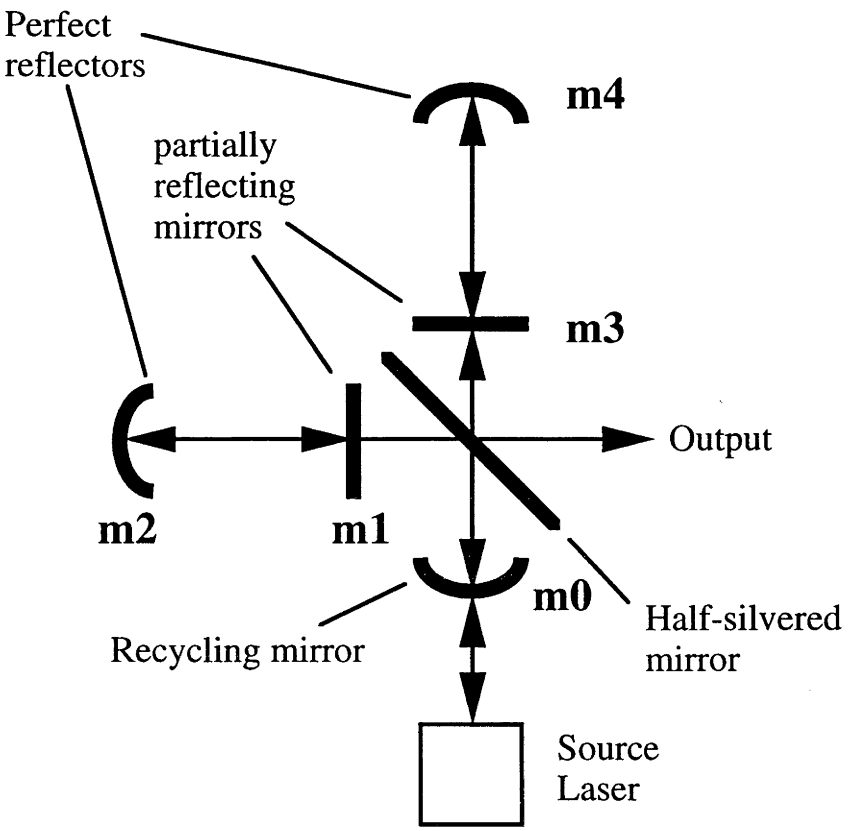

Figure 9.3: Resonant Michelson Interferometer

For a reciprocal mirror, the 2×2 matrix is self-transpose[Pietzsch, 1989]. The mirror is assumed to be symmetric, *i.e.* appears the same to wave a_1 as it does to wave B_1, so that $r_1 = r_1'$. A lossless mirror has a unitary scattering matrix[Pietzsch, 1989], so that its scattering matrix must have the form:

$$\mathbf{S}_{m1} = \begin{pmatrix} r_1 & i\sqrt{1-r_1^2} \\ i\sqrt{1-r_1^2} & r_1 \end{pmatrix} \tag{9.11}$$

where r_1 is the mirror's reflexion co-efficient. Let:

$$\mathbf{M} = \frac{1}{\sqrt{2}} \begin{pmatrix} 1 & i \\ i & 1 \end{pmatrix} \tag{9.12}$$

be the transfer matrix of the 2×2 symmetric coupler, by analogy with (9.11). In the absence of the feedback links, the optical fibre network in Fig-9.4 obeys:

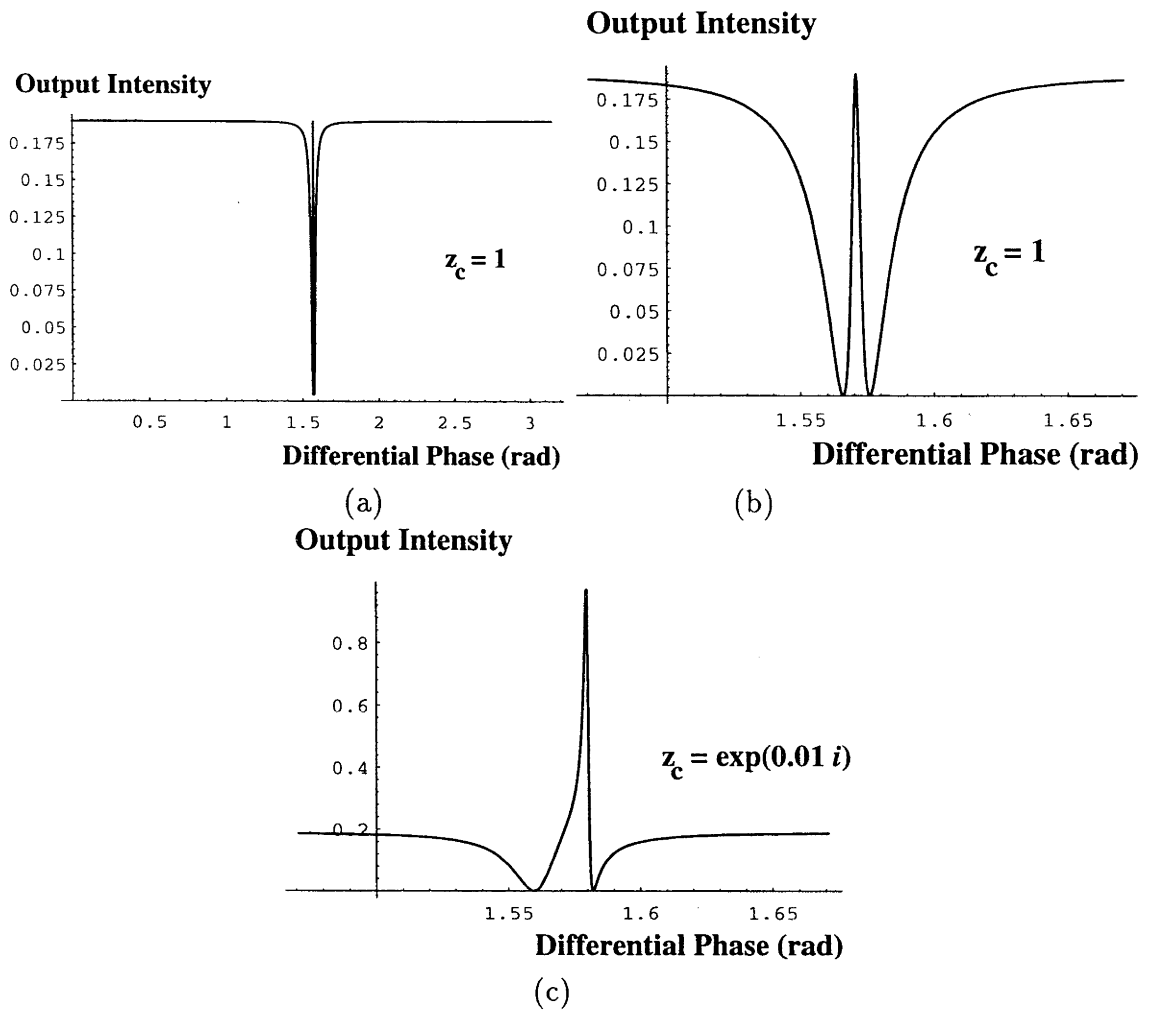

Figure 9.5: Interferometer response; *(a)* $z_c = 1$; *(b)* close up of *(a)*; *(c)* $z_c = \exp(0.01i)$

the magnitude *and* phase of $S_{jk} = T(z_c, z_d)$ to be independent of the common-mode phase delay, z_c. However, observe that (9.8) expresses T as its *unique* Taylor series with respect to z_c about the point $z_c = 0$, thus T is independent of z_c if and only if the terms $\mathbf{G}^T\mathbf{C}(z_d)\mathbf{D}z_c$, $\mathbf{G}^T\mathbf{C}(z_d)\mathbf{SC}(z_d)\mathbf{D}z_c^2$, ... all vanish. However, this implies that $T = F$ and is independent of z_d (with (9.8) considered as the unique Laurent series in z_d about $z_d = 0$) so that:

If an element of a linear optical network's scattering matrix is a function of two optical lengths L_1 and L_2, then this scattering matrix element **must** *have some dependence on the common-mode length, $L_1 + L_2$. If not, then it has no dependence on the differential mode length $L_1 - L_2$ either and is therefore completely independent*

$$b_5 = \frac{\sqrt{1-r^2}}{\sqrt{2}} \begin{pmatrix} -(1+rr_0) & i(1-rr_0) \end{pmatrix} \begin{pmatrix} a_1 \\ a_3 \end{pmatrix} - r\sqrt{1-r_0^2}\, a_0 \qquad (9.15)$$

In the absence of the feedback links, ports 2 and 4 are completely decoupled from the input, the output and from ports 1 and 2 and so $a_2 = -b_2$ and $a_4 = -b_4$. Thus, using (9.14) and (9.15) we find:

$$\mathbf{S} = \begin{pmatrix} r - \frac{r_0(1-r^2)}{2} & 0 & -i\frac{r_0(1-r^2)}{2} & 0 \\ 0 & -1 & 0 & 0 \\ -i\frac{r_0(1-r^2)}{2} & 0 & r + \frac{r_0(1-r^2)}{2} & 0 \\ 0 & 0 & 0 & -1 \end{pmatrix}; \quad \mathbf{D} = -\frac{\sqrt{1-r^2}\sqrt{1-r_0^2}}{\sqrt{2}} \begin{pmatrix} 1 \\ 0 \\ i \\ 0 \end{pmatrix} \qquad (9.16)$$

$$\mathbf{G} = -\frac{\sqrt{1-r^2}}{\sqrt{2}} \begin{pmatrix} -(1+rr_0) \\ 0 \\ i(1-rr_0) \\ 0 \end{pmatrix}; \quad F = -r\sqrt{1-r_0^2} \qquad (9.17)$$

Using (9.9), some aspects of this interferometer's behaviour are shown in Fig-9.5, where $r = 0.95$ and $r_0 = 0.9$. For each plot, z_c is constant, $z_d = \exp(i\theta)$ and the intensity $|T(z_c, z_d)|^2$ is plotted as a function of θ. In *(a)* $z_c = 1$ and *(b)* is a close-up of *(a)* for $\theta \approx \pi/2$. Plot *(c)* is the same close up for $z_c = \exp(0.01i)$, *i.e.* with the common-mode phase varied by 0.01 radian so that T is a sensitive function of z_c in this case.

9.5 General Linear, Differential Interferometers

9.5.1 Differential Intensity *and* Phase Response

Using the general description of linear optical networks formulated in §9.3, we shall now derive complete characterisations of the class of interferometers whose outputs depend *only* on the difference of two optical lengths.

Consider first an element S_{jk} of the scattering matrix of a general linear optical network. Suppose that S_{jk} depends on two optical lengths. The physical interpretation of S_{jk} is the complex amplitude of the wave output from port j in response to a unit-amplitude excitation of port k when all other ports are undriven. Hence, S_{jk} can be interpreted as a network transfer function $T(z_c, z_d)$. Suppose we require *both*

Zehnder interferometers. The proof assumes the magnitude of $T(z_c, z_d)$ to be independent of z_c for unit-magnitude z_c and z_d and then derives the most general possible $T(z_c, z_d)$ fulfilling this condition.

Note that $T(z_c, z_d)$ is a rational function of z_c and z_d (equation (9.9)). A rational function $\omega(z)$ has a constant magnitude on the unit circle if and only if its poles p_k and zeros q_k are symmetrical with respect to the unit circle[Papoulis, 1977][Oppenheim and Schafer, 1975, §7.2], *i.e.* $q_k = 1/p_k^*$ and

$$\omega(z) = \omega_0 \, z^{n_0} \frac{\prod_k \left(z - \frac{1}{p_k^*}\right)}{\prod_k (z - p_k) a}$$

which is equivalent to (the c_k are symmetric functions of the co-efficients p_k):

$$\omega(z) = \omega_0 \, z^{n_0} \frac{c_0 + c_1 z + c_2 z^2 + \ldots + c_{N-1} z^{N-1} + c_N z^N}{c_N^* + c_{N-1}^* z + c_{N-2}^* z^2 + \ldots + c_1^* z^{N-1} + c_0^* z^N} \tag{9.18}$$

where n_0 is an integer, *i.e.* the denominator co-efficients are the conjugates of those in the numerator written in backward order. Now $T(z_c, z_d)$ is a ratio of polynomials in z_c whose co-efficients are polynomial functions of z_d and, by assumption, the magnitude of $T(z_c, z_d)$ is independent of z_c for $|z_c| = |z_d| = 1$. Therefore:

$$T(z_c, z_d) = T_0(z_d) z_c^{n_0} \frac{c_0(z_d) + c_1(z_d) z_c + \ldots + c_N(z_d) z_c^N}{(c_N(z_d))^* + (c_{N-1}(z_d))^* z_c + \ldots + (c_0(z_d))^* z_c^N} \tag{9.19}$$

Here the functions $T_0(z_d)$, $c_0(z_d)$, ... , $c_N(z_d)$ correspond to the constants ω_0, c_0, ... ,c_N in (9.5.2); we must allow for their being functions of z_d. Note that $z_d^* = z_d^{-1}$ for $|z_d| = 1$, hence (9.19) can be written as:

$$\begin{aligned} T(z_c, z_d) &= T_0(z_d) z_c^{n_0} \frac{\sum_{j=0}^{N} \sum_{k=0}^{M} c_{j,k} z_d^k z_c^j}{\sum_{j=0}^{N} \left(\sum_{k=0}^{M} c_{N-j,k} z_d^k \right)^* z_c^j} \\ &= T_0(z_d) z_c^{n_0} z_d^M z_c^{-N} \frac{\sum_{j=0}^{N} \sum_{k=0}^{M} c_{j,k} z_d^k z_c^j}{\sum_{k=0}^{M} \left(\sum_{j=0}^{N} c_{j,M-k} z_c^j \right)^* z_d^k} = T_0(z_d) P(z_c, z_d) \end{aligned} \tag{9.20}$$

of L_1 and L_2.

This result is relevant to integrated optical devices in particular. For example, one may wish to implement an accurately known, absolute optical delay of a certain phase ϕ between the two ports with constant attenuation $\mathcal{A}$, so that $S_{jk} = \mathcal{A}\exp(i\phi)$, $\mathcal{A} < 1$. It is desirable that *both* the magnitude and phase of S_{jk} should be differential functions of two optical lengths for good device temperature insensitivity. By the above result, such an implementation is impossible. Note that this result is *not* contradicted by the designs of §8.3; there, temperature drifts will cause a phase change common to all the elements of the transfer matrices in question, but only *relative* phase changes *between* transfer matrix elements affect the suitability of the devices in question for their intended purpose. We shall return to this consideration below when only *relative* phase changes within the transfer matrix are important.

9.5.2 Differential Intensity Response Only

In interferometry, a less stringent requirement is sought as only the output intensity need be a differential function of two lengths. The output phase is irrelevant since most detectors cannot detect phase, the whole purpose of interferometry being to convert phase- to intensity-variations. We accordingly ask:

Given the network of Fig-9.1, when can two paths link ports 1 to 4 as shown such that the transfer function magnitude $|T(z_c, z_d)|$ is a function of only z_d for all z_c, z_d on the unit circle?

The assumption that z_c and z_d must lie on the unit circle is equivalent to an assumption of lossless links (equation (9.7)). Lossy links can usually be accounted for by replacing z_c by $\mathcal{A}z_c$, where $\mathcal{A} < 1$ is an attenuation. The attenuation varies far less than the phase delay, for the small length variations normally encountered in interferometry.

It will now be proven that if an interferometer is differential, its output intensity as a function of z_d has the same form as that of the classical Michelson or Mach

where $P(z_c, z_d) = T(z_c, z_d)/T_0(z_d)$. By regarding $P(z_c, z_d)$ as a ratio of polynomials in z_d whose co-efficients are polynomials in z_c, we can reverse the above reasoning to apply (9.18) to $P(z_c, z_d)$; this function then has unit magnitude for *all* z_c *and* z_d, so that the only variation in the transfer-function magnitude can arise from $T_0(z_d)$, which will now be shown to have a particularly simple form.

$T_0(z_d)$ is expanded as the unique Laurent series about $z_d = 0$ and $P(z_c, z_d)$ is expanded as the unique Laurent series with respect to z_c about $z_c = 0$, thus representing $T(z_c, z_d)$ as an infinite series with terms of the form $t_{j,k} z_c^j z_c^k$. The term $z_c^j z_d^k$ represents a component of the output light that has travelled the upper link $(j + k)/2$ times in Fig-9.1 and the lower link $(j - k)/2$ times. Hence, for real, causal interferometers, neither $j + k$ nor $j - k$ is negative, so that $j \geq 0$, $|k| \leq j$. Consider *any* term $z_c^u z_d^v$ in the Laurent expansion for $P(z_c, z_d)$. The powers of z_d in the Laurent expansion for $T_0(z_d)$ cannot be greater than $u - v$ nor less than $-(u+v)$ and the Laurent series for $T_0(z_d)$ must be finite:

$$T_0(z_d) = \frac{t_0 + t_1 z_d + \ldots + t_m z_d^m}{z_d^n} \tag{9.21}$$

where m and n are integers. The number of zeros of $T_0(z_d)$, equal to m, is now calculated from (9.8). These zeros are also zeros of $T(z_c, z_d)$ which are independent of z_c; at such a zero, (9.8) gives:

$$F = 0; \quad \mathbf{G}^T \left(\mathbf{C}(z_d)\, \mathbf{S}\right)^R \mathbf{C}(z_d)\, \mathbf{D} = 0 \text{ for } R = 0,\ 1,\ 2,\ 3, \ldots \tag{9.22}$$

Only the terms for $R = 0$, 1 2 and 3 need be considered as the Cayley-Hamilton theorem[Michel and Herget, 1981, §4.5] shows that all higher powers of $\mathbf{C}(z_d)\, \mathbf{S}$ are linear expressions in cubic or lower powers. Hence, $T_0(z_d)$ has a zero if and only if $F = 0$ and:

$$\begin{aligned}
&\mathbf{G}^T\, \mathbf{C}(z_d)\, \mathbf{D} = \tfrac{1}{z_d}\left(\tau_{00} + \tau_{02} z_d^2\right) = 0 \\
&\mathbf{G}^T\, \mathbf{C}(z_d)\, \mathbf{S}\, \mathbf{C}(z_d)\, \mathbf{D} = \tfrac{1}{z_d^2}\left(\tau_{10} + \tau_{12} z_d^2 + \tau_{14} z_d^4\right) = 0 \\
&\mathbf{G}^T \left(\mathbf{C}(z_d)\, \mathbf{S}\right)^2 \mathbf{C}(z_d)\, \mathbf{D} = \tfrac{1}{z_d^2}\left(\tau_{20} + \tau_{22} z_d^2 + \tau_{24} z_d^4 + \tau_{16} z_d^6\right) = 0 \\
&\mathbf{G}^T \left(\mathbf{C}(z_d)\, \mathbf{S}\right)^3 \mathbf{C}(z_d)\, \mathbf{D} = \tfrac{1}{z_d^2}\left(\tau_{30} + \tau_{32} z_d^2 + \tau_{34} z_d^4 + \tau_{36} z_d^6 + \tau_{38} z_d^8\right) = 0
\end{aligned} \tag{9.23}$$

by direct computation of the terms in (9.22). The τ_{jk} are functions of the elements of $\mathbf{D}$, $\mathbf{G}$ and $\mathbf{S}$. Thus, $T_0(z_d)$ can have at most eight zeros in pairs of the form $\pm z_0$.

A straightforward computation of the terms in (9.23) shows that there can be only four zeros in two pairs of the form $\pm z_0$, as follows. The number of zeros of $T_0(z_d)$ is bounded by the lowest polynomial degree in (9.23). Hence there are at most two zeros $\pm\sqrt{\tau_{00}/\tau_{02}}\, i$ unless $\tau_{00} = \tau_{02} = 0$, in which case (9.22) shows that:

$$\begin{gathered}
\tau_{10} = -\frac{g_1}{d_1}\left(d_2^2 S_{11} + d_1 d_2 (S_{12} - S_{21}) - d_1^2 S_{22}\right) \\
\tau_{14} = -\frac{g_3}{d_3}\left(d_4^2 S_{33} + d_3 d_4 (S_{34} - S_{43}) - d_3^2 S_{44}\right) \\
\tau_{20} = (S_{12} + S_{21})\tau_{10}; \quad \tau_{26} = (S_{34} + S_{43})\tau_{14} \\
\tau_{30} = (S_{12}^2 + S_{12}S_{21} + S_{21}^2 + S_{11}S_{22})\tau_{10}; \quad \tau_{38} = (S_{34}^2 + S_{34}S_{43} + S_{43}^2 + S_{33}S_{44})\tau_{14}
\end{gathered} \tag{9.24}$$

Now, $T_0(z_d)$ can have at most four roots, defined by the second equation in the set (9.23), unless $\tau_{10} = \tau_{12} = \tau_{14} = 0$. However, the latter would imply that $\tau_{20} = \tau_{26} = \tau_{30} = \tau_{38} = 0$, and the remaining equations can still have at most four roots in pairs of the form $\pm z_0$. Hence, for a wholly differential interferometer, the most general form of the system transfer function magnitude is:

$$|T_0(z_d)| = \left|t_0 + t_2 z_d^2 + t_4 z_d^4\right| \tag{9.25}$$

This function can be realised by the generalised classical Michelson interferometer shown in Fig-9.6. The classical Mach-Zehnder corresponds to either $t_0 = 0$ or $t_4 = 0$.

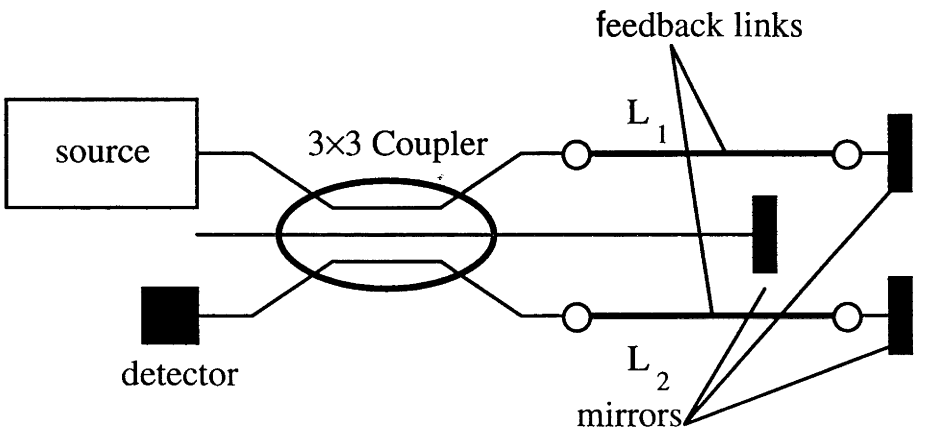

Figure 9.6: Generalised Michelson Interferometer

This proof does not exclude the existence of a resonant, differential interferometer. However, its transfer-function magnitude would have the same form as that

of the device in Fig-9.6 and its sensitivity could not exceed that of the Michelson interferometer in §9.5.3.

Note also that the proof does not exclude an interferometer which is both more sensitive than the Michelson and also insensitive to small common-mode path length variations *at a particular value of* z_d. (9.9) can have the structure imposed by (9.18) at finitely many values of z_d on the unit circle and still be a globally nonconstant function of z_c.

It should lastly be noted that there are schemes that do achieve resonant, differential behaviour by violating the assumptions underlying the proofs in this Chapter[Farahi *et al.*, 1988; Ilyama *et al.*, 1990]. Such schemes make use of partially-coherent sources and polychromatic light and would seem to be far less practical than standard, monochromatic-light interferometers.

9.5.3 Maximally Sensitive Michelson Interferometer

We now find values of t_0, t_2 and t_4 such that the phase sensitivity in (9.25) is maximised, given the constraint $|T_0(z_d)| \leq G_{max}$. If the system is passive, $G_{max} \leq 1$, otherwise $G_{max} > 1$ corresponds to the presence of gain[2]. Let $z_d = \exp(i\theta_d)$, then:

$$\begin{aligned} |T_0|^2 &= |t_0|^2 + |t_2|^2 + |t_4|^2 + 2|t_2||t_0|\cos(2\theta_d + \phi_2 - \phi_0) + \\ &\quad 2|t_4||t_2|\cos(2\theta_d + \phi_4 - \phi_2) + 2|t_4||t_0|\cos(4\theta_d + \phi_4 - \phi_0) \\ s_p &= \frac{d|T_0|^2}{d\theta_d} = -4|t_2||t_0|\sin(2\theta_d + \phi_2 - \phi_0) - \\ &\quad 4|t_4||t_2|\sin(2\theta_d + \phi_4 - \phi_2) - 8|t_4||t_0|\sin(8\theta_d + \phi_4 - \phi_0) \end{aligned} \tag{9.26}$$

where $\phi_j = \arg(t_j)$ and s_p is the phase-sensitivity. The maximum of $|T_0|$ is $t_0+t_2+t_4$ and occurs when $2\theta_d + \phi_2 - \phi_0 = 2\theta_d + \phi_4 - \phi_2 = 0$, thus the gain constraint is $t_0 + t_2 + t_4 = G_{max}$. The expression for θ_d maximising s_p is unwieldy and not conducive to further analysis, so we proceed by observing that the sensitivity is

[2]Clearly, if $|T_0| \leq G_{max}$, then the phase-sensitivity is maximised for $|T_0| = G_{max}$. Suppose that we find the system with maximal phase-sensitivity subject to $|T_0| = r < G_{max}$, then we can scale t_0, t_2 and t_4, thus multiplying this maximum sensitivity by the factor G_{max}/r and increasing $|T_0|$ to G_{max}.

A straightforward computation of the terms in (9.23) shows that there can be only four zeros in two pairs of the form $\pm z_0$, as follows. The number of zeros of $T_0(z_d)$ is bounded by the lowest polynomial degree in (9.23). Hence there are at most two zeros $\pm\sqrt{\tau_{00}/\tau_{02}}\, i$ unless $\tau_{00} = \tau_{02} = 0$, in which case (9.22) shows that:

$$\begin{gathered}
\tau_{10} = -\frac{g_1}{d_1}\left(d_2^2 S_{11} + d_1 d_2 (S_{12} - S_{21}) - d_1^2 S_{22}\right) \\
\tau_{14} = -\frac{g_3}{d_3}\left(d_4^2 S_{33} + d_3 d_4 (S_{34} - S_{43}) - d_3^2 S_{44}\right) \\
\tau_{20} = (S_{12} + S_{21})\tau_{10}; \quad \tau_{26} = (S_{34} + S_{43})\tau_{14} \\
\tau_{30} = (S_{12}^2 + S_{12}S_{21} + S_{21}^2 + S_{11}S_{22})\tau_{10}; \quad \tau_{38} = (S_{34}^2 + S_{34}S_{43} + S_{43}^2 + S_{33}S_{44})\tau_{14}
\end{gathered} \tag{9.24}$$

Now, $T_0(z_d)$ can have at most four roots, defined by the second equation in the set (9.23), unless $\tau_{10} = \tau_{12} = \tau_{14} = 0$. However, the latter would imply that $\tau_{20} = \tau_{26} = \tau_{30} = \tau_{38} = 0$, and the remaining equations can still have at most four roots in pairs of the form $\pm z_0$. Hence, for a wholly differential interferometer, the most general form of the system transfer function magnitude is:

$$|T_0(z_d)| = \left|t_0 + t_2 z_d^2 + t_4 z_d^4\right| \tag{9.25}$$

This function can be realised by the generalised classical Michelson interferometer shown in Fig-9.6. The classical Mach-Zehnder corresponds to either $t_0 = 0$ or $t_4 = 0$.

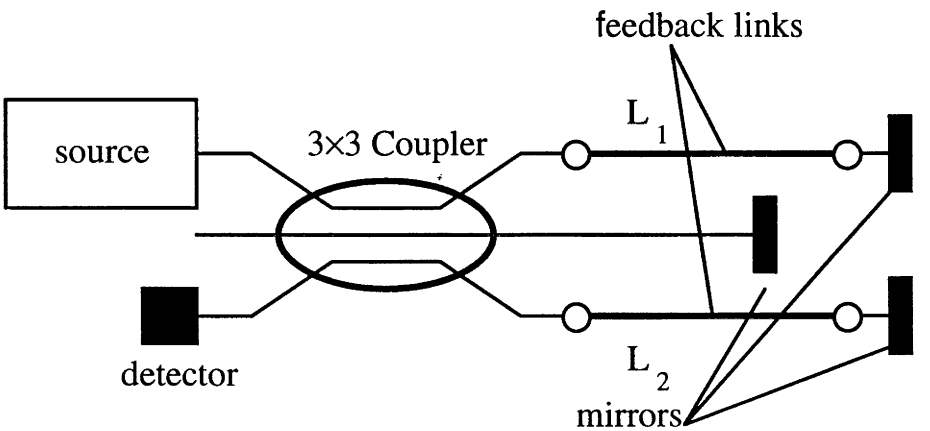

Figure 9.6: Generalised Michelson Interferometer

This proof does not exclude the existence of a resonant, differential interferometer. However, its transfer-function magnitude would have the same form as that

of the device in Fig-9.6 and its sensitivity could not exceed that of the Michelson interferometer in §9.5.3.

Note also that the proof does not exclude an interferometer which is both more sensitive than the Michelson and also insensitive to small common-mode path length variations *at a particular value of* z_d. (9.9) can have the structure imposed by (9.18) at finitely many values of z_d on the unit circle and still be a globally nonconstant function of z_c.

It should lastly be noted that there are schemes that do achieve resonant, differential behaviour by violating the assumptions underlying the proofs in this Chapter[Farahi *et al.*, 1988; Ilyama *et al.*, 1990]. Such schemes make use of partially-coherent sources and polychromatic light and would seem to be far less practical than standard, monochromatic-light interferometers.

9.5.3 Maximally Sensitive Michelson Interferometer

We now find values of t_0, t_2 and t_4 such that the phase sensitivity in (9.25) is maximised, given the constraint $|T_0(z_d)| \leq G_{max}$. If the system is passive, $G_{max} \leq 1$, otherwise $G_{max} > 1$ corresponds to the presence of gain[2]. Let $z_d = \exp(i\theta_d)$, then:

$$\begin{aligned} |T_0|^2 &= |t_0|^2 + |t_2|^2 + |t_4|^2 + 2|t_2||t_0|\cos(2\theta_d + \phi_2 - \phi_0) + \\ &\quad 2|t_4||t_2|\cos(2\theta_d + \phi_4 - \phi_2) + 2|t_4||t_0|\cos(4\theta_d + \phi_4 - \phi_0) \\ s_p &= \frac{d|T_0|^2}{d\theta_d} = -4|t_2||t_0|\sin(2\theta_d + \phi_2 - \phi_0) - \\ &\quad 4|t_4||t_2|\sin(2\theta_d + \phi_4 - \phi_2) - 8|t_4||t_0|\sin(8\theta_d + \phi_4 - \phi_0) \end{aligned} \tag{9.26}$$

where $\phi_j = \arg(t_j)$ and s_p is the phase-sensitivity. The maximum of $|T_0|$ is $t_0+t_2+t_4$ and occurs when $2\theta_d + \phi_2 - \phi_0 = 2\theta_d + \phi_4 - \phi_2 = 0$, thus the gain constraint is $t_0 + t_2 + t_4 = G_{max}$. The expression for θ_d maximising s_p is unwieldy and not conducive to further analysis, so we proceed by observing that the sensitivity is

[2]Clearly, if $|T_0| \leq G_{max}$, then the phase-sensitivity is maximised for $|T_0| = G_{max}$. Suppose that we find the system with maximal phase-sensitivity subject to $|T_0| = r < G_{max}$, then we can scale t_0, t_2 and t_4, thus multiplying this maximum sensitivity by the factor G_{max}/r and increasing $|T_0|$ to G_{max}.

overbounded by $|s_p| \leq \hat{s} = 4|t_2||t_0| + 4|t_4||t_2| + 8|t_4||t_0|$. We firstly solve the simpler problem of maximising $\hat{s}$; it then turns out that there is indeed a value of θ_p *realising* the overbound, *i.e.* for which $|s_p| = \hat{s}$. Thus, the problems of maximising $|s_p|$ and $\hat{s}$ turn out to be equivalent. $\hat{s}$ is maximised[3], subject to the gain constraint, by setting $t_2 = 0$ and $t_0 = t_4 = G_{max}/2$, with $8\theta_p + \phi_4 - \phi_0 = \pi/2$ realising $|s_p| = \hat{s}$. This corresponds to a classical two-arm Michelson interferometer with a symmetric, equi-splitting 2×2 directional coupler as the beamsplitter, which gives the maximum phase-sensitivity possible for a differential interferometer using monochromatic light.

9.5.4 Differential Intensity and Relative Phase Response

Recall that a linear optical network's scattering matrix elements cannot be independent of both z_c and z_d also, where z_c and z_d refer to the common- and differential-mode delays imposed by any two optical lengths. However, often only the *relative* phases between the scattering matrix elements are important, as in §§6.1.5, 8.2, 8.3.

Let two scattering matrix elements be $T_1(z_c, z_d)$ and $T_2(z_c, z_d)$ and consider when the magnitudes $|T_1|$, $|T_2|$, *together with* their *relative* phase $\arg(T_1/T_2)$, are independent of z_c. Thus, both the magnitude *and* phase of:

$$\frac{T_1}{T_2} = \frac{F_1 \; + \; \mathbf{G}_1^T \, \mathbf{C}_1(z_d) \, \mathbf{D}_1 \, z_c + \mathbf{G}_1^T \, \mathbf{C}_1(z_d) \, \mathbf{S}_1 \, \mathbf{C}_1(z_d) \, \mathbf{D}_1 \, z_c^2 + \ldots}{F_2 \; + \; \mathbf{G}_2^T \, \mathbf{C}_2(z_d) \, \mathbf{D}_2 \, z_c + \mathbf{G}_2^T \, \mathbf{C}_2(z_d) \, \mathbf{S}_2 \, \mathbf{C}_2(z_d) \, \mathbf{D}_2 \, z_c^2 + \ldots} \tag{9.27}$$

must be independent of z_c, *i.e.* $T_1/T_2 = \lim_{z_c \to 0} T_1/T_2$ for all complex z_c so that:

$$\frac{T_1}{T_2} = \frac{\mathbf{G}_1^T \; (\mathbf{C}_1(z_d) \, \mathbf{S}_1)^{N_1 - 1} \; \mathbf{C}_1(z_d) \, \mathbf{D}_1 \, z_c^{N_1}}{\mathbf{G}_2^T \; (\mathbf{C}_2(z_d) \, \mathbf{S}_2)^{N_1 - 1} \; \mathbf{C}_2(z_d) \, \mathbf{D}_2 \, z_c^{N_1}} \tag{9.28}$$

Here F_1, G_1^T, ... (*resp.* F_2, G_2^T, ...) are the quantities defined in §9.3 for T_1 (*resp.* T_2). However, $|T_1|$ and $|T_2|$ are individually independent of z_c, so, by (9.25):

$$T_1(z_d) = t_{10} + t_{12} z_d^2 + t_{14} z_d^4; \quad T_2(z_d) = t_{20} + t_{22} z_d^2 + t_{24} z_d^4 \tag{9.29}$$

[3]By the method of Lagrange Multipliers, we must solve:

$$\frac{\partial(4|t_2||t_0| + 4|t_4||t_2| + 8|t_4||t_0| + \lambda(t_0 + t_2 + t_4))}{\partial t_j} = 0$$

for some constant λ.

are the most general forms that the scattering matrix elements can take if their magnitudes and relative phase are to be independent of the common-mode optical delay.

9.6 Conclusions

This Chapter has discussed the advantages of differential operation in avoiding the detrimental effects of source laser frequency jitter and temperature drifts in integrated optical circuits.

The transfer function was derived for a general linear optical network when its behaviour depends on two optical lengths and was applied to a proposed resonant interferometer. Using the general transfer function, it was proven that no element of a general linear N-port's scattering matrix can be made a wholly differential function of two lengths, *i.e.* the dependence on the sum of the lengths cannot be annulled without annulling the dependence on the difference between these lengths also. It was then shown that if the network's transfer function magnitude is a wholly differential function of two optical lengths, then this transfer function has the same form as that of the Michelson or Mach-Zehnder interferometers, proving that the Michelson interferometer attains the greatest sensitivity of all differential interferometers. Further, the most general form of a linear network's scattering parameters was derived if the parameter magnitudes and *relative* phases must be wholly differential functions of two optical lengths.

There exist schemes achieving resonant, differential behaviour through violation of the assumptions underlying the proofs of this Chapter. Such schemes employ partially-coherent or polychromatic light.

With reference to the appraisals in §8.6, the results of this Chapter are important to the future of planar devices in that they exclude the use of optical feedback and resonance in passive linear networks unless *(i)* adequate steps are taken to temperature-stabilise the device concerned; or *(ii)* feedback control of optical lengths is implemented to counteract temperature drift-induced strains; or *(iii)* the device's intended function is to measure temperature drift-induced strain.

Chapter 10

Adiabatic Mode Multiplexors

10.1 Introduction

All the planar devices studied in the previous chapters derive their behaviour from interferometric effects, *i.e.* the beating between optical modes. This Chapter is devoted to the design of a very different device, the *adiabatic forked splitter*, which seeks to separate a waveguide's eigenfields physically so that they *cannot* interfere, thus bestowing an outstanding wavelength *independence* on the device. In contrast, since the optical delays between modes are wavelength sensitive, so is the behaviour of any device depending on modal interferometric effects.

The adiabatic splitter concept is not new, having been *experimentally* proven for the cases of the 2-forked splitter in the 1970s[Yajima, 1978; Burns and Milton, 1980] and the so-called *warped mode* microwave coupler in the mid-1980s[Islam and Carroll, 1986]; more, recently, its implementation in planar integrated optics has been studied[Shani *et al.*, 1991]. Here, we generalise the device to several modal channels, study its systematic design in detail and thus underline the important design issues. We also study problems arising in the interfacing of the adiabatic Y-splitter to other optical system components.

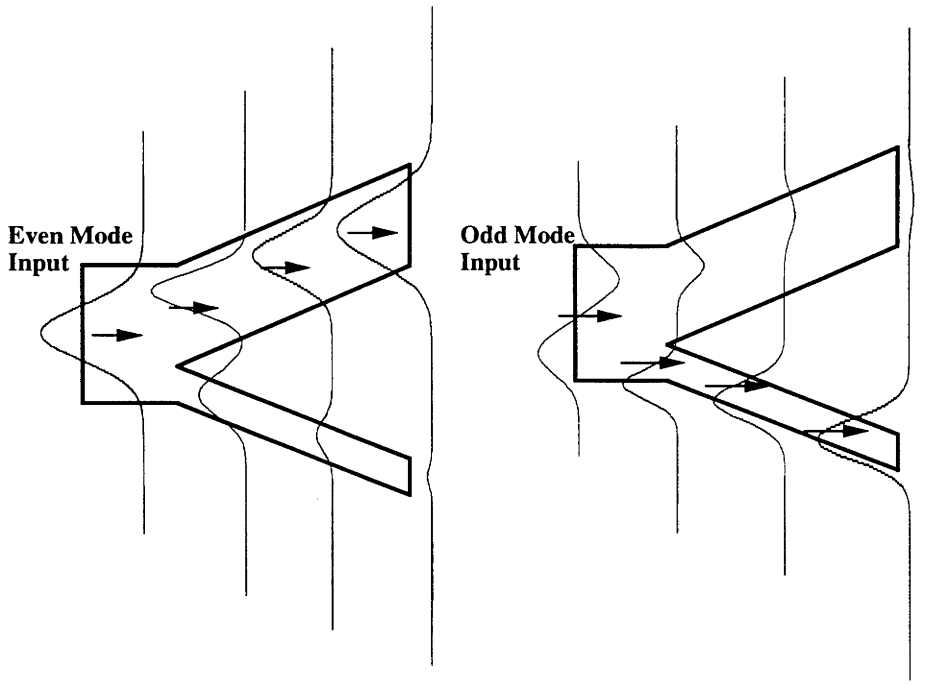

Figure 10.1: Adiabatic Mode Evolution in Asymmetric Y-Splitter

10.2 Basic Concepts and Design Considerations

10.2.1 Adiabatic Mode Separation

The basic two-channel scheme is shown in Fig-10.1 and, as in Chapter-3, the key to understanding this device is the concept of *local modes*, *i.e.* the modes of a translationally-invariant waveguide with the same cross-section as that of the splitter at the axial position in question. In *adiabatic* devices, the cross-sectional evolution with axial distance is so slow that negligible power is transferred between the local modes, hence, if power is input to the device wholly in one mode, then the corresponding local mode at the output carries almost all of the input power.

In Fig-10.1, the local modes at the device input are the even and odd modes of the square-core waveguide. At the output, the local modes are the modes of an asymmetric coupler, which are almost exactly the eigenfields of the two constituent rectangular/slab waveguides in isolation if these guides are single-moded, sufficiently different and weakly coupled. As the waveguides become weakly coupled, the two bound eigenfields of the composite structure are well approximated by linear superpositions of the individual waveguide eigenfields[Snyder and Love, 1983, §18-18] and

the ratio of the waveguide power in the thick waveguide to that in the thin guide is given by α_1 (*resp.* α_2) when the fundamental (*resp.* second) local mode is present at the system output, where:

$$\alpha_1 = \frac{(\beta_1-\beta_2)^2}{2C^2} + 1 + \frac{\beta_1-\beta_2}{C}\sqrt{1+\frac{(\beta_1-\beta_2)^2}{4C^2}} \rightarrow \frac{(\beta_1-\beta_2)^2}{C^2} \text{ as } C \rightarrow 0;$$
$$\alpha_2 = \frac{1}{\alpha_1} = \frac{(\beta_1-\beta_2)^2}{2C^2} + 1 - \frac{\beta_1-\beta_2}{C}\sqrt{1+\frac{(\beta_1-\beta_2)^2}{4C^2}} \rightarrow \frac{C^2}{(\beta_1-\beta_2)^2} \text{ as } C \rightarrow 0 \tag{10.1}$$

Here β_1, β_2 are the two waveguide propagation constants and C the coupling coefficient between them. If, as in Fig-10.1, only the even *(respectively: odd)* mode is driven at the input, the even mode energy will be almost wholly channelled into the wide *(respectively: narrow)* output waveguide provided the device is adiabatic. Conversely, by the Reciprocity Law, with the roles of input and output swapped and the wide *(respectively: narrow)* waveguide only driven, only the even *(respectively: odd)* mode will be excited at the left-hand end of the device.

10.2.2 Adiabatic Y-Splitter Applications

A Y-splitter behaving as described above would find many applications in diverse fields. These include:

- Mode multiplexing, where different communications channels are provided by the modes of a multimode waveguide, in particular, at the same wavelength (Fig-10.2);
- As a modalmetric sensor, where a sensed measurand affects each mode of a multimoded waveguide differently and thus can be measured by finding the modal content of the waveguide's output light (Fig-10.3);
- In scanning confocal microscopy (Fig-10.4).

In the multiplexing application, each channel is input to one branch of an input Y-splitter and excites only one of the guide's modes. The output Y-splitter then demultiplexes the combined signals, so long as the coupling between the modes can be kept acceptably low along the waveguide. It is important to note that the multiplexing of signals *of the same wavelength* can be effected with this technique. To limit

channel crosstalk in the many-moded waveguide, the beatlength between the modes used must be very short. Since the beatlengths between the twin-moded waveguide trunks to be considered are similar to the those between the polarisation states of contemporary polarisation-preserving fibre, the likely crosstalk performance of the multiplexing scheme can be roughly estimated by considering the experimentally-observed separation maintained between polarisation states in such fibre.

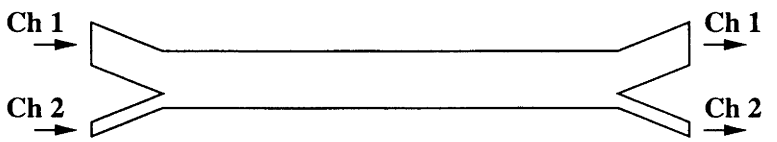

Figure 10.2: Two-channel, mode-multiplexed communications

One hundred metres of such fibre achieves roughly a 20dB extinction ratio[1] with a beatlength of the order of 1.5mm[Corning, 1993]. Now, the two modes of the trunk waveguide in Fig-10.2 have U-parameters, as defined in [Snyder and Love, 1983, §§12-8 through 12-13] obeying $U_1^2 - U_2^2 \approx 2kn_{cl}\rho^2\Delta\beta = 4\pi kn_{cl}\rho^2/L_{1,2}$, where $L_{1,2}$ is the beatlength between the two modes. For $U_1 \approx 1.5$, $U_2 \approx 2$, $\rho = 5\mu$m, $n_{cl} = 1.5$ and $\lambda = 1.5\mu$m, $L_{1,2} \approx 0.5$mm, *i.e.* comparable to the polarisation preserving fibre's beatlength. Hence, the extinction ratio performance of the polarisation preserving fibre and that of the trunk in Fig-10.2 would be similar and communication hop lengths of up to a few kilometres may be attainable with contemporary components. Thus, the multiplexing technique may well be workable for such applications as Local Area Networks (LANs) and other short-haul links where extreme bandwidth is required.

In the modalmetric (Fig-10.3) sensor, the measurand changes the modal content of the light within the waveguide, whether by preferential modal attenuation or by introducing coupling between the modes. The adiabatic Y-splitter can be used to inject light of a known modal content into the sensing waveguide and also to deduce the output light's modal content, thus effecting a measurement. The advantage of such schemes over the sensing of a measurand's effect on a single mode is that

[1]The extinction ratio ξ is the ratio of the power input to a given mode or polarisation state of a waveguide to the power that has coupled into other modes when it has reached the waveguide's output.

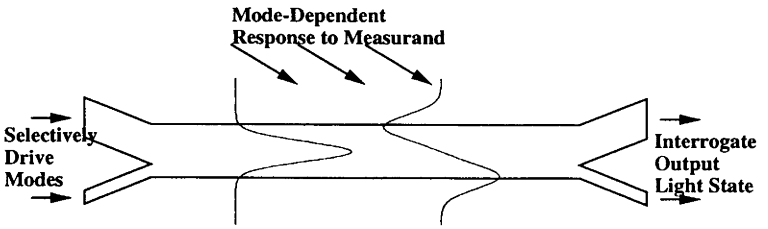

Figure 10.3: Basic modalmetric sensing principle

the *relative* modal content is important in the scheme of (Fig-10.3); such a relative measure is unaffected by spurious effects such as source laser power variation or splicing loss. Moreover, if light is introduced into a single mode, then the light coupled into the undriven mode can be sensed. Small effects causing coupling to the undriven mode can be readily measured with sensitive detectors, whereas it would be almost impossible to detect these effects through induced loss from the driven mode, as such loss may well be a ten-thousandth of the input power. This is especially true if the laser source fluctuates by even the smallest amount. Examples of modalmetric sensing schemes that could well benefit from the adiabatic Y-splitter are to be found in [Lefevre *et al.*, 1990; Dunphy, 1987; Romaniak and Dorosz, 1989; Tammela, 1987; Kersey *et al.*, 1984; Mermelstein, 1986; Shajenko, 1982].

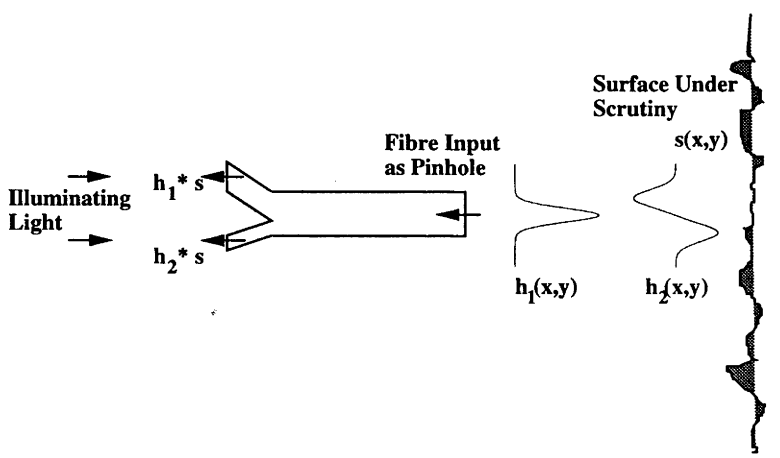

Figure 10.4: Scanning confocal microscope principle with optical fibre as pinhole

A final example application arises in scanning confocal microscopy[Wilson and Sheppard, 1984; Hewlett, 1991], schematically illustrated in Fig-10.4. In the optical fibre configuration of this scheme[Delaney *et al.*, 1994; Delaney *et al.*, 1993], light

scattered from the object under scrutiny is focussed onto the end of an interrogating fibre, which serves as the microscope's pinhole. The surface is scanned by the fibre and the resulting image, built up by recording the fibre's output intensity as a function of transverse position, is the convolution of the light field scattered from the surface with the fibre's eigenfield. The use of different eigenfields thus corresponds to the use of different two-dimensional image processing templates[Oppenheim and Schafer, 1975]. The use of, for example, the fibre's odd $HE_{2,1}$ mode in the scheme is tantamount to an edge-detection[Wilson *et al.*, 1994; Juskaitis and Wilson, 1992] (*equivalently* high-pass filtering) and control of the eigenfield's polarisation controls the direction of the edges detected.

10.2.3 Departures from Adiabaticity: Delineation Criteria

We now investigate how quickly the waveguide cross-section can change with axial distance in Fig-10.1 if the two-moded device is to be approximately adiabatic. The splitter's *extinction ratios* $\xi_{o,e}$ and $\xi_{e,o}$ quantify its departure from perfect adiabaticity and are defined as follows. If power is input into the even (*respectively: odd*) mode at the left hand end of the device in Fig-10.1, then a fraction of this power, $\xi_{o,e}$ (*respectively:* $\xi_{e,o}$) will be output in the thin (*respectively: thick*) waveguide's bound mode at the right-hand end of the device owing to nonadiabaticity. Conversely, if power is input to the thick (*respectively: thin*) waveguide at the right-hand end of the device, a small fraction will be output from the left hand end in the odd (*respectively: even*) mode of the two moded waveguide and the matrix Reciprocity Law (§6.6) predicts that this fraction is $\xi_{e,o}$ (*respectively:* $\xi_{e,o}$). Hence two, and not four, extinction ratios wholly characterise the device's departure from adiabaticity.

When the device is nearly adiabatic and radiation losses are small, it can be shown that[Love *et al.*, 1991]:

$$\xi_{o,e} \approx \xi_{e,o} \approx \left| \int_0^z C_{1,2}(u) \exp\left(i \int_0^u (\beta_1(v) - \beta_2(v)) dv \right) du \right|^2 \qquad (10.2)$$

and only one ratio[2], ξ, is needed to characterise the device.

[2]When the splitter is designed so that power oscillates sinusoidally between the modes (*i.e.* if (10.3) holds), the quantity ξ is equivalent to F^2 in the notation of [Snyder and Love, 1983, §29-3]. However, the notation of [Snyder and Love, 1983] is defined only in the context of sinusoidally-

To design a splitter with a given extinction ratio ξ, one studies the coupled local mode equations[Burns and Milton, 1980][Snyder and Love, 1983, Ch-31] and the principle is *precisely* the same as that used to derive the loss delineation criterion in §4.3. Such a splitter is defined[Rowland *et al.*, 1991; Love *et al.*, 1991; Burns and Milton, 1980] by:

$$\frac{C_{1,2}}{\beta_1 - \beta_2} = \frac{1}{2}\sqrt{\frac{\xi}{1-\xi}} \approx \frac{\sqrt{\xi}}{2} \quad \text{for} \quad \xi << 1 \tag{10.3}$$

and, with one mode only excited, power oscillates between the driven and undriven modes with maximum power transfer ξ and beatlength $2\pi/\sqrt{(\beta_1 - \beta_2)^2 + 4C_{1,2}^2}$, *i.e.* the power lost from the driven mode never exceeds[3] ξ. Here, β_1 and β_2 are the local modal propagation constants and the coupling co-efficient C_{12} [Love *et al.*, 1991]:

$$C_{12}(z) = \frac{k}{2n_{cl}(\beta_1 - \beta_2)} \int_{A_\infty} \frac{\partial n^2}{\partial z} \hat{\psi}_1 \hat{\psi}_2 dA \tag{10.4}$$

is proportional to the angle $\Omega \approx dw/dz$ between the two Y-branches, where $w(z)$ is the separation between the waveguides and z the axial distance along the device. We normalise w with respect to the sum of the two Y-branch widths w_1 and w_2, which will be constant in all the devices of this Chapter, *i.e.* $w = W/(w_1 + w_2)$, where W is the absolute waveguide separation.

The splitter defined by (10.3) is the shortest Y-splitter with maximum extinction ratio ξ for given input and output cross-sections[4]. Therefore, to calculate the

periodic power transfer between modes and we define ξ here for more general cases where this condition does not necessarily hold.

[3]If the two coupled local mode equations are written in matrix form $d\mathbf{a}(z)/dz = \mathbf{C}\mathbf{a}(\mathbf{0})$ then the condition (10.3) is equivalent to translational-invariance of the *eigenvectors* of $\mathbf{C}$. Thus the coupled mode equations' solution can be written in the form $\mathbf{a}(\mathbf{z}) = \mathbf{P} \exp\left(i \operatorname{diag}[\int_0^z \beta_1(u)du, \int_0^z \beta_2(u)du]\right) \mathbf{P}^\dagger \mathbf{a}(\mathbf{0})$, where the β_j are the splitter's bound mode propagation constants. For lossless materials, the β_j are both real and power oscillates sinusoidally between the two modes.

[4]Assuming that, in (10.2), $C_{1,2}(z)$ changes little over the length-scale $1/(\beta_1 - \beta_2)$, the integral will oscillate sinusoidally. Over any length comparable to $1/(\beta_1 - \beta_2)$, the undriven mode's amplitude can therefore be represented approximately by:

$$a_0 - i\frac{C_{1,2}}{\beta_1 - \beta_2}(\exp(i(\beta_1 - \beta_2)z) - 1) = a_0 + \frac{2C_{1,2}}{\beta_1 - \beta_2} \sin\left((\beta_1 - \beta_2)\, z\right)$$

The term a_0 arises because $C_{1,2}$ does vary slightly over each beatlength, thus the average level a_0 about which the integral oscillates slowly drifts over length-scales much greater than $1/(\beta_1 - \beta_2)$.

shortest device achieving a given extinction ratio, one notes that $C_{12}/(\beta_1 - \beta_2)$ is proportional to the splitting angle $\Omega \approx dw/dz$. If the constant of proportionality (calculated by putting $dw/dz = 1$ into (10.4)) is denoted by c and plotted against w, as in Fig-10.5, the shortest device is defined by:

$$\frac{dw}{dz} = \frac{\sqrt{\xi}}{2c} \quad \Rightarrow \quad z_\infty = \frac{2}{\sqrt{\xi}} \int_0^\infty c \, dw \tag{10.5}$$

where both z and z_∞ are normalised with respect to $w_1 + w_2$ and z_∞ is the normalised device length needed to bend the thicker arm through a right angle relative to the thiner arm, thus $2/\sqrt{\xi}$ times the area under the $c - w$ curve is the minimum possible device length with maximum extinction ratio ξ. Clearly, a splitter whose arms bend through angles of $\pi/2$ radians relative to one another violates the small-angle assumptions, but (10.5) gives a qualitative measure of the required device length.

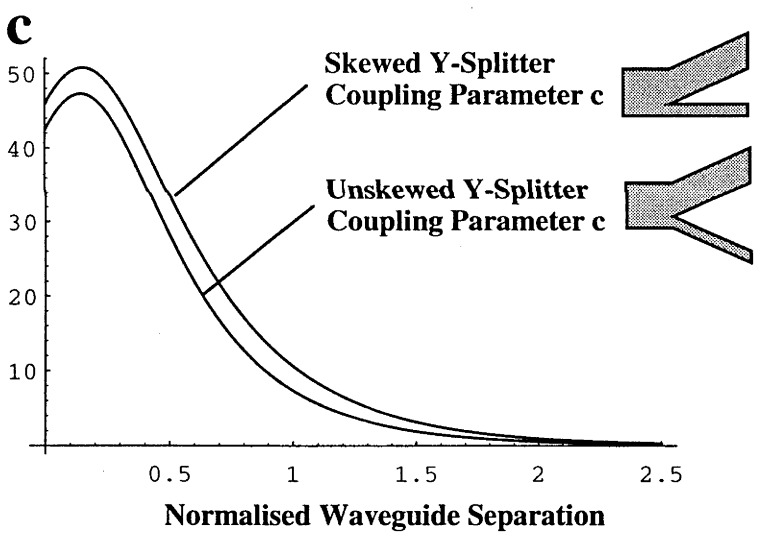

Figure 10.5: Coupling parameters for 7:3 asymmetry; skewed and unskewed splitters

---

If the undriven mode's power is less than a specified extinction ratio ξ, then $C_{1,2}/(|\beta_1 - \beta_2|) \leq \sqrt{\xi} - |a_0|$. $C_{1,2}$ is proportional to the angle Ω at which the two Y-splitter branches can separate and the most rapidly splitting junction corresponds to maximum $C_{1,2}$. This maximum cannot exceed $\sqrt{\xi}(\beta_1 - \beta_2)/2$ and decreases below this value as the drift a_0 increases. However, (10.3) is equivalent to $C_{1,2} = (\sqrt{\xi}/2)d\phi/dz$, where ϕ is the phase of the exponential in (10.2), and, given this condition, a_0 is held precisely at zero because the integral varies exactly sinusoidally with $\phi(z)$. Hence the extinction ratio is limited to ξ *and* it achieves the maximum allowable Ω at all points, *i.e. the splitter is optimally short for the given input and output cross-sections.*

There can be significant differences between the coupling parameters for unskewed and skewed devices, which are both schematically shown in Fig-10.5. In this case, however, the bound mode coupling induced by either skewed and unskewed designs is similar, whereas the corresponding curves for radiation loss differ significantly between the designs, as will be shown in §10.2.4. The relative merits of skewed and unskewed designs examined further in §§-10.2.4 and 10.3.1.

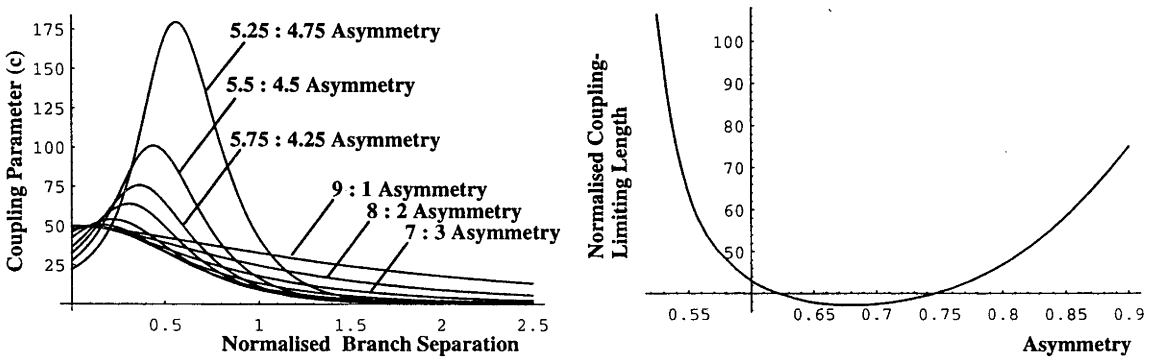

Figure 10.6: Comparison of *(a)* coupling parameters and *(b)* total device lengths for various degrees of asymmetry

In Fig-10.6*(a)*, the $c - w$ curves are plotted for step-index slab Y-splitters of various degrees of asymmetry. For each curve, the freespace wavelength is taken to be $1.5\mu m$, the *sum* of the two branch widths is $20\mu m$ (so that, for example, the curve labelled 7 : 3 asymmetry in Fig-10.6 corresponds to a Y-splitter with branches of $14\mu m$ and $6\mu m$ widths), the cladding refractive index is 1.5 and that of the core is chosen in each case to make the V-value of the wider waveguide exactly $\pi/2$, *i.e.* to be as high as possible whilst still keeping both Y-branches single moded[5].

In Fig-10.6*(b)*, the area under the curves in Fig-10.6*(a)* (proportional to the minimum device length) is plotted against the wider Y-branch's width divided by the sum of the two Y-branch widths (so that, for example, 0.7 on the horizontal axis of the lower plot corresponds to branch widths in the ratio 7:3). There is an optimum degree of asymmetry of about 7:3 since, for higher degrees of asymmetry, the core

[5]If the wider Y-branch were two moded, then, at some point along the device, there would be three bound local modes and any power coupled to the third bound mode would be lost since the two Y-branches must ultimately be spliced to single-mode waveguides at the device's output.

refractive index must be very low to ensure single-modedness of both waveguides. However, the penalty for the use of higher asymmetries than 7:3 is slight and the main design consideration is that the asymmetry should exceed 6:4, the actual value being unimportant.

$2/\sqrt{\xi}$ times the quantity plotted in Fig-10.6*(b)* gives the device length necessary to achieve an extinction ratio of ξ. Thus, the area under the $c-w$ curve for the device with 7 : 3 asymmetry is 37.46. As w is normalised with respect to a 20μm total branch width, the z_∞ necessary to achieve a -20dB extinction ratio ($\xi = 0.01$) is $2 \times 37.46 \times 20\mu\text{m}/\sqrt{0.01} \approx 14.98$mm.

It should be noted that the $c-w$ curves in Fig-10.6 are another way of presenting the delineation curves in §4.3. Superimposed on a $c-w$ curve, the designer plots $\sqrt{\xi}/(2\Omega)$ against w for the proposed Y-splitter, where $\Omega = dw/dz$ is the splitting angle for the proposed design and ξ is the designer's target extinction ratio. Only if this plot lies above the $c-w$ curve at all points can the design achieve the required adiabaticity.

10.2.4 Radiation Loss

In the design of the adiabatic Y-splitter, the radiation loss must be acceptably small. This was accomplished in the designs of Chapters-6, 7 and 8 by trial and error - if a design suffered too much excess loss, it was redesigned with smaller waveguide skew angles and bend curvatures until the excess loss was acceptable. In Chapter-4, the approach was more sophisticated, using the delineation curve approach to limit the coupling between a fundamental fibre mode and the nearest cladding mode, as in [Love *et al.*, 1991]. Here we study loss to the radiation field in somewhat more detail, as it can differ for skewed and equivalent unskewed devices. The details of the analysis are to be found in Appendix-10.6, which assumes that only coupling to radiation modes propagating at small angles to the z-direction (*i.e.* co-linear with the thin waveguide in the skewed device of Fig-10.5) is important. Thus the conclusions drawn below will not hold as the two splitter prongs become appreciably nonparallel and the radiation loss delineation criteria will be valid only close to the two-moded input of the prong.

The calculations of Appendix-10.6 give the following expression for the total

radiation loss P_{rad} from a bound mode with propagation constant β_0 and normalised profile $\hat{\psi}_0$, with the splitter's two branches at angles Ω_1 and Ω_2 relative to the z-axis.

$$P_{rad} = \frac{\pi k^{\frac{7}{2}} n_{cl}^{\frac{3}{2}} (n_{co} - n_{cl})^2}{2\sqrt{2}\mathcal{V}^2 (\beta_0 - k n_{cl})^{\frac{5}{2}}} \times$$

$$\frac{\left(\Omega_1 \left(\hat{\psi}_0\big|_{x=d+w_1} \cos(w_1 \mathcal{V}) - \hat{\psi}_0\big|_{x=d}\right) + \Omega_2 \left(\hat{\psi}_0\big|_{x=-d-w_2} \cos(w_2 \mathcal{V}) - \hat{\psi}_0\big|_{x=-d}\right)\right)^2}{\sin^2(w_1 \mathcal{V}) + \sin^2(w_2 \mathcal{V})} \tag{10.6}$$

Therefore, one can design a Y-splitter with a given maximum excess loss η by choosing Ω_1, Ω_2 to ensure $P_{rad} < \eta$. Here $\mathcal{V} = k\sqrt{n_{co}^2 - n_{cl}^2}$ has the dimensions of inverse length and is a modification of the waveguide parameter.

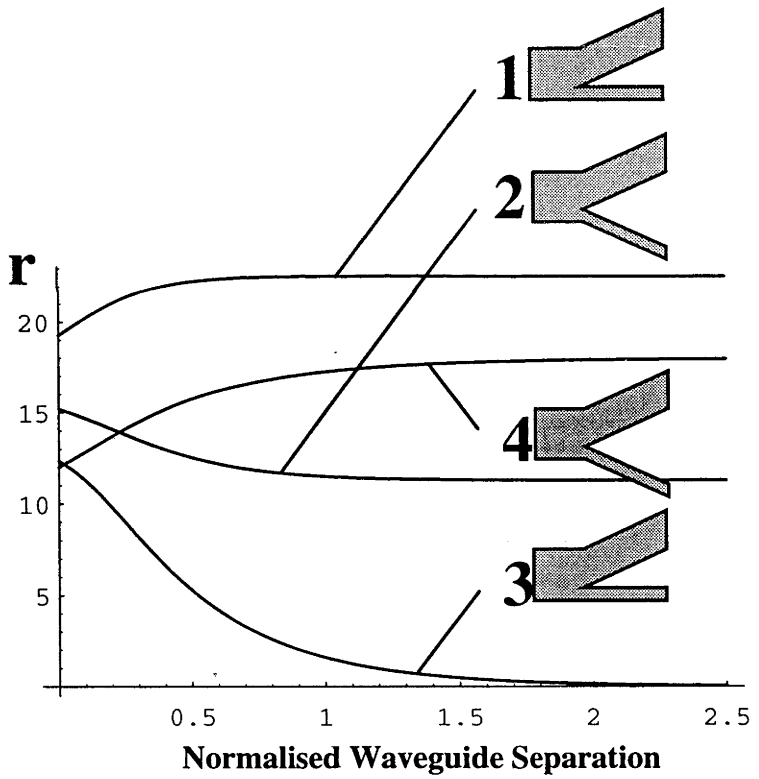

Figure 10.7: Radiation parameters for 7:3 asymmetry: r_1 for loss from the fundamental mode for the skewed (*curve 1*) and unskewed (*curve 2*) designs; r_2 for skewed (*curve 3*) and unskewed (*curve 4*) designs

By plotting $r = \sqrt{P_{rad}}/2$ *as calculated from (10.6)* for a total splitting angle $\Omega_1 + \Omega_2$ of 1 radian, a quantity analogous to the coupling parameter c of §10.2.3 is

obtained, since $\sqrt{P_{rad}}$ is proportional to $\Omega_1 + \Omega_2$. There is one radiation parameter for each of the system's bound modes: parameters r_1 and r_2 relate to loss from the fundamental and second modes, respectively, and are plotted against normalised branch separation in Fig-10.7 for the splitters studied in §10.2.3. The fundamental mode suffers less loss and the second mode more loss in the unskewed design compared to the skewed design. Thus, depending on the application, there may be significant advantages in the one design rather than the other.

The plots in Fig-10.8 are analogous to those in Fig-10.6, except that c is replaced by r_1 and r_2. Thus, $2/\sqrt{\epsilon}$ times the quantity plotted in Figs-10.8*(c) & (d)* gives the normalised device length for a radiation loss less than ϵ. Note that $\int_0^\infty r dw$ is not, in general, convergent, so that the device lengths plotted in Fig-10.8 are the lengths necessary to separate the branches to a reasonably wide separation, taken to be 2.5 times the total branch width.

Hence, the optimal splitting ratio for minimum excess loss is again about 7:3, *i.e.* such an asymmetry will give a minimum-length device for a given excess loss.

10.3 Numerical Simulations

10.3.1 Optimally Short Devices

A skewed-design slab waveguide Y-splitter obeying (10.3) with an extinction ratio of -20dB ($\xi = 0.01$) was designed. Slab waveguides were used so that the eigenfields ψ_1 and ψ_2 in (10.4) could be evaluated analytically, as branch separation w varied, at each step of the integration of (10.5).. The branch widths are 14μm and 6μm and the thick branch's V-value is $\pi/2$, *i.e.* the optimal 7:3 branch width ratio is used and the resulting splitter is schematically shown in Fig-10.9.

The maximum branch angle Ω was limited to 0.015 radians after point L in Fig-10.9*(a)* to allow accurate simulation of the device by the BPM, as discussed in Chapter-2. When the branches reach a separation of 50μm at point E, an output transition region T brings them back to a parallel configuration for output at O. T is such that the thick waveguide's slope Ω suffers no discontinuity and the waveguide follows a parabolic path to become parallel to the thin waveguide over a distance of 500μm, so that T adds a further 3.75mm separation between the branches.

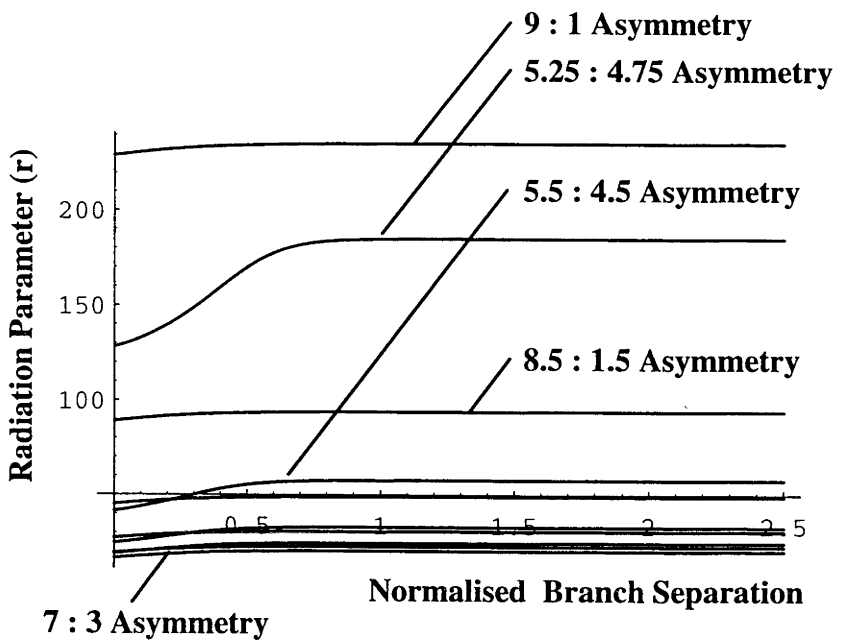

(a)

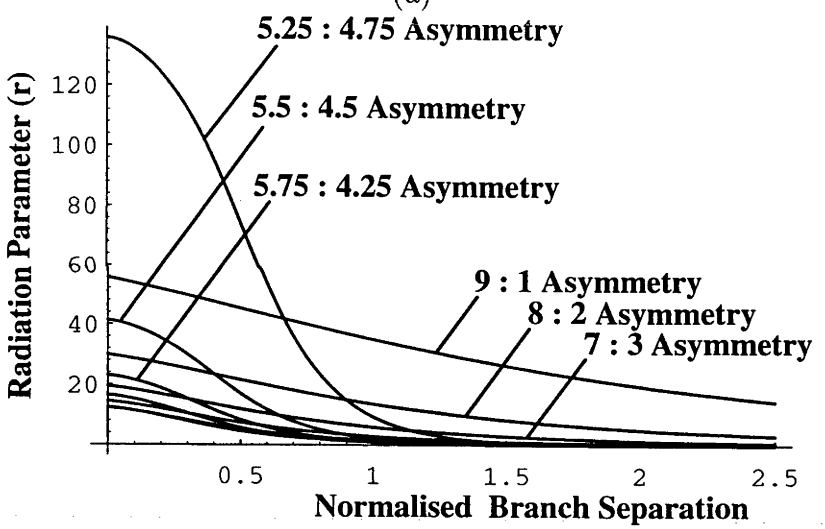

(b)

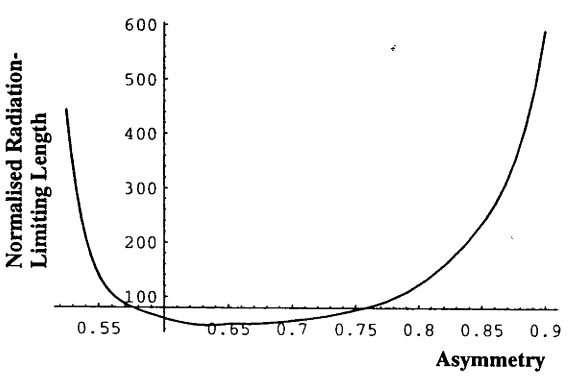

(c)

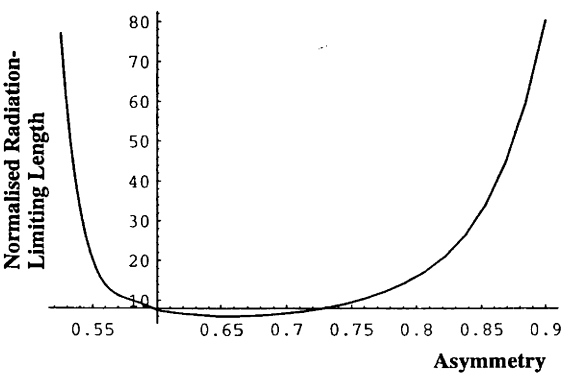

(d)

Figure 10.8: Comparison of radiation parameters and total device lengths for various degrees of asymmetry: *(a)* fundamental and *(b)* second mode radiation parameters; normalised device lengths yielding specified radiation loss from the *(c)*

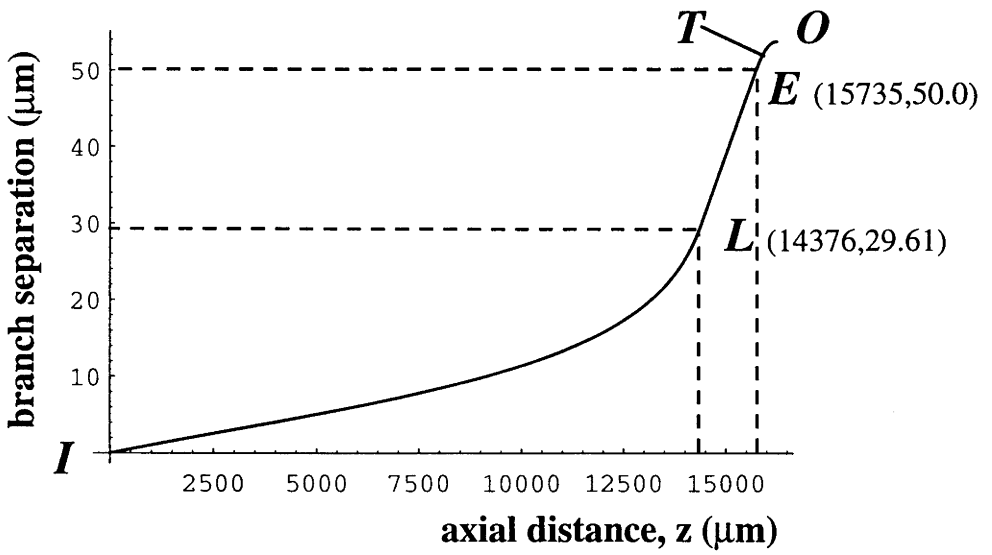

(a)

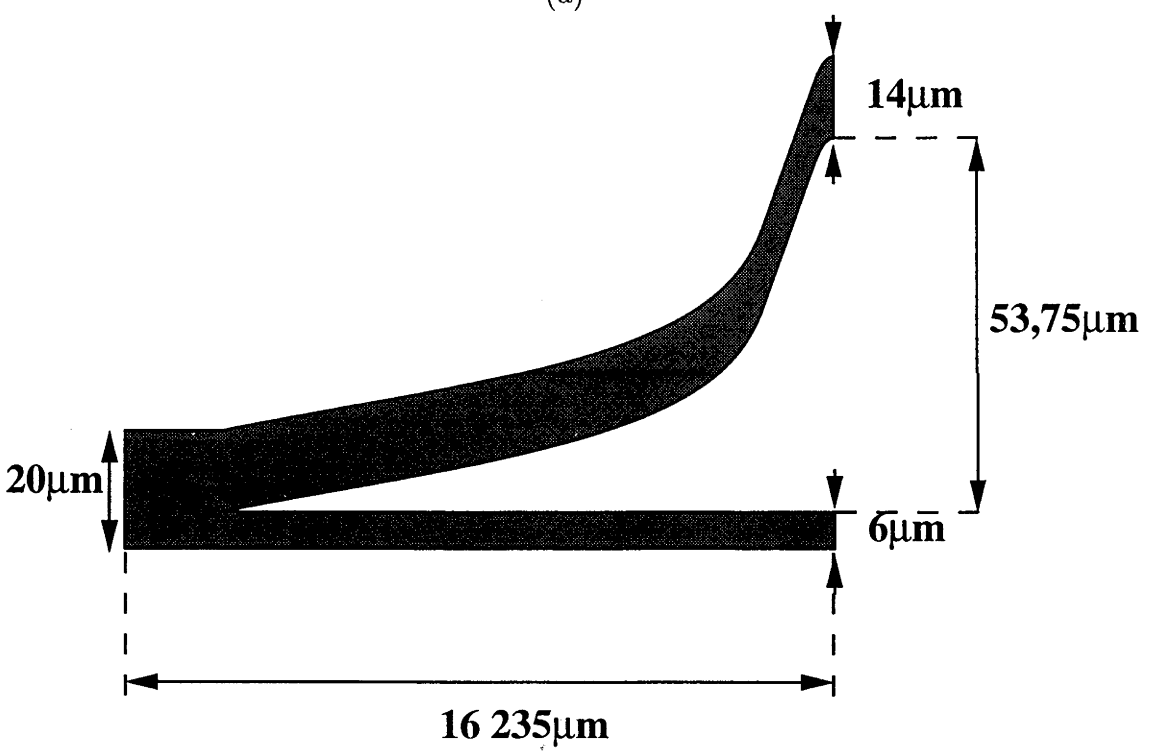

(b)

Figure 10.9: Optimally short skewed Y-splitter: *(a)* branch separation against axial distance and *(b)* schematic device plan view.

A BPM simulation of the device was undertaken, with unit power input into the even mode at I. At each simulation step, the overlaps between the field and the local mode fields were calculated and the squared magnitudes of these results are plotted in Fig-10.10. The two bound mode powers are sinusoidal functions of the relative

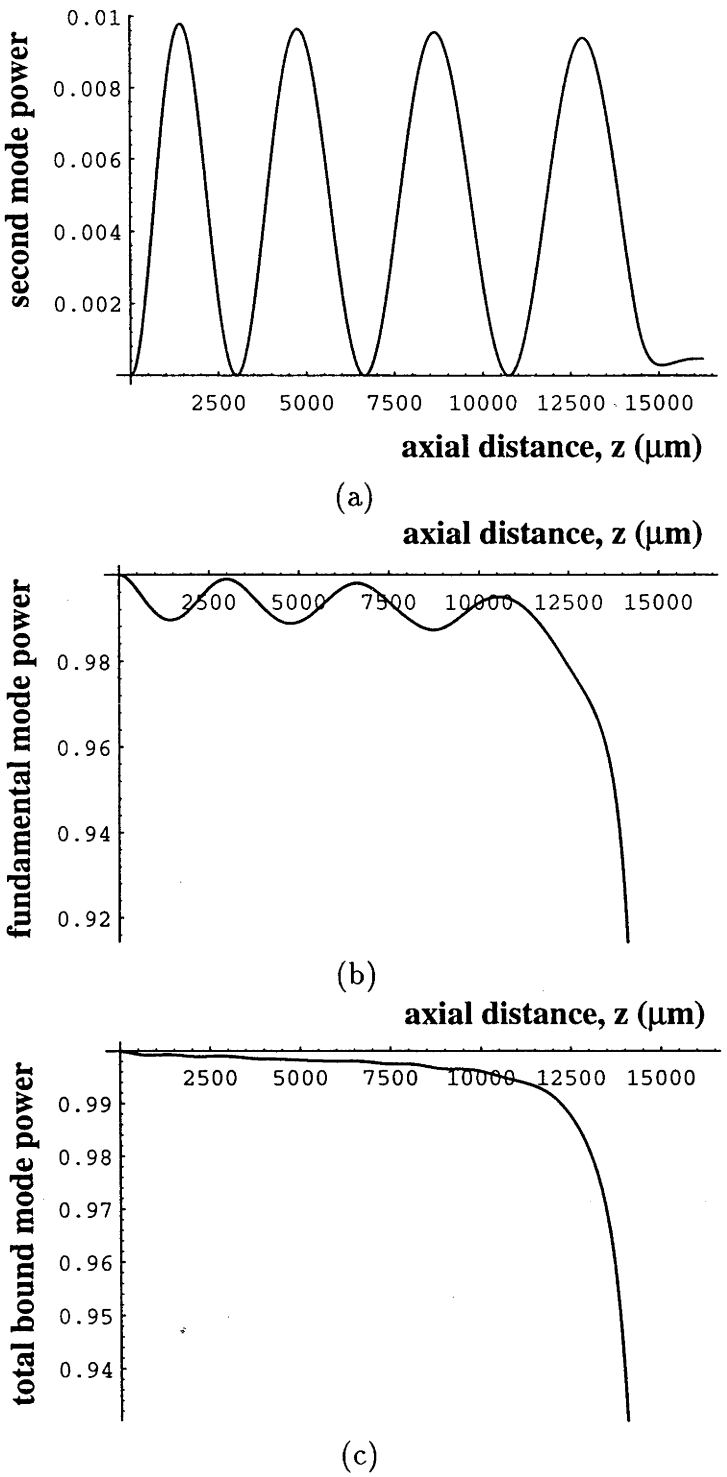

Figure 10.10: Evolution of bound mode powers for fundamental mode excitation: *(a)* periodic power coupling to and from the undriven second mode; *(b)* power in the fundamental mode, oscillating precisely out of phase with the second mode power and *(c)* total power in both bound modes, monotonically decreasing owing to radiation loss.

modal phase $\phi_{1,2} = \int_0^z (\beta_1(u) - \beta_2(u))du$ as predicted in [Burns and Milton, 1980] and [Rowland *et al.*, 1991]. Beyond L, where (10.3) is not fulfilled, this result does not hold. Moreover, radiation loss from both modes distorts the sinusoidal power transfer, as in Fig-10.10*(b)*. Note that the sum of the squared magnitudes of the local bound mode complex amplitudes, as calculated by the overlaps, *underestimates* the system's bound mode power, for it does not account for the thick waveguide's tilt. This tilt should be accounted for in any output power calculation, as in §10.3.3, since it is significant for angles as small as 0.015 radians (0.86°), *i.e.* the system radiation loss is not as severe as Fig-10.10*(c)* implies.

The simulations were repeated for the odd mode only input, thus allowing the calculation of the device's transfer matrix U_Y:

$$\left.\begin{pmatrix} a_e \\ a_o \end{pmatrix}\right|_O = U_Y \left.\begin{pmatrix} a_e \\ a_o \end{pmatrix}\right|_I ;$$
$$U_Y = \begin{pmatrix} 0.425673 + 0.827438i & 0.017448 - 0.017914i \\ 0.022279 - 0.000672i & 0.523750 + 0.791181i \end{pmatrix} \tag{10.7}$$

which relates the output local modal amplitudes to those of the input. The excess loss for the device is 0.62dB (*resp:* 0.45dB) for the even(*resp: odd*) mode input and the corresponding extinction ratio is $\xi_{o,e} = -33$dB (*resp:* $\xi_{e,o} = -32$dB). The evolution of the field intensity along the device as found by the BPM is shown in Fig-10.11. Two further simulations, with unit power eigenfields input into the output waveguides at O, verify that the system's backward transfer matrix is the transpose of U_Y, in agreement with the matrix Reciprocity Law (6.22).

As predicted by the curves 1 and 3 in Fig-10.7, the fundamental, rather than second, mode suffers the greater radiation loss. The radiation curves serve only as a qualitative guide, since their derivation rests on an assumption that all fields remain directed at only small angles to the z-direction. Thus, the curves become unreliable as the branches split and the angles between them increase. For a typical value of $r_1 \approx 20$ and a representative splitting angle 5×10^{-3} radian, the curves predict a loss of $(20 \times 5 \times 10^{-3} \times 2)^2 = 0.04$ *i.e.* 0.2dB.

A BPM analysis was undertaken for the design of Fig-10.12, which is the same as that of Fig-10.9 except that both the branch slopes are equal to half the thick waveguide's slope in Fig-10.9, *i.e.* the device achieves the same branch separation

over the same length as before. In this case, the extinction ratios are $\xi_{o,e} = -32$dB, $\xi_{e,o} = -34$dB and the even and odd mode excess radiation losses are 0.143dB and 0.59dB, respectively (*c.f.* 0.62dB and 0.45dB, respectively, for the skewed Y-splitter losses). Given curves 2 and 4 of Fig-10.7, the improved loss performance in the unskewed case for the fundamental over the second mode is not unexpected.

Finally, we note that if the splitter obeys (10.3), it can be designed to achieve far smaller extinction ratios than ξ by careful choice of the device length, because, if one bound mode alone is input into the device, *all* the input power periodically returns to the input mode. Thus, if the device's output coincides with such a period, a much shortened device, for which $\xi = 0.01$ in (10.3) for example, can have an extinction ratio as low as 0.001. Fig-10.10 shows that it is this condition that fortuitously leads to extinction ratios significantly smaller than the -20dB design goal. However, this condition is in general difficult to achieve in practice and, furthermore, the device is likely to suffer increased wavelength dependence as its relative modal delays must lie within a narrow range.

Splitter shapes other than the optimal have been appraised by the BPM and easily achieve similar extinction ratios and excess losses, provided the essential features of the optimal splitter are reproduced, *i.e.* small splitting angles and waveguide curvatures in the early stages of the split increasing to allow the branches to separate more quickly after a sufficient branch separation has been reached. Hence, we can conclude that:

Low-loss adiabatic Y-splitters with low extinction ratios are not critically dependent on the precise splitting shape used, as long as there is reasonable asymmetry between the fork widths (between 6:4 and 8:2) and the optimal splitter's qualitative shape is approximately reproduced.

10.3.2 Wavelength Response

The discussion in §10.2.1 depends only on wavelength in so far that the degree of adiabaticity for a given device varies only slightly with wavelength owing to changes in the eigenfields and therefore their coupling. Otherwise, the devices are essentially

wavelength independent and we now test this assertion with the BPM.

The device to be simulated is a step-index profile slab-waveguide device whose dimensions are shown in Fig-10.13; the cladding refractive index is 1.5 and that of the core is such that the 9μm wide waveguide has a V-value of $\pi/2$ at $\lambda = 1.5\mu$m, *i.e.* its second mode is barely cut off. The device was simulated using an even mode input to the two-moded waveguide[6] at various wavelengths and the extinction ratios and excess losses calculated are plotted in Fig-10.14. This plot shows the device to be usable over an extremely wide wavelength band, as expected. However, as the wavelength becomes shorter than $1.5\mu m$, the $9\mu m$-wide waveguide becomes two moded and loss to a third system mode increases considerably, as discussed in §10.2.3; this simulation thus underlines the the importance of keeping all the prongs in an adiabatic Y-splitter single moded. Note, however, that the extinction ratio *improves* considerably with decreasing wavelength as the thicker waveguide becomes overmoded.

For wavelengths longer than $1.5\mu m$, the higher-order system mode becomes very weakly guided and spread out, thereby increasing radiation loss. Hence, the device's excess loss is minimum for the nominal working wavelength, *i.e.* where the thickest prong becomes two-moded.

10.3.3 Three Channel Splitter

We extend the adiabatic Y-splitter concept to multipronged devices separating the power in more than two bound modes into separate single mode waveguides. Three channel splitters of the general forms shown in Figs-10.15 and 10.16 were analysed with the BPM for various combinations of w_1, w_2 and w_3 and lengths L and Y_e as shown.

The branch paths all have parabolic trajectories, such that the spacing between neighbouring waveguides obeys:

$$Y = Y_e \frac{z^2}{L^2} \tag{10.8}$$

where z is the axial distance, L the device length, $Y(z)$ the spacing between neigh-

[6]The even mode was recalculated for each different wavelength used.

bouring guides and $Y_e = Y(L)$, the output spacing. For the unskewed waveguides of Fig-10.16, the bending radii are:

$$R = \frac{\left(1 + \left(\frac{dY}{dz}\right)^2\right)^{\frac{3}{2}}}{\frac{d^2Y}{dz^2}} = \frac{L^2}{2Y_e} \quad \text{when} \quad z = 0 \tag{10.9}$$

and the value $R = L^2/(2Y_e)$ is the minimum bending radius. For the skewed waveguide of Fig-10.15, these formulas apply to the middle branch, the outer branch having twice the bending curvature.

The devices all have step-index profile slab waveguides, a nominal working wavelength of 1.5μm, cladding index of 1.5 and core indices such that the thickest output waveguide is barely two moded, *i.e.* has a V-values of $\pi/2$. Thus, the input waveguide's V value is:

$$V = \frac{\pi}{2}\left(\frac{w_1 + w_2 + w_3}{\max(w_1, w_2, w_3)}\right) \tag{10.10}$$

Note that the input waveguide's thickness must be at least twice that of the thickest waveguide, otherwise it will be two- rather than three-moded, and so the maximum degree of asymmetry in the output waveguides is constrained. This problem could be somewhat alleviated by downtapering the input waveguide before it meets the three branches, so that the third mode becomes leaky for only a short length along the device.

The results of these simulations are summarised in Tables-10.1 and 10.2. In Table-10.1, the design column states whether the splitter is skewed (S) or unskewed (U) and R is the minimum radius of curvature of any of the guides in the device. In Table-10.2, P_{jk} is the power output from guide number j (corresponding to the width w_j in Figs-10.15 and 10.16) when unit power is input into the input waveguide's k^{th} mode ($k = 1$, fundamental mode, $k = 2$, first odd mode, $k = 3$, second even mode). ξ_M is the maximum decibel extinction ratio, or the maximum crosstalk between modal channels and ϵ_M is the maximum decibel excess loss[7].

In calculating the output power from these devices, care must be taken that the angle of inclination between the output waveguide and the plane $z = L$ is properly accounted for, even though it may be only of the order of a degree or less. If

[7]Defined as $-10\log_{10}(P_{out}/P_{in})$

Simulation Number	Design	w_1 μm	w_2 μm	w_3 μm	L mm	Y_e μm	R m
1	S	5	7	9	15	30	1.875
2	S	9	7	5	15	30	1.875
3	S	5	7	9	10	30	0.833
4	U	5	7	9	15	30	3.75
5	U	5	7	9	10	30	1.667

Table 10.1: Definitions of 3-splitters simulated by BPM

Simulation Number	$P_{1,1}$	$P_{2,1}$	$P_{3,1}$	$P_{1,2}$	$P_{2,2}$	$P_{3,2}$
1	1.03948×10^{-6}	0.00493262	0.986040	0.000121887	0.984693	0.00493374
2	0.987693	0.00338638	3.50437×10^{-6}	0.00344457	0.986297	0.000127819
3	7.13769×10^{-5}	0.0484234	0.945418	0.00483590	0.940052	0.0484750
4	9.60784×10^{-6}	0.0358135	0.954878	0.000105262	0.954498	0.0359604
5	0.000400748	0.103413	0.889927	0.00310027	0.886876	0.104011

Simulation Number	$P_{1,3}$	$P_{2,3}$	$P_{3,3}$	ϵ_M (dB)	ξ_M (dB)
1	0.987467	0.000107295	1.08365×10^{-7}	0.054	-23
2	1.57002×10^{-6}	9.71717×10^{-5}	0.987063	0.056	-24
3	0.986132	0.00469892	5.17485×10^{-5}	0.04	-13
4	0.987029	0.000162630	3.25694×10^{-6}	0.056	-14.4
5	0.987355	0.00323543	4.53728×10^{-6}	0.041	-9.8

Table 10.2: Results of 3-splitter BPM simulations

this inclination angle is θ_0, then the inclination of the output field's phase front roughly equals θ_0. Thus, if the output field is $\Phi(x,y)$, it is necessary to calculate the overlap between $\Phi(x,y)\exp(i\beta\sin(\theta_0)x)$ and the output waveguide's eigenfield $\psi(z,y)$, where the x-axis is in the plane of the bend along with the z-axis and has its origin at the waveguide's centre. For $\theta_0 = 0.01$ radians and a waveguide halfwidth of 5μm, the maximum phase $\beta\sin(\theta_0)x$ in the exponential is 0.314 radians or 18^o, which is highly significant.

Case 2 investigates the effect of permuting the the waveguide widths in Case 1, and it is seen that this produces very little difference in either the excess loss or extinction ratio. This may seem somewhat surprising, as the excess loss does not

Mode Number	U	W	β	$L_B(\mu\text{m})$
1	1.228888	3.453037	6.291786	2004.2
2	2.420308	2.752406	6.288651	2004.2
3	3.469685	1.181064	6.284192	1409.1

Table 10.3: Input waveguide modal properties

increase appreciably, even when the most weakly guided mode propagates along the most bent waveguide. However, the null effect simply shows that the waveguide curvatures are not enough to cause appreciable excess loss. As in Chapter-2, the predicted small losses may well arise from the BPM rather than the physical device. One effect that is not surprising, however, is that the highest excess loss is associated with the inputs driving the most bent branches.

10.3.4 Three-Channel Splitter: General Patterns

The most striking feature of these simulations is the marked crosstalk performance superiority (typically 10dB or better) of the skewed as opposed to unskewed designs. Another interesting observation is that the input of the highest order (*i.e.* second even) mode always yields the lowest crosstalk (*e.g.* 0.0001 or -40dB as opposed to 0.005 or -23dB for both the other modes in simulation 1). Again, this may seem at first surprising; however, the waveguide parameters and propagation constants for the input guide ($V = 21\pi/18$) are as given in Table-10.3, where L_B is the beatlength between the given mode and the bound mode with the closest propagation constant. We have seen that the extinction ratio between modes j and k is proportional to $C_{j,k}^2/(\beta_j - \beta_k)^2$, which in turn is proportional to $1/(\beta_j - \beta_k)^4$. Thus, the above simple calculations predict that the highest order mode have extinction ratios of the order of $(2004/1409)^4$ or 6dB better than the extinction ratios pertaining to coupling between the other two modes.

10.3.5 Fourth and Higher-Order Splitters

Given that the simulations show the adiabatic Y-splitter concept to be workable for three modal channels, we now examine four channels. The device shown in Fig-

$P_{1,1}$	9.78103 x 10^{-8}	$P_{1,2}$	3.10421 x 10^{-5}	$P_{1,3}$	0.00197849	$P_{1,4}$	0.991362
$P_{2,1}$	2.15101 x 10^{-5}	$P_{2,2}$	0.0143663	$P_{2,3}$	0.982513	$P_{2,4}$	0.000328530
$P_{3,1}$	0.0128609	$P_{3,2}$	0.970451	$P_{3,3}$	0.0138933	$P_{3,4}$	7.60176 x 10^{-8}
$P_{4,1}$	0.982245	$P_{4,2}$	0.0149175	$P_{4,3}$	0.000180261	$P_{4,4}$	5.79499 x 10^{-8}
ξ_M	-18.3dB		ϵ_M	0.021dB			

Table 10.4: Results of 4-splitter BPM simulations

Mode Number	U	W	β	$L_B(\mu\text{m})$
1	1.307625	4.853484	6.286439	9027.6
2	2.598340	4.302885	6.285743	9027.6
3	3.842282	3.240842	6.284636	5675.9
4	4.919316	1.032722	6.283333	4822.1.1

Table 10.5: Input waveguide modal properties

10.17 was simulated and the BPM results are summarised in Table-10.4. The device length is $L = 50$mm, the output waveguide separation 30μm, the waveguide widths are 9μm, 11μm, 13μm and 15μm, as shown, and the branches follow parabolic paths as for the 3-channel Y-splitter. Again, the core refractive index is chosen so that the thickest waveguide has $V = \pi/2$. The best extinction ratios are obtained for the highest-order mode input. Typically, they are about 15dB better than the others (0.0003 as opposed to 0.01) because, as before, the shortest modal beatlengths are between modal pairs including the highest order mode, as shown in Table-10.5.

It was found numerically that a 50mm device length was the shortest achievable for an extinction ratio $\xi = 0.01$. We can be reasonably confident that this length is close to the shortest theoretically achievable by the following simple argument. The device's extinction ratio is given approximately by 4 $\max(C_{j,k}^2/(\beta_j - \beta_k)^2)$. If a splitter with invariant shape is scaled, the coupling co-efficients $C_{j,k}$, being proportional to the angles within the device, scale as $1/\mathcal{L}$, where $\mathcal{L}$ is the device length. Moreover, as discussed above, $C_{j,k}$ is roughly proportional to $1/(\beta_j - \beta_k)$, assuming that the overlap integral in (10.4) is reasonably independent of the mode shapes. Thus, for a splitter of a given shape, we find:

$$\xi \alpha \frac{k^2\Delta}{\mathcal{L}^2\Delta\beta^4} \tag{10.11}$$

where $\Delta\beta = \min(\beta_j - \beta_k)$ and $\Delta = (n_{co}^2 - n_{cl}^2)/(2n_{co}^2)$. Now, as the input waveguide becomes heavily overmoded, the propagation constants of the fundamental and first odd modes are the closest together and the waveguide U-parameters approach $\pi/2$ and π. Thus:

$$\min(\beta_j - \beta_k) = \beta_1 - \beta_2 \approx \sqrt{k^2 n_{co}^2 - \frac{\pi^2}{4\rho^2}} - \sqrt{k^2 n_{co}^2 - \frac{\pi^2}{\rho^2}} \approx \frac{3\pi^2}{8\rho^2 k n_{co}} \tag{10.12}$$

Since $\rho \approx N\rho_0$, for N modal channels, we obtain the following dimensionless ratio which is approximately proportional to the device's extinction ratio:

$$\xi \; \alpha \; \frac{k^6 \rho_0^8 N^8}{\mathcal{L}^2} \tag{10.13}$$

Hence, to achieve a given extinction ratio, the device length *is proportional to* N^4 and thus the difficulty of achieving good channel separation increases dramatically for increasing numbers of channels. For smaller N, the effect is not quite so dramatic as predicted by (10.13) as $U_2 - U_1 < \pi/2$; in this case, the spacing between propagation constants is more regular and the minimum difference between neighbouring propagation constants will vary more like $k(n_{co} - n_{cl})/N$. Thus, the device length required for a given extinction ratio will vary more like N^2 rather than N^4 for smaller numbers of modal channels. Both these two extremes more than account for the dramatic device length increase necessary for reasonable extinction ratios with four modal channels. (10.13) also shows that the adiabatic Y-splitter concept can clearly *not* be extended to an arbitrary number of channels and that four channels is probably the practical limit; (10.13) gives a device length of at least 100mm for five channels.

10.4 Rectangular Core Waveguide Adiabatic Splitters

Having demonstrated the adiabatic splitter concept with slab waveguides, we now seek to extend our analysis to more practical devices by studying adiabatic Y-splitters with rectangular, step-index cores. This will allow us to address, in particular, some of the practical problems that will arise in the use of the adiabatic

Y-splitter for scanning confocal microscopy, such as the alignment of the splitter and its input and output waveguides.

The systematic design of optimally short devices, as in §§10.2.3 and 10.3.1 is nontrivial for rectangular core guides since the two-dimensional eigenfields must be calculated at each axial step of the design by a computationally time-consuming procedure such as the Fourier Decomposition Method (FDM). Given that the adiabatic Y-splitter's performance does not depend critically on the device's shape as long as it has the same qualitative features as the optimal design, it is expedient to base the design of these devices on smooth branch-splitting trajectories, such as the parabolic and cosinusoidal paths of the previous sections.

We first address the necessary constraints of *(i)* ensuring single modedness in the splitter outputs, for rectangular core waveguides and *(ii)* splicing the adiabatic Y-splitter to input and output fibres.

10.4.1 Single-Modedness of Rectangular Core Waveguides

As in the foregoing sections, the splitter is designed so that the second mode of the thickest branch is barely cut off. Now, as discussed in [Ladouceur, 1992], there is no analytical solution to the scalar wave equation for the rectangular core, step-index waveguide, hence, the following semi-analytical technique has been used to check the single-modedness of all output waveguides in the devices simulated as part of this thesis. [Sammut, 1982] shows empirically that, to a good approximation over an extremely wide range of aspect ratios, a step-index rectangular core waveguide will be at the point of second mode cutoff if an elliptical core step-index waveguide with the *same* Δ, *core area and aspect ratio* is also at second mode cutoff. Cutoff V-values based on the solution of Mathieu's Equation for step index elliptical core waveguides with a wide range of aspect ratios are available in [Rengarajan and Lewis, 1980] and, through the empirical result of [Sammut, 1982], a least-squares line fit to the data in [Rengarajan and Lewis, 1980] yields the following relationship between the aspect ratio α and cutoff V value (V_{cutoff}) of a step-index rectangular core waveguide:

$$V_{cutoff} = 1.43751 + 0.67105\alpha \tag{10.14}$$

where, as in [Ladouceur, 1992], the V value of a rectangular core waveguide with side halfwidths ρ_x and ρ_y is given by $V = k\sqrt{\rho_x \rho_y}\sqrt{n_{co}^2 - n_{cl}^2}$. For example, when applied to a 14μm $\times$ 20μm square core waveguide, (10.14) shows that a V-value is required to achieve the point of second-mode cutoff and if the cladding refractive index is 1.447, a core index of $n_{co} = 1.447822472$ for $\lambda = 1.32\mu$m (*i.e.* $\Delta = 5.69 \times 10^{-4}$) is required to put the waveguide at the point of second mode cutoff.

A better method for finding modal cutoffs than the above is that found in [Hewlett and Ladouceur, 1994]. This newer method is an extension of the Fourier Decomposition Method and was briefly referred to in Chapter-2.

10.4.2 Splicing and Alignment of the Adiabatic Y-Splitter

[Hewlett *et al.*, 1993] considers the problem of splicing round core fibres to rectangular core waveguides and its main conclusion, for the present purposes, is that splice loss is minimised when the fibre and rectangular cores have equal area (provided that the core and cladding refractive indices are the same in both cases) and that this conclusion is not very sensitive to the precise waveguide shape, provided it retains sufficient symmetry. For simplicity, we shall therefore assume that the equal-area condition is satisfied by the waveguides on both sides of all splices. In the following, we extend this analysis to multimoded waveguides, since there is the possibility of crosstalk between the modal channels arising from *(i)* offsets at splices and *(ii)* the difference between the two waveguide cross-sections joined at a splice. However, *(ii)* is only relevant to three- or more channel splitters since a two channel splitter's input waveguide has only one odd and one even mode, which are *always* orthogonal if of the same polarisation.

The scanning confocal microscope application(§10.2.2, [Wilson *et al.*, 1994]) proposes, for an optical-fibre-based apparatus, the use of the fibre's first odd mode as an edge-detecting image processing template. For such a scheme to be successful, the polarisation, *i.e. orientation*, of the template eigenfield must be well controlled as it propagates from the surface under scrutiny along the fibre to the detectors. [Wilson *et al.*, 1994] uses a round core fibre with polarisation controllers to achieve this. It may well be advantageous in such an application, however, to use a birefringent fibre to maintain the correct polarisation without the need for a polarisation-controlling

adjustment. Hence, we consider the splicing of the multimode end of a Y-splitter onto a birefringent elliptical core fibre.

The input waveguide is taken to be rectangular, with step-profile core of dimensions 20μm $\times$ 14μm. The cladding's refractive index is 1.447 and that of the core is 1.4482442 ($\Delta = 8.6 \times 10^{-4}$). The split is intended to be into two branches with core cross-sections 14μm $\times$ 14μm and 6μm $\times$ 14μm, and so the former waveguide has $V = 2.0$ at $\lambda = 1.32$. The input guide is assumed to be spliced onto an elliptical core guide with the same core area and aspect ratio.

The two bound eigenfields of the input rectangular and elliptical core waveguides were calculated by the FDM. This method can be extended in an elegant way to accommodate elliptical core fibres because, in the notation of Chapter-2 and (2.3), [Hewlett, 1994] shows that there are *analytical* expressions for the matrix elements in the FDM in the case of elliptical and round core step-index profile waveguides given by:

$$\left\langle \psi_{\mu,\nu}, k^2 n^2(x,y) \psi_{\sigma,\omega} \right\rangle =$$

$$2ba\left(s(\mu-\omega,\nu-\sigma) - s(\mu+\omega,\nu-\sigma) - s(\mu-\omega,\nu+\sigma) + s(\mu+\omega,\nu+\sigma)\right)$$

where

$$s(j,k) = \frac{J_1\left(\frac{\pi}{L_x L_y}\sqrt{(jL_y a)^2 + (kL_x b)^2}\right)}{\sqrt{(jL_y a)^2 + (kL_x b)^2}} \cos\left(\frac{j\pi}{2}\right)\cos\left(\frac{k\pi}{2}\right) \tag{10.15}$$

Here the simulation domain (Fig-10.18) is $0 \leq x \leq L_x$, $0 \leq y \leq L_y$; the ellipse has major and minor axes of length a and b parallel to the x and y axes respectively and is centred at the point $(L_x/2, L_y/2)$.

When the fields of the rectangular and elliptical core waveguides have been determined by the FDM, the overlap $p(x,y)$ between them as a function of their relative offset (x,y) is most conveniently calculated as a fast convolution between modes ψ and $\bar{\psi}$ of the different waveguides, *i.e.* the inverse fast Fourier transform (FFT) of the product of the FFTs of ψ and $\bar{\psi}$.

Fig-10.19 shows a contour plot of the overlap between the odd bound mode of the two-moded elliptical core fibre with the fundamental even mode of the rectangular

core in dB as a function of relative offset between the guides. This overlap as a function of a purely x-direction offset is also shown and the corresponding plot for overlaps between the square-core guide's odd mode and the fibre's even mode is almost identical. The overlaps between the two fundamental modes and two odd modes are both very close to 100%, even for large offsets, as found in [Hewlett *et al.*, 1993] and are plotted in Fig-10.20.

As expected, an offset purely in the y direction gives no overlap between the even and odd modes since it does not break the even symmetry of the waveguides about the axis of symmetry of the modal fields. However, such an offset couples the corresponding even and odd fields with the orthogonal polarisation. It can be seen that a relative offset of about $\pm 0.5\mu$m can be tolerated in this case if an extinction ratio of 30dB is required between the modal channels; for more realistic waveguide dimensions, with all dimensions scaled down threefold, this value would be about $\pm 0.15\mu$m.

Note that active alignment may well enhance the alignment of the fibre to the splitter. Fig-10.21 shows the block diagram of such a scheme for a splitter configured for use with a scanning confocal microscope. The detector is aligned approximately with the thinner output waveguide. It is only necessary that it should intercept a reasonable proportion (say 50%) of the waveguide power output. Next, the fundamental mode of the the input fibre is excited. When the fibre is precisely aligned to the splitter, the output from the detector will be a minimum. In contrast, active alignment of single-mode fibres to waveguides seeks to *maximise* the power transferred across a splice, thus small changes to a high power must be detected. Hence, active alignment by minimisation of the output from the thin waveguide will probably be more accurate than any active alignment which maximises the power transferred across the splice in the fundamental mode.

The splicing calculations were repeated for a three-moded system. Again, the core refractive index is 1.4482442 but the rectangular core now measures 30μm $\times$ 14μm. It is three moded and intended to be split into three waveguides of cross-sectional dimensions 14μm $\times$ 14μm, 10μm $\times$ 14μm and 6μm $\times$ 14μm. The overlaps were calculated for a splice onto an elliptical core fibre of the same core area and aspect ratio. Fig-10.22 shows the crosstalk between the different pairs of modal

channels as functions of offsets in the x- and y-directions, *i.e.* the splice's extinction ratios, as a function of offset. In this case, the splice must be aligned to within $\pm 0.3\mu$m to achieve a -30dB extinction ratio. Crosstalk between the fundamental fibre's mode and the splitter's second even mode does *not* vanish, even for perfect alignment and the best possible splice extinction ratio is -30dB. The same holds for crosstalk between the fibre's second even mode and the splitter's fundamental because the pairs of modes are not quite orthogonal, owing to the difference between the waveguide geometries. This problem could be alleviated by prolonged fusion splicing to blur the transition between the two waveguides.

Fig-10.23 shows the splice loss for the three system modes as a function of offset, thus showing the marked sensitivity rise with modenumber in the sensitivity to misalignment.

10.4.3 Two-Dimensional Cross-Section Y-Splitters

Here we confirm that the results of §10.3.1 substantially hold for waveguides with a two-dimensional cross-section. A two-channel Y-splitter with a rectangular core input waveguide of dimensions $20\mu\text{m} \times 14\mu\text{m}$ splitting into two guides of dimensions $14\mu\text{m} \times 14\mu\text{m}$ and $6\mu\text{m} \times 14\mu\text{m}$ was simulated using the BPM. The core's refractive index is 1.4482442 and that of the cladding 1.447 so that $V = 2$ at $\lambda = 1.32\mu$m for the larger guide. The plan view of the device, defining the splitting trajectory of the branches, is as in Fig-10.13, except that the output waveguide dimensions are as just given. The output waveguide separation is $y_f = 40\mu$m, the device length $L = 15mm$ and the path of the $14\mu\text{m} \times 14\mu\text{m}$ section guide is:

$$y = y_f \frac{1 - \cos\left(\frac{\pi z}{L}\right)}{2} \tag{10.16}$$

and the $6\mu\text{m} \times 14\mu\text{m}$ waveguide is straight. A BPM simulation for the device's bound modes gives the excess losses and extinction ratios in row C_1 of Table-10.6, where $P_{j,k}$ is the power output from the j^{th} thickest output guide when the k^{th} mode is input to the system.

The simulation was repeated with the different branch splitting path:

Coupler	$P_{1,1}$	$P_{2,1}$	$P_{1,2}$	$P_{2,2}$
C_1	0.98654	3.6998×10^{-3}	3.6989×10^{-3}	0.86325
C_2	0.98687	1.9516×10^{-3}	2.5038×10^{-3}	0.87351

Table 10.6: Performance of the 2-channel Y-splitters

Coupler	$P_{1,1}$	$P_{2,1}$	$P_{3,1}$	$P_{1,2}$	$P_{2,2}$
C_1	0.8767	3.423×10^{-3}	2.812×10^{-3}	3.549×10^{-3}	0.9666
C_2	0.8413	1.058×10^{-3}	5.633×10^{-3}	1.275×10^{-3}	0.9698

Coupler	$P_{3,2}$	$P_{1,3}$	$P_{2,3}$	$P_{3,3}$
C_1	4.117×10^{-3}	2.149×10^{-3}	4.753×10^{-3}	0.7028
C_2	1.924×10^{-3}	4.681×10^{-3}	2.270×10^{-3}	0.9133

Table 10.7: Performance of the 3-channel Y-splitters

$$y = y_f \frac{1 - \cos\left(\frac{\pi z^2}{L^2}\right)}{2} \tag{10.17}$$

i.e. with a smaller rate of increase of curvature near the device's input but with more rapid branch splitting once the separation reaches a few waveguide widths. The results are summarised in row C_2 of Table-10.6 and show slightly better extinction ratio (-26dB as opposed to -24dB) and excess loss (0.59dB as opposed to 0.64dB) performance.

The performance of a two-dimensional cross-section three-channel splitter was also investigated. All refractive index values are the same as for the two-channel splitter, but the input waveguide is rectangular core with cross-sectional dimensions 30μm $\times$ 14μm and splits into three waveguides of dimension 14μm $\times$ 14μm, 10μm $\times$ 14μm and 6μm $\times$ 14μm. The device plan view is as in Fig-10.15 except that the splitting trajectories are now given by (10.8) rather than (10.16) and the thickest waveguide follows the most curved path, the thinnest being straight. The output waveguide separations are $y_f = 40\mu$m and the device length is $L = 30$mm. The simulation results for input into each of the three input eigenfields are summarised in row C_1 of Table-10.7. Here again, the notation $P_{j,k}$ is as for Table-10.6 and the multimoded waveguide modes are numbered as in Table-10.2.

These simulations were repeated for a device with precisely the same dimensions but with a core refractive index of 1.448943936, for which the thickest output waveguide has $V = 2.5$, *i.e.* the system is slightly overmoded. The results are as summarised in row C_2 of Table-10.7 and show a superior excess loss performance at the expense of a slightly worse extinction ratio than for the coupler of C_1.

10.5 Conclusions

This chapter has analysed adiabatic, asymmetric Y-splitters. Such splitters have potential applicability to telecommunications by allowing the multiplexing of different channels onto the different modes of a multimoded waveguide, even if all channels are at the same wavelength. By examining the beatlength between modes and using it as a measure of such a scheme's ability to maintain acceptably low crosstalk between different channels, it can be concluded that the maximum hop length practically possible for the mode-multiplexing application will be of the order of 10km. Beyond such a hop length, interchannel crosstalk will increase to unacceptable levels ($\leq -20dB$).

Another application for the splitters is in modalmetric sensing, where the devices would be used to selectively drive the different modes of a multimoded sensing waveguide and to measure the modal content of its output. A further application is in scanning confocal microscopy, where the detection of a specimen using different modes of a multimoded waveguide is equivalent to using different image-processing templates, which effect real-time edge-detection and other image processing functions as the image is acquired.

Simple coupled-mode theories were used to derive delineation curves to design optimally-short two-channel devices with desired extinction ratios and excess loss. When the device is designed with a constant mismatch parameter $(\beta_1 - \beta_2)/C_{12} = 2/\sqrt{\xi}$, power oscillates sinusoidally between the driven undriven mode, the maximum power transfer being ξ. Thus, the device's extinction ratio is *limited* to ξ, for an arbitrarily long device. Using a BPM simulation for a two-moded splitter, this property was verified, notwithstanding the neglect of radiation in the coupled mode theory. The coupling and radiation delineation criteria were verified to work reliably

and are thus a useful design tool for the asymmetric adiabatic Y-splitter.

BPM simulations confirm that the adiabatic Y-splitter is independent to all but the grossest changes in operating wavelength. The optimal working wavelength, for minimum excess-loss, seems to be that where the thickest (most strongly-guiding) output guide is closest to second mode cutoff. If the wavelength is any shorter, the thickest guide becomes overmoded, thus allowing coupling of power to its second mode. This power must ultimately be lost as the output guides are spliced onto single moded waveguides. If the wavelength is any longer than the optimal wavelength, the bent guides become more weakly guiding and thus their fields could suffer increased loss.

§10.3.5 extended the adiabatic splitter concept to four and more channels. It was shown that the device length required for four channels is dramatically increased compared to that required for three channels and a simple argument shows that the required device length for a given extinction ratio varies as N^4, provided $N >> 1$, where N is the number of modal channels. For smaller values of N, the variation is like N^2. Thus, there is a practical limit to the number of modal channels that can be multiplexed.

The problem of splicing of the multimoded input of the adiabatic Y-splitters to external waveguides was investigated and it was found that the coupling between modes caused by realistic splices is not excessive and will not make mode multiplexing schemes unworkable, at least for up to three modal channels. Moreover, an active alignment scheme was proposed which could produce highly accurate splices. However, owing to the difference between the waveguide geometries, there is nonzero interchannel crosstalk, even for perfectly aligned splices when $N \geq 3$. Thus, the minimum possible extinction ratio for a mode multiplexed system with $N \geq 3$ is about -30dB; however, this problem may be alleviated by prolonged splice fusion time.

Finally, the adiabatic Y-splitter concept was reverified numerically by simulations of more realistic rectangular core waveguide devices.

10.6 Appendix: Radiation Loss Calculations

The radiation loss formula (10.6) is derived using the concepts of radiation modes and local mode coupling[Snyder and Love, 1983, Ch-25 and §§-31-14, 31-15]. For the slab Y-splitter, a local radiation mode's general form is:

$$\psi(\mathcal{Q},x) = \begin{cases} \psi_1(\mathcal{Q},x) = A_1 e^{i\mathcal{Q}x} + B_1 e^{-i\mathcal{Q}x}; & x > d + w_1 \\ \psi_2(\mathcal{Q},x) = A_2 e^{i\mathcal{U}x} + B_2 e^{-i\mathcal{U}x}; & d < x \leq d + w_1 \\ \psi_3(\mathcal{Q},x) = A_3 e^{i\mathcal{Q}x} + B_3 e^{-i\mathcal{Q}x}; & |x| \leq d \\ \psi_4(\mathcal{Q},x) = A_4 e^{i\mathcal{U}x} + B_4 e^{-i\mathcal{U}x}; & -d - w_2 \leq x < -d \\ \psi_5(\mathcal{Q},x) = A_5 e^{i\mathcal{Q}x} + B_5 e^{-i\mathcal{Q}x}; & x < -d - w_2 \end{cases} \tag{10.18}$$

where $\psi_j(\mathcal{Q},x)$ is the radiation eigenfield in the j^{th} slab region and the waveguide parameters are given by $\mathcal{U} = \sqrt{\mathcal{V}^2 + \mathcal{Q}^2}$, $\mathcal{V} = k\sqrt{n_{co}^2 - n_{cl}^2}$, $\mathcal{Q} = \sqrt{k^2 n_{cl}^2 - \beta^2}$ and $\beta < kn_{cl}$ is the radiation eigenfield's propagation constant. Note that $\mathcal{U}$, $\mathcal{V}$ and $\mathcal{Q}$ are not the usual dimensionless waveguide parameters and, unlike for bound fields, there is no requirement that $\psi(\mathcal{Q},x) \to 0$ as $|x| \to \infty$. $\mathcal{Q}$ takes any positive real value below $\mathcal{Q} < kn_{cl}$ instead of being restricted to a discrete set of values as for bound eigenfields. The radiation field $\phi(z)$ is expressible as:

$$\phi(z,x) = \int_{\mathcal{Q}=0}^{\mathcal{Q}=kn_{cl}} b(\mathcal{Q},z)\psi(x,\mathcal{Q},z)d\mathcal{Q} \tag{10.19}$$

where $b(\mathcal{Q},z)$ represents the amplitudes of the continuum of radiation modes. This formalism can be extended to accommodate bound modes, by extending the range of integration to include the imaginary axis between $\mathcal{Q} = 0i$ and $\mathcal{Q} = \mathcal{V}i$ and using the superposition weighting $b(\mathcal{Q},z) = b_0(z)\delta(\mathcal{Q} - \mathcal{W}_0 i)$, where $b_0(z)$ is the amplitude of the discrete bound mode, $\mathcal{W}_0 = \sqrt{\beta_0^2 - k^2 n_{cl}^2}$ is the cladding waveguide parameter, β_0 is the (real) propagation constant and $\delta()$ denotes the Dirac delta function.

The application of the derivation in [Snyder and Love, 1983, §31-14] for the radiation field leads to the following system of coupled mode equations:

$$\begin{aligned} &\frac{\partial b(\mathcal{Q},z)}{\partial z} - i\beta(\mathcal{Q})\underline{(}\mathcal{Q},z) = \\ &\int_{A_\infty}\int \frac{b(\mathcal{Q}',z)}{4\mathcal{N}(\mathcal{Q})}\left(\mathbf{h}(\mathcal{Q}) \times \frac{\partial \mathbf{e}(\mathcal{Q}')}{\partial z} - \mathbf{e}(\mathcal{Q}) \times \frac{\partial \mathbf{h}(\mathcal{Q}')}{\partial z}\right).\hat{\mathbf{z}}d\mathcal{Q}'dA \end{aligned} \tag{10.20}$$

where $\mathcal{N}(\mathcal{Q})$ is the normalisation defined by:

$$\int_{A_\infty} \mathbf{e}(\mathcal{Q}) \times \mathbf{h}(\mathcal{Q}').\hat{\mathbf{z}} d\mathcal{Q}' dA = \mathcal{N}(\mathcal{Q})\delta(\mathcal{Q} - \mathcal{Q}') \tag{10.21}$$

For the problems considered in this Chapter, the power is predominantly in a bound mode and we need to quantify the power coupled to the radiation field. Coupling between radiation modes is negligible in this case and we need only to consider terms wherein $\mathbf{e}(\mathcal{Q}')$ and $\mathbf{h}(\mathcal{Q}')$ pertain to a bound mode. In this case, with all fields normalised, the coupled local mode equations become:

$$\begin{aligned} &\frac{\partial b(\mathcal{Q}, z)}{\partial z} - i\beta(\mathcal{Q}) b(\mathcal{Q}, z) = \\ &\frac{b_0(z)}{4} \int_{A_\infty} \left(\hat{\mathbf{h}}(\mathcal{Q}) \times \frac{\partial \hat{\mathbf{e}}_0}{\partial z} - \hat{\mathbf{e}}(\mathcal{Q}) \times \frac{\partial \hat{\mathbf{h}}_0}{\partial z} \right) .\hat{\mathbf{z}} dA \end{aligned} \tag{10.22}$$

Furthermore, the discussion of [Snyder and Love, 1983, §31-15] can be applied to give:

$$C(\mathcal{Q}) = \sqrt{\frac{\epsilon_0}{\mu_0}} \frac{k}{4} \frac{1}{\beta(\mathcal{Q}) - \beta_0} \int_{A_\infty} \hat{\mathbf{e}}(\mathcal{Q}).\hat{\mathbf{e}}_0 \frac{\partial n^2}{\partial z} dA \tag{10.23}$$

which, for weakly guiding structures whose fields are nearly transverse, reduces to:

$$C(\mathcal{Q}) = \frac{k}{2n_{cl}} \frac{1}{\beta(\mathcal{Q}) - \beta_0} \int_{A_\infty} \frac{\partial n^2}{\partial z} \hat{\psi}(\mathcal{Q}) \hat{\psi}_0 dA \tag{10.24}$$

where $\hat{\psi}_0$ is the normalised local bound mode. The coupled local mode equations can be written as:

$$\frac{\partial b(\mathcal{Q}, z)}{\partial z} - i\beta(\mathcal{Q}) b(\mathcal{Q}, z) = C(\mathcal{Q}) b_0(z) \tag{10.25}$$

and, using the techniques of [Snyder and Love, 1983, §28-4]:

$$\begin{aligned} &C(\mathcal{Q}) \approx \frac{k(n_{co} - n_{cl})}{\beta_0 - \beta(\mathcal{Q})} \times \\ &\left(\Omega_1 \left(\hat{\psi}\hat{\psi}_0 \Big|_{x=d+w_1} - \hat{\psi}\hat{\psi}_0 \Big|_{x=d} \right) + \Omega_2 \left(\hat{\psi}\hat{\psi}_0 \Big|_{x=-d-w_2} - \hat{\psi}\hat{\psi}_0 \Big|_{x=-d} \right) \right) \end{aligned} \tag{10.26}$$

The total power radiated can be found analogously to the derivation of extinction ratio (10.2):

$$P_{rad} = \int_{\mathcal{Q}=0}^{\mathcal{Q}=kn_{cl}} \left| \int_0^z C(\mathcal{Q},u) \exp\left(i\beta_0 u - i\int_0^u \beta(\mathcal{Q},v)dv\right) du \right|^2 d\mathcal{Q} \qquad (10.27)$$

Continuity of fields and their first derivatives in (10.18) leads to:

$$\begin{aligned}
&A_1 = \\
&e^{-iw_1\mathcal{Q}}\left(\left(\frac{i(\mathcal{Q}^2+\mathcal{U}^2)}{2\mathcal{Q}\mathcal{U}}\sin(\mathcal{U}w_1)+\cos(\mathcal{U}w_1)\right)A_3 + e^{-2id\mathcal{Q}}\frac{i\mathcal{V}^2}{2\mathcal{Q}\mathcal{U}}sin(\mathcal{U}w_1)B_3\right)\\
&B_1 = \\
&e^{iw_1\mathcal{Q}}\left(-e^{2id\mathcal{Q}}\frac{i\mathcal{V}^2}{2\mathcal{Q}\mathcal{U}}sin(\mathcal{U}w_1)A_3 + \left(\cos(\mathcal{U}w_1)-\frac{i(\mathcal{Q}^2+\mathcal{U}^2)}{2\mathcal{Q}\mathcal{U}}\sin(\mathcal{U}w_1)\right)B_3\right)\\
&A_2 = \frac{\mathcal{Q}+\mathcal{U}}{2\mathcal{U}}e^{id(\mathcal{Q}-\mathcal{U})}A_3 + \frac{\mathcal{U}-\mathcal{Q}}{2\mathcal{U}}e^{-id(\mathcal{Q}+\mathcal{U})}B_3\\
&B_2 = \frac{\mathcal{U}-\mathcal{Q}}{2\mathcal{U}}e^{id(\mathcal{Q}+\mathcal{U})}A_3 + \frac{\mathcal{Q}+\mathcal{U}}{2\mathcal{U}}e^{id(\mathcal{U}-\mathcal{Q})}B_3\\
&A_4 = \frac{\mathcal{Q}+\mathcal{U}}{2\mathcal{U}}e^{id(\mathcal{U}-\mathcal{Q})}A_3 + \frac{\mathcal{U}-\mathcal{Q}}{2\mathcal{U}}e^{id(\mathcal{Q}+\mathcal{U})}B_3\\
&B_4 = \frac{\mathcal{U}-\mathcal{Q}}{2\mathcal{U}}e^{id(\mathcal{Q}+\mathcal{U})}A_3 + \frac{\mathcal{Q}+\mathcal{U}}{2\mathcal{U}}e^{id(\mathcal{Q}-\mathcal{U})}B_3\\
&A_5 = \\
&e^{iw_2\mathcal{Q}}\left(\left(\cos(\mathcal{U}w_2)-\frac{i(\mathcal{Q}^2+\mathcal{U}^2)}{2\mathcal{Q}\mathcal{U}}\sin(\mathcal{U}w_2)\right)A_3 - e^{2id\mathcal{Q}}\frac{i\mathcal{V}^2}{2\mathcal{Q}\mathcal{U}}sin(\mathcal{U}w_2)B_3\right)\\
&B_5 = \\
&e^{-iw_2\mathcal{Q}}\left(e^{-2id\mathcal{Q}}\frac{i\mathcal{V}^2}{2\mathcal{Q}\mathcal{U}}sin(\mathcal{U}w_2)A_3 + \left(\frac{i(\mathcal{Q}^2+\mathcal{U}^2)}{2\mathcal{Q}\mathcal{U}}\sin(\mathcal{U}w_2)+\cos(\mathcal{U}w_2)\right)B_3\right)
\end{aligned} \qquad (10.28)$$

The eigenfield can then be normalised by using the results:

$$\begin{aligned}
\int_a^\infty e^{i\omega x}dx &= e^{i\omega a}\left(\pi\delta(\omega)-\frac{i}{\omega}\right)\\
\int_{-\infty}^{-a} e^{i\omega x}dx &= e^{-i\omega a}\left(\pi\delta(\omega)+\frac{i}{\omega}\right)
\end{aligned} \qquad (10.29)$$

which are interpreted in the generalised function sense[Lighthill, 1958]. The normalisation constant is:

$$\mathcal{N}(\mathcal{Q}) = \pi\left(|A_1(\mathcal{Q})|^2 + |B_1(\mathcal{Q})|^2 + |A_5(\mathcal{Q})|^2 + |B_5(\mathcal{Q})|^2\right) \qquad (10.30)$$

If the waveguide's cross-section varies only slowly with z, the integral with respect to z in (10.27) is approximately:

$$\left|\int_0^z C(\mathcal{Q},u)\exp\left(\left(i\beta_0-\sqrt{k^2n_{cl}^2-i\mathcal{Q}^2}\right)u\right)du\right|^2\approx$$
$$2|C(\mathcal{Q})|^2\frac{1-\cos\left(\left(\beta_0-\sqrt{k^2n_{cl}^2-\mathcal{Q}^2}\right)z\right)}{\left(\beta_0-\sqrt{k^2n_{cl}^2-\mathcal{Q}^2}\right)^2} \tag{10.31}$$

When this quantity is integrated with respect to $\mathcal{Q}$ over the interval $[0, kn_{cl}]$, the oscillating term $\cos\left(\left(\beta_0-\sqrt{k^2n_{cl}^2-\mathcal{Q}^2}\right)z\right)$ vanishes as $z\to\infty$, by the Riemann-Lebesgue lemma[Lighthill, 1958]. The power coupled to the radiation field undergoes damped oscillation about its final asymptotic value:

$$P_{rad}=2\int_{\mathcal{Q}=0}^{\mathcal{Q}=kn_{cl}}\frac{|C(\mathcal{Q})|^2}{\left(\beta_0-\sqrt{k^2n_{cl}^2-\mathcal{Q}^2}\right)^2}d\mathcal{Q} \tag{10.32}$$

Since the waveguide is weakly guiding, $\beta_0\approx kn_{cl}$, the term $1/\left(\beta_0-\sqrt{k^2n_{cl}^2-\mathcal{Q}^2}\right)^2$ is significant only for $\mathcal{Q}<<kn_{cl}$ and decreases rapidly as $\mathcal{Q}\to kn_{cl}$. Hence, the first order Taylor expansion with respect to $\mathcal{Q}$ of the radiation field can be used for $|C(\mathcal{Q})|$. Also, the range of integration can be extended to $[0,\infty)$ with little change because the integrand becomes vanishingly small for $\mathcal{Q}>kn_{cl}$. This leads to (10.6).

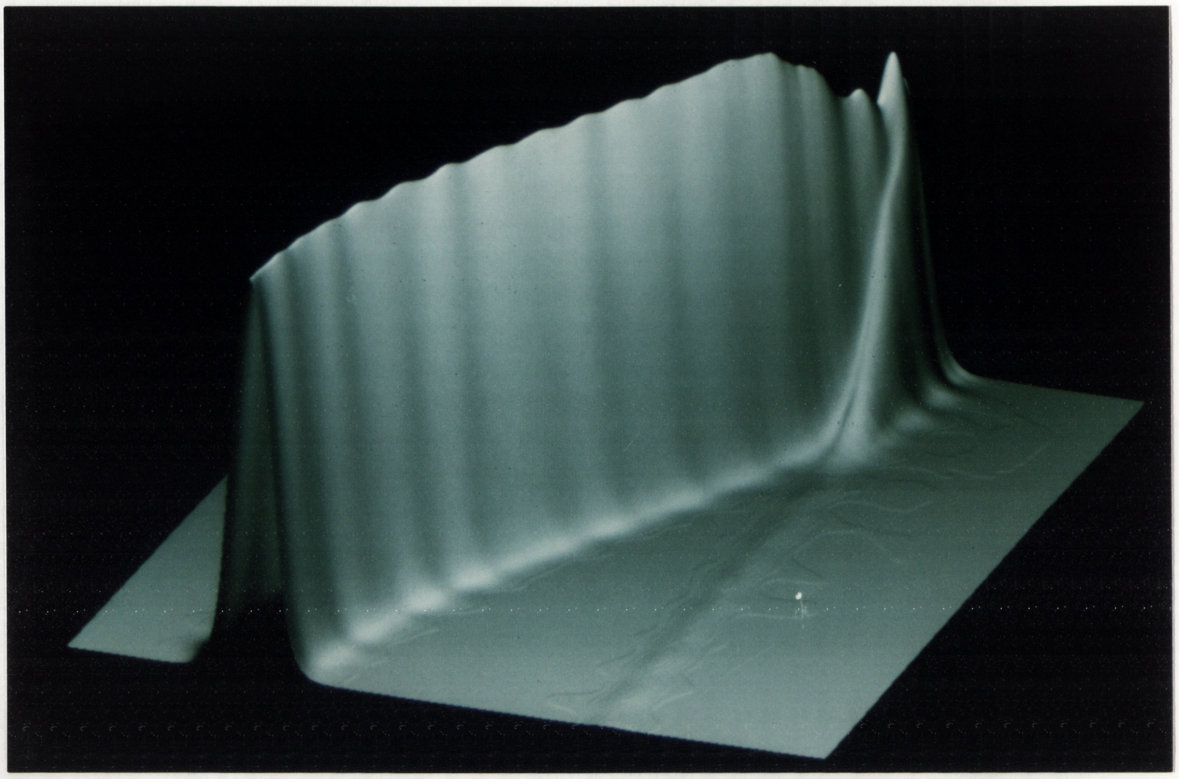

(a)

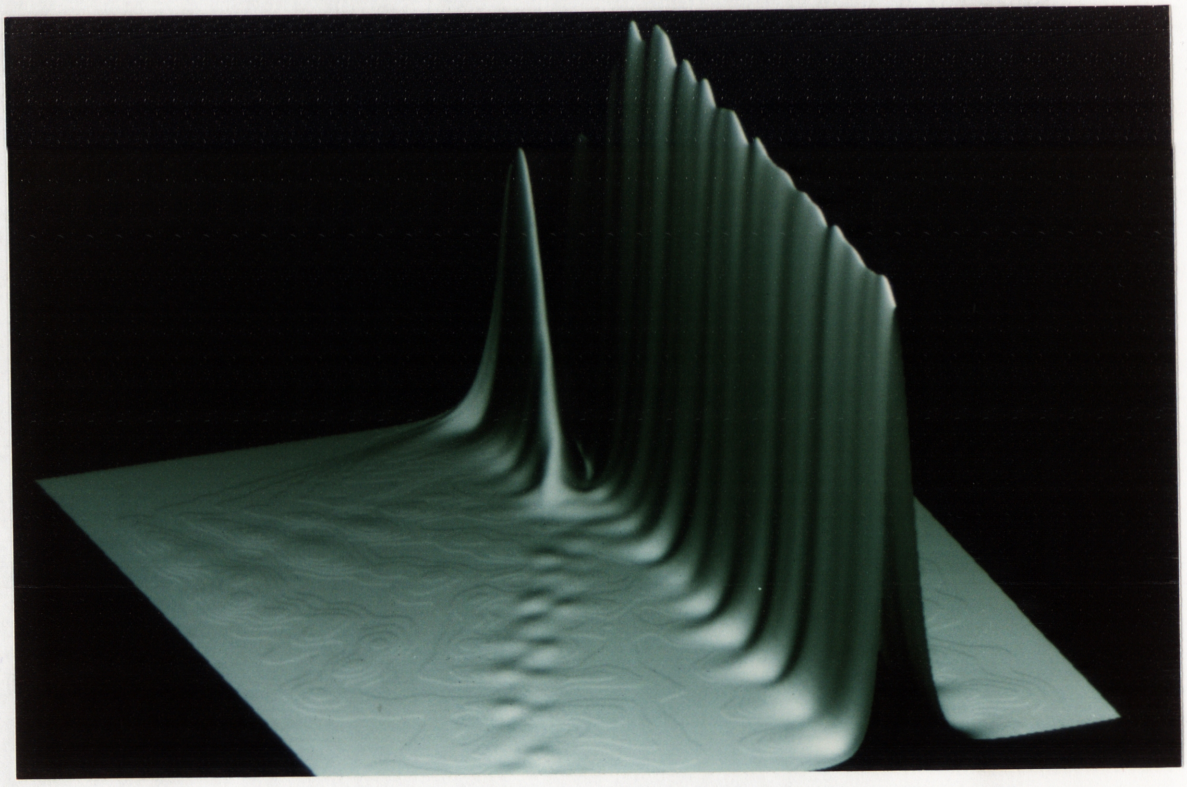

(b)

Figure 10.11: Evolution of intensity within asymmetric Y-splitter for *(a)* even and *(b)* odd mode input to the system

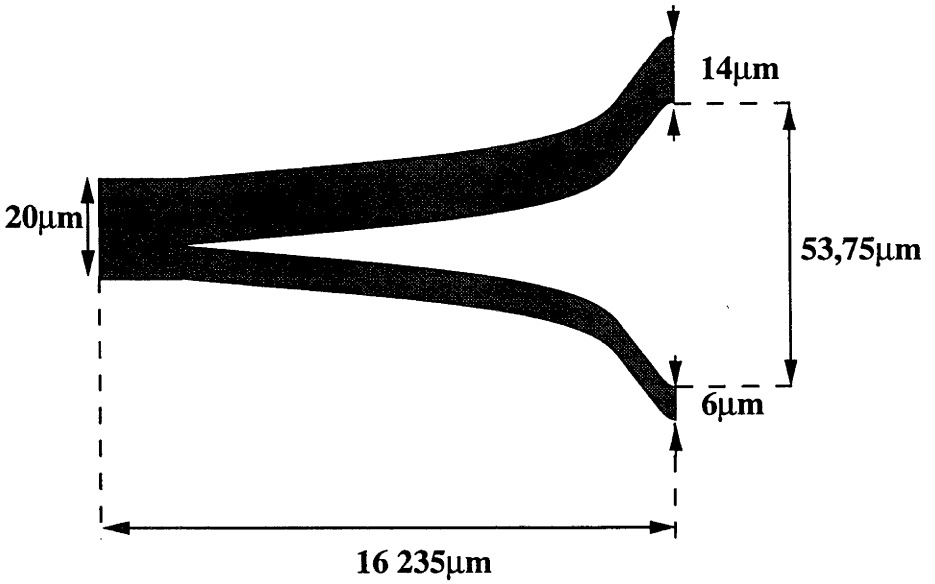

Figure 10.12: Optimally short unskewed Y-splitter

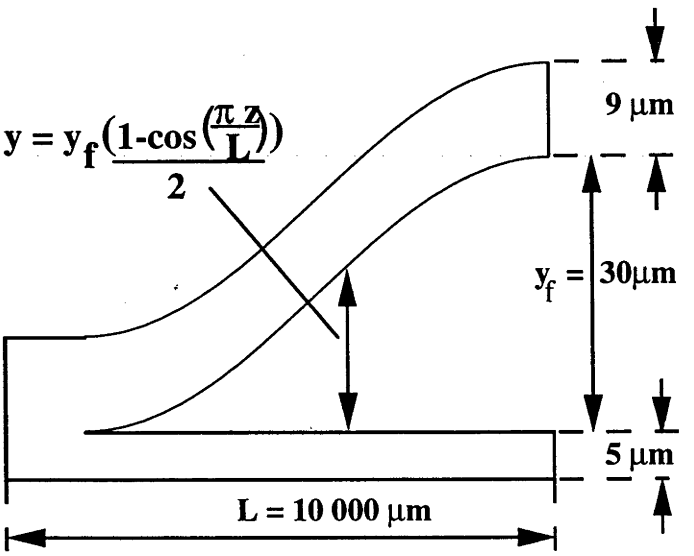

Figure 10.13: Wavelength response simulation subject

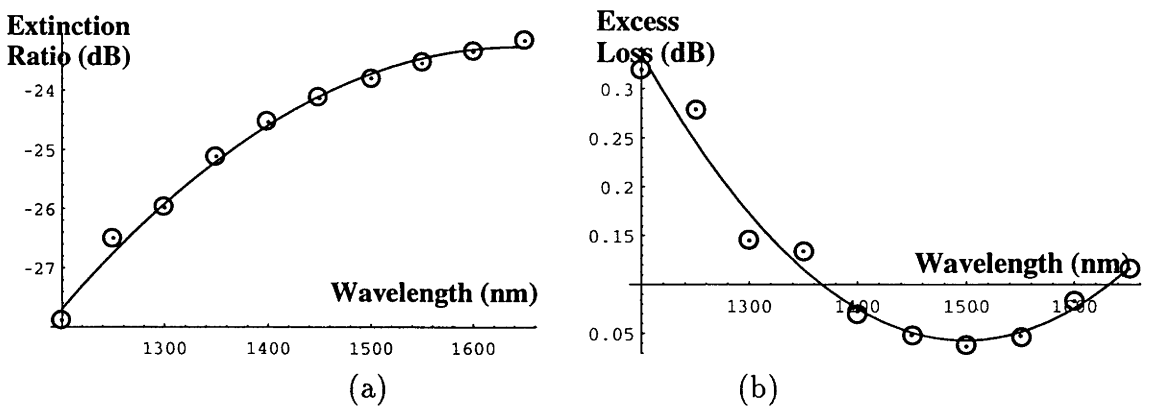

Figure 10.14: *(a)* Extinction ratio and *(b)* excess loss as a function of wavelength for a 2-channel adiabatic Y-splitter

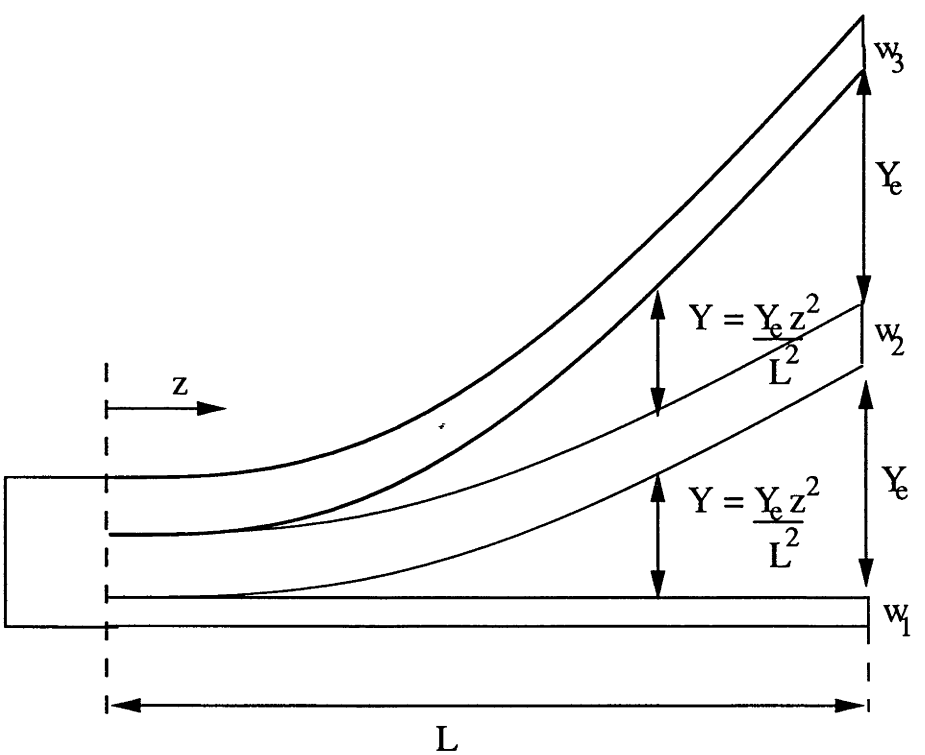

Figure 10.15: Skewed Y-Splitter

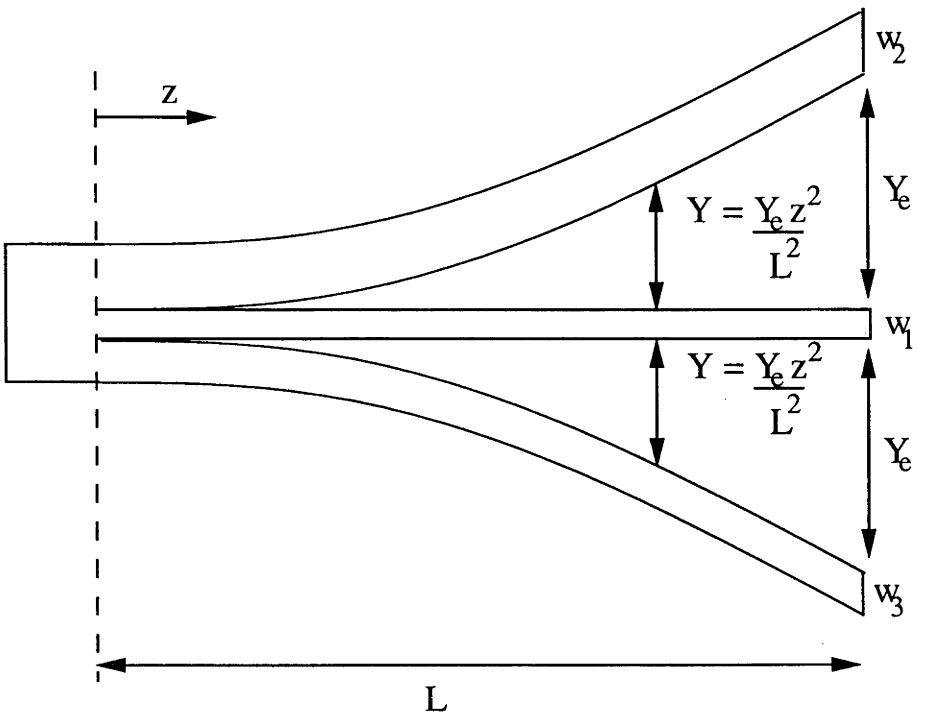

Figure 10.16: Unskewed Y-Splitter

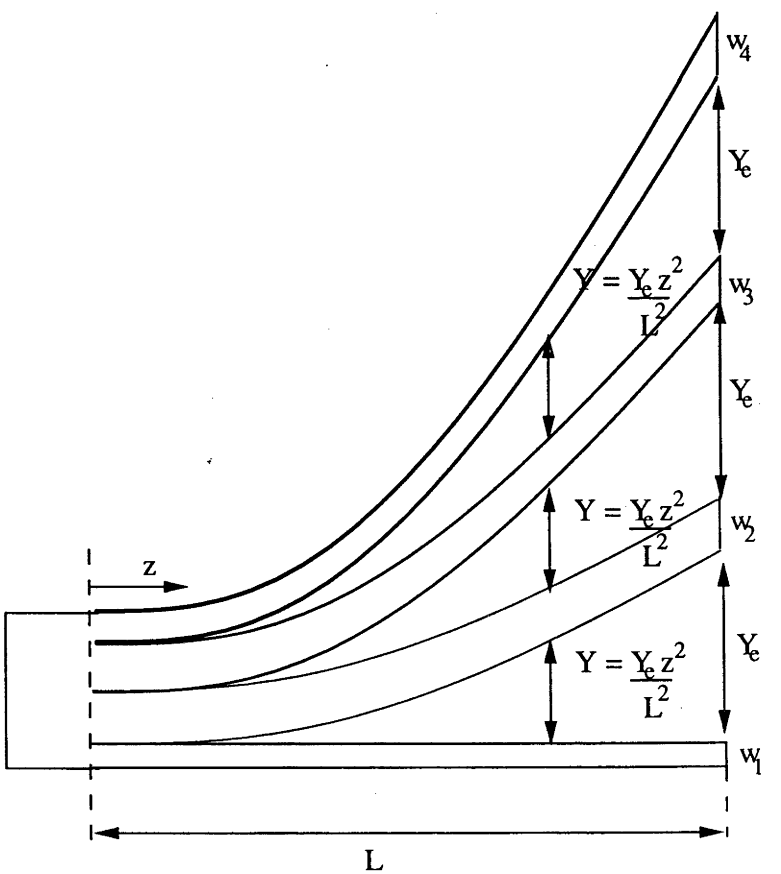

Figure 10.17: Four-channel Y-splitter

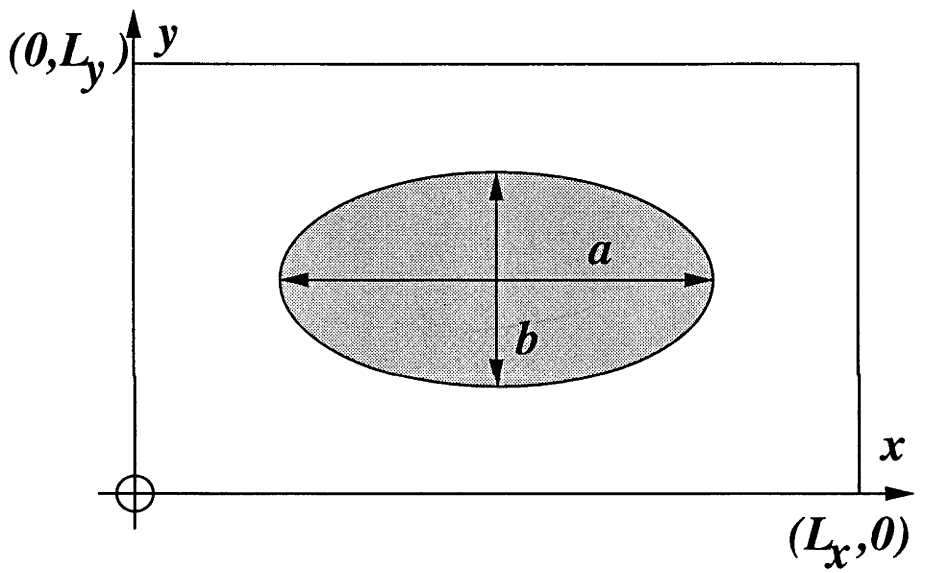

Figure 10.18: Definition of elliptical-core waveguide

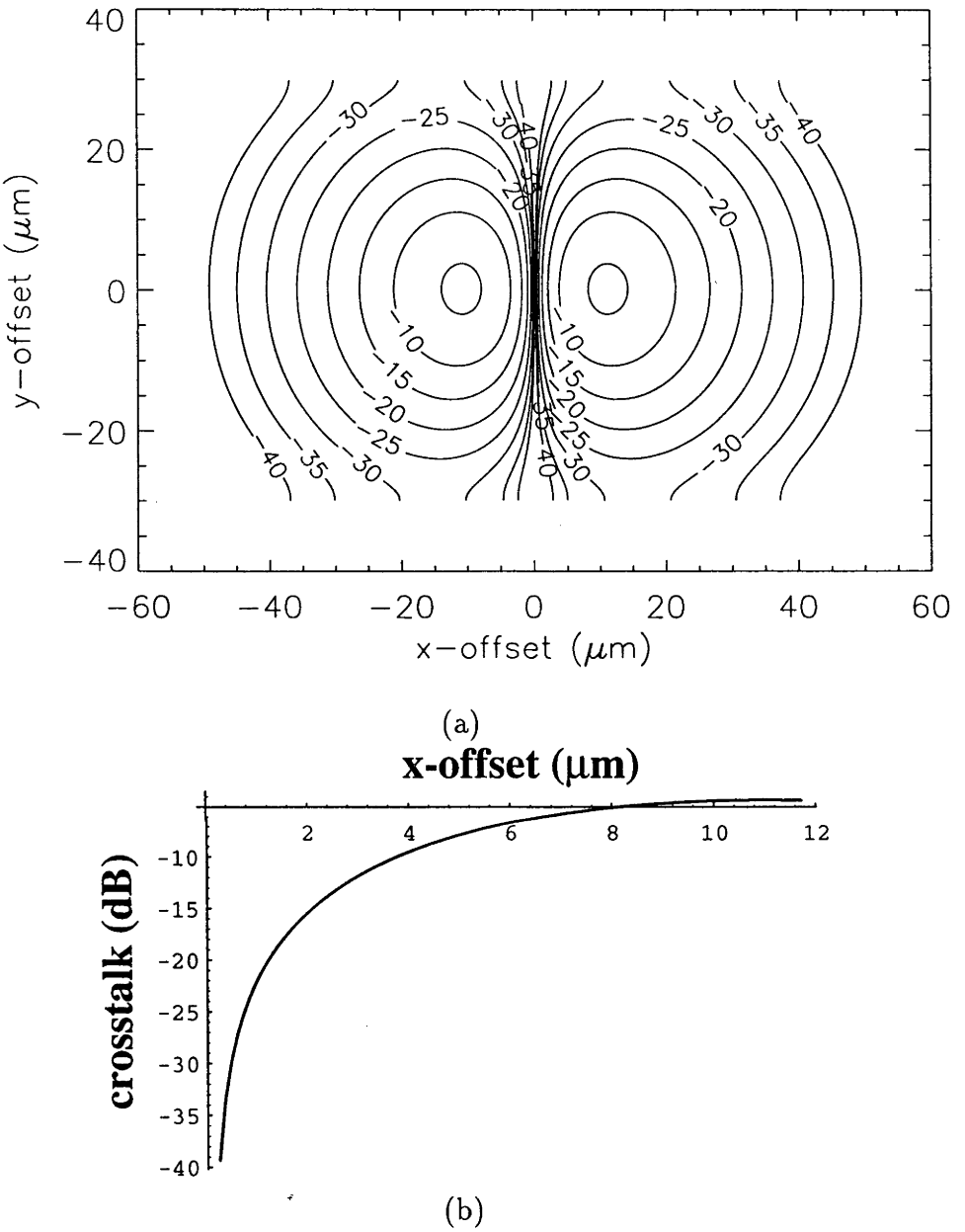

Figure 10.19: *(a)* Crosstalk between the two modal channels of an asymmetric, adiabatic Y-splitter caused by misalignment between the device and its input two-moded fibre as a function of offset; -40 to -5dB contours plotted in 5dB steps and *(b)* greater detail for small offsets purely in the x-direction

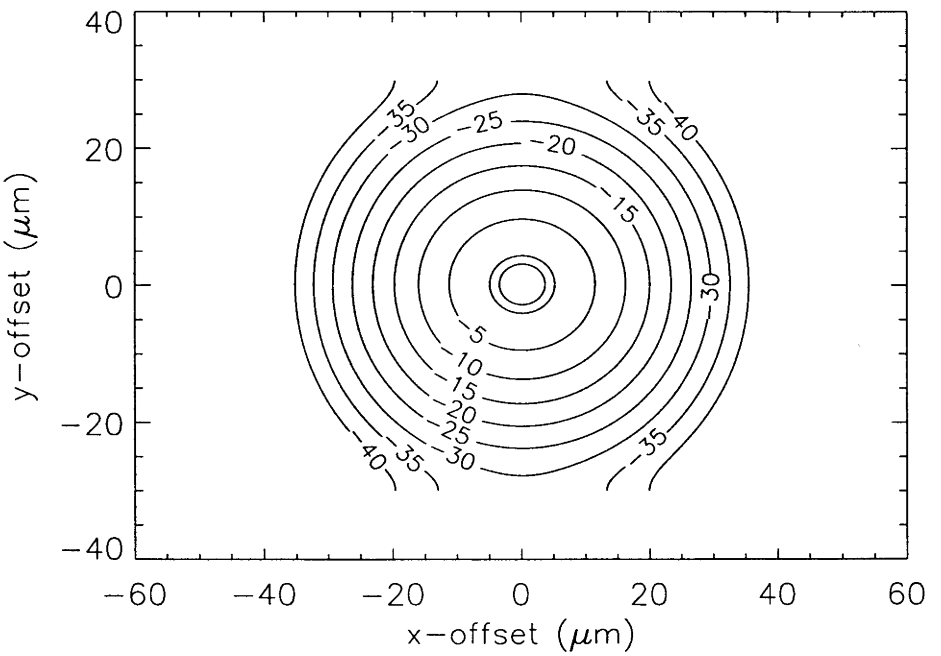

(a)

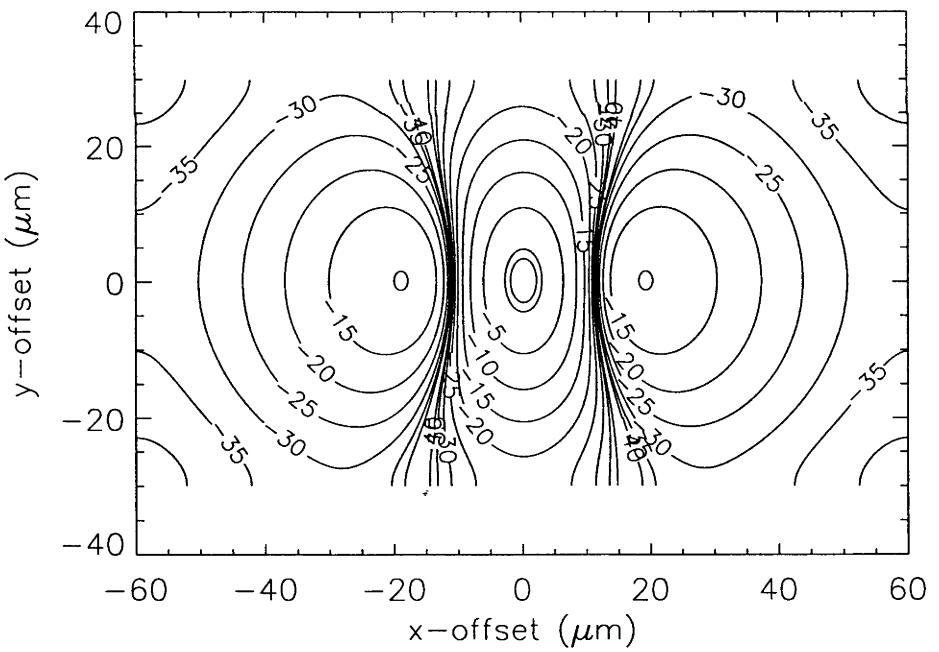

(b)

Figure 10.20: *(a)* Overlap between the fundamental modes of the fibre and Y-splitter input as a function of offset; the 40 to 5dB splice loss contours are plotted in 5dB steps together with those for 1dB and 0.5dB splice loss; *(b)* corresponding plot for overlap between the fibre's and Y-splitter input's odd modes.

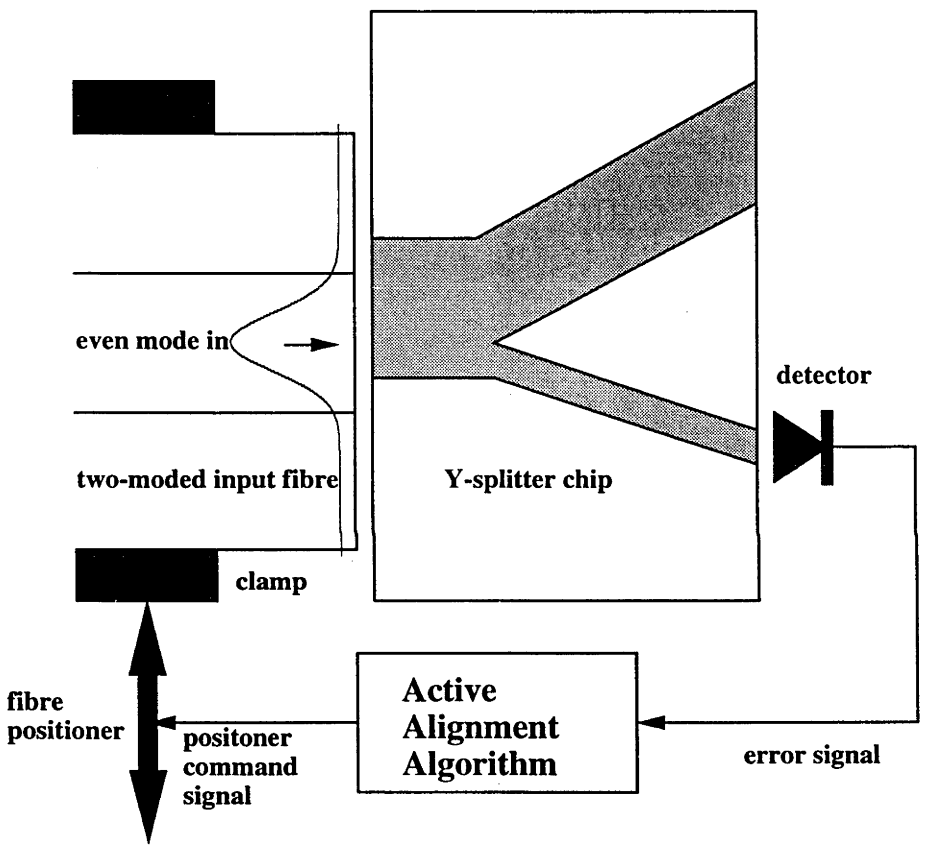

Figure 10.21: Active alignment between a 2-channel mode splitter and its input fibre

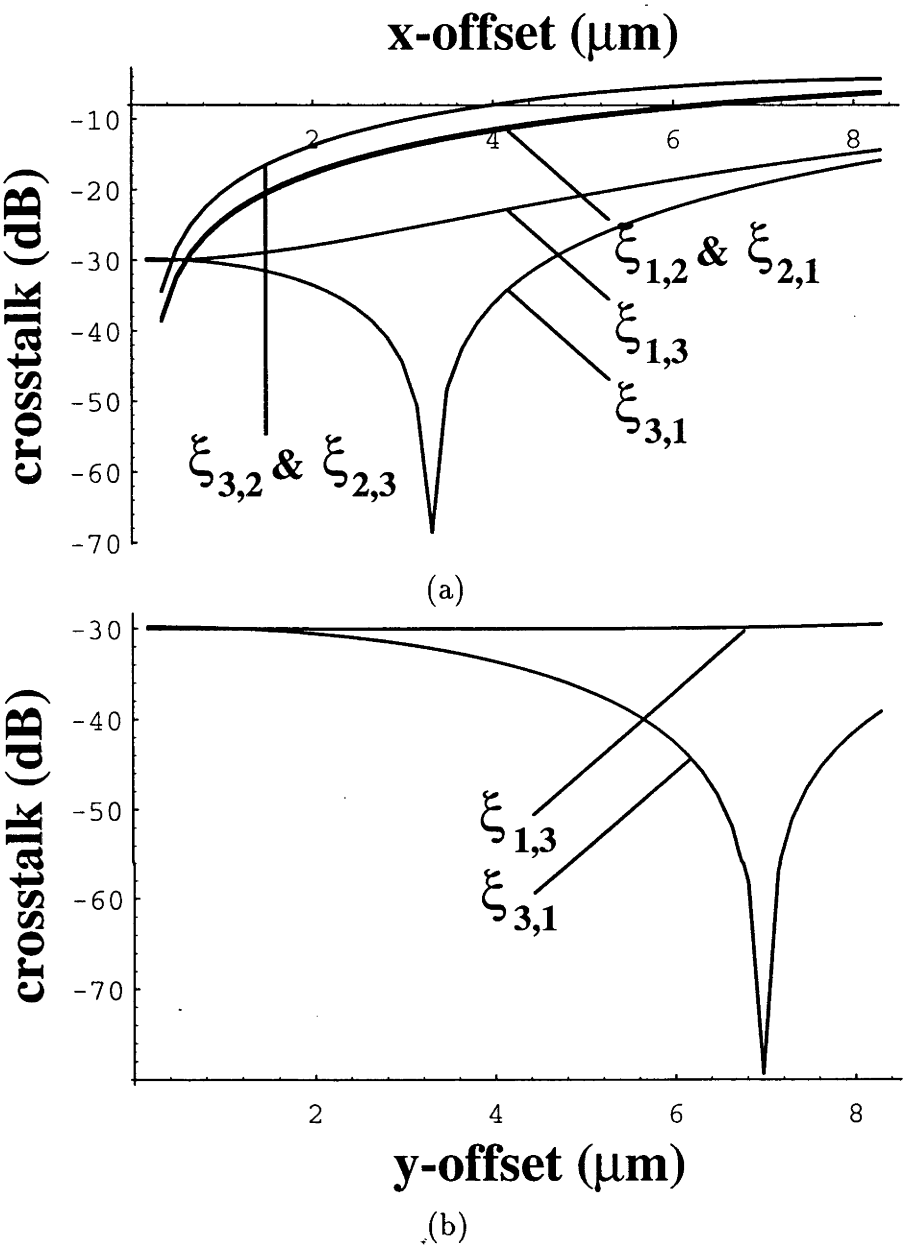

Figure 10.22: *(a)* Crosstalk between modal channels as a function of splice offset in the x-direction; $\xi_{j,k}$ is the overlap between the splitter's j^{th} and elliptical core fibre's k^{th} mode (1 = fundamental, 2 = first odd, 3 = second even); *(b)* corresponding plots for y-direction misalignment; there is no overlap between odd and even modes

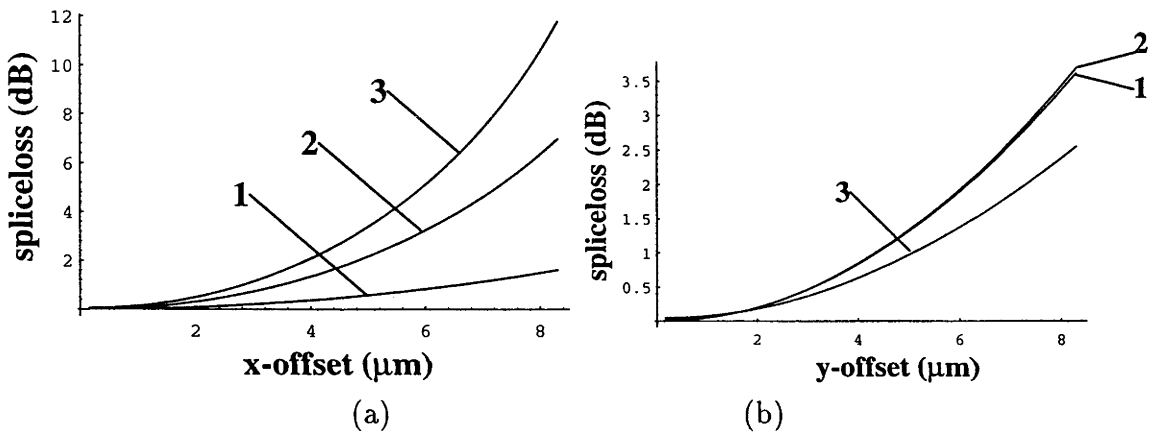

Figure 10.23: Splice loss as a function of misalignment for the three modal channels (1 = fundamental, 2 = first odd, 3 = second even): *(a)* x-offsets; *(b)* y-offsets

References

Abd-El-Hamid, G. and Davies, P. A. (1989). Fibre-optic double ring resonator. *Electronics Letters*, **25**, 224–225.

Adar, R., Shani, Y., Henry, C. H., Kistler, R. C., Blonder, G. E. and Olsson, N.A. (1991). Measurement of very low-loss silica on silicon waveguides with a ring resonator. *Applied Physics Letters*, **58**, 445–448.

Analog-Devices, Inc. (1990). *1990/91 Linear Products Handbook.* Datasheet for AD517 Trimmed, Precision IC Op Amp.

Anderson, B. D. O. (1979). *Linear Optimal Control.* New Jersey: Prentice Hall.

Ankiewicz, A. and Peng, G. D. (1992). Generalised Gaussian Approximation For Single-Mode Fibers. *IEEE J. Lightwave Tech.*, **10**, 22–27.

Ankiewicz, A. and Rühl, F. (1994). Effect of dopant distribution on optimization of Pr-doped fibre amplifiers. *Optical and Quantum Electronics*, **26**, in press.

Bergen, A. R. (1986). *Power systems analysis.* New Jersey: Prentice Hall.

Birks, T. A. and Li, Y. W. (1992). The Shape of Fiber Tapers. *IEEE J. Lightwave Tech.*, **10**, 432–438.

Bjarklev, A., Hansen, S. L. and Povlsen, J. H. (1989). Large Signal Modelling of an Erbium Doped Fibre Amplifier. *SPIE Fibre Laser Sources and Amplifiers*, **1171**, 118–129.

Bjarklev, A., Lumholt, O., Povlsen, J. H., Rasmussen, T., Rottwitt, K., Dahl-Petersen, S. and Larsen, C. C. (1992). New Tapered Active Fibres for Very Low Noise Applications. *Electronics Letters*, **28**, 34–36.

Born, M. and Wolf, E. (1980). *Principles of Optics.* Oxford: Pergamon Press.

Bröckner, T. and Dieck, T. (1985). *Representations of Compact Lie Groups.* New York: Springer Verlag.

Burns, W. K. and Milton, F. (1980). An Analytic Solution for Mode Coupling in Optical Waveguide Branches. *IEEE J. Quantum Electronics*, **QE-16**, 446–454.

Carroll, J. E. and Rigg, P. R. (1980). Matrix theory for n-line microwave coupler design. *IEE Proceedings Part H*, **127**, 309–314.

Chaoyu, Y., Jiangde, P. and Bingkun, Z. (1989). Tunable Nd^{3+}-doped fibre ring laser. *Electronics Letters*, **25**, 224–225.

Cochrane, P. and Heatly, D. J. T. (1992, December). Future Developments in Gbit Optical Fibre Systems. *Pages 6–9 of: Proc.* 17^{th} *Australian Conf. Optical Fibre Tech.*

Corning, Inc. (1993). *Datasheet for P1930 Elliptical-Core Polarization-Maintaining Singel-Mode Optical Fiber.*

Daino, B., Gregori, G. and Wabnitz, S. (1985). Stability Analysis of Nonlinear Coherent Coupling. *J. App. Phys*, **58**, 4512–4514.

Davis, P. J. (1979). *Circulant Matrices.* New York: John Wiley & Sons.

Delaney, P.M., Harris, M. R. and King, R.G. (1993). Novel microscopy using fibre optic confocal imaging and its suitability for subsurface blood vessel imaging in vivo. *Clinical and Experimental Pharmachology & Physiology*, **20**, 197.

Delaney, P.M., Harris, M. R. and King, R.G. (1994). Fibre-optic laser scanning confocal microscope suitable for fluoresence imaging. *Applied Optics*, **33**, 573.

Dunphy, J. R. (1987). Distributed Strain Sensing with Twin-Core Fibre Optic Sensor. *ISA Transactions*, **26**, 7–10.

Engen, G. F. and Hoer, C. A. (1984). Application of an arbitrary 6-port junction to power measurement problems. *IEEE Trans. Instrumentation & Measurement*, **IM-21**, 470–474.

Farahi, F., Jakahashi, N., Jones, J. D. C. and Jackson, D. A. (1988). Multiplexed sensing systems utilizing all fiber ring resonators. *SPIE Fibre Optic and Laser Sensors III*, **SPIE Vol.1011**.

Feit, M. D. and Fleck, J. A. (1978). Light Propagation in Graded-Index Optical Fibres. *Applied Optics*, **17**, 3990–3998.

Fritschel, P., Shoemaker, D. and Weiss, R. (1992). Demonstration of light recycling in a Michelson interferometer with Fabry-Perot cavities. *Applied Optics*, **31**, 1412–1418.

Geers, D. G., Bassett, I. M. and Hewlett, S. J. (1993, December). Numerical Characterisation of Twin-core Fibre: Scalar and Vector Solutions. *Pages 348–351 of: Proc.* 18^{th} *Australian Conf. Optical Fibre Tech.*

Ghatak, A. and Thyagarajan, K. (1989). *Optical Electronics.* Cambridge, England: Cambridge University Press. Chapters 8 & 9.

Giles, C. R. and Desurvire, E. (1991a). Modeling Erbium-Doped Fiber Amplifiers. *IEEE J. Lightwave Technology*, **9**, 271–283.

Giles, C. R. and Desurvire, E. (1991b). Propagation of Signal and Noise in Concatenated Erbium- Doped Fiber Optical Amplifiers. *IEEE J. Lightwave Tech*, **9**, 147–154.

Giroult-Matlakowski, G., Armand, S., Jarnyk, M. and Boswell, R. W. (1992, December). Low temperature plasma assisted deposition of thick silica layers ($1\mu rmm \rightarrow 20\mu$m) for optical planar waveguide devices using the helicon diffusion reactor. *Pages 332–335 of: Proc.* 17^{th} *Australian. Conf. Optical Fibre Technology.*

Glodge, D. (1976). *Optical Fibre Technology.* New York: IEEE Press.

Grunnet-Jepsen, A., Schüsler, K., Dahl-Petersen, S., Palsdottir, B., Bjarklev, A., Rottwitt, K., Povlsen, J. H. and Rasmussen, T. (1992). Noise Characteristics of erbium-Doped Fiber Amplifier Pumped at 980nm. *SPIE Fiber Laser Sources and Amplifiers* IV, **1789**, 140–144.

Gunton, D. J. (1978). Design of wideband codirectional couplers and their realisation at microwave frequencies using coupled comblines. *Microwaves, Optics and Acoustics*, **2**, 19–30.

Haus, H. A. (1984). *Waves and Fields in Optoelectronics.* Englewood Cliffs, New Jersey: Prentice-Hall.

Heaton, J. M., Wright, D. R., Parker, J. T., Hughes, B. T., Birbeck, J. C. H. and Hilton, K.P. (1992). A phased array optical scanning (PHAROS) device used as a 1-to-9 way switch. *IEEE J. Quantum Electronics*, **28**, 678–685.

Henry, C. H. and Shani, Y. (1991). Analysis of Mode Propagation in Optical Waveguide Devices by Fourier Expansion. *IEEE J. Quantum Electronics*, **27**, 523–530.

Henry, W. M. (1991, December). Modes and Power Splitting in a 5×5 Coupler with Applications to Coherent Detection. *Pages 52–55 of: Proc.* 16^{th} *Australian. Conf. Optical Fibre Technology.*

Herscher, B. A. and Carroll, J. E. (1982). Design Technique for Multiport Combline Couplers with Single Port Excited. *IEE Proceedings Part H, Microwave Optics & Antennas*, **129**, 61–67.

Hewlett, S. J. (1991). *Imaging Strategies in Scanning Optical Microscopy.* Department of Engineering Science, University of Oxford: D.Phil. thesis.

Hewlett, S. J. (1994). *Private correspondence with S. J. Hewlett, Optical Sciences Centre, Australian National University.*

Hewlett, S. J. and Ladouceur, F. (1994). Modified Fourier decomposition method: numerical analysis of dielectric waveguides down to modal cut-off. *submitted to IEEE J. Lightwave Tech.*, **12**.

Hewlett, S. J., Ladouceur, F. and Love, J. D. (1993). Splice loss in single and twin-core buried channel waveguide devices. *Optical and Quantum Electronics*, **26**, 45–62.

Hunt, B. R. (1971). A Matrix Theory Proof if the Discrete Convolution Theorem. *IEEE Trans. Audio and Electroacoustics*, **AU-19**, 285–288.

Ilyama, K., Arai, K., Hayashi, K. and Ida, Y. (1990, December). Sensitivity enhancing scheme of optical sensor by utilizing optical loops. *Pages 121–124 of: Proc. 7th Int. Conf. Optical Fibre Sensors.*

Ise, Mikio and Takeuchi, Masaru. (1990). *Lie Groups I and II.* Rhode Island, USA: American Mathematical Society.

Islam, S. and Carroll, J. E. (1986). Warped-mode multiway combline directional couplers. *IEE Proceedings Part H*, **133**, 81–90.

Jaroszewiz, Z. and Pluta, M. (1990). *Interferometry '89: 100 years after Michelson.* SPIE Vol. 1121.

Jauch, J. M. and Rohrlich, F. (1976). *The Theory of Photons and Electrons.* New York: Springer-Verlag.

Juskaitis, R. and Wilson, T. (1992). Surface profiling with scanning optical microscopes using two-mode optical fibers. *Applied Optics*, **31**, 4569–4574.

Kath, W. L. and Kriegsmann, A. (1988). Optical tunnelling: radiation losses in bent fibre-optic waveguides. *IMA Journal of Applied Mathematics*, **41**, 85–103.

Kersey, A. D., Corke, M. and Jackson, D. A. (1984). Linearised Polarimetric Optical Fibre Sensor Using Hetrodyne Type Signal Recovery Scheme. *Electronics Letters*, **20**, 209–211.

Ladouceur, F. (1992). *Buried Channel Waveguides & Devices.* Ph.D. thesis, Optical Sciences Centre, Australian National University.

Laming, R. I. and Payne, D. N. (1990). Noise Characteristics of erbium-Doped Fiber Amplifier Pumped at 980nm. *IEE Photonics Tech. Let.*, **2**, 418–421.

Laming, R. I., Zervas, M. N. and Payne, D. N. (1992). Erbium-Doped Fiber Amplifier with 54 dB Gain and 3.1 dB Noise Figure. *IEE Photonics Tech. Let.*, **4**, 1345–1347.

Landau, L. D. and Lifschitz, E. M. (1970). *Theory of Elasticity.* Oxford: Pergamon Press.

Lefevre, H. C., Desforges, F. X., Martin, P. and Simonpietri, P. (1990, December). Two Mode Fibre Gauge for Dual Measurement of Temperature and Strain. *Pages 387–390 of: Proc. 7th Int. Conf. Optical Fibre Sensors.*

Lerminiaux, C. (1992, December). Ion Exchange Devices. *Pages 330–331 of: Proc. 17th Australian. Conf. Optical Fibre Technology.*

Lewandowski, J., Syms, R. R. A., Madden, S. and Green, M. (1991). Buried channel waveguides in plasma-enhanced chemical vapour deposited silicon oxynitride layers on silicon substrates, formed by electron-beam irradiation. *Optical & Quantum Electronics*, **23**, 703–711.

Lighthill, M. J. (1958). *An Introduction to Fourier Analysis and Generalised Functions.* Cambridge: Cambridge University Press.

Love, J. D., Henry, W. M., Stewart, W. J., Black, R. J., Lacroix, S. and Gonthier, F. (1991). Tapered single-mode fibres and devices: Part 1: Adiabaticity criteria; Part 2: Experimental and Theoretical Quantification. *IEE Proceedings*, **138**, 343–364.

Luff, G. F., Probert, P. J. and Carroll, J. E. (1984). Real-time reflectometer. *IEE Proceedings Part H, Microwave Optics & Antennas*, **131**, 186–190.

Magnus, W. (1954). On the Exponential Solution of Differential Equations for a Linear Operator. *Comm. Pure & Applied Math.*, **VII**, 649–673.

Marcuse, D. (1991). *Theory of dielectric optical waveguides.* San Diego, California: Academic Press, Inc.

Matera, F. and Wabnitz, S. (1986). Nonlinear Polarization Evolution and Instability in a Twisted Birefringent Fibre. *Optics Letters*, **11**, 467–469.

Mears, R. J., Reekie, L., Poole, S. B. and Payne, D. N. (1985). Neodymium-doped silica single-mode fibre lasers. *Electronics Letters*, **21**, 738–740.

Mears, R. J., Reekie, L., Jauncey, I. M. and Payne, D. N. (1987). High-gain, rare-earth-doped fibre amplifier at 1.54μm. *Proc. 1987 OFC, paper W12*, February.

Meltz, G. and Morey, W. W. (1991). Bragg Grating Formation and Germanosilicate Fiber Photosensitivity. *SPIE*, **1516**, 185–199.

Mermelstein, M. D. (1986). Fibre-Optic Polarimetric D.C. Magnetometer Utilising a Composite Metallic Glass Resonator. *IEEE J. Lightwave Technology*, **LT-9**, 1376–1380.

Michel, A. N. and Herget, C. J. (1981). *Mathematical Foundations in Engineering and Science.* New Jersey: Prentice Hall.

Mortimore, D. B. (1985). Wavelength flattened fused couplers. *Electronics Letters*, **21**, 742–743.

Mortimore, D. B. (1989). Monolithic 4 × 4 Single-Mode Fused Coupler. *Electronics Letters*, **25**, 682–683.

Nagano, K., Kawakami, S. and Nishida, S. (1978). Change of the refractive index in an optical fiber due to external forces. *Applied Optics*, **17**, 2080–2085.

Normand, J. M. (1980). *A Lie Group: Rotations in Quantum Mechanics.* Amsterdam: North Holland Publishing Company.

Okamura, H. and Iwatsuki, K. (1990, December). Fibre-optic sensor using an injection-locked local laser. *Pages 135–137 of: Proc. 7th Int. Conf. Optical Fibre Sensors.*

Oppenheim, A. V. and Schafer, R. W. (1975). *Digital Signal Processing.* Englewood Cliffs, New Jersey: Prentice-Hall.

Papoulis, A. (1977). *Signal Analysis.* New York: Mc Graw-Hill.

Payne, D. N. (1992). Active Fibres and Optical Amplifiers. *Fiber and Integrated Optics*, **11**, 191–219.

Pedersen, B., Bjarklev, A., Povlsen, J. H., Dybdal, K. and Larsen, C. C. (1991). The Design of Erbium-Doped Fiber Amplifiers. *IEEE J. Lightwave Tech*, **9**, 1105–1112.

Peng, G. D. and Ankiewicz, A. (1991). Modified Gaussian approach for the design of optical fiber couplers of arbitrary core shapes. *Applied Optics*, **30**, 2533–2545.

Peroni, M. and Tamburrini, M. (1989). Gain in Erbium-Doped Fiber Amplifiers: A Simple Analytical Solution for the Rate Equations. *Optics Letters*, **15**, 842–844.

Pietzsch, J. (1989). Scattering Matrix Analysis of 3 × 3 Fibre Couplers. *IEEE J. Lightwave Technology*, **7**, 303–307.

Poole, S. B., Payne, D. N. and Fermann, M. E. (1985). Fabrication of low-loss optical fibres containing rare-earth ions. *Electronics Letters*, **21**, 737–738.

Press, W. H., Flannery, B. P., Teukolsky, S. A. and Vetterling, W. T. (1990). *Numerical recipes in C: The art of scientific computing.* Cambrige, England: Cambridge University Press.

Rengarajan, S. R. and Lewis, J. E. (1980). First higher-mode cutoff in two-layer elliptical fibre waveguides. *Electronics letters*, **16**, 263–264.

Rigg, P. R. and Carroll, J. E. (1980). Three-line broadband codirectional microwave couplers using planar comb and herringbone microstrip lines. *IEE Proceedings Part H*, **127**, 315–322.

Romaniak, R. S and Dorosz, J. (1989). Multicore Micro-optics. *Int. J. Optoelectronics*, **4**, 201–219.

Rowland, D. R. and Love, J. D. (1993). Evanescent-Wave Coupling of Whispering-Gallery-Modes of a Dielectric Cylinder. *IEEE Proc. J*, **140**, 177–188.

Rowland, D. R., Chen, Y. and Snyder, A.W. (1991). Tapered Mismatched Couplers. *IEEE J. Lightwave Technology*, **9**, 567–570.

Royden, H. L. (1968). *Real Analysis.* New York: Collier-Macmillan.

Rühl, F. F. (1991). Prediction of Optimum Fibre Lengths for Erbium Doped Fibre Amplifiers. *Electronics Letters*, **27**, 769–770.

Sagle, A. A. and Walde, R. E. (1973). *Introduction to Lie Groups and Lie Algebras.* New York: Academic Press. Section 1.6 introduces the Lie algebra

concept. Chapter 3 discusses topological groups, in particular, Section 3.2 discusses subgroups, Section 3.3 discusses connected groups and gives a proof that any connected group is generated by an arbitrarily small neighbourhood of the identity. Chapter 5 discusses the Lie algebra of a Lie group. Chapter 6 discusses Lie subgroups and subalgebras and how they are related.

Saleh, B. E. A. and Teich, M. C. (1991). *Fundamentals of Photonics.* New York: John Wiley & Sons, Inc.

Sammut, R. A. (1982). Momentary look at noncircular monomode fibres. *Electronics letters*, **18**, 221–222.

Shajenko, P. (1982). Multimode Optical Fibres as Sensing Devices. *Applied Optics*, **21**, 4185–4186.

Shani, Y., Henry, C. H., Kistler, R. C., Kazarinov, R. F. and Orlowsky, K.J. (1991). Integrated Optic Adiabatic Devices on Silicon. *IEEE J. Quantum Electronics*, **27**, 556–566.

Sheem, S. K. (1981). Optic Fibre Interferometers with [3 × 3] Directional Couplers: Analysis. *Journal of Applied Physics*, **52**, 3865–3872.

Shimoda, K., Takahashi, H. and Townes, C. H. (1957). Fluctuations in Amlification of Quanta with Application to Maser Amplifiers. *J. Physical Society of Japan*, **12**, 686–700.

Shoemaker, D., Fritschel, P., Glaime, J., Chrielensen, N. and Weiss, R. (1991). Prototype Michelson interferometer with Fabry-Perot cavities. *Applied Optics*, **30**, 3133–3138.

Smith, D. W. (1993, December). Progress towards end-to-end photonic networks. *Pages 87–92 of: Proc.* 18^{th} *Australian. Conf. Optical Fibre Technology.*

Snitzer, E. (1961). Maser action of Nd^{3+} in glass. *Phys. Rev. Lett.*, **7**, 444.

Snyder, A. W. and Ankiewicz, A. (1988). Optical Fiber Couplers - Optimal Solution for Unequal Cores. *IEEE J. Lightwave Tech.*, **6**, 463–474.

Snyder, A. W. and Love, J. D. (1983). *Optical Waveguide Theory.* London: Chapman & Hall Ltd.

Snyder, A. W., Mitchell, D. J., Poladian, L., Rowland, D. R. and Chen, Y. (1991). Physics of Nonlinear Fibre Couplers. *J. Optical Society America B*, **8**, 2102–2118.

Spiegel, M. R. (1974). *Vector Analysis.* New York: McGraw-Hill, Inc.

Stokes, L. F., Chodorow, M. and Shaw, H. J. (1983). Sensitive all-single-mode-fibre resonant ring interferometer. *IEEE J. Lightwave Technology*, **1**, 110–115.

Stone, J. (1974). Nd doped fiber lasers. *Applied Optics*, **13**, 1256.

Tamir, T. (1990). *Guided Wave Optoelectronics.* New York: Springer-Verlag.

Tammela, S. (1987). Co-axial Double Waveguide Single-Mode Fiber Coupler. *SPIE Fiber Optic Sensors II*, **798**, 393–395.

Thylen, L. (1983). The beam propagation method: an analysis of its applicability. *Optical and Quantum Electronics*, **15**, 433–439.

Timoshenko, S. P. (1957). *Strength of Materials.* New York: Van Nostrand.

Timoshenko, S. P. (1973). *Mechanics of Materials.* New York: Van Nostrand Reinhold.

Timoshenko, S. P. and Goodier, J. N. (1970). *Theory of Elasticity.* New York: McGraw-Hill.

Townsend, J. E., Poole, S. B. and Payne, D. N. (1987). Yb^{3+} sensitised Er^{3+} doped silica optical fibre with ultrahigh transfer efficiency and gain. *Electronics Letters*, **23**, 329–331.

Townsend, J. E., Barnes, W. L. and Jedrzejewski, K. P. (1991). Yb^{3+} sensitised Er^{3+} doped silica optical fibre with ultrahigh transfer efficiency and gain. *Electronics Letters*, **27**, 1958–1959.

Travis, A. R. L. and Carroll, J. E. (1989). The design of Optical Multiports for Coherent Detection. *Int. J. Optoelectronics*, **4**, 19–32.

Travis, A. R. L. and Carroll, J. E. (1990, December). Possible Multiport for Phase/polarisation Insensitive Coherent Detection. *Pages 297–300 of: Proc. 7th Int. Conf. Optical Fibre Sensors.*

Vance, R. W. C. and Barrow, R. (1990, December). Interferometer Considerations for an Optical Magnetometer. *Pages 245–248 of: Proc. 7th Int. Conf. Optical Fibre Sensors.*

Varadarajan, V. S. (1974). *Lie Groups, Lie Algebras and Their Representations.* New Jersey: Prentice Hall, Inc.

Walker, N. G. and Carroll, J. E. (1984). Simultaneous phase and amplitude measurements on optical signals using a multiport junction. *Electronics Letters*, **20**, 981–983.

Walpole, R. E. and Meyers, R. H. (1978). *Probability and Statistics for Engineers and Scientists.* New York: Collier Macmillan.

Wei, J. and Norman, E. (1963). Lie Algebraic Solutions of Linear Differential Equations. *J. Mathematical Physics*, **4**, 575–581.

Wei, J. and Norman, E. (1964). On Global Representations of the Solutions of Linear Differential Equations as a Product of Exponentials. *Proc. Am. Math. Soc*, 327–334.

Wilson, T. and Sheppard, C. (1984). *Theory and Practice of Scanning Optical Microscopy.* London, England: Academic Press Inc.

Wilson, T., Juskaitis, R. and Tan, J.B. (1994). Differential Imaging in Confocal Microscopy. *submitted to Journal of Microscopy.*

Yajima, H. (1973). Dielectric Thin-Film Optical Branching Waveguide. *Appl. Phys. Lett.*, **22**, 647–649.

Yajima, H. (1978). Coupled Mode Analysis of Dielectric Planar Branching Waveguides. *IEEE J. Quantum Electronics*, **QE-14**, 749–755.

Yeo, S. P. and Tey, K. H. (1989). Electromagnetic Model of Symmetrical Six-Port Waveguide Junction. *Electronics Letters*, **25**, 456–457.

Yue, C. Y., Peng, J. D., Liao, Y. B. and Zhou, B. K. (1988). Fibre ring resonator with finesse of 1260. *Electronics Letters*, **24**, 622–623.